Springer Theses
Recognizing Outstanding Ph.D. Research

Ke Wang

The Earliest Stages of Massive Clustered Star Formation: Fragmentation of Infrared Dark Clouds

Springer

Springer Theses

Recognizing Outstanding Ph.D. Research

Aims and Scope

The series "Springer Theses" brings together a selection of the very best Ph.D. theses from around the world and across the physical sciences. Nominated and endorsed by two recognized specialists, each published volume has been selected for its scientific excellence and the high impact of its contents for the pertinent field of research. For greater accessibility to non-specialists, the published versions include an extended introduction, as well as a foreword by the student's supervisor explaining the special relevance of the work for the field. As a whole, the series will provide a valuable resource both for newcomers to the research fields described, and for other scientists seeking detailed background information on special questions. Finally, it provides an accredited documentation of the valuable contributions made by today's younger generation of scientists.

Theses are accepted into the series by invited nomination only and must fulfill all of the following criteria

- They must be written in good English.
- The topic should fall within the confines of Chemistry, Physics, Earth Sciences, Engineering and related interdisciplinary fields such as Materials, Nanoscience, Chemical Engineering, Complex Systems and Biophysics.
- The work reported in the thesis must represent a significant scientific advance.
- If the thesis includes previously published material, permission to reproduce this must be gained from the respective copyright holder.
- They must have been examined and passed during the 12 months prior to nomination.
- Each thesis should include a foreword by the supervisor outlining the significance of its content.
- The theses should have a clearly defined structure including an introduction accessible to scientists not expert in that particular field.

More information about this series at http://www.springer.com/series/8790

Ke Wang

The Earliest Stages of Massive Clustered Star Formation: Fragmentation of Infrared Dark Clouds

Doctoral Thesis accepted by
Peking University, Beijing, China

Springer

Author
Dr. Ke Wang
European Southern Observatory (ESO)
Garching bei München
Germany

Supervisors
Dr. Qizhou Zhang
Harvard–Smithsonian
Center for Astrophysics
Cambridge, MA
USA

Prof. Yuefang Wu
Department of Astronomy
Peking University
Beijing
China

ISSN 2190-5053
ISBN 978-3-662-44968-4
DOI 10.1007/978-3-662-44969-1

ISSN 2190-5061 (electronic)
ISBN 978-3-662-44969-1 (eBook)

Library of Congress Control Number: 2014951331

Springer Heidelberg New York Dordrecht London

Printed on acid-free paper

Springer is part of Springer Science+Business Media (www.springer.com)

Parts of this thesis have been published in the following journal articles

Ke Wang, Qizhou Zhang, Leonardo Testi, Floris van der Tak, Yuefang Wu, Huawei Zhang, Thushara Pillai, Friedrich Wyrowski, Sean Carey, Sarah Ragan, and Thomas Henning: "Hierarchical fragmentation and differential star formation in the Galactic 'Snake': infrared dark cloud G11.11-0.12". Monthly Notices of the Royal Astronomical Society (MNRAS), 2014, 439, 3275 (Reproduced with permission).

Ke Wang, Qizhou Zhang, Yuefang Wu, Hua-bai Li, and Huawei Zhang: "Protostellar Outflow Heating in a Growing Massive Protocluster". Astrophysical Journal Letters (ApJL), 2012, 745, L30 (Reproduced with permission).

Ke Wang, Qizhou Zhang, Yuefang Wu, and Huawei Zhang: "Hierarchical Fragmentation and Jet-like Outflows in IRDC G28.34+0.06: A Growing Massive Protostar Cluster". Astrophysical Journal (ApJ), 2011, 735, 64 (Reproduced with permission).

Qizhou Zhang, Ke Wang: "IRDC G030.88+00.13: A Tale of Two Massive Clumps". Astrophysical Journal (ApJ), 2011, 733, 26 (Reproduced with permission).

Ke Wang, Yuefang Wu, Liang Ran, Wentao Yu, and Martin Miller: "The relation between ^{13}CO $J = 2 - 1$ line width in molecular clouds and bolometric luminosity of associated IRAS sources". Astronomy and Astrophysics (A&A), 2009, 507, 369 (Reproduced with permission).

To my grandma and grandpa.

Supervisor's Foreword

Analogous to the Bok globules discovered in the 1940s, infrared dark clouds (IRDCs for short) are interstellar clouds of dense gas and dust that absorb background radiation. In contrast to the Bok globules that are isolated pockets of interstellar material opaque in the optical wavelengths, IRDCs contain larger columns of dust and gas, thus appearing dark even in the infrared wavelengths. Since the early discovery in the 1990s with the *Infrared Space Observatory*, IRDCs have been found in large numbers using Galactic-wide surveys conducted by the *Midcourse Space Experiment* and the *Spitzer* and *Herschel* space telescopes.

The large reservoir of dense gas and dust in IRDCs makes them the natural nursery for stars. Relative to molecular clouds with embedded infrared sources, a lack of infrared emission combined with the large reservoir of dense gas at low temperatures makes IRDCs the ideal laboratory for investigating the early evolutionary stage of star formation.

Ke Wang's Ph.D. thesis work presented in this book focuses on the formation of massive stars. Since most massive stars are found in a cluster environment accompanied by stars with a range of stellar masses, their formation involves a cloud that collapses and fragments into multiple dense cores. The initial stellar mass function typically peaks at 0.5 $M_{\odot}$, a value that coincides well with the thermal Jeans mass for the physical conditions in the cloud that forms a massive cluster. The main difficulty in the cluster star formation is making massive stars whose masses are an order of magnitude larger than the thermal Jeans mass. To investigate the early fragmentation in cluster forming clouds, Ke Wang selected massive and dense IRDC clouds that contain sufficient gas to form massive stars with a cluster, but have few signs of star formation. Using radio interferometers, he observed these clouds at high angular resolutions to uncover the early fragmentation and to investigate the thermal dynamic state of the fragments. He found that dense cores forming massive stars are at least a factor of 10 more massive than the thermal Jeans mass, and therefore cannot be explained by thermal Jeans fragmentation. Instead, the mass of the fragments is consistent with the turbulent Jeans mass. Likewise, when comparing the fragment mass to the projected spatial separation of fragments, he found that the massive cores are consistent with a turbulent supported

fragmentation. At even higher angular resolutions, cores continue to fragment into less massive entities, indicating a hierarchical fragmentation of materials in cluster star formation.

Ke Wang's work represents one of the first high angular resolution observations directly tackling the problem of massive core formation. These observations provide direct physical insight into the formation process as well as the physical and chemical properties of the cores that form massive stars. His research lays the groundwork for further studies of a statistically significant sample to investigate the formation and evolution of massive cores. Sensitive observations with more powerful telescopes such as ALMA will offer further insight and reveal the evolution path between infant and mature massive protostars.

Cambridge, MA, August 2014

Dr. Qizhou Zhang
Astrophysicist, Harvard–Smithsonian CfA

Acknowledgments

From a kid wondering about the starry sky with his twinkling eyes to a professional astronomer making scientific discoveries using the world's most powerful telescopes, I owe appreciation to many people who have helped realize my childhood dream.

My Ph.D. adventure started at Peking University (PKU), most work was carried out at the Harvard–Smithsonian Center for Astrophysics (CfA), and this thesis was assembled during my first postdoc at the Kapteyn Astronomical Institute.

I am deeply thankful to my supervisor at Harvard CfA, Qizhou Zhang, for his motivation, guidance, and encouragement all these years. It was an honor to work with such an outstanding scientist who has immense knowledge and is always ready to help. I have learned a lot from him professionally and personally, and will continuously benefit from this in the future.

I sincerely thank my supervisor at PKU, Yuefang Wu, for introducing radio astronomy to me and guiding me all the way from my first years at PKU. As a pioneer in star formation research in China, Prof. Wu has been active in the research frontier for over half a century. Her passion for astronomy has influenced me greatly.

I am also grateful to my pre-doctoral research review committee Phil Myers and T.K. Sridharan at Harvard, for their careful review and constructive suggestions on my research progress during my stay at the CfA.

I would also like to thank the professors at the PKU astronomy department who have supervised me for short research projects or taught me various courses: Profs. Xiaowei Liu, Huawei Zhang, Renxin Xu, Xuebing Wu, Zuhui Fan, Fukun Liu, Jian Zhang, and Jiansheng Chen.

I am indebted to colleagues and friends who offered hospitality and shared experience in the many exciting (or boring) nights and days at various observatories across the world. This is the most entertaining part of being an observer. Just to name a few: Bingang Ju and Dengrong Lu at PMO for my first ever scientific

observations; the SMA operators Shelbi Hostler, Erin Brassfield, Anil Dosaj, and Ryan Howie; my fellow SMA second-shift team Sergio Martin-Ruiz and and Tim van Kempen; my VLA host Aeree Chung; my GBT friends Jim Braatz and Jaime Pineda; my CSO expert Ruisheng Peng; and my CARMA host Thushara Pillai, Jens Kauffman, and Woojin Kown. Special thanks to the SMA scheduler Glen Petipas for allowing me to make last minute changes to my observing scripts for optimal observations.

Thanks Sean Carey, Jim Jackson, Jill Rathborne, Jonathan Swift, Edward T. Chambers, Sarah E. Ragan, and Thomas Henning for sharing their data. Thanks to the referees whose comments improved the quality of my papers. Thanks to anyone who had come to my talk, poster, and who had an inspiring conversation with me during seminars and conferences.

I acknowledge financial support from the SMA pre-doctoral fellowship, China Scholarship Council, and the European Erasmus Mundus Lotus post-doctoral fellowship during my stay at Harvard and Kapteyn.

Many thanks to my group members and colleagues at Harvard, PKU, and Kapteyn for sharing the wonderful years in Cambridge/Boston, Beijing, and Groningen. The CfA group members Baobab Hauyu Liu, Roberto Galván-Madrid, Izaskun Jimenez-Serra, Daniel Espada, Keping Qiu, Xuepeng Chen, Steve Longmore, Gemma Busquet, Laura Gómez, Pau Frau, Katherine Johnstone, and Claudia Cyganowski, thank you for valuable discussion within and outside group meetings. Special thanks to Mark Reid for a number of discussions on masers. I learned a lot about radio interferometer from the SMA team members including Charlie Qi, Lei Zhu, Jinwen Wu, Mark Gurwell, Taco Ken Yong, and Bob Wilson. The many CfA predocs and postdocs including Hua-bai Li, Thushara Pillai, Jens Kauffman, Jan Forbrich, Arielle Moullet, Sofia Dai, Viven U, Tao Wang, Guanwen Fang, and Aeree Chung, have my gratitude for making daily life so wonderful in Cambridge.

Thank you, my fellow classmates and friends at PKU, for your support which made the earlier life of a Ph.D. student easier: Wei Wang, Shulin Li, Zhixia Shen, Youling Yue, Lei Qian, Xuan Fang, Xian Chen, Lei Zhu, Xin Guan, Jerry Xue, Yidong Xu, Xiaojia Zhang, Ran Li, Zhaoyu Li, Meng Yu, Shuo Li, Heling Yan, Haibo Yuan, Tie Liu, Zhiyuan Ren, and Wenwen Zuo. The PKU 2007 astronomy undergrads, it was a great pleasure to be your mentor during your first years of astronomy. I enjoyed the friendship with you all, and I hope to see you in profession in the near future.

I sincerely thank Floris van der Tak for hosting me at Kapteyn. Thanks to the group members Zsófia Nagy, Kuo-Song Wang, Evgenia Koumpia, Maja Kazmierczak, and Yunhee Choi, my officemates Eva Busekool, Federico Lelli, my friends Yanping Chen, Guobao Zhang, and Wim Zwister for a wonderful stay. I already miss the rain in Groningen.

Thank you, the crystal clear sky in the countryside of Chongqing, southwest China. Without the starry nights in childhood my life would probably be another story.

I would like to thank my mother and father for their immeasurable support for my education and career. None of my achievements would have been possible without them. I also thank my brother Shunyi for all the happiness we shared since childhood. Xiaojin, my wife, my dear love, my soul mate, thank you for all you have done for me in these years: being the first reader of my papers and books, sharing my excitement of every discovery, and encouraging me during hard times. I am so lucky to have you in my life.

Contents

Acronyms

AIPS	Astronomical Image Processing System
ALMA	Atacama Large Millimeter/submillimeter Array
APEX	Atacama Pathfinder EXperiment
ATCA	Australia Telescope Compact Array
CARMA	Combined Array for Research in Millimeter Astronomy
CASA	Common Astronomy Software Applications
CSO	Caltech Submillimeter Observatory
EVLA	Expanded Very Large Array
FCRAO	Five College Radio Astronomy Observatory
FWHM	Full-Width-Half-Maximum
GBT	Green Bank 100 m Telescope
GILDAS	Grenoble Image and Line Data Analysis Software
GRS	Galactic Ring Survey
HMSC	High-mass Starless Core
IMF	Initial Mass Function
IRAM	Institut de Radioastronomie Millimétrique
IRAS	Infrared Astronomical Satellite
IRDC	Infrared Dark Cloud
ISO	Infrared Space Observatory
JCMT	James Clerk Maxwell Telescope
JVLA	Karl G. Jansky Very Large Array
KOSMA	Kölner Observatorium für SubMillimeter Astronomie
LSR	Local Standard of Rest
LTE	Local Thermodynamic Equilibrium
MIR	Millimeter Interferometry Reduction
MIRIAD	Multichannel Image Reconstruction, Image Analysis and Display
MSX	Midcourse Space Experiment

SED	Spectral Energy Distribution
SMA	Submillimeter Array
UC HII	Ultra-compact HII region
VLA	Very Large Array
YSO	Young Stellar Object

Chapter 1
Scientific Background

1.1 Star Formation

1.1.1 A Brief History

The starry night is one of the most intriguing views from Earth. Stars are the basic elements of the Universe. Their origin is therefore a fundamental question in astronomy. Across the Milky Way, the Sun seems like a "normal" star, but it is unique for human beings. The formation of the Sun directly determines how our home planet formed, and how life originated on Earth. Since the Big Bang, generations of stars born and die. Through their life cycles, stars burn hydrogen and helium into heavier elements. These elements constitute a rich Universe today and a vibrant planet Earth, including the curious mankind itself.

Where do we come from? The "nebular hypothesis" about the origin of the Solar system was first suggested by Swedish philosopher Emanuel Swedenborg in 1743 and was then expanded by German philosopher Immanuel Kant in 1755. Later in 1796, French astronomer Pierre-Simon Laplace further developed the hypothesis (Swedenborg 1734; Kant 1755; Laplace 1796; Woolfson 1993). According to the "nebular hypothesis", the Solar system originated from a slowly rotating gaseous nebula which, due to gravity, gradually collapses and becomes flat, and finally evolves into a planetary system. Despite of historical limitations, the hypothesis is indeed suggestive in the sense that (a) it pointed out that stars are formed in gaseous nebulae (or clouds), and (b) it had realized the central role of gravity. In the same era, German-British astronomer William Herschel noticed through his observations that there are "holes" between the field stars (Herschel 1785). Until early 20th century, American astronomer Barnard realized that the "holes" are actually gaseous and dusty nebulae which obscure background starlight (Barnard 1919). Later, Dutch-American astronomer Bok pointed out that those dark nebulae, especially those globular in morphology, are birth places of stars (now known as "Bok globules", Bok 1948). This marks the beginning of modern star formation research.

K. Wang, *The Earliest Stages of Massive Clustered Star Formation: Fragmentation of Infrared Dark Clouds*, Springer Theses,
DOI 10.1007/978-3-662-44969-1_1

1.1.2 Formation of Low-Mass, Isolated Stars

Since the identification of Bok globules in 1940s, extensive observational and theoretical studies about star formation have been carried out in the following decades, finally leading to a widely accepted "standard model" in late 1980s (Shu et al. 1987). The key physical picture is, stars form through gravitational collapse of molecular clouds. Molecular clouds are widespread in the interstellar medium (ISM) (Weinreb et al. 1963; Wilson et al. 1970; Dame et al. 1987, 2001). When the cloud is massive enough, the inward gravity exceeds all outward pressure combined (including thermal pressure, turbulence, magnetic field, rotation), and the cloud starts to collapse. The critical mass due to thermal pressure (which is the dominant pressure in low-mass regime) is Jeans mass (Jeans 1928)

$$M_{\rm J} = \frac{\pi^{5/2} c_s^3}{6\sqrt{G^3\rho}} \simeq 2.8 \left(\frac{T}{10\,{\rm K}}\right)^{\frac{3}{2}} \left(\frac{n}{10^4\,{\rm cm^{-3}}}\right)^{-\frac{1}{2}} M_\odot\,. \tag{1.1}$$

Gravitational potential energy is converted into radiation which escapes through the still optically thin gas. The collapse takes a time scale of free-fall time

$$t_{\rm ff} = \left(\frac{3\pi}{32G\rho}\right)^{\frac{1}{2}} \simeq 2.6 \times 10^6 \left(\frac{n}{200\ {\rm cm^{-3}}}\right)^{-\frac{1}{2}} {\rm yr}\,. \tag{1.2}$$

That is, the densest part collapses first. This inside-out dynamical collapse finally leads the inner gas to become optically thick. Radiation cannot escape anymore, hence the gas is heated up and the inner pressure increases. This dramatic process finally lead to the thermonuclear fusion of hydrogen in the Kelvin-Helmholtz time scale

$$t_{\rm KH} = \frac{GM_\star^2}{R_\star L_\star} \simeq 3 \times 10^7 \left(\frac{M_\star}{1M_\odot}\right)^2 \left(\frac{R_\star}{1R_\odot}\right)^{-1} \left(\frac{L_\star}{1L_\odot}\right)^{-1} {\rm yr}\,. \tag{1.3}$$

The "standard model" involves the following stages.

Stage 1—Formation of a slowly rotating core embedded in a molecular cloud clump. Initially, turbulence and magnetic fields balance the self gravity of the clump, but the supports gradually leak through ambipolar diffusion. Supercritial clumps contract and may fragment into multiple cores.

Stage 2—Inside-out dynamic collapse of cores. Embedded in the collapsing envelope of gas and dust is a protostar which grows through disk accretion. The protostar accrets mass from the disk, and the disk is fed by gas infall from the envelope. The two accretion processes dominate the luminosity of the protostar.

Stage 3—Formation of bipolar outflows. Channeled by stellar winds, the extra angular momentum brought into the disk from accretion is ejected out through the rotational poles, where resistance is weakest resistance. This leads to collimated jets and bipolar outflows. In general, the protostar gains a net growth by accretion and outflows.

Stage 4—Protostar and a circumstellar disk. The outflow opening angle widens as time proceeds, and eventually sweeps up most materials in the 4π steradians, revealing the protostar and a surrounding remnant disk.

Afterwards, planets form in the circumstellar disk and a star-planet system is born. This stage is often refereed as pre-main sequence evolution of a star, but sometimes it is also known as Stage 5 of star formation.

This classic model describes the formation of an isolated, solar-like star. It has been largely confirmed by observations in the past decades. By comparing optical dark clouds (especially Bok globules) and *Infrared Astronomical Satellite* (IRAS) infrared point source catalog, a large number of young stellar objects (YSOs) are identified. Spectral energy distribution (SED) of YSOs are used to infer the amount of dust, in order to classify the evolutionary stages. Observationally, YSOs are categorized in four classes (Class 0, I, II, III) according to SED features, roughly correspond to Stage 2–5.[1] The "dark cloud" in Fig. 1.1 is younger than Class 0, sometimes referred as Class -1.

1.1.3 Formation of High-Mass Stars in Clusters

The standard model for low-mass star formation cannot be directly applied to high-mass stars. Observations show that most stars, including low- and high-mass stars, are formed in clusters, where high-mass stars are almost exclusively found near the center of a cluster (Lada and Lada 2003). The stellar initial mass function (IMF) of a cluster, which describes the number of stars as a function of stellar mass, is in the form of (Kroupa 2001)

$$\xi(m) \propto m^{-\alpha}, \alpha = \begin{cases} 2.3, & 0.5 < m/M_\odot < 50 \\ 1.3, & 0.08 < m/M_\odot < 0.5 \\ -0.3, & 0.01 < m/M_\odot < 0.08 \end{cases} \tag{1.4}$$

IMF was originally pointed out by Salpeter (1955), when the index α was found to be 2.35 for $m > 1\,M_\odot$ stars, a value that is still very close to observations today. The high-mass part of IMF is also known as Salpeter function. IMF appears to be universal in different clusters, indicating that the stars are formed in the same way. Because stellar mass is a fundamental parameter that determines stellar properties, any cluster formation theory should reproduce IMF. The form of IMF shows that the number of stars drops dramatically towards the high-mass end. In the Milky Way, high-mass stars make up only about 1 % in number, but they provide about 99 % of the ultra-violet (UV) photons (Kennicutt 1998).

[1] In fact, for a given YSO, the observed SED is determined by many factors (e.g., geometric orientation in the sky) beside the evolutionary stage, therefore statistical study and modeling is needed (Robitaille et al. 2007).

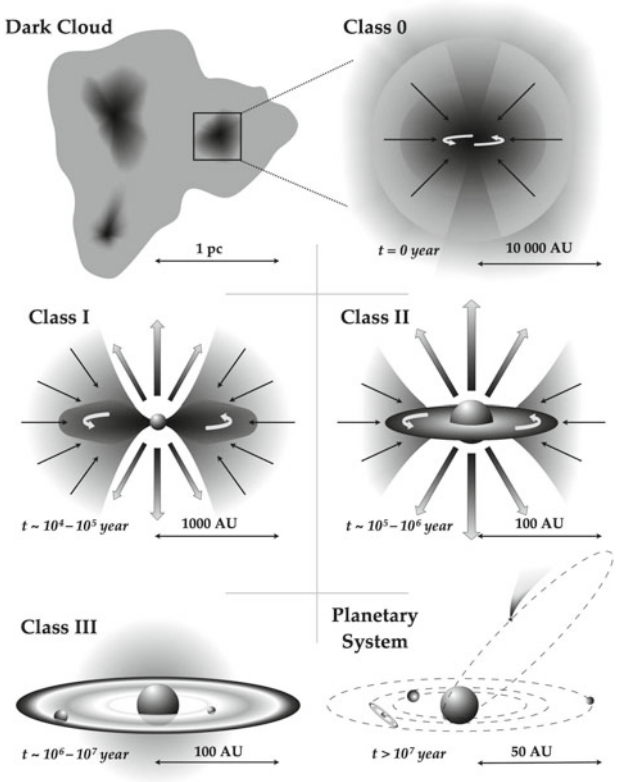

Fig. 1.1 Evolutionary phases in the "standard model" for low-mass star formation, from *dark clouds* to *planetary systems*. The classification is inferred based on SED features (Class 0, I, II, III). *Dark clouds* are sometimes referred as Class −1 [*Credit* Dishoeck and Blake (1998), Frieswijk (2008), reproduced with permission of Prof. Ewine van Dishoeck]

Conventionally, stars weigh heavier than $8\,M_\odot$ are defined as high-mass stars, corresponding to spectral type B3. These stars have two important difference than their low-mass counterpart: (1) The peak of their SEDs shifts to UV. UV radiation can ionize the parent molecular cloud, and thereby change its physical properties; (2) $t_{\rm KH} \lesssim t_{\rm ff}$, the time scale to contract and light hydrogen burning is comparable or less than free-free time scale, which means that high-mass stars continue to accrete mass after they turn to the main sequence. In another word, high-mass stars do not have a "pre-main sequence" similar to low-mass stars. For example, an O-type star spends 10–20 % time of its main sequence embedded in the molecular cloud where it is born.

The formation and early evolution of high-mass stars is an important open question in astronomy today. Compared to low-mass stars, high-mass stars are much less in number, but they dominate the evolution of interstellar medium (ISM) and galaxies. From birth to death, high-mass stars dramatically influence the ISM throughout

their life cycles: during formation, the accreting protostars inject numerous energy and momentum into the ISM through massive outflows; during their short life, energetic stellar winds and UV radiation ionize the ambient ISM; their death follows stunning supernovae which return the enriched material into the ISM. The entire process takes only the order of 10^6 yrs. Generation by generation, high-mass stars shape the physical and chemical properties of the ISM, and affect next generation of star formation. Despite of their defining importance, the formation of high-mass stars is still a mystery. Both theory and observation face many challenges (Beuther et al. 2007; Zinnecker and Yorke 2007).

1.1.3.1 Theoretical Models

The key problem is that the radiation pressure from forming high-mass protostars can reach high enough to halt accretion, and therefore stop the growth in mass. This is the so-called "radiation pressure problem" or "luminosity problem". Assuming spherically symmetric accretion, the upper limit of the stellar mass is 10 $M_\odot$ (Wolfire and Cassinelli 1987). But of course, more massive stars do exist. Theoretical models must overcome this problem and let the mass build up continue. Two major models have been proposed.

In the "monolithic collapse" model (McKee and Tan 2002, 2003; Krumholz et al. 2005, 2009), high-mass stars form through mass accretion similar to low-mass stars, but with two orders of magnitude higher accretion rate. Radiation pressure leaks through a cavity penetrated by outflow jets. In this model, all final stellar mass comes from the initial core which harbor the protostar.

In the "competitive accretion" model (Bonnell et al. 1997, 2004; Bonnell and Bate 2006), molecular cloud clumps first fragment into cores of Jeans mass, each core forms a low-mass protostar, then all these protostars accrete mass competitively from a general pool of gravitationally unbound gas within the clump to continue mass build up. The accretion rate is proportional to the already bound core mass, known as Bondi-Hoyle accretion. The final stellar mass is determined by the result of the competition.

Both models are able to reproduce the IMF, but the origin of final stellar mass is different: either from the immediate core (monolithic collapse) or from the larger, more general clump (competitive accretion).

1.1.3.2 Observational Studies

Ideally, in order to test theoretical models, a picture of the early evolutionary should be established through observational studies. However, observations of high-mass star formation regions face several challenges, including a small sample size, large distance, clustered environment, and heavy extinction. Because of their fast evolution, it is difficult to sample different evolutionary phase from observations; typical distance to high-mass star forming regions are several kilo parsecs (kpc) which is at least 10 times more distant than low-mass star formation regions; high-mass

stars form in a clustered environment which usually involves confusion; high-mass stars continue to accrete after main sequence, while they are still heavily embedded in dense molecular cores, invisible at wavelengths up to mid-infrared (MIR). Therefore, observational studies of high-mass star formation regions, especially the early phases, have been focusing on infrared and (sub)millimeter regimes. But at long wavelengths resolution becomes an severe issue. Nevertheless, in the past two decades, remarkable progresses have been made by numerous observations using space-based infrared telescopes and ground-based radio telescopes (including single dish and interferometers). Upon until now, several stages are recognized.

The first stage is a massive, cold molecular clump which embeds denser cores. Example of this stage are infrared dark clouds (IRDCs) identified in late 1990s (Perault et al. 1996; Egan et al. 1998; Carey et al. 1998). IRDCs are cold and dense molecular clouds that appear as shadows in the MIR sky, when viewed against bright Galactic background radiation. They have a large range of mass and size ($<10^2$–$10^4\,M_\odot$, 1–10 pc). Dense clumps embedded in IRDCs are thought to be birthplaces of high-mass stars. Recent observations show that most IRDCs do not show active star formation activities in general, but faint IR point sources are found in some local clumps, which are likely new born protostars (Sect. 1.2.2).

The second stage is high-mass protostellar objects (HMPOs) (Sridharan et al. 2002; Beuther et al. 2002). At this stage, the still accreting central protostar has reached 8 $M_\odot$. Accretion luminosity makes HMPOs bright in mid- and far-IR. When radiative heating elevates the temperature of the envelope up to >100 K, numerous molecules are evaporated from ice mantles to gas phase. This stage is also known as hot cores, characterized by rich spectral lines, including those from complex organic molecules.

The third stage is HII regions. At this stage the UV radiation from the protostar starts to ionize the ambient gas; observable are free-free emission and H radio recombination lines. The star enters main sequence and starts to sweep up circumstellar materials. The ionized region expands from hyper-compact HII region, ultra-compact HII region, to HII region.

Of course, the boundaries of these three stages are not sharp at all. For example, some IRDCs can contain HMPOs in local clumps. Historically, due to technical reasons, our understanding of these stages is in the reversed order: HII regions first, then HMPOs, and the studies on IRDCs emerge only in recent years. This thesis focuses on IRDCs.

1.1.4 Questions Raised

The outstanding question is, what determines the final stellar mass, the immediate core, or the larger clump? In Chap. 2 we will see that high-mass stars indeed tend to form in more massive molecular structures. More and more studies show that the core mass function (CMF) has a similar form to IMF (Könyves et al. 2010), suggesting that the stellar mass function is determined by the formation of the cores, i.e., the fragmentation of molecular clouds.

Controversy between the aforementioned two major theories continues since more than a decade ago. Recent observations reveal outflow-disk systems in high-mass protostars similar to their low-mass counterpart (Zhang et al. 1998; Beuther et al. 2002; Keto 2002; Zhang 2005; Cesaroni et al. 2007a; Kraus et al. 2010). This seems to favor a scaled up version of disk accretion. The monolithic collapse model requires high-mass protostars to have accumulated all the mass before the core collapse. The model assumes an initial core mass of the order $10^2\,M_\odot$. However, typical temperature and density in massive star formation clumps determine a Jeans mass of about $1\,M_\odot$. This presents a theoretical puzzle, since more massive cores are unstable against fragmentation. How to suppress fragmentation? Krumholz (2006) and Krumholz et al. (2010) point out that the radiative heating from previously formed low-mass stars can elevate the temperature up to 100 K, or to change the equation of state of the gas, making the M_J to increase to $10^2\,M_\odot$; alternatively, McKee and Tan (2002) start directly from cold cores of $10^2\,M_\odot$.

Still, the question is unresolved. Do high-mass stars form from competitive accretion of Jeans mass cores (Bonnell et al. 1997, 2004), or from monolithic collapse of massive cores (McKee and Tan 2002)? If the latter, how are the massive cores supported against fragmentation? By protostellar heating (Krumholz et al. 2005), turbulence (Padoan and Nordlund 2004; Gong and Ostriker 2011), or magnetic fields?

This thesis addresses these questions by observational studies. First, I carry out a survey towards a large sample, and study the statistical difference between the initial conditions of low- and high-mass star formation. Then, I use high-resolution interferometric imaging to study how IRDC clumps fragment to initiate massive star formation. Finally, based on these observations, I suggest an evolutionary picture from the fragmentation of molecular clouds to the formation of high-mass protostars. This is the first general picture for the early phase prior to hot cores.

1.2 Targets and Observing Strategy

1.2.1 Infrared Point Sources

In 1983, the *Infrared Astronomical Satellite* (*IRAS*) accomplished the first all sky mapping in mid-IR and far-IR (12, 25, 60, 100 μm) and released a point source catalog (PSC, Beichman et al. 1988). Similar to the study of low-mass YSOs, identification of high-mass YSOs is inferred form the *IRAS* color, based on SED characters. Using color-color diagram (Wood and Churchwell 1989, hereafter WC89) noticed that sources associated with known UC HII show distinguishable colors than other *IRAS* point sources. This is because, those point sources have embedded young massive O stars, thus have similar SED properties. WC89 then suggested a color criteria to identify sources with OB stars embedded. The WC89 color criteria selected 1,717 such candidates, which became samples for many follow up studies (Zhang et al. 2001; Sridharan et al. 2002; Beuther et al. 2002; Zhang et al. 2005; Wang et al. 2009). Later, other color criteria were developed to identify earlier stages like HMPOs

(Chap. 2; Molinari et al. 1998; Palla et al. 1991). However, the presence of infrared point source means internal heating has started, therefore this stage is obviously not the earliest stage in evolution. Millimeter/sub-millimeter continuum sources without an infrared counterpart, present an even earlier stage known as high-mass starless cores (HMSC, Sridharan et al. 2005). Studies of stages earlier than HMPOs rely on IR surveys with a higher sensitivity (Sect. 1.2.2).

1.2.2 Infrared Dark Clouds

Indicated by the name, "infrared dark clouds" (IRDCs) are dark clouds observed at infrared wavelength (Fig. 1.2). Like optical dark clouds (Sect. 1.1.1), the discovery of

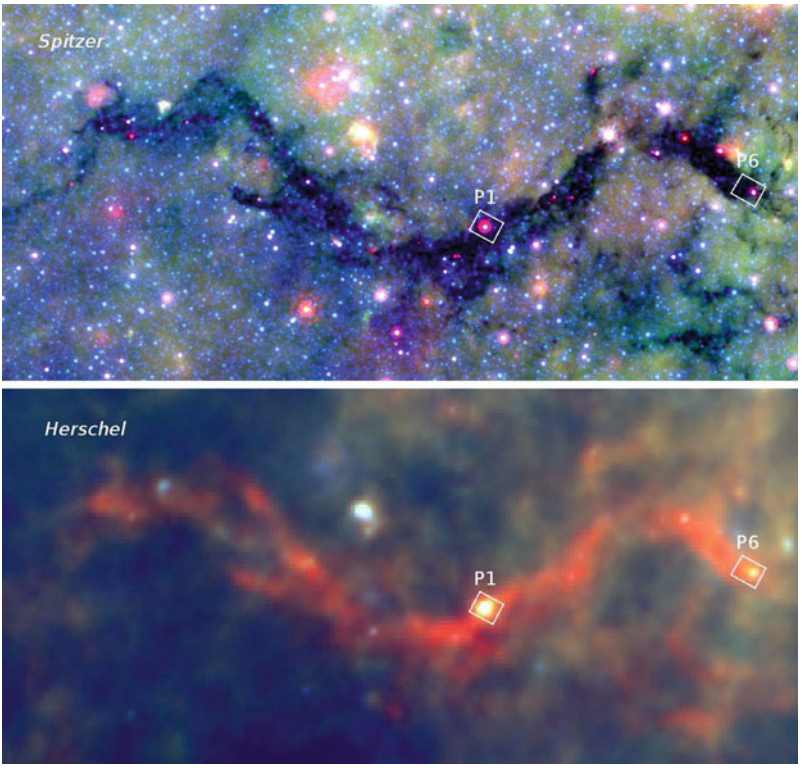

Fig. 1.2 Panoramic view of the Snake nebula (G11.11–0.12), a prime example of IR-dark clouds. The *upper* panel shows a *Spitzer* composite view at mid-infrared wavelengths (*red*/*green*/*blue* = 24/8/4.5 μm), outlining the dark features; the *lower* panel shows a *Herschel* composite image at far-infrared wavelengths (*red*/*green*/*blue* = 350/160/70 μm), highlighting the emission from cold dust. The match between the absorption and emission between the mid-IR and far-IR views indicates that the dust is cold (about 15 K). Two *white boxes* label regions we zoom-in with SMA deep imaging (Chap. 4) [*Credit* Ke Wang (ESO)]

infrared dark clouds was never intended. In 1995–1998, the European and US space missions *Infrared Space Observatory* (*ISO*) and *Midcourse Space Experiment* (*MSX*) surveyed the Galactic plane in selected regions. *ISO* mapped $| l | \leq 45°$, $| b | \leq 6°$ at 7 and 15 μm; *MSX* mapped $| l | \leq 91°$, $| b | \leq 6°$ at four bands between 4 and 25 μm. Both surveys revel a large population of dark clouds widely spread over the Galactic plane. Those IRDCs have optical depth of 1–4 at mid-IR wavelengths (Carey et al. 1998; Hennebelle et al. 2001). Compared with *IRAS* data, majority of the IRDCs are dark at 7–100 μm, and are filamentary in morphology. IRDCs do not appear to be associated with any known molecular structures, and they represent a new type of "newly discovered, cold, dense, and isolated clouds" (Egan et al. 1998; Hennebelle et al. 2001).

Carey et al. (1998, 2000) were among the first to observe IRDCs in molecular line (H_2CO) and dust continuum (450, 850 μm). They conclude that IRDCs are by nature cold and dense molecular clouds. Later, more observations in CO and NH_3 unveil typical temperature $T < 20$ K and density $n > 10^5$ cm^{-3} in IRDCs (Carey et al. 1998; Pillai et al. 2006). Millimeter/sub-millimeter dust continuum observations find typical size of IRDCs 1–10 pc, mass 10^2–10^3 $M_\odot$, and that IRDCs often harbor denser clumps. The clumps have a similar mass and size to molecular clumps with known massive YSOs, but have a lower luminosity and smaller line width, therefore they are thought to be precursors to massive YSOs(Sridharan et al. 2005; Ragan et al. 2006; Rathborne et al. 2006).

Simon et al. (2006a) and Peretto and Fuller (2009) generated comprehensive IRDC catalogs based on *MSX* and *Spitzer* Galactic plane surveys, respectively. Each of the catalog contains about 11,000 IRDCs, but 80 % of the sources do not overlap between the two catalogs. Simon et al. (2006b) matched the *MSX* catalog with the ^{13}CO (1–0) emission obtained from the Galactic Ring Survey (GRS, Jackson et al. 2006), and determined radial velocity of 313 IRDCs in the first Galactic quadrant, then calculated kinematic distance. Jackson et al. (2008) determined kinematic distance to 210 IRDCs in the fourth Galactic quadrant directly using CS (2–1). Those IRDCs distributed well in the Scutum-Centaurus arm of the Milky Way (Fig. 1.3). Because in normal spiral galaxies, OB stars concentrate on spiral arms, the spatial distribution of IRDCs suggest they are closely related with massive star formation.

Launched in 2009, the *Herschel* space observatory made the first Galactic plane survey in far-IR and sub-millimeter wavelengths (Molinari et al. 2010), making it possible to measure the full SED at all key wavelengths of star-forming clouds. IRDCs absorb Galactic background mid-IR emission,[2] and emit at longer wavelengths (far-IR, mm/submm). Figure 1.2 shows a comparison between mid-IR and far-IR views of a typical IRDC G11.11–0.12. The cold dust in the cloud glows at far-IR. By fitting SED of each pixel, Peretto et al. (2010) find in most IRDCs that the temperature drops towards into the dense center, indicating the lack of an internal heating source and suggest the IRDCs are about to or undergo collapse and fragmentation (Larson 2005). G11.11–0.12 shows a filamentary morphology. Sensitive *Herschel* images

[2] Mainly emitted from polycyclic aromatic hydrocarbons (PAHs) concentrated at 3.3, 6.2, 7.7, 8.6, and 11.2 μm (Tielens 2008).

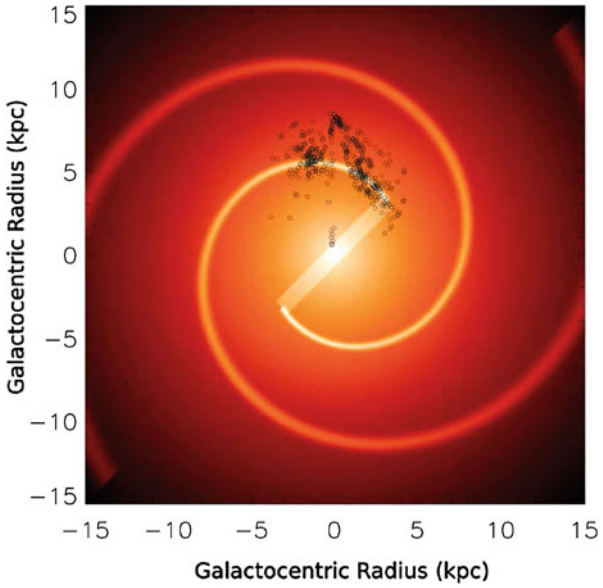

Fig. 1.3 Galactic distribution of IRDCs superimposed on the Milky Way spiral arm model (Benjamin et al. 2006). IRDCs are concentrated on spirial arms, indicating their close connection with the formation of OB stars [*Credit* Jackson et al. (2008), reproduced with permission of the AAS]

have revealed a large number of filamentary structures associated with IRDCs (André et al. 2010; Men'shchikov et al. 2010), and all nearest low-mass star forming clouds are filamentary (Myers 2009), indicative a close connection between filaments and molecular cloud fragmentation and subsequent star formation.

The identification of a large number of IRDCs have significantly enlarged the sample size of high-mass star formation regions. Because of their extreme physical properties, IRDCs are ideal laboratories to study early evolutionary stages. Since the first identification, IRDCs have soon become the frontier in the study of high-mass star formation. Deep millimeter and sub-millimeter dust continuum images have revealed dense molecular clumps ($\sim$1 pc, $\sim 10^3\,M_\odot$) that are suitable to form massive star clusters (Rathborne et al. 2006). Majority of those clumps do not show significant star formation activities, but some of them do show some signatures, for example: faint mid-IR point sources (YSOs), diffuse 4.5 μm emission (trace outflow shocks), and masers (excited by protostars) (Wang et al. 2006; Chambers et al. 2009; Cyganowski et al. 2008). Among these IRDC clumps, massive ($\gtrsim 10^3\,M_\odot$), low-lumonosity ($\lesssim 10^3\,L_\odot$) ones are excellent targets to study the early phase of massive star formation.

In summary, studies on IRDCs have opened a new era in observational study of massive star formation. Numerical simulations and analytic works have started to incorporate observations of IRDCs. We have learned much new knowledge about the early phase in high-mass star formation during the past 15 years, and given time, the study of IRDCs will largely advance our understanding of high-mass star formation.

However, most studies of IRDCs so far have used single dish telescopes with low angular resolution, and no dedicated high-angular-resolution studies have been performed on the structure of IRDC clump and the fragmentation of filaments their in. These are the main focus of this thesis.

1.2.3 Radio Interferometer

As aforementioned, the typical temperature of molecular clouds determines the peak of their SEDs to fall in far-IR wavelengths. However, the Earth's atmosphere is opaque at far-IR, therefore ground-based telescopes can hardly observe at far-IR, even at sites with extremely good weather condition. Space-based telescopes can, of course, but are much more expensive and cannot be used routinely. The most recent far-IR space observatory *Herschel* has a diameter of 3.5 m, the largest ever space telescope, reaching a 25″ resolution at 350 μm, but still insufficient for high-resolution studies. For reference, 1″ is equivalent to 1 AU at a distance of 1 pc. Typical distance of high-mass star formation regions is several kpc, where 1″ corresponds to several 10^3 AU. This is the typical size of accretion disks around massive protostars (Cesaroni et al. 2007b). Therefore, detailed observations of high-mass star formation regions typically require angular resolutions of better than 1″. No existing far-IR telescopes can reach such a resolution. Fortunately, at longer wavelengths, in the sub-millimeter, millimeter, and centimeter regimes, sub-arcsecond resolution can be archived routinely using aperture synthesis technique—through radio interferometers. In the past decades, observational studies in star formation usually start with sing dish surveys of a large sample, and then select the most promising sources to be observed with high-resolutions using interferometers.

Radio astronomy has a short history. In 1932, radio engineer Jansky accidentally discovered the radio emission from the Milky Way, marking the birth of radio astronomy (Jansky 1933a, b). Inspired by Jansky's discovery, Grote Reber built a dedicated antenna to confirm the discovery. He then performed the first radio survey of the sky and found many radio sources (Reber 1940, 1944). In the entire 1940s, Reber was probably the only radio astronomy in the world. After the world war II, radar technique was applied to radio astronomy and large telescopes and interferometers were built in the following decades. Nowadays, major telescopes working in the submm/mm/cm wavelength regime include interferometers JVLA, SMA, PdBI, CARMA, and single dishes GBT, APEX, IRAM, KOSMA, JCMT, CSO, Mopra and Nobeyama. The next generation submm/mm interferometer ALMA (Atacama Large Millimeter/submillimeter Array) has started early science observations since 2011 and has been officially inaugurated in 2013. More about radio telescopes and interferometers can be found in text books (Wilson et al. 2009; Taylor et al. 1999).

A radio interferometer comprises of n antennae spread out in a certain area. Connection between any of the two antennae form a so-called "baseline". There are $n(n-1)/2$ baselines in total. The direct measurement is the interference pattern (also known as "correlation") of each antenna pair. By accurately measuring the phase of

the correlation one can derive the spatial distribution of the emission source, at a resolution equivalent to a single dish with a diameter of the baseline length. One sampling returns $n(n-1)/2$ vectors, including amplitude and phase (orientation of the baseline with respective to the source), called "visibility". Suppose we sample once per 3 s, a huge amount of data will be obtained during a few hours of observation. Following the rotation of the Earth, the baseline network projected on to the source changes and steadily fill in the (u, v) space, which is the Fourier transformation of the source image. Therefore, to obtain the source image in (x, y) space, one needs to perform inverse Fourier transform offline. This is called "imaging". In real observations, astronomical signals always come with noise of different origins: some from the atmosphere, and some from the instrument. Separating signal from noise is done offline in calibration. Usually there are three standard calibrations: (1) antenna gain in amplitude and phase as a function of time (sometimes simply called "gain calibration" or "phase calibration"); (2) bandpass gain as a function of frequency; and (3) absolute flux calibration. The latter two calibrations are the same as single dish telescopes, i.e., through observation of standard sources with known flux and bandpass shape. The antenna gain is special for interferemeters; it is calibrated by periodically switching the telescope from the source to a nearby calibrator (a bright point source, usually a quasar), interpolating the antenna gain measured from the calibrator (nearby therefore signal passes through similar atmosphere), and applying the gain to the source. Calibration and imaging are accomplished after observations using dedicated software.

The resolution of an interferometric observation is determined by the projected length of all the baselines, where longer baselines probe smaller angular scales. The final resolution is in between the two angular scales corresponding to the shortest and longest baselines. In practice, the resolution, called the synthesized beam, is a fitting to all the visibility data points weighted in a certain way. The weighting can be regarded as part of the (u, v) sampling, and will be de-convolved in the imaging process. Therefore, based on the needs of the research, we can weight the visibility data in different ways. For example, "natural weighting" takes the density of data points in the (u, v) space, resulting the highest sensitivity in the final image; the "uniform weighting" method weights each data point equally, resulting the highest resolution; and the "robust weighting" allows observers to optimize between resolution and sensitivity. In some cases, it is useful to perform additional edition to the (u, v) data, for example to select only the shorter baselines or to taper longer baselines, in order to achieve a less elongated and more round synthesized beam, for a short observation (e.g., Sect. 4.2.2).

As one can imagine, the shortest possible baseline between two antennae is the sum of the radii of the two dishes. The shortest baseline determines the largest angular scale an interferometer can probe. Larger scales are filtered out, known as "flux missing" or "short spacing" problem. Adding data from single dish telescopes can solve the problem. A single dish telescope of a diameter D can be regard as an interferometer which consists of infinite number of baselines ranging from $0-D$. For high-resolution studies the short spacing is not critical, but if large scale is concerned, single dish data should be combined. For instance, the Institut de Radioastronomie Millimétrique (IRAM) 30 m telescope is usually used to fill the zero spacing for the

Plateau de Bure Interferometer (PdBI). The next generation interferometer ALMA has a dedicated compact array and a total power array specifically designed to overcome this problem.

The field of view (FoV) of a radio interferometer is determined by the primary beam of each elementary antenna. Primary beam is the antenna response as a function of spatial direction projected on the plane of the sky, usually close to a 2D Gaussian function. The full-width-half-maximum (FWHM) of the Gaussian function is used to describe the primary beam size. Outside of the FWHM, the antenna response is usually not well characterized. A single-pointing observation probes a sky area roughly the primary beam size.[3] Extended sources larger than the primary beam can be covered by mosaic observations, which combines individual pointings Nyquist sampled over the source size. On-the-Fly (OTF) mapping (Mangum et al. 2007), a technique widely used in single dish observations, is planned for ALMA, the first time for an interferometer (Rodríguez-Fernández et al. 2012).

1.3 Thesis Outline

This thesis aims to establish a general evolutionary picture of the extremely early phase of massive clustered star formation through observational studies. In Chap. 2, we select from the *IRAS* point source catalog a sample of 135 extremely red YSOs and perform a survey in ^{13}CO (2 – 1) using the KOSMA 3 m telescope. Combining our new survey with data in the literature, we find a correlation between the line width in molecular clouds and bolometric luminosity of associated infrared point sources, which suggests that massive stars tend to form in more turbulent cloud structures.

In Chaps. 3, 4, and 5, we present high-resolution observational studies of three massive, low-luminosity IRDCs: G28.34+0.06, G11.11–0.12, and G30.88+0.13, respectively. These IRDCs are the most well studied IRDCs and represent slightly different evolutionary stages. We use SMA to observe mm/submm continuum and spectral line emission, JVLA to observe multiple inverse transitions of NH_3 as well as H_2O and CH_3OH masers, and GBT to observe NH_3 transitions. The SMA dust continuum images resolve the detailed structure and fragmentation; the wide-band SMA spectral line data cover outflow tracers (e.g., CO, SiO) and characteristic hot core lines (e.g., CH_3OH, CH_3CN); NH_3 is a good thermometer in dense and cold gas; finally, masers are signatures of star formation activities. Our high-resolution, high-sensitivity observations reveal a common picture of hierarchical fragmentation where turbulence plays a dominant role, which challenges some of the leading theoretical models.

Chapter 6 summarizes the findings, implications, and future perspectives, and suggest a new observational-driven picture of how massive star formation in a clustered environment may begin.

[3] In fact, signals beyond the FWHM size is received as well, but dramatically attenuated. In some rare cases, if the signal is strong (e.g., masers) it can affect the source within the FoV (e.g., Sects. 4.2.2 and 5.3.3).

References

André, P., Men'shchikov, A., Bontemps, S., Könyves, V.,Motte, F., Schneider, N., Didelon, P., Minier, V., Saraceno, P., Ward-Thompson, D., di Francesco, J., White, G., Molinari, S., Testi, L., Abergel, A., Griffin, M., Henning, T., Royer, P., Merín, B., Vavrek, R., Attard, M., Arzoumanian, D., Wilson, C.D., Ade, P., Aussel, H., Baluteau, J., Benedettini, M.,Bernard, J., Blommaert, J.A.D.L., Cambrésy, L., Cox, P., di Giorgio, A., Hargrave, P., Hennemann, M., Huang, M., Kirk., J., Krause, O., Launhardt, R., Leeks, S., Le Pennec, J., Li, J.Z., Martin, P.G., Maury, A., Olofsson, G., Omont, A., Peretto, N., Pezzuto, S., Prusti, T., Roussel, H., Russeil, D.,Sauvage, M., Sibthorpe, B., Sicilia-Aguilar, A., Spinoglio, L., Waelkens, C., Woodcraft, A., Zavagno, A.: From filamentary clouds to prestellar cores to the stellar IMF: Initial highlights from the Herschel Gould Belt Survey.Astron. Astrophys. **518**, L102 (2010). doi:10.1051/0004-6361/201014666, arXiv:1005.2618

Barnard, E.E.: On the dark markings of the sky, with a catalogue of 182 such objects. Astrophys. J. **49**, 1–24 (1919). doi:10.1086/142439

Beichman, C.A., Neugebauer, G., Habing, H.J., Clegg, P.E., Chester, T.J. (eds.) Infrared astronomical satellite (IRAS) catalogs and atlases. Volume 1: Explanatory Supplement, vol. 1 (1988)

Benjamin, R.A., Churchwell, E., Haffner, M.: GLIMPSE team the sagittarius spiral arm of the galaxy: now you see it, now you don't. In: American Astronomical Society Meeting Abstracts, Bulletin of the American Astronomical Society, vol. 38, p. 242.05 (2006)

Beuther, H., Schilke, P., Menten, K.M., Motte, F., Sridharan, T.K., Wyrowski, F.: High-mass protostellar candidates. II. Density structure from dust continuum and CS emission. Astrophys. J. **566**, 945–965 (2002a). doi:10.1086/338334, arXiv:astro-ph/0110370

Beuther, H., Schilke, P., Sridharan, T.K., Menten, K.M., Walmsley, C.M., Wyrowski, F.: Massive molecular outflows. Astron. Astrophys. **383**, 892–904 (2002b). doi:10.1051/0004-6361:20011808, arXiv:astro-ph/0110372

Beuther, H., Churchwell, E.B., McKee, C.F., Tan, J.C.: The Formation of massive stars. Protostars and Planets V pp. 165–180 (2007). arXiv:astro-ph/0602012

Bok, B.J.: Dimensions and masses of dark nebulae. Harv. Obs. Monogr. **7**, 53 (1948)

Bonnell, I.A., Bate, M.R.: Star formation through gravitational collapse and competitive accretion. Mon. Not. RAS **370**, 488–494 (2006). doi:10.1111/j.1365-2966.2006.10495.x, arXiv:astro-ph/0604615

Bonnell, I.A., Bate, M.R., Clarke, C.J., Pringle, J.E.: Accretion and the stellar mass spectrum in small clusters. Mon. Not. RAS **285**, 201–208 (1997)

Bonnell, I.A., Vine, S.G., Bate, M.R.: Massive star formation: nurture, not nature. Mon. Not. RAS **349**, 735–741 (2004). doi:10.1111/j.1365-2966.2004.07543.x. arXiv:astro-ph/0401059

Carey, S.J., Clark, F.O., Egan, M.P., Price, S.D., Shipman, R.F., Kuchar, T.A.: The physical properties of the midcourse space experiment galactic infrared-dark clouds. Astrophys. J. **508**, 721–728 (1998). doi:10.1086/306438

Carey, S.J., Feldman, P.A., Redman, R.O., Egan, M.P., MacLeod, J.M., Price, S.D.: Submillimeter observations of midcourse space experiment galactic infrared-dark clouds. Astrophys. J. Lett. **543**, L157–L161 (2000). doi:10.1086/317270

Cesaroni, R., Galli, D., Lodato, G., Walmsley, C.M., Zhang, Q.: Disks around young O-B (Proto) stars: observations and theory. In: Reipurth, B., Jewitt, D., Keil, K. (eds.) Protostars and Planets V, pp. 197–212 (2007a)

Cesaroni, R., Galli, D., Lodato, G., Walmsley, C.M., Zhang, Q.: Disks around young O-B (Proto) stars: observations and theory. Protostars and Planets V, pp. 197–212 (2007b). arXiv:astro-ph/0603093

Chambers, E.T., Jackson, J.M., Rathborne, J.M., Simon, R.: Star formation activity of cores within infrared dark clouds. Astrophys. J. Suppl. **181**, 360–390 (2009). doi:10.1088/0067-0049/181/2/360

Cyganowski, C.J., Whitney, B.A., Holden, E., Braden, E., Brogan, C.L., Churchwell, E., Indebetouw, R., Watson, D.F., Babler, B.L., Benjamin, R., Gomez, M., Meade, M.R., Povich, M.S., Robitaille,

T.P., Watson, C.: A catalog of extended green objects in the GLIMPSE survey: a new sample of massive young stellar object outflow candidates. Astron. J. **136**, 2391–2412 (2008). doi:10.1088/0004-6256/136/6/2391, arXiv:0810.0530

Dame, T.M., Ungerechts, H., Cohen, R.S., de Geus, E.J., Grenier, I.A., May, J., Murphy, D.C., Nyman, L.A., Thaddeus, P.: A composite CO survey of the entire milky way. Astrophys. J. **322**, 706–720 (1987). doi:10.1086/165766

Dame, T.M., Hartmann, D., Thaddeus, P.: The milky way in molecular clouds: a new complete CO survey. Astrophys. J. **547**, 792–813 (2001). doi:10.1086/318388, arXiv:astro-ph/0009217

Egan, M.P., Shipman, R.F., Price, S.D., Carey, S.J., Clark, F.O., Cohen, M.: A population of cold cores in the galactic plane. Astrophys. J. Lett. **494**, L199 (1998). doi:10.1086/311198

Frieswijk, W.: Early stages of clustered star formation: massive dark clouds throughout the Galaxy. (2008). irs.ub.rug.nl/ppn/308037146

Gong, H., Ostriker, E.C.: Dense core formation in supersonic turbulent converging flows. Astrophys. J. **729**, 120 (2011). doi:10.1088/0004-637X/729/2/120, arXiv:1101.2650

Hennebelle, P., Pérault, M., Teyssier, D., Ganesh, S.: Infrared dark clouds from the ISOGAL survey. Constraints on the interstellar extinction curve. Astron. Astrophys. **365**, 598–611 (2001). doi:10.1051/0004-6361:20000052

Herschel, W.: On the construction of the heavens. Royal Society of London Philosophical Transactions Series I. **75**, pp. 213–266 (1785)

Jackson, J.M., Rathborne, J.M., Shah, R.Y., Simon, R., Bania, T.M., Clemens, D.P., Chambers, E.T., Johnson, A.M., Dormody, M., Lavoie, R., Heyer, M.H.: The Boston University-five college radio astronomy observatory galactic ring survey. Astrophys. J. Suppl. **163**, 145–159 (2006). doi:10.1086/500091, arXiv:astro-ph/0602160

Jackson, J.M., Finn, S.C., Rathborne, J.M., Chambers, E.T., Simon, R.: The galactic distribution of infrared dark clouds. Astrophys. J. **680**, 349–361 (2008). doi:10.1086/587539

Jansky, K.G.: Electrical phenomena that apparently are of interstellar origin. Pop. Astron. **41**, 548 (1933a)

Jansky, K.G.: Radio waves from outside the solar system. Nature **132**, 66 (1933b). doi:10.1038/132066a0

Jeans, J.H.: Astronomy and Cosmogony. Cambridge University Press, Cambridge (1928)

Kant, I.: Allgemeine Naturgeschichte und Theorie des Himmels, 2nd edn. Königsberg & Leibzig (1755)

Kennicutt, R.C. Jr.: The global schmidt law in star-forming galaxies. Astrophys. J. **498**, 541 (1998). doi:10.1086/305588, arXiv:astro-ph/9712213

Keto, E.: An ionized accretion flow in the ultracompact H II region G10.6-0.4. Astrophys. J. **568**, 754–760 (2002). doi:10.1086/339056

Könyves, V., André, P., Men'shchikov, A., Schneider, N., Arzoumanian, D., Bontemps, S., Attard, M., Motte, F., Didelon, P., Maury, A., Abergel, A., Ali, B., Baluteau, J., Bernard, J., Cambrésy, L., Cox, P., di Francesco, J., di Giorgio, A.M., Griffin, M.J., Hargrave, P., Huang, M., Kirk, J., Li, J.Z., Martin, P., Minier, V., Molinari, S., Olofsson, G., Pezzuto, S., Russeil, D., Roussel, H., Saraceno, P., Sauvage, M., Sibthorpe, B., Spinoglio, L., Testi, L., Ward-Thompson, D., White, G., Wilson, C.D., Woodcraft, A., Zavagno, A.: The aquila prestellar core population revealed by Herschel. Astron. Astrophys. **518**, L106 (2010). doi:10.1051/0004-6361/201014689, arXiv:1005.2981

Kraus, S., Hofmann, K.H., Menten, K.M., Schertl, D., Weigelt, G., Wyrowski, F., Meilland, A., Perraut, K., Petrov, R., Robbe-Dubois, S., Schilke, P., Testi, L.: A hot compact dust disk around a massive young stellar object. Nature. **466**, pp. 339–342 (2010). doi:10.1038/nature09174, arXiv:1007.5062

Kroupa, P.: On the variation of the initial mass function. Mon. Not. RAS **322**, 231–246 (2001). doi:10.1046/j.1365-8711.2001.04022.x, arXiv:astro-ph/0009005

Krumholz, M.R.: Radiation feedback and fragmentation in massive protostellar cores. Astrophys. J. Lett. **641**, L45–L48 (2006). doi:10.1086/503771, arXiv:astro-ph/0603026

Krumholz, M.R., McKee, C.F., Klein, R.I.: The formation of stars by gravitational collapse rather than competitive accretion. Nature **438**, 332–334 (2005). doi:10.1038/nature04280

Krumholz, M.R., Klein, R.I., McKee, C.F., Offner, S.S.R., Cunningham, A.J.: The formation of massive star systems by accretion. Science **323**, 754 (2009). doi:10.1126/science.1165857, arXiv:0901.3157

Krumholz, M.R., Cunningham, A.J., Klein, R.I., McKee, C.F.: Radiation feedback, fragmentation, and the environmental dependence of the initial mass function. Astrophys. J. **713**, pp. 1120–1133 (2010). doi:10.1088/0004-637X/713/2/1120, arXiv:1001.0971

Lada, C.J., Lada, E.A.: Embedded clusters in molecular clouds. Annu. Rev. Astron. Astrophys. **41**, 57–115 (2003). doi:10.1146/annurev.astro.41.011802.094844, arXiv:astro-ph/0301540

Laplace, P.S.: (1796) Exposition du Système du Monde, new edition (1984) : edn. Fayard, Paris

Larson, R.B.: Thermal physics, cloud geometry and the stellar initial mass function. Mon. Not. RAS **359**, 211–222 (2005). doi:10.1111/j.1365-2966.2005.08881.x, arXiv:astro-ph/0412357

Mangum, J.G., Emerson, D.T., Greisen, E.W.: The on the fly imaging technique. Astron. Astrophys. **474**, pp. 679–687 (2007). doi:10.1051/0004-6361:20077811, arXiv:0709.0553

McKee, C.F., Tan, J.C.: Massive star formation in 100,000 years from turbulent and pressurized molecular clouds. Nature **416**, 59–61 (2002). arXiv:astro-ph/0203071

McKee, C.F., Tan, J.C.: The formation of massive stars from turbulent cores. Astrophys. J. **585**, 850–871 (2003). doi:10.1086/346149, arXiv:astro-ph/0206037

Men'shchikov, A., André, P., Didelon, P., Könyves, V., Schneider, N., Motte, F., Bontemps, S., Arzoumanian, D., Attard, M., Abergel, A., Baluteau, J., Bernard, J., Cambrésy, L., Cox, P., di Francesco, J., di Giorgio, AM., Griffin, M., Hargrave, P., Huang, M., Kirk, J., Li, J.Z., Martin, P., Minier, V., Miville-Deschênes, M., Molinari, S., Olofsson, G., Pezzuto, S., Roussel, H., Russeil, D., Saraceno, P., Sauvage, M., Sibthorpe, B., Spinoglio, L., Testi, L., Ward-Thompson, D., White, G., Wilson, C.D., Woodcraft, A., Zavagno, A.: Filamentary structures and compact objects in the aquila and polaris clouds observed by Herschel. Astron. Astrophys. **518**, L103 (2010). doi:10.1051/0004-6361/201014668, arXiv:1005.3115

Molinari, S., Brand, J., Cesaroni, R., Palla, F., Palumbo, G.G.C.: A search for precursors of ultracompact H II regions in a sample of luminous IRAS sources. II. VLA Obs. Astron. Astrophysics. **336**, 339–351 (1998)

Molinari, S., Swinyard, B., Bally, J., Barlow, M., Bernard, J.P., Martin, P., Moore, T., Noriega-Crespo, A., Plume, R., Testi, L., Zavagno, A., Abergel, A., Ali, B., André, P., Baluteau, J.P., Benedettini, M., Berné, O., Billot, N.P., Blommaert, J., Bontemps, S., Boulanger, F., Brand, J., Brunt, C., Burton, M., Campeggio, L., Carey, S., Caselli, P., Cesaroni, R., Cernicharo, J., Chakrabarti, S., Chrysostomou, A., Codella, C., Cohen, M., Compiegne, M., Davis, C.J., de Bernardis, P., de Gasperis, G., Di Francesco, J., di Giorgio, A.M., Elia, D., Faustini, F., Fischera, J.F., Fukui, Y., Fuller, G.A., Ganga, K., Garcia-Lario, P., Giard, M., Giardino, G., Glenn, J., Goldsmith, P., Griffin, M., Hoare, M., Huang, M., Jiang, B., Joblin, C., Joncas, G., Juvela, M., Kirk, J., Lagache, G., Li, J.Z., Lim, T.L., Lord, S.D., Lucas, P.W., Maiolo, B., Marengo, M., Marshall, D., Masi, S., Massi, F., Matsuura, M., Meny, C., Minier, V., Miville-Deschênes, M.A., Montier, L., Motte, F., Müller, T.G., Natoli, P., Neves, J., Olmi, L., Paladini, R., Paradis, D., Pestalozzi, M., Pezzuto, S., Piacentini, F., Pomarès, M., Popescu, C.C., Reach, W.T., Richer, J., Ristorcelli, I., Roy, A., Royer, P., Russeil, D., Saraceno, P., Sauvage, M., Schilke, P., Schneider-Bontemps, N., Schuller, F., Schultz, B., Shepherd, D.S., Sibthorpe, B., Smith, H.A., Smith, M.D., Spinoglio, L., Stamatellos, D., Strafella, F., Stringfellow, G., Sturm, E., Taylor, R., Thompson, M.A., Tuffs, R.J., Umana, G., Valenziano, L., Vavrek, R., Viti, S., Waelkens, C., Ward-Thompson, D., White, G., Wyrowski, F., Yorke, H.W., Zhang Q: Hi-GAL the herschel infrared galactic plane survey. Pub. ASP **122**, pp. 314–325 (2010). doi:10.1086/651314, arXiv:1001.2106

Myers, P.C.: Filamentary structure of star-forming complexes. Astrophys. J. **700**, pp. 1609–1625 (2009). doi:10.1088/0004-637X/700/2/1609, arXiv:0906.2005

Padoan, P., Nordlund, A.: The mysterious origin of brown dwarfs. Astrophys. J. **617**, 559–564 (2004). doi:10.1086/345413, arXiv:astro-ph/0205019

Palla, F., Brand, J., Comoretto, G., Felli, M., Cesaroni, R.: Water masers associated with dense molecular clouds and ultracompact H II regions. Astron. Astrophys. **246**, 249–263 (1991)

Perault, M., Omont, A., Simon, G., Seguin, P., Ojha, D., Blommaert, J., Felli, M., Gilmore, G., Guglielmo, F., Habing, H., Price, S., Robin, A., de Batz, B., Cesarsky, C., Elbaz, D., Epchtein, N., Fouque, P., Guest, S., Levine, D., Pollock, A., Prusti, T., Siebenmorgen, R., Testi, L., Tiphene, D.: First ISOCAM images of the milky way. Astron. Astrophys. **315**, L165–L168 (1996)

Peretto, N., Fuller, G.A.: The initial conditions of stellar protocluster formation. I. A catalogue of Spitzer dark clouds. Astron. Astrophys. **505**, pp. 405–415 (2009). doi:10.1051/0004-6361/200912127, arXiv:0906.3493

Peretto, N., Fuller, G.A., Plume, R., Anderson, L.D., Bally, J., Battersby, C., Beltran, M.T., Bernard, J.P., Calzoletti, L., Digiorgio, A.M., Faustini, F., Kirk, J.M., Lenfestey, C., Marshall, D., Martin, P., Molinari, S., Montier, L., Motte, F., Ristorcelli, I., Rodón, J.A., Smith, H.A., Traficante, A., Veneziani, M., Ward-Thompson, D., Wilcock, L.: Mapping the column density and dust temperature structure of IRDCs with Herschel. Astron. Astrophys. **518**, L98 (2010). doi:10.1051/0004-6361/201014652, arXiv:1005.1506

Pillai, T., Wyrowski, F., Carey, S.J., Menten, K.M.: Ammonia in infrared dark clouds. Astron. Astrophys. **450**, 569–583 (2006). doi:10.1051/0004-6361:20054128, arXiv:astro-ph/0601078

Ragan, S.E., Bergin, E.A., Plume, R., Gibson, D.L., Wilner, D.J., O'Brien, S., Hails, E.: Molecular line observations of infrared dark clouds: seeking the precursors to intermediate and massive star formation. Astrophys. J. Suppl. **166**, 567–584 (2006). doi:10.1086/506594. arXiv:astro-ph/0606284

Rathborne, J.M., Jackson, J.M., Simon, R.: Infrared dark clouds: precursors to star clusters. Astrophys. J. **641**, 389–405 (2006). doi:10.1086/500423, arXiv:astro-ph/0602246

Reber, G.: Notes: cosmic static. Astrophys. J. **91**, 621–624 (1940). doi:10.1086/144197

Reber, G.: Cosmic static. Astrophys. J. **100**, 279 (1944). doi:10.1086/144668

Robitaille, T.P., Whitney, B.A., Indebetouw, R., Wood, K.: Interpreting spectral energy distributions from young stellar objects. II. Fitting observed SEDs using a large grid of precomputed models. Astrophys. J. Suppl. **169**, pp. 328–352 (2007). doi:10.1086/512039, arXiv:astro-ph/0612690.

Rodríguez-Fernández, N., Pety, J., Lonjaret, M., Roche, J.C., Gueth, F.: Imaging on-the-fly ALMA observations. In: Ballester, P., Egret, D., Lorente, N.P.F. (eds.) Astronomical Data Analysis Software and Systems XXI, Astronomical Society of the Pacific Conference Series, vol. 461, p. 715 (2012)

Salpeter, E.E.: The luminosity function and stellar evolution. Astrophys. J. **121**, 161 (1955). doi:10.1086/145971

Shu, F.H., Adams, F.C., Lizano, S.: Star formation in molecular clouds—observation and theory. Annu. Rev. Astro. Astrophys. **25**, 23–81 (1987). doi:10.1146/annurev.aa.25.090187.000323

Simon, R., Jackson, J.M., Rathborne, J.M., Chambers, E.T.: A catalog of midcourse space experiment infrared dark cloud candidates. Astrophys. J. **639**, 227–236 (2006a). doi:10.1086/499342, arXiv:astro-ph/0511079

Simon, R., Rathborne, J.M., Shah, R.Y., Jackson, J.M., Chambers, E.T.: The characterization and galactic distribution of infrared dark clouds. Astrophys. J. **653**, 1325–1335 (2006b). doi:10.1086/508915

Sridharan, T.K., Beuther, H., Schilke, P., Menten, K.M., Wyrowski, F.: High-mass protostellar candidates. I. the sample and initial results. Astrophys. J. **566**, 931–944 (2002). doi:10.1086/338332, arXiv:astro-ph/0110363

Sridharan, T.K., Beuther, H., Saito, M., Wyrowski, F., Schilke, P.: High-mass starless cores. Astrophys. J. Lett. **634**, L57–L60 (2005). doi:10.1086/498644, arXiv:astro-ph/0508421

Swedenborg, E.: Latin: Opera Philosophica et Mineralia (English: Philosophical and Mineralogical Works). Principia 1 (1734)

Taylor, G.B., Carilli, C.L., Perley, R.A. (eds.): Synthesis Imaging in Radio Astronomy II, Astronomical Society of the Pacific Conference Series, vol. 180, (1999)

Tielens, A.G.G.M.: Interstellar polycyclic aromatic hydrocarbon molecules. Annu. Rev. Astron. Astrophys. **46**, 289–337 (2008). doi:10.1146/annurev.astro.46.060407.145211

van Dishoeck, E.F., Blake, G.A.: Chemical evolution of star-forming regions. Annu. Rev. Astron. Astrophys. **36**, 317–368 (1998). doi:10.1146/annurev.astro.36.1.317

Wang, K., Wu, Y.F., Ran, L., Yu, W.T., Miller, M.: The relation between ^{13}CO $J = 2 - 1$ line width in molecular clouds and bolometric luminosity of associated IRAS sources. Astron. Astrophys. **507**, pp. 369–376 (2009). doi:10.1051/0004-6361/200811104, arXiv:0909.3312

Wang, Y., Zhang, Q., Rathborne, J.M., Jackson, J., Wu, Y.: Water masers associated with infrared dark cloud cores. Astrophys. J. Lett. **651**, L125–L128 (2006). doi:10.1086/508939

Weinreb, S., Barrett, A.H., Meeks, M.L., Henry, J.C.: Radio observations of OH in the interstellar medium. Nature **200**, 829–831 (1963). doi:10.1038/200829a0

Wilson, R.W., Jefferts, K.B., Penzias, A.A.: Carbon monoxide in the orion nebula. Astrophys. J. Lett. **161**, L43 (1970). doi:10.1086/180567

Wilson, T.L., Rohlfs, K., Hüttemeister, S.: Tools of Radio Astronomy. Springer, Berlin (2009). doi:10.1007/978-3-540-85122-6

Wolfire, M.G., Cassinelli, J.P.: Conditions for the formation of massive stars. Astrophys. J. **319**, 850–867 (1987). doi:10.1086/165503

Wood, D.O.S., Churchwell, E.: Massive stars embedded in molecular clouds—their population and distribution in the galaxy. Astrophys. J. **340**, 265–272 (1989). doi:10.1086/167390

Woolfson, M.M.: The solar—origin and evolution. Q. J. RAS **34**, 1–20 (1993)

Zhang, Q.: Massive star disks. In: Cesaroni, R., Felli, M., Churchwell, E., Walmsley, M. (eds.) Massive Star Birth: a Crossroads of Astrophysics, IAU Symposiyum, vol. 227, pp. 135–144 (2005). doi:10.1017/S174392130500445X

Zhang, Q., Hunter, T.R., Sridharan, T.K.: A rotating disk around a high-mass young star. Astrophys. J. Lett. **505**, L151–L154 (1998). doi:10.1086/311609

Zhang, Q., Hunter, T.R., Brand, J., Sridharan, T.K., Molinari, S., Kramer, M.A., Cesaroni, R.: Search for CO outflows toward a sample of 69 high-mass protostellar candidates: Frequency of occurrence. Astrophys. J. Lett. **552**, L167–L170 (2001). doi:10.1086/320345

Zhang, Q., Hunter, T.R., Brand, J., Sridharan, T.K., Cesaroni, R., Molinari, S., Wang, J., Kramer, M.: Search for CO outflows toward a sample of 69 high-mass protostellar candidates. II. Outflow properties. Astrophys. J. **625**, 864–882 (2005). doi:10.1086/429660

Zinnecker, H., Yorke, H.W.: Toward understanding massive star formation. Annu. Rev. Astron. Astrophys. **45**, pp. 481–563 (2007). doi:10.1146/annurev.astro.44.051905.092549, arXiv:0707.1279

Chapter 2
An Infrared Point Source Survey

Abstract In this chapter, we search for evidence of a relation between properties of young stellar objects (YSOs) and their parent molecular clouds to understand the initial conditions of high-mass star formation. A sample of 135 sources was selected from the Infrared Astronomical Satellite (*IRAS*) Point Source Catalog, on the basis of their red color to enhance the possibility of discovering young sources. Using the Kölner Observatorium für SubMillimeter Astronomie (KOSMA) 3-m telescope, a single-point survey in ^{13}CO $J = 2 - 1$ was carried out for the entire sample, and 14 sources were mapped further. Archival mid-infrared (MIR) data were compared with the ^{13}CO emissions to identify evolutionary stages of the sources. A ^{13}CO observed sample was assembled to investigate the correlation between ^{13}CO line width of the clouds and the luminosity of the associated YSOs. We identified 98 sources suitable for star formation analyses for which relevant parameters were calculated. We detected 18 cores from 14 mapped sources, which were identified with eight pre-UC H II regions and one UC H II region, two high-mass cores earlier than pre-UC H II phase, four possible star forming clusters, and three sourceless cores. By compiling a large (360 sources) ^{13}CO observed sample, a good correlation was found between the ^{13}CO line width of the clouds and the bolometric luminosity of the associated YSOs, which can be fitted as a power law, $\lg(\Delta V_{13}/\,\mathrm{kms}^{-1}) = (-0.023 \pm 0.044) + (0.135 \pm 0.012)\lg(L_{bol}/L_{\odot})$. Results show that luminous ($>10^3\,L_{\odot}$) YSOs tend to be associated with both more massive and more turbulent ($\Delta V_{13} > 2\,\mathrm{kms}^{-1}$) molecular cloud structures.

2.1 Introduction

The past decades have witnessed significant progress in the study of high-mass star formation. Observations at millimeter and submillimeter wavelengths (Zhang et al. 1998; Beuther et al. 2002; Keto 2002; Zhang 2005; Cesaroni et al. 2007) suggest that massive proto B stars can form by disk mediated accretion, which is similar to the scenario that produces low-mass stars. However, most of the studies focus on relatively evolved stages, when the central star has already formed and hydrogen burning has begun, characterized by surrounding ultra compact (UC) H II regions and strong emission from complex molecules (Churchwell 2002). In contrast, the

K. Wang, *The Earliest Stages of Massive Clustered Star Formation: Fragmentation of Infrared Dark Clouds*, Springer Theses,
DOI 10.1007/978-3-662-44969-1_2

extremely early stages are poorly understood to date. In particular, knowledge to evolutionary stages prior to the onset of H II regions are crucial to understanding the initial conditions of high-mass star formation.

It is known that stars are formed in molecular clouds. Therefore, the relation between forming stars and parent clouds is important to understand the formation process and the properties of the eventual stars. On galaxy scales, star formation activities are usually described by the so-called Schmidt-Kennicutt law, which relates the star formation rate (SFR) to the surface density of gas: $\Sigma_{\rm SFR} \propto \Sigma_{\rm gas}^{N}$, where the index $N = 1 - 2$ (Schmidt 1959; Kennicutt 1998; Gao and Solomon 2004). Studies of Galactic dense cores have shown that this relation may be universal and can be connected to Galactic star formation (Wu et al. 2005a). Larson (1981) studied the turbulence in star forming clouds and found a strong correlation between the internal velocity dispersion σ of the region and its size L: $\sigma\,({\rm kms}^{-1}) \propto L\,({\rm pc})^{0.38}$. This relation, also called the Larson law, is valid for low-mass cores but is found break down in high-mass cores $\gtrsim 10^3 M_\odot$ (Caselli and Myers 1995; Plume et al. 1997; Guan et al. 2008). This is indicative of the different status of turbulence in low- and high-mass cores. The breakdown of the Larson law can be interpreted as evidence of widespread supersonic turbulence in high-mass cores, in contrast to subsonic turbulent low-mass cores (Plume et al. 1997). A molecular line width is an observational indicator of turbulence in clouds, and bolometric luminosity is an indicator of forming stars. Any relation between these quantities may help us to understand the initial star forming process.

This chapter presents results from a ^{13}CO $J = 2 - 1$ survey towards 135 *IRAS* sources using the KOSMA 3-m telescope. To search for high-mass star forming regions in their early stages, we select a sample on the basis of their red *IRAS* color to enhance the possibility of finding young sources. We present the primary results and investigate the relation between line width in molecular clouds and bolometric luminosity of associated infrared sources. We describe our sample selection in Sect. 2.2 and observations in Sect. 2.3. In Sect. 2.4 we present statistical results of the single-point survey (Sect. 2.4.1) and follow-up mapping (Sect. 2.4.2). We discuss the $\Delta V - L$ relation as well as other relations in Sect. 2.5, and summarize the chapter in Sect. 2.7.

2.2 Sample

We selected the sample from the Infrared Astronomical Satellite (*IRAS*) Point Source Catalog (PSC, Beichman et al. 1988) version 2.1 according to our developed color criteria (Wu et al. 2003), namely:

(a) $f_{100\mu{\rm m}} < 500$ Jy, $\lg(f_{25\mu{\rm m}}/f_{12\mu{\rm m}}) \geqslant 0.7$, $\lg(f_{60\mu{\rm m}}/f_{12\mu{\rm m}}) \geqslant 1.4$, where f_λ is the flux density;
(b) lack of 6 cm radio continuum radiation to exclude potential H II associations;
(c) declination $\delta > -20°$, so that targets are accessible to the telescope KOSMA.

Criterion (a) was chosen so that the sample sources were redder and possibly fainter, thus may be younger than those selected based on the traditional Wood and Churchwell (1989) color criteria. Criterion (b) helps to exclude any known H II regions brighter than current detection limit. Therefore, the sample should represent extremely young stellar objects (YSOs), mostly at evolutionary stages earlier than the UC H II phase. The 6 cm radio continuum data was extracted from three surveys: (1) $0° < \delta < 75°$ 4.85 GHz radio continuum survey completed by Gregory and Condon (1991) with the 91-m NRAO telescope; (2) $-29° < \delta < 9.5°$ 4.85 GHz radio continuum survey led by Griffith et al. (1994) with the 64-m Parkes telescope; and (3) $-9.5° < \delta < 10°$ 4.85 GHz radio continuum survey led by Griffith et al. (1995) with the 64-m Parkes telescope.

Criteria (a) and (c) lead to 500 sources being selected from the PSC, which contains 245,889 sources. However, only 135 sources were observed because of limited observing time and after applying criterion (b). These sources make the sample and are concentrated across the Galactic plane over a wide range of longitude, $10° < l < 230°$.

2.3 Observations with KOSMA

A single-point survey in ^{13}CO $J = 2 - 1$ (220.398 GHz) was carried out from September 2002 to March 2003 using the Kölner Observatorium für SubMillimeter Astronomie (KOSMA[1]) 3-m telescope on Gornergrat near Zermatt in Switzerland. All of the sample sources were surveyed in ^{13}CO $J = 2 - 1$. About half of the sample sources were also observed in ^{12}CO $J = 2 - 1$ (230.538 GHz) and 14 of them were mapped in ^{13}CO $J = 2 - 1$.

The beamwidth of the KOSMA at 230 GHz was 130″. The pointing accuracy was superior to 10″. The telescope was equipped with a dual-channel SIS receiver, which had a noise temperature of 150 K. A high resolution spectrometer with 2048 channels was employed and the spectral resolution was 165.5 KHz, giving a velocity resolution of 0.22 kms^{-1}. The main beam temperature ($T_{\rm mb}$) had been corrected for the effects of Earth's atmosphere, antenna cover loss, radiation loss, and forward spillover and scattering efficiency (92 %). From the calibrated Jupiter observations, the main beam efficiency η_{mb} was estimated as 68 % during our observation. On-the-fly mode was adopted during mapping, with a mapping step of 60″. Most maps were extended until the line intensity decreased to half of the maximum value or even lower. The GILDAS[2] software package (CLASS/GREG/SIC) was used for the data reduction (Guilloteau and Lucas 2000).

[1] The KOSMA 3 m radiotelescope at Gornergrat-Süd Observatory is operated by the University of Cologne and supported by special funding from the Land NRW. The Observatory is administered by the Internationale Stiftung Hochalpine Forschungsstationen Jungfraujoch und Gornergrat, Bern.

[2] Available at http://www.iram.fr/IRAMFR/GILDAS.

2.4 Results

2.4.1 Survey

Among the entire sample of 135 *IRAS* sources, we identified 98 sources suitable for star formation analyses (another 37 sources were excluded either because they had multiple components or bad baselines, or failed to be detected), of which 60 have both ^{13}CO $J = 2 - 1$ and ^{12}CO $J = 2 - 1$ data. Figure 2.1 presents example spectra

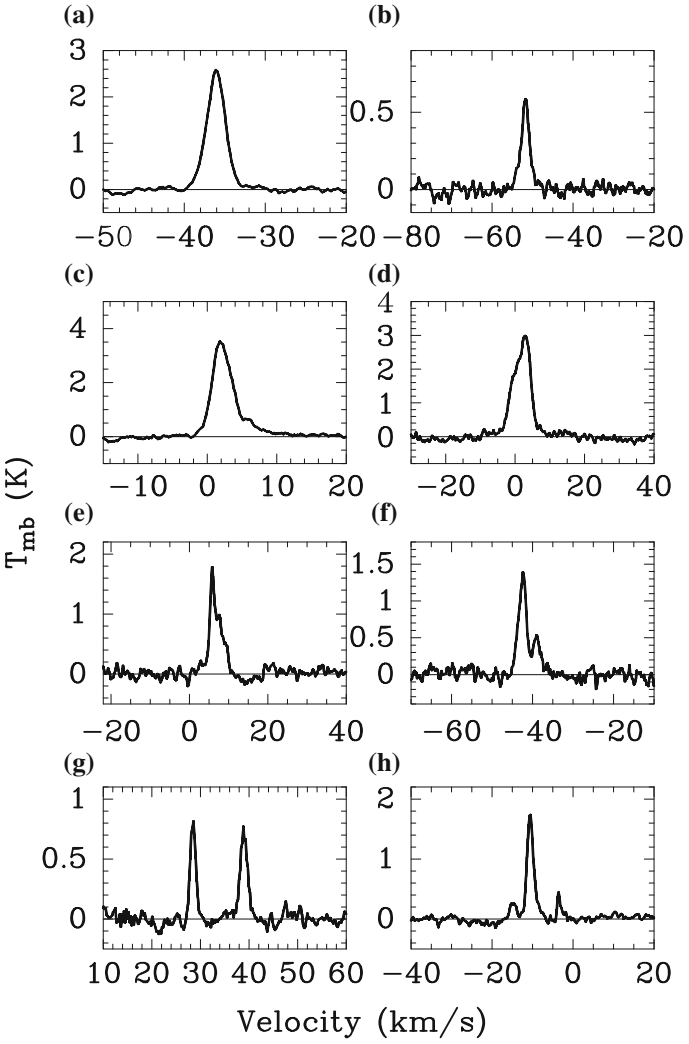

Fig. 2.1 Example spectra of ^{13}CO $J = 2 - 1$ towards the *IRAS* sources given in the text [*Credit* Wang et al. (2009), reproduced with permission © ESO]

of ^{13}CO $J = 2 - 1$: (a) *IRAS* 00117+6412, a perfect Gaussian profile; (b) *IRAS* 02541+6208, a fairly narrow line width; (c) *IRAS* 06067+2138, a broad line with red wing, also seen in $J = 1 - 0$ transition (Wu et al. 2003); (d) *IRAS* 20326+3757, a blue wing; (e) *IRAS* 18278−0212, red asymmetry; (f) *IRAS* 21379+5106, two peaks; (g) *IRAS* 19348+2229, two components; and (h) *IRAS* 02485+6902, multiple components.

Observed and derived parameters are listed in an online Table 2.1, starting with *IRAS* name and its J2000 equatorial coordinates in Cols. (1) to (3). By Gaussian fit, we obtain the observed parameters including main beam temperature $T_{\rm mb}$, local standard of rest velocity $V_{\rm LSR13}$, and ^{13}CO $J = 2 - 1$ line width (full width at half-maximum) ΔV_{13} for each source, listed in Cols. (4) to (7). When a line profile is obviously non-Gaussian, the parameters are measured with a cursor (e.g.Wu et al. 2003), and the velocity uncertainty is given as the velocity resolution; when the line profile has distinctive multiple components, only the strongest component is shown, indicated by a character *m* in corresponding $T_{\rm mb}$ columns.

The distance to most sources was unavailable in the literature. The kinematic distances were calculated based on the radial velocity $V_{\rm LSR13}$ and the velocity field of the outer Galaxy given by Brand and Blitz (1993). When two kinematic distances were available, we selected the closer one, except when the closer distance is too small (<100 pc). For 8 sources, however, no reasonable distances could be calculated in this way and we assumed that the distance to these sources is 1 kpc. These are marked as * in the distance Col. (8) of Table 2.1.

The bolometric luminosity was calculated based on the distances and the *IRAS* fluxes in four bands (12, 25, 60, 100 μm), following the formula given by Casoli et al. (1986)

$$L_{\rm bol} = 5.4 D^2 (f_{12\mu{\rm m}}/0.79 + f_{25\mu{\rm m}}/2 + f_{60\mu{\rm m}}/3.9 + f_{100\mu{\rm m}}/9.9)\, L_\odot,$$

where D is the distance in kpc and f_λ is the flux density in Jansky. The uncertainties in luminosity originate in the kinematic distances and the quality of the *IRAS* source fluxes. Most of the sample sources have high or moderate quality in all the four bands. Twenty-one sources with upper limit fluxes in one or two bands are marked as *u* luminosity in Col. (9) of Table 2.1.

Assuming local thermodynamic equilibrium (LTE) and that the ^{13}CO $J = 2 - 1$ transition is optically thin (i.e. $\tau_{13} < 1$), we derive excitation temperatures, optical depth and column densities for ^{13}CO, using radiation transfer equation (Garden et al. 1991). Based on the assumption of LTE, ^{13}CO and ^{12}CO share the same excitation temperature $T_{\rm ex}$, which can be derived from the main beam temperature of optically thick ^{12}CO, $T_{\rm mb12}$. When $\tau_{13} > 1$, an optical depth correction factor $C_\tau = \tau_{13}/(1 - e^{-\tau_{13}})$ is multiplied by its corresponding column density. The relative CO abundance [^{12}CO/H$_2$] is estimated to extend from 2.5×10^{-5} (Rodriguez et al. 1982) to 10^{-4} (Garden et al. 1991), and we adopt the median value of 6.25×10^{-5}. Using the terrestrial [^{12}C/^{13}C] ratio of 89, we adopt a value for [^{13}CO/H$_2$] of 7.0×10^{-7} when computing the column density of H$_2$. These parameters are listed in Cols. (10) to (13). References of former works are given in the last Col. (14) of Table 2.1.

Table 2.1 Observed and derived parameters of surveyed sources

Source	Observed parameters						Derived parameters						
IRAS	α(J2000) (h m s)	δ(J2000) (° ′ ″)	T_{mb12} (K)	T_{mb13} (K)	V_{LSR13} (kms^{-1})	ΔV_{13} (kms^{-1})	D (kpc)	L_{bol} ($10^3\ L_\odot$)	T_{ex} (K)	τ_{13}	$N(^{13}CO)$ (10^{15} cm^{-2})	$N(H_2)$ (10^{21} cm^{-2})	References
(1)	(2)	(3)	(4)	(5)	(6)	(7)	(8)	(9)	(10)	(11)	(12)	(13)	(14)
00117+6412[m]	00 14 27.7	+64 28 46	5.72(0.12)	2.55(0.05)	−36.06(0.01)	2.77(0.03)	3.6	4.29	10.50	0.57	5.53	7.87	1N, 2, 3N, 4N, 6, 7, 8
00412+6638	00 44 15.2	+66 54 41	2.64(0.07)	0.81(0.14)	−68.00(0.22)	3.32(0.22)	7.35	15.25	6.96	0.35	3.12	4.44	2N, 4
00468+6527	00 49 55.8	+65 43 39	2.31(0.08)	1.17(0.07)	−63.67(0.03)	2.60(0.08)	6.74	34.30	6.55	0.67	4.51	6.42	2, 4
00557+5612[m]	00 58 44.4	+56 28 16	8.37(0.05)	3.72(0.05)	−29.96(0.01)	2.17(0.01)	2.94	1.47[u]	13.34	0.57	5.84	8.32	11
01134+6429	01 16 48.1	+64 45 37	5.03(0.06)[s]	1.29(0.06)	−54.36(0.02)	2.20(0.06)	3[a]	1.31	9.73	0.29	2.18	3.10	2, 4
02413+6037	02 45 12.5	+60 49 44	2.52(0.06)[s]	0.93(0.04)	−61.56(0.02)	2.22(0.06)	7.47	10.45[u]	6.81	0.44	2.58	3.68	
02485+6902	02 53 07.2	+69 14 36	4.11(0.04)[s]	1.70(0.05)[s]	−10.52(0.01)	1.94(0.03)	1.09	0.21	8.70	0.51	3.11	4.43	2N
02541+6208	02 58 13.7	+62 20 31	2.28(0.06)	0.59(0.03)	−51.68(0.22)	2.09(0.22)	5.88	6.43[u]	6.51	0.29	1.55	2.20	2, 4
03101+5821[m]	03 14 04.7	+58 33 08	4.84(0.05)	2.37(0.04)	−38.27(0.01)	2.38(0.02)	4.2	1.20	9.52	0.65	5.03	7.16	2, 4N, 6
03258+3104[m]	03 28 56.8	+31 14 44	13.57(0.11)	6.78(0.05)	7.56(0.01)	3.27(0.01)	0.22[a]	0.03[u]	18.76	0.68	15.29	21.78	1N
03414+3200[m]	03 44 36.4	+32 09 25	17.20(0.10)	6.08(0.07)	8.40(0.01)	1.71(0.01)	0.3[b]	0.05[u]	22.48	0.43	7.44	10.59	1N, 2N
04365+4717	04 40 16.8	+47 23 04	4.06(0.05)[s]	1.65(0.08)	−34.75(0.03)	2.59(0.07)	6.9[b]	4.37	8.64	0.50	4.04	5.75	2N, 4
05155+0707	05 18 17.1	+07 11 01	–	3.34(0.06)	−1.45(0.01)	2.37(0.02)	0.46[a]	0.03	–	–	–	–	
05168+3634[m]	05 20 16.2	+36 37 21	3.39(0.06)	2.61(0.09)	−15.18(0.22)	2.43(0.22)	6.08[c]	17.13	7.86	1.37	14.79	21.05	1N, 2N, 3, 5, 6, 7, 8, 10
05221+4139	05 25 39.8	+41 41 50	2.16(0.06)	0.79(0.07)	−25.81(0.05)	2.75(0.13)	10.36	32.75	6.36	0.43	3.05	4.34	2N
05271+3059	05 30 21.2	+31 01 27	2.32(0.07)	0.75(0.06)	−19.73(0.22)	4.36(0.22)	16.5[b]	72.86	6.56	0.37	4.22	6.01	2
05334+3149	05 36 41.1	+31 51 14	–	1.35(0.06)	−15.98(0.22)	3.77(0.22)	16.5[b]	97.73	–	–	–	–	2N, 3N
05450+0019	05 47 34.6	+00 20 08	6.87(0.09)	3.64(0.07)	9.41(0.22)	4.19(0.22)	0.5[d]	0.04	11.74	0.73	12.76	18.17	
06067+2138[m]	06 09 48.0	+21 38 11	–	3.49(0.05)	1.73(0.22)	3.37(0.22)	0.61	0.03[u]	–	–	–	–	2N, 6, 10
06103+1523[m]	06 13 15.1	+15 22 36	6.22(0.07)	2.97(0.09)	15.99(0.02)	3.01(0.04)	3.78	9.49	11.04	0.63	6.91	9.84	1N, 2N, 3N, 6, 7, 8
06104+1524A	06 13 21.3	+15 23 57	–	3.24(0.19)	16.26(0.03)	2.50(0.07)	3.87	10.59	–	–	–	–	2N, 3N, 5N, 6

(continued)

Table 2.1 (continued)

Source	Observed parameters						Derived parameters						
IRAS	α(J2000) (h m s)	δ(J2000) (° ′ ″)	T_{mb12} (K)	T_{mb13} (K)	V_{LSR13} (kms^{-1})	ΔV_{13} (kms^{-1})	D (kpc)	L_{bol} ($10^3\,L_\odot$)	T_{ex} (K)	τ_{13}	$N(^{13}CO)$ (10^{15} cm^{-2})	$N(H_2)$ (10^{21} cm^{-2})	References
(1)	(2)	(3)	(4)	(5)	(6)	(7)	(8)	(9)	(10)	(11)	(12)	(13)	(14)
06306+0232	06 33 15.8	+02 30 22	–	1.43(0.08)	25.49(0.03)	2.28(0.06)	3.32	0.88	–	–	–	–	
06331+1102	06 35 56.0	+11 00 18	–	2.66(0.10)	22.71(0.22)	2.75(0.22)	3.89	2.58	–	–	–	–	6
06381+1039	06 40 58.0	+10 36 49	9.47(0.19)	2.64(0.10)	7.64(0.02)	2.92(0.05)	1.11	0.20[u]	14.50	0.32	4.99	7.11	6
06382+1017	06 41 03.3	+10 15 01	7.70(0.08)	3.52(0.09)	7.60(0.01)	2.93(0.04)	1.1	0.17	12.63	0.60	7.88	11.22	
06501+0143	06 52 45.6	+01 40 15	–	1.73(0.07)	45.07(0.02)	2.85(0.05)	6.52	9.44	–	–	–	–	
07024−1102[m]	07 04 45.7	−11 07 15	–	4.47(0.06)	16.90(0.22)	1.89(0.22)	1.64	0.57	–	–	–	–	6
07111−1211	07 13 29.9	−12 16 51	–	1.22(0.08)	15.71(0.03)	2.37(0.09)	1.53	0.20	–	–	–	–	
07119−1210A	07 14 17.7	−12 15 14	–	2.04(0.10)	15.23(0.03)	2.67(0.06)	1.48	0.23	–	–	–	–	2N
07207−1435	07 23 01.3	−14 41 33	–	1.95(0.13)	53.17(0.04)	2.77(0.09)	5.58	14.50	–	–	–	–	2
17576−1845	18 00 34.3	−18 45 17	–	1.06(0.12)	21.96(0.08)	4.38(0.20)	3.11	1.35	–	–	–	–	
18145−1557	18 17 26.7	−15 56 20	–	1.81(0.20)	25.93(0.07)	4.09(0.19)	2.81	4.07	–	–	–	–	3N
18205−1316	18 23 21.6	−13 15 02	–	2.43(0.12)	22.48(0.22)	2.89(0.22)	2.24	1.52	–	–	–	–	
18236−1241	18 26 24.7	−12 39 37	–	2.07(0.10)[s]	64.57(0.03)	4.33(0.08)	4.6	15.85	–	–	–	–	
18278−0212	18 30 28.0	−02 10 48	–	1.79(0.08)	5.86(0.22)	3.01(0.22)	0.39	0.02	–	–	–	–	
18301−0853	18 32 55.2	−08 51 23	–	2.19(0.14)	79.05(0.04)	3.35(0.10)	4.97	13.66	–	–	–	–	
18314−0820	18 34 09.0	−08 17 52	–	4.07(0.08)	105.17(0.22)	4.01(0.22)	6.08	24.52	–	–	–	–	3N
18324−0855	18 35 10.5	−08 52 35	–	0.92(0.10)	3.72(0.03)	0.88(0.09)	0.26	0.03	–	–	–	–	1
18358−0112	18 38 25.9	−01 09 51	–	2.51(0.07)	9.43(0.22)	3.67(0.22)	0.67	0.05	–	–	–	–	
18403−0445	18 38 34.4	−03 32 06	–	1.76(0.10)[s]	45.74(0.03)	3.25(0.08)	3.16	4.66	–	–	–	–	1, 6
18502+0033	18 52 47.6	+00 36 51	–	2.33(0.10)	104.90(0.03)	5.26(0.07)	1*	0.50	–	–	–	–	
18502+0034	18 52 50.9	+00 38 03	–	2.40(0.12)	104.70(0.04)	5.55(0.09)	1*	0.52	–	–	–	–	6

(continued)

Table 2.1 (continued)

Source	Observed parameters						Derived parameters						
IRAS	α(J2000) (h m s)	δ(J2000) (° ′ ″)	T_{mb12} (K)	T_{mb13} (K)	V_{LSR13} (kms^{-1})	ΔV_{13} (kms^{-1})	D (kpc)	L_{bol} (10^3 $L_\odot$)	T_{ex} (K)	τ_{13}	$N(^{13}CO)$ (10^{15} cm^{-2})	$N(H_2)$ (10^{21} cm^{-2})	References
(1)	(2)	(3)	(4)	(5)	(6)	(7)	(8)	(9)	(10)	(11)	(12)	(13)	(14)
18532+0047	18 55 50.6	+00 51 22	–	1.24(0.09)^s	58.94(0.05)	4.65(0.13)	3.83	8.96	–	–	–	–	3N, 8
18545+0202	18 57 02.6	+02 06 23	–	1.45(0.10)^s	44.87(0.04)	3.68(0.13)	2.99	3.45	–	–	–	–	
18578+0313	19 00 21.1	+03 17 45	–	0.97(0.08)^s	59.74(0.06)	5.16(0.14)	3.93	3.53	–	–	–	–	
19002+0454	19 02 42.0	+04 58 49	–	1.56(0.13)^s	68.58(0.06)	3.75(0.15)	4.67	8.71	–	–	–	–	3N, 7
19011+0450	19 03 36.9	+04 55 15	–	1.38(0.13)	50.07(0.07)	4.52(0.17)	3.35	4.28	–	–	–	–	
19029+0556	19 05 23.8	+06 01 24	–	2.11(0.13)	58.44(0.22)	4.54(0.22)	3.97	12.65	–	–	–	–	
19031+0621	19 05 36.4	+06 26 09	–	1.65(0.10)	73.36(0.03)	2.38(0.07)	5.41	24.87	–	–	–	–	1
19056+0624	19 08 02.9	+06 29 11	–	1.16(0.12)^s	66.07(0.06)	3.44(0.17)	4.66	4.51	–	–	–	–	
19205+1358	19 22 53.9	+14 04 11	2.10(0.09)	0.60(0.07)	61.86(0.07)	3.43(0.17)	1*	0.31^u	6.28	0.32	2.80	3.99	
19215+1410	19 23 49.4	+14 16 20	–	0.80(0.07)	58.00(0.07)	5.43(0.16)	1*	0.16	–	–	–	–	6N
19216+1658	19 23 52.4	+17 04 01	3.08(0.10)	0.92(0.07)	1.67(0.06)	6.48(0.14)	10.6	62.46^u	7.50	0.34	6.18	8.80	
19282+1742	19 30 30.5	+17 48 30	–	2.82(0.08)	61.14(0.22)	2.84(0.22)	1*	0.49	–	–	–	–	3N, 6
19286+1722	19 30 54.0	+17 28 46	–	0.88(0.07)	45.48(0.05)	3.24(0.10)	4.78	6.57	–	–	–	–	6
19291+1713	19 31 23.4	+17 19 42	–	1.45(0.07)^s	48.07(0.03)	3.41(0.07)	1*	0.38	–	–	–	–	
19298+1707	19 32 08.5	+17 13 35	4.97(0.15)^s	0.87(0.07)	56.61(0.05)	2.64(0.11)	1*	0.19^u	9.67	0.19	1.69	2.40	
19348+2229	19 36 59.8	+22 36 08	–	0.82(0.05)^s	28.48(0.02)	1.31(0.05)	2.66	1.10	–	–	–	–	6N
20145+3645	20 16 27.5	+36 54 58	2.70(0.11)	1.10(0.07)	−56.37(0.04)	3.54(0.12)	10.86	50.37	7.04	0.50	4.76	6.78	
20149+3913^m	20 16 42.6	+39 23 15	6.91(0.08)	4.61(0.13)	3.82(0.02)	2.97(0.04)	1.7^f	0.30^u	11.79	1.06	16.85	24.00	6, 9
20178+3723	20 19 43.1	+37 33 13	6.03(0.09)	1.96(0.10)	3.93(0.02)	1.84(0.05)	4.08	1.02^u	10.83	0.38	2.69	3.83	
20227+4154	20 24 31.4	+42 04 17	7.74(0.08)	3.18(0.12)	5.54(0.02)	2.72(0.05)	2^a	2.74	12.68	0.52	6.37	9.06	3, 7

(continued)

Table 2.1 (continued)

Source	Observed parameters						Derived parameters						
IRAS	α(J2000) (h m s)	δ(J2000) (° ′ ″)	$T_{\rm mb12}$ (K)	$T_{\rm mb13}$ (K)	$V_{\rm LSR13}$ (kms^{-1})	ΔV_{13} (kms^{-1})	D (kpc)	$L_{\rm bol}$ ($10^3\,L_\odot$)	$T_{\rm ex}$ (K)	τ_{13}	$N(^{13}{\rm CO})$ (10^{15} cm^{-2})	$N({\rm H_2})$ (10^{21} cm^{-2})	References
(1)	(2)	(3)	(4)	(5)	(6)	(7)	(8)	(9)	(10)	(11)	(12)	(13)	(14)
20231+3440	20 25 16.0	+34 50 06	3.60(0.07)	1.90(0.14)	5.46(0.04)	2.70(0.09)	1[a]	0.19	8.11	0.72	5.72	8.14	
20261+3922	20 27 58.8	+39 32 07	2.63(0.08)[s]	1.19(0.19)	−54.99(0.09)	2.79(0.20)	10.01	32.70	6.95	0.57	4.28	6.09	
20281+4038	20 29 54.8	+40 48 52	5.50(0.08)[s]	2.05(0.06)	−2.51(0.02)	2.36(0.04)	4.11	6.56	10.25	0.45	3.86	5.50	
20290+4052	20 30 50.8	+41 02 25	3.70(0.08)[s]	1.60(0.10)	−1.51(0.04)	3.15(0.10)	3.89	2.79	8.23	0.54	5.12	7.28	
20326+3757	20 34 33.0	+38 08 02	9.05(0.11)	2.99(0.09)	2.79(0.22)	5.81(0.22)	3.66	2.74[u]	14.06	0.39	11.72	16.69	
20330+4109	20 34 48.5	+41 20 21	4.07(0.11)[s]	0.67(0.07)[s]	−30.82(0.05)	2.19(0.12)	7.09	10.04[u]	8.65	0.17	1.19	1.69	
20345+4024	20 36 24.1	+40 35 08	4.12(0.10)	0.82(0.09)	1.31(0.06)	2.58(0.13)	3.34	1.59[u]	8.71	0.21	1.73	2.47	
20444+4629	20 46 08.3	+46 40 41	6.51(0.09)	3.65(0.07)	−3.71(0.01)	2.09(0.02)	2.91	3.98	11.36	0.80	6.67	9.50	2N, 3N, 7
20508+4825	20 52 28.2	+48 36 30	1.55(0.05)[s]	0.92(0.07)	−6.63(0.04)	2.58(0.11)	2.98	1.17[u]	5.55	0.84	5.27	7.51	2N
21025+4912	21 04 15.4	+49 24 25	1.32(0.04)[s]	0.74(0.06)	−73.44(0.05)	2.86(0.12)	10.08	9.15[u]	5.23	0.76	5.27	7.50	2
21246+5512	21 26 14.4	+55 25 57	0.76(0.05)	0.49(0.06)	−69.33(0.05)	1.84(0.13)	8.72	15.33	4.37	0.93	4.14	5.90	2N
21293+5535	21 30 55.7	+55 48 49	4.42(0.06)	1.17(0.06)	−71.13(0.03)	4.13(0.09)	8.85	8.25[u]	9.05	0.30	3.97	5.65	2, 4
21334+5039	21 35 09.2	+50 53 09	4.64(0.07)	2.36(0.07)	−45.05(0.22)	2.75(0.22)	5[a]	23.53	9.30	0.68	6.21	8.84	2
21379+5106	21 39 40.8	+51 20 35	2.88(0.07)	1.39(0.07)	−42.27(0.22)	2.17(0.22)	5.9	5.18	7.25	0.63	3.73	5.32	2
21391+5026	21 40 57.3	+50 39 53	2.56(0.07)	1.02(0.07)	−40.55(0.04)	2.50(0.09)	5.77	5.67	6.86	0.48	3.22	4.58	2
21391+5802[m]	21 40 42.4	+58 16 10	–	5.80(0.07)	0.68(0.01)	2.99(0.02)	0.75[e]	0.26	–	–	–	–	1N, 2N, 3, 7, 8
21418+5403	21 43 29.8	+54 16 56	3.62(0.06)	0.86(0.06)	−60.07(0.04)	3.24(0.10)	7.51	22.24	8.13	0.26	2.51	3.58	2N
21519+5613	21 53 39.2	+56 27 46	4.26(0.06)	2.07(0.08)	−62.72(0.02)	3.11(0.05)	7.3[a]	15.75	8.87	0.64	6.31	8.98	2, 3, 4, 8
22051+5848	22 06 50.7	+59 02 47	2.40(0.06)	1.51(0.07)	−1.77(0.02)	1.39(0.04)	0.77	0.08[u]	6.66	0.93	3.38	4.82	2N, 4

(continued)

Table 2.1 (continued)

Source	Observed parameters						Derived parameters						
IRAS	α(J2000) (h m s)	δ(J2000) (° ′ ″)	T_{mb12} (K)	T_{mb13} (K)	V_{LSR13} (kms^{-1})	ΔV_{13} (kms^{-1})	D (kpc)	L_{bol} (10^3 $L_\odot$)	T_{ex} (K)	τ_{13}	$N(^{13}CO)$ (10^{15} cm^{-2})	$N(H_2)$ (10^{21} cm^{-2})	References
(1)	(2)	(3)	(4)	(5)	(6)	(7)	(8)	(9)	(10)	(11)	(12)	(13)	(14)
22198+6336[m]	22 21 27.6	+63 51 42	10.55(0.01)	5.39(0.07)	−11.10(0.22)	2.65(0.22)	1.67	1.53[u]	15.63	0.70	11.49	16.36	1N, 2N, 3, 7, 8
22305+5803	22 32 24.3	+58 18 58	4.57(0.07)	1.80(0.06)	−52.41(0.02)	2.68(0.05)	5.94	14.28	9.22	0.48	4.25	6.05	2, 4, 6, 8
22506+5944[m]	22 52 38.6	+60 00 56	11.01(0.07)	3.18(0.05)	−51.61(0.22)	2.43(0.22)	3.5[d]	6.83	16.11	0.34	5.56	7.92	1N, 2N, 3, 4N, 6, 7, 8, 10
22539+5758	22 56 00.0	+58 14 46	7.32(0.06)	3.59(0.07)	−54.19(0.01)	2.97(0.03)	3.5[d]	10.68	12.23	0.66	8.47	12.07	2, 4, 5
23011+6126	23 03 13.1	+61 42 26	5.12(0.07)	2.25(0.06)	−11.03(0.22)	1.93(0.22)	0.73[d]	0.09	9.83	0.56	3.75	5.34	2, 4, 6

Note Column (1) is source name shown in order of ascending *IRAS* number. Columns (2) and (3) list J2000 equatorial coordinates of each source. Column (4) lists the main beam temperature of ^{12}CO $J = 2 - 1$ if available, and Cols. (5)–(7) list the main beam temperature, local standard of rest velocity and line width of ^{13}CO $J = 2 - 1$, with 1σ rms level in parenthesis. Column (8) is kinematic distance except for otherwise labeled. Column (9) lists the bolometric luminosity with asterisk (*) if one (or two) *IRAS* band flux is upper limit. Column (10) is excitation temperature. Column (11) is the opacity of ^{13}CO. Columns (12)–(13) present average ^{13}CO and H_2 column densities. Column (14) lists former works if available

References (1) 6.7 GHz methanol maser survey (Szymczak et al. 2000); (2) 22 GHz water maser survey (Wouterloot et al. 1993); (3) 22 GHz water maser (Palla et al. 1991); (4) 1665/67 MHz OH maser survey (Wouterloot et al. 1993); (5) HCO^+ $J = 1 - 0$ survey (Richards et al. 1987); (6) CS $J = 2 - 1$ survey (Bronfman et al. 1996); (7) NH_3 $(J,K) = (1,1)$ (2,2) survey (Molinari et al. 1996); (8) CO $J = 2 - 1$ outflow mapping (Zhang et al. 2005; Kim and Kurtz 2006); (9) CO, CS mapping (Ao et al. 2004); (10) CO mapping (Guan et al. 2008); (11) CO mapping (Lee and Jung 2003). N means non-detection

[a–f] Distance from

[a] Wu et al. (2004)

[b] Wouterloot et al. (1993)

[c] Molinari et al. (1996)

[d] Harju et al. (1993)

[e] Matthews (1979)

[f] Motte et al. (2007)

* Kinematic distance unavailable, set as 1 kpc

[m] Mapped source

[s] More than one velocity component, only the strongest one listed

[u] Upper limit

The distribution of ^{13}CO $J = 2 - 1$ line width of this sample has a mean of 3.09 kms^{-1} and a standard deviation of 1.06 kms^{-1}. This line width is relatively smaller than that of typical bright/red *IRAS* sources associated with water masers (3.5 kms^{-1}, (Wu et al. 2001); note that this value was measured in $J = 1 - 0$ transition), while significantly larger than that of a molecular cloud hosting intermediate-mass star formation activities ($\sim$2 kms^{-1}, Sun et al. (2006), averaged throughout the Perseus cloud). The luminosities are distributed over a wide range, from 20 $L_\odot$ to about 10^5 $L_\odot$, with a mean of 10^4 $L_\odot$. The high dispersion of luminosities indicates that these sources are embedded in very different environments. This luminosity distribution is similar to the young *'low'* sources of Molinari et al. (1996) (see their Fig. 6), in agreement with the assumption that our sample group may be relatively younger than that chosen by traditional color criteria. The excitation temperature T_{ex} ranges from 4.4 to 22.5 K, with an average of 9.7 K. This suggests that very cold gases surround the sample sources, colder than those surrounding the luminous *IRAS* sources (Zhu and Wu 2007). The ^{13}CO column densities are (1.2–28.7) $\times 10^{15}$ cm^{-2}, with an average of 6.2 $\times$ 10^{15} cm^{-2}, while H_2 column densities are (1.7–40.8) $\times 10^{21}$ cm^{-2}, with an average of 8.9 $\times 10^{21}$ cm^{-2}. These densities are roughly close to the critical value for gravitational collapse (Hartquist et al. 1998).

2.4.2 Mapping

To improve our understanding of the properties of the surveyed sample, 14 sources were mapped in ^{13}CO $J = 2 - 1$ and compared with archival mid-infrared (MIR) continuum data. Mapped sources were selected from the surveyed sample as those with only single emission component, and they almost evenly cover longitude $70° < l < 230°$, avoiding low Galactic longitudes, where ^{13}CO lines are often affected by multiple velocity components from the Galactic molecular ring. Using these sources as a guide, maps were extended until at least one core was resolved. We name a map on the basis of its guide source name, as outlined in Fig. 2.2. In four cases, one map resolved two cores, resulting in 18 cores in total. We found that 13 cores are associated with the original guide sources, two cores are associated with other *IRAS* sources, and three cores have no embedded infrared source (sourceless hereinafter). A core is named after its associated *IRAS* source; for a sourceless core, it is named after its nearest *IRAS* source plus relative direction to the core (e.g., 20067+3415NE). See Table 2.2 for core properties.

The core size (Col. 2 of Table 2.2) is defined as an equivalent linear size $R = \sqrt{A/\pi}$, where A is the projected area of each cloud within the 50 % contour (highlighted in Fig. 2.2). It is corrected for the effect of beam smearing by multiplying its value by a factor $\sqrt{\theta_{obs}^2 - \theta_{mb}^2}/\theta_{obs}$, where θ_{obs} is the angular diameter of the core and θ_{mb} is the beamwidth. For three cores, the observed angular diameters are comparable to the beamwidth, so that the cores are just marginally resolved and the corresponding core sizes are highly uncertain. In a few cases, maps were not complete

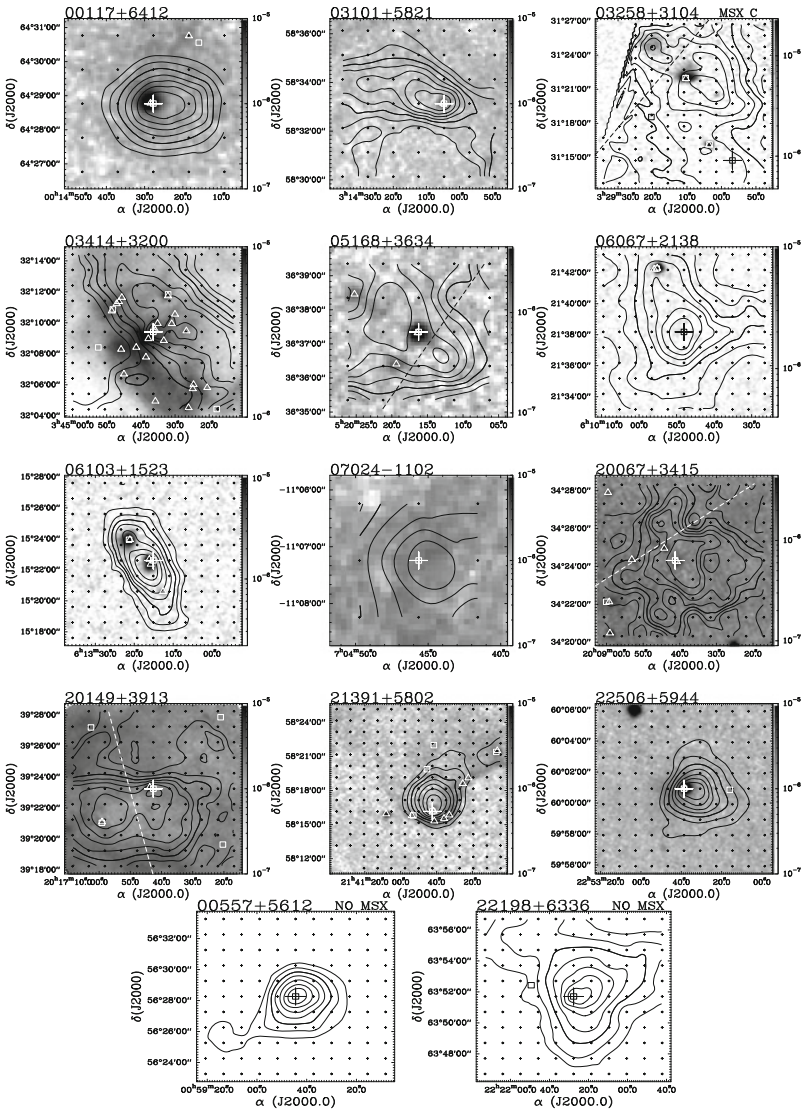

Fig. 2.2 ^{13}CO $J = 2-1$ integrated intensity contours overlay on the *Midcourse Space Experiment* (*MSX* Price et al. 2001) band A (8.28 μm) images as background, if available. Maps are listed in order of name, except the two without *MSX* data. *IRAS* 03258+3104 has no band A data and we use band C instead; *IRAS* 00557+5612 and 22198+6336 both have no *MSX* data available, as labeled on the top of their relevant sub-figures. *IRAS* point sources are denoted by *squares* while *MSX* point sources by *triangles*. *Small crosses* represent observed points, while *large crosses* denote the original guide sources (Sect. 2.4.2), as labeled on the top of each map. *Dash lines* schematically separate resolved cores. For integration, only intensity over three times of the standard deviation (3σ) is considered. Contour levels begin from 30 to 90 % by 10 % of the peak intensity, while 50 % level is highlighted by a *solid thick contour*. For *MSX* images, the grey scale wedge is shown on the *right side*; the unit is W m^{-2} sr^{-1} [*Credit* Wang et al. (2009), reproduced with permission © ESO]

Table 2.2 Core properties

Core	R (pc)	$\overline{\Delta V}_{13}$ (kms^{-1})	$L_{\rm bol}$ ($10^3 L_\odot$)	Peak $n(H_2)$ (10^3 cm^{-3})	$M_{\rm LTE}$ ($M_\odot$)	$M_{\rm vir}$ ($M_\odot$)	α^*
(1)	(2)	(3)	(4)	(5)	(6)	(7)	(8)
00117+6412	0.57	2.58	4.29	5.13	1.8E+2	4.8E+2	2.7
00557+5612	1.08	2.05	1.47[u]	1.66	6.6E+2	5.7E+2	0.9
03101+5821	>1.08	2.52	1.20	1.76	>5.8E+2	8.6E+2	1.5
03260+3111[a]	>0.23	3.05	0.29	15.96	>1.6E+2	2.6E+2	1.6
03260+3111NE[s]	0.11	2.51	–	15.96	8.0E+1	8.8E+1	1.1
03414+3200	>0.34	1.92	0.05[u]	5.35	>8.5E+1	1.6E+2	1.8
05168+3634	>2.41	2.86	17.13	1.57	>1.2E+4	2.4E+3	0.2
05168+3634SW[s]	0.60[m]	2.61	–	1.57	3.0E+3	5.2E+2	0.2
06067+2138	0.55	3.36[b]	0.03[u]	3.83[c]	2.5E+2	7.8E+2	3.1
06103+1523	1.97	2.56	9.49	1.02	2.8E+3	1.6E+3	0.6
07024+1102	>0.11[m]	1.99	0.57	64.73[c]	>9.0E+0	5.8E+1	6.4
20067+3415	1.76	3.80[b]	1.14	1.14	3.9E+3	3.2E+3	0.8
20067+3415NE[s]	0.45[m]	3.67	–	1.14	9.7E+2	7.5E+2	0.8
20149+3913	0.43	3.19	0.30[u]	2.62	1.4E+3	5.5E+2	0.4
20151+3911[a]	>1.30	3.83	0.70[u]	2.62	>4.1E+3	2.4E+3	0.6
21391+5802	0.32	2.78	0.26	11.87[c]	1.3E+2	3.1E+2	2.4
22198+6336	1.22	2.21[b]	1.53[u]	2.39	1.7E+3	7.5E+2	0.4
22506+5944	1.31	2.88	6.83	1.40	1.0E+3	1.4E+3	1.4
Average[†]	0.98	2.80	3.02	4.95	1.9E+3	1.1E+3	1.3

Note [a] Not guide *IRAS* source. Luminosity calculated based on *IRAS* fluxes and distance: 03260+3111 at 0.4 kpc (Harju et al. 1998) and 20151+3911 at 1.7 kpc (Motte et al. 2007). [b] Average spectrum fitted with two Gaussian profiles, list the stronger one. [c] No ^{12}CO data, density calculated by assuming reasonable $T_{\rm ex}$ (see text). [m] Core's angular diameter comparable to beamwidth, marginally resolved. [s] Sourceless core. [u] Upper limit. [†] Average calculating does not include values of marginally resolved cores, except for the line width column. [*] $\alpha = M_{\rm vir}/M_{\rm LTE}$

to 50 % of the peak intensity, and can only infer lower limits to R (indicated by a symbol '>'). The average line width of each core (Col. 3) is determined by combining all the spectra in the core and then fitting a Gaussian profile to the average spectrum. In a few cases, the average spectra show line asymmetry/absorption and need to be fitted with two Gaussian profiles, and then the line width of the stronger profile is given. The typical uncertainty in the average line width is 0.04 kms^{-1}. Column (4) lists the luminosity also given in Table 2.1 for reference. Peak volume densities for H_2, $n(H_2)$ (Col. 5), and the LTE core masses, $M_{\rm LTE}$ (Col. 6), are calculated based on both R and the peak ^{13}CO column densities determined by interpolating the maps. For three maps (*IRAS* 06067+2138, 07024−1102, and 21391+5802), however, no $N(^{13}{\rm CO})$ are available in Table 2.1 because of a lack of ^{12}CO data. To estimate their core properties, we assume reasonable excitation temperatures: for *IRAS* 06067 and 07024, we assume a typical $T_{\rm ex}$ of 15 K; and for *IRAS* 21391, we assume that $T_{\rm ex}$ equals the dust

temperature (25 K, Beltrán et al. 2002). Column (7) presents the virial mass derived from the sizes and line widths following MacLaren et al. (1988). The ratio of virial to LTE mass $\alpha = M_{\rm vir}/M_{\rm LTE}$ is listed in the last Col. (8) of Table 2.2. We exclude the marginally resolved cores when computing averages except for the line width column.

Overall, the core mass ranges from $\sim 10^2 M_\odot$ to $10^4 M_\odot$, the linear size from 0.11 to 2.41 pc, and molecular hydrogen density is in the range $\sim 10^3 - 10^4\,{\rm cm}^{-3}$. The luminosities are once again, distributed across a wide range, from $30\,L_\odot$ to $1.7 \times 10^4 L_\odot$. Overall, the line width $\overline{\Delta V}_{13} > \sim 2\,{\rm km s}^{-1}$, and has an average of $2.80\,{\rm km s}^{-1}$, smaller than that of the entire surveyed sample. We find an average value of 1.3 for the ratio of virial to LTE core mass, α. Overall the mapping sample infers $\alpha \sim 1$, indicating that most of the cores appear to be virialized.

Comparisons between ^{13}CO maps and MIR images are presented in Fig. 2.2, and a detailed evolutionary identification of individual mapped sources is presented in Sect. 2.6.

2.5 Discussion

2.5.1 The Line Width-Luminosity Relation

The empirical correlation of line width versus luminosity has been found by various authors from observations in C^{18}O (Saito et al. 2001; Ridge et al. 2003), as well as in NH_3 (Wouterloot et al. 1988; Myers et al. 1991; Harju et al. 1993; Ladd et al. 1994; Jijina et al. 1999). The line width is in general found to increase with luminosity, for different $\lg(\Delta V)/\lg(L_{\rm bol})$ slopes: 0.13–0.19 for NH_3 (Jijina et al. 1999) and 0.11 for C^{18}O (Saito et al. 2001). Given the relatively wide availability of the archival ^{13}CO data, it is helpful to compile an up-to-date ^{13}CO observed sample to investigate the luminosity-line width relation in case of ^{13}CO.

In Fig. 2.3, we plot in logarithmic space the line width versus luminosity from our sample and other ^{13}CO observed samples adopted from the literature (Beichman et al. 1986; Dent et al. 1985; Fischer et al. 1985; Yamashita et al. 1989; Wu et al. 2001, 2004; Ridge et al. 2003). This sample contains 360 sources in total. One finds that the luminosity of the *IRAS* sources is well correlated with the ^{13}CO line width, as fitted by a power law:

$$\lg\left(\frac{\Delta V_{13}}{\rm km\,s^{-1}}\right) = (-0.023 \pm 0.044) + (0.135 \pm 0.012)\lg\left(\frac{L_{\rm bol}}{L_\odot}\right),$$

where the correlation coefficient c.c. = 0.69. This suggests that the mass of the forming stellar objects is linked to the dynamic status of their parent clouds. Saito et al. (2001) measured a similar correlation in the Centaurus tangential region and suggested that the mass of the formed stars is determined by the internal velocity dispersion of the dense cores. If the velocity dispersion is a reliable indicator of the turbulence, this is consistent with the idea that turbulence is different in high-mass

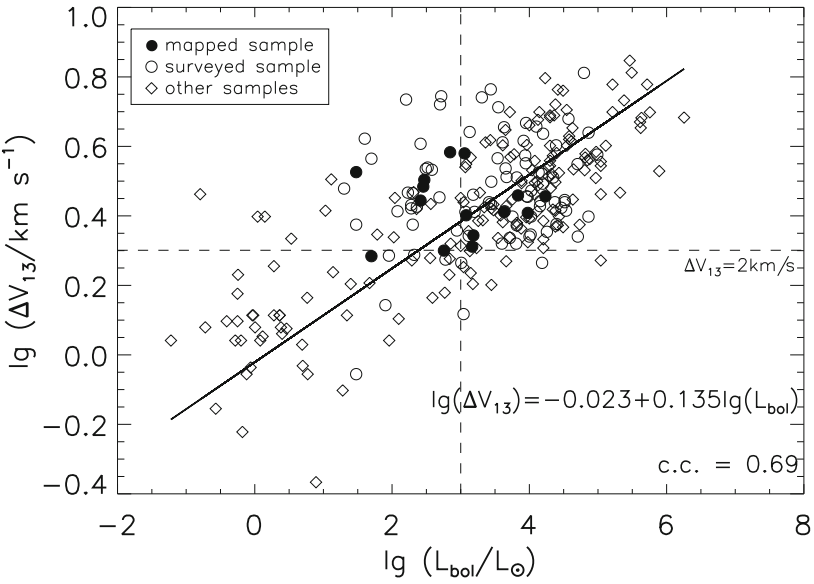

Fig. 2.3 Line width plotted versus bolometric luminosity of 360 ^{13}CO observed sources: surveyed sources (*open circles*), mapped sources (*filled circles*), and other samples adopted from the literature (*diamonds*). *Solid line* represents a least squares fitting to the data, and the *dash lines* represent the luminosity/line-width criteria (Sect. 2.5.1) [*Credit* Wang et al. (2009), reproduced with permission © ESO]

and low-mass cores. We note that the ^{13}CO line widths adopted from the literature were measured from $J = 1 - 0$ transition with smaller beams.

It is generally agreed that embedded infrared point sources of high luminosity ($\geq 10^3 L_\odot$) but without associated H II regions are good candidates for high-mass YSOs in the pre-UC H II phase (e.g. Wu et al. 2006, and references therein). However, sufficiently young massive objects are not necessarily bright at infrared wavelengths; some of them have no infrared counterparts. High-mass objects at sufficiently young evolutionary stages could be quite faint in infrared ranges either because they are not yet mature enough to have developed infrared emission or they are embedded very deeply in cold dust. For instance, Sridharan et al. (2005) identified several 1.2 mm emitting high-mass starless cores (HMSCs) that exhibit absorption or no emission at the MIR wavelengths; a centimeter-emitting UC H II region was also found without an infrared counterpart (Forbrich et al. 2008). In our mapped sample, faint ($<10^3 L_\odot$) sources associated with very massive ($>10^3 M_\odot$) cores (20149, 20151) do exist. Although we cannot rule out the possibility that these two sources could evolve to only low-mass stars, it is very likely that the clouds will eventually fragment to form high-mass stars, given the large amount of gas therein.

Hereafter, for clarity, our *luminosity criterion* refers to bolometric luminosity $L_{\rm bol} \geq 10^3\ L_\odot$, and our *line-width criterion* refers to line width ΔV(^{13}CO $J = 2 - 1$)>2 kms^{-1}. According to the $\Delta V - L$ relation above, luminosity $L_{\rm bol} = 10^3\ L_\odot$

corresponds to $\Delta V_{13} = 2.42^{+0.49}_{-0.41}\,\mathrm{kms}^{-1}$. Because high-mass stars are far more luminous than their low-mass counterparts, luminous *IRAS* sources ($\geq 10^3\,L_\odot$) are likely to be high-mass stellar objects. Therefore, we tentatively (not exclusively) suggest the lower limit, $\Delta V_{13} = 2\,\mathrm{kms}^{-1}$, as a characteristic value for the line-width criterion, analogous to the widely used luminosity criterion. Objects with line width larger than this characteristic value are probably high-mass objects. The line-width criterion includes 94.5 % sources that also satisfy the luminosity criterion (Fig. 2.3), which implies that line width may be a key parameter in measuring the masses of the forming stellar objects in the cores, at least in our sample. We note that this criterion ($2\,\mathrm{kms}^{-1}$) is larger than the typical line width of low mass cores ($1.3\,\mathrm{kms}^{-1}$, (Myers et al. 1983)), and smaller than the average line width of high-mass cores ($3.5\,\mathrm{kms}^{-1}$, Wu et al. 2001).

Applying the luminosity/line-width criteria to our sample, there are 68 sources satisfying luminosity criterion, 65 (95.6 %) of which also satisfy line-width criterion. We suggest that the 65 sources are candidate high-mass star formation regions in a pre-UC H II phase. For the remaining 30 less luminous sources, 23 of them satisfy the line-width criterion but not the luminosity criterion. We suggest that the 23 sources are high-mass YSO candidates earlier than pre-UC H II phase.

2.5.2 Core Masses and Line Widths

The core masses provide a direct test of our line-width criterion. Figure 2.3 includes 15 cores with luminosities listed in Table 2.2. We exclude sourceless cores and marginally resolved cores in the discussion in this section, because the former's luminosity cannot be determined and latter's estimated size and mass are highly uncertain. The remaining 14 luminosity-available cores can be divided into two groups: group I, which do not satisfy the luminosity criterion, including 03414, 21391, 03260, 20149, 06067, 20151; and group II, satisfying the luminosity criterion, including 00557, 22198, 03101, 06103, 00117, 05168, 22506, 20067 (in order of increasing line width). All group II cores also satisfy the line-width criterion, and they are located in the upper right panel of Fig. 2.3. They are very massive, their estimated masses being higher than several $10^2 M_\odot$, except core 00117 ($1.8 \times 10^2 M_\odot$). On the other hand, group I cores mostly satisfy the line-width criterion. They are relatively less massive than group II cores, their masses being typically $\sim 10^2 M_\odot$ or more, with two very massive cores 20149 and 20151 ($> 10^3 M_\odot$). The only case that does not satisfy the line-width criterion, core 03414, has the lowest mass in group I. We note that all group I cores are still significantly more massive than the low-mass cores (Myers et al. 1983).

The high-mass nature of group I cores confirms again (in addition to the previously mentioned cores 20149, 20151) that the luminosity criterion cannot be applied to some young sources. On the other hand, the line-width criterion is applicable to our sample. While in terms of inferring mass, line width may not be as direct an indicator as luminosity, it is helpful when luminosity is unavailable or is affected by

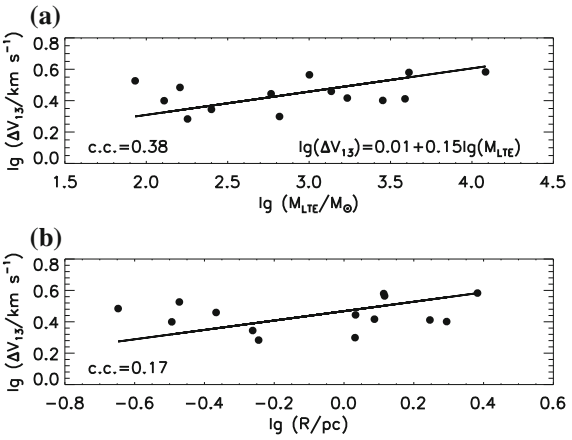

Fig. 2.4 Relations between ^{13}CO line width ΔV_{13} and other physical parameters of molecular cores: **a** LTE mass $M_{\rm LTE}$, and **b** size R. In both cases, the filed circles represent data and solid lines are linear fitting results to the data. The fitting function and correlation coefficient are labeled in each panel [*Credit* Wang et al. (2009), reproduced with permission © ESO]

large uncertainty (e.g., due to distance ambiguity, flux upper limit), which is often the case. In addition, line width can be measured observationally more easily and more accurately than luminosity.

In Fig. 2.4a, we plot lg(ΔV_{13}) versus lg $M_{\rm LTE}$. A weak correlation is evident in the data, with a correlation coefficient of 0.38. This may indicate that, for molecular clouds with associated YSOs, the ^{13}CO line width at some degree is related to the cloud mass, and massive cores tend to have larger line widths. This weak correlation, together with the strong $\Delta V - L$ correlation, indicates that massive stars are more likely to form in massive molecular cores. The core mass and associated *IRAS* luminosity in our mapped sample are indeed well correlated (c.c. $= 0.76$). However, this correlation may need to be corrected for distance effects (0.3–6.08 kpc for mapped sample) because both mass and luminosity are proportional to D^2. Nevertheless, strong mass-luminosity correlations were reported in other regions or samples that have far smaller distance differences than our sample (Dobashi et al. 1996; Saito et al. 2001; Ridge et al. 2003). Figure 2.4b plots line width ΔV_{13} and core size R in logarithm. With an average virial mass of $1.1 \times 10^3\ M_\odot$, the cores exhibit no correlation between size and line width. This indicates that the Larson law is invalid for our mapped sample, consistent with the results of previous works (Plume et al. (1997), $\langle M_{\rm vir}\rangle > 3.8 \times 10^3\ M_\odot$; Guan et al. (2008), $\langle M_{\rm vir}\rangle = 5.6 \times 10^3\ M_\odot$). The correlations in Fig. 2.4 are unaffected by distance, because the line width and distance of the plotted cores are not correlated (c.c. $= 0.04$).

We conclude that, based on the currently available sample, YSOs with higher bolometric luminosity ($>10^3\ L_\odot$), tend to be associated with more massive molecular cloud structures, which are usually more turbulent, and have a large ^{13}CO line width, $\Delta V_{13} > 2\,{\rm km\,s^{-1}}$. It is important to note that, the characteristic value ($2\,{\rm km\,s^{-1}}$) may not be universal, and can vary from region to region and/or from line to line. Further mapping of more clouds, as well as higher angular resolution data if available, are required to examine the line-width criterion proposed here.

2.6 Individual Analyses

In Fig. 2.2, we compare the integrated intensity of ^{13}CO emissions to *IRAS* (point sources) and *MSX* (point sources and images) data. We use the most sensitive band (band A, centered on 8.28 μm) images of *MSX* when available. We note that maps in Fig. 2.2 are labeled by the original guide sources (Sect. 2.4.2). *IRAS* 03258+3104 has no band A data and we use band C (centered on 12.13 μm) instead. *IRAS* 00557+5612 and 22198+6336 both have no *MSX* data. Individual analyses of each map are presented as follows.

IRAS 00117+6412: ^{13}CO emission peak coincides well with *IRAS* and *MSX* point sources, and there are also strong counterparts in all four *MSX* bands. This distinctive ^{13}CO core is massive ($1.8 \times 10^2 M_\odot$), in agreement with the conclusion deduced from the luminosity/line-width criteria (Sect. 2.5.1). We therefore suggest that it is a pre-UC H II region. Strong 22 GHz water maser (Wouterloot et al. 1993) and outflow activity (Zhang et al. 2005; Zhao et al. 2003) have been detected within this area, providing evidence of active star formation.

IRAS 00557+5612: *MSX* data are unavailable close to this region, but the *IRAS* source matches well to the ^{13}CO core peak. A core as massive as $6.6 \times 10^2 M_\odot$ agrees with the conclusion deduced from the luminosity/line-width criteria. We therefore suggest that it is a pre-UC H II region. A velocity gradient of 0.36 kms^{-1} pc^{-1} from northeast to southwest is inferred, yielding a rotating angular velocity of 1.16×10^{-14} s^{-1}. According to ^{13}CO $J = 1 - 0$ and HCO$^+$ mapping by Zhu and Wu (2007), two subcores exist within this core.

IRAS 03101+5821: ^{13}CO emission coincides with infrared point sources and image as well. A core more massive than $5.8 \times 10^2 M_\odot$ agrees with the conclusion drawn from the luminosity/line-width criteria. We therefore suggest that it is a pre-UC H II region. A 22 GHz water maser has been detected within this area (Wouterloot et al. 1993).

IRAS 03258+3104: a *MSX* band A image is unavailable for this region and we use band C instead. ^{13}CO emission within this area is more diffuse than that in former sources. At least two cores (03260+3111 and 03260+3111NE) are resolved within an area of 0.34 pc. The larger core coincides with *IRAS* 03260+3111, which does not satisfy our color selection criteria and was suggested as an UC H II region by Churchwell et al. (1990). Taking both their line width and luminosity into account, we suggest that core 03260+3111 is a high-mass object in UC H II phase, while 03260+3111NE is a sourceless core. The original guide source of the map, *IRAS* 03258+3104, is not associated with any resolved ^{13}CO core. It has been suggested to be a Class 0 object driving a low-mass bipolar CO outflow (Knee and Sandell 2000).

IRAS 03414+3200: ^{13}CO is quite diffuse across the entire area of 0.34 pc, so that no distinctive ^{13}CO core is found. However, several infrared point sources are evident close to the 90 % contour within one beam, superimposed on a steep density gradient. Although its mass ($> 85 M_\odot$) and line width 1.92 kms^{-1}) are relatively low in all the mapped sources, it appears to be a star forming cluster.

IRAS 05168+3634: at least two cores (05168+3634 and 05168+3634SW) are present within 3.01 pc. The dominant northeastern core appears to be associated with

the infrared sources. The total core mass higher than $1.5 \times 10^4 M_\odot$ agrees with the conclusion deduced from the luminosity/line-width criteria. We suggest that the dominant core is a high-mass star forming region in pre-UC H II phase, and the SW core is a sourceless core. This is consistent with results from Molinari et al. (1996). Strong outflow activity was identified (Brand et al. 1994; Zhang et al. 2005) at the position of the NE core, and the outflow driving source appears deviated to the infrared source *IRAS* 05168+3634. A 22 GHz water maser was detected by Palla et al. (1991) in this region.

IRAS 06067+2138: ^{13}CO core coincides with the *IRAS* point source but is without *MSX* counterpart. The core mass $M_{\rm LTE}$ ($2.5 \times 10^2 M_\odot$) is only one third of its virial mass $M_{\rm vir}$ ($7.8 \times 10^2 M_\odot$), indicating that the core is not yet gravitationally bound. Taking its large line width (3.36 kms^{-1}) into account, we suggest that it is a high-mass object earlier than pre-UC H II phase.

IRAS 06103+1523: ^{13}CO emission coincides with both infrared point sources and image. A core as massive as $2.8 \times 10^3 M_\odot$ agrees with the conclusion deduced from the luminosity/line-width criteria. *IRAS* 06103+1523 is found to be two point sources by *MSX* data, implying that a fine structure may exist there. A denser molecular tracer (e.g., N_2H^+ or HCO^+) and a higher resolution (several arcsec) are needed to study these fine structures. We therefore suggest that it is a high-mass star forming cluster.

IRAS 07024-1102: ^{13}CO map is incomplete but a core is clearly evident. The core coincides with the *IRAS* point source but does not have a *MSX* counterpart. Although its luminosity ($570\,L_\odot$) is a little lower than the luminosity criterion, it does generate a line width (1.99 kms^{-1}) very close to the line-width criterion. We therefore suggest that it is a high-mass object earlier than pre-UC H II phase.

IRAS 20067+3415: the ^{13}CO gas distribution is quite complex in this region. At least two cores (20067+3415 and 20067+3415NE) are revealed. The dominant southwestern core coincides with infrared point sources, while the northeastern core is a sourceless core. Several sub-structures are revealed within an area of 2.21 pc with total mass of $4.9 \times 10^3 M_\odot$. Thus, we suggest that core 20067+3415 is a high-mass star forming cluster. The MIR emission and luminosity are relatively weak compared to those of other pre-UC H II regions, indicating a very early evolutionary stage.

IRAS 20149+3913: ^{13}CO emission reveals two cores (20149+3913 and 20151+3911); both also coincide with infrared point sources and image. They do not satisfy the luminosity criterion but have large line widths, consistent with their high masses. Both sources are located in the Cygnus X molecular cloud complex and were mapped in 1.2 mm continuum (Motte et al. 2007), yielding masses $8\,M_\odot$ and $23\,M_\odot$, respectively (see Table 1 and Fig. 13 in their paper). Here we suggest that both cores are pre-UC H II regions.

IRAS 21391+5802: ^{13}CO emission detects a distinctive core and a belt of gas distributed along the southeast to northwest direction, which is coincident with the MIR background and several point sources. The core mass $M_{\rm LTE}$ ($1.3 \times 10^2 M_\odot$) is roughly half of its virial mass $M_{\rm vir}$ ($3.1 \times 10^2 M_\odot$), indicating that the core is not yet gravitationally bound, responsible for a large line width (2.78 kms^{-1}). Taking its relatively small size (0.32 pc) into account, we suggest that it is a star forming cluster where high-mass stars could eventually form. A 22 GHz water maser and outflow were identified in this region (Palla et al. 1991; Zhang et al. 2005).

IRAS 22198+6336: *MSX* data are unavailable near this region, but the *IRAS* source matches the ^{13}CO core peak well. A core as massive as $1.7 \times 10^3 M_\odot$ agrees with the conclusion deduced from the luminosity/line-width criteria. A 22 GHz water maser and outflow were identified in this region (Palla et al. 1991; Zhang et al. 2005). We therefore suggest that it is a pre-UC H II region.

IRAS 22506+5944: ^{13}CO core coincides well with a luminous *IRAS* point source and a bright *MSX* counterpart. A core as massive as $1.0 \times 10^3 M_\odot$ agrees with the conclusion deduced from the luminosity/line-width criteria. Thus, we suggest that it is a pre-UC H II region. Outflow activity (Wu et al. 2005b; Zhang et al. 2005) and a 22 GHz water maser (Palla et al. 1991) were identified, indicating that active star formation process is underway.

In summary, ^{13}CO $J = 2 - 1$ mapping reveals at least 18 massive cores from 14 maps. By means of individual analyses, we identify eight pre-UC H II regions and one UC H II region, two high-mass cores earlier than pre-UC H II phase, four possible star forming clusters, and three sourceless cores.

2.7 Conclusions

We have carried out a ^{13}CO $J = 2 - 1$ survey of 135 *IRAS* sources selected as potential YSOs earlier than UC H II regions. Our main findings are summarized as follows:

1. Ninety-eight sources have good enough emission profile for analysis; some of them show asymmetric line profiles of ^{13}CO $J = 2 - 1$. The line width is 3.09 kms^{-1} and excitation temperature is 9.7 K, on average. The H_2 column densities are (1.7–40.8) $\times 10^{21}$ cm^{-2}. Sixty-five sources are suggested to be candidate precursors of UC H II regions.
2. Fourteen sources were mapped and resolved as eighteen cores, which have been identified with eight pre-UC H II regions and one UC H II region, two high-mass cores earlier than pre-UC H II phase, four possible star forming clusters, and three sourceless cores.
3. For molecular clouds with known associated YSOs and measured $L_{\rm bol}$, ^{13}CO line width ΔV_{13} of the clouds is correlated with the bolometric luminosity of the YSOs. Based on the current ^{13}CO observed sample (360 sources in total), this correlation can be fitted as a power law, $\lg(\Delta V_{13}/\,\mathrm{kms}^{-1}) = (-0.023 \pm 0.044) + (0.135 \pm 0.012) \lg(L_{\rm bol}/L_\odot)$.
4. Luminous ($>10^3\ L_\odot$) YSOs tend to be produced in more massive and more turbulent ($\Delta V_{13} > 2\,\mathrm{kms}^{-1}$) molecular cloud structures.

References

Ao, Y., Yang, J., Sunada, K.: ^{13}CO, C^{18}O, and CS observations toward massive dense cores. Astron. J. **128**, 1716–1732 (2004). doi:10.1086/423906

Beichman, C.A., Myers, P.C., Emerson, J.P., Harris, S., Mathieu, R., Benson, P.J., Jennings, R.E.: Candidate solar-type protostars in nearby molecular cloud cores. Astrophys. J. **307**, 337–349 (1986). doi:10.1086/164421

Beichman, C.A., Neugebauer, G., Habing, H.J., Clegg, P.E., Chester, T.J. (eds.) Infrared astronomical satellite (IRAS) catalogs and atlases. Volume 1: Explanatory Supplement, vol. 1 (1988)
Beltrán, M.T., Girart, J.M., Estalella, R., Ho, P.T.P., Palau, A.: IRAS 21391+5802: the molecular outflow and its exciting source. Astrophys. J. **573**, 246–259 (2002). doi:10.1086/340592, arXiv:astro-ph/0203206
Beuther, H., Schilke, P., Sridharan, T.K., Menten, K.M., Walmsley, C.M., Wyrowski, F.: Massive molecular outflows. Astron. Astrophys. **383**, 892–904 (2002). doi:10.1051/0004-6361:20011808, arXiv:astro-ph/0110372
Brand, J., Blitz, L.: The velocity field of the outer galaxy. Astron. Astrophys. **275**, 67 (1993)
Brand, J., Cesaroni, R., Caselli, P., Catarzi, M., Codella, C., Comoretto, G., Curioni, G.P., Curioni, P., di Franco, S., Felli, M., Giovanardi, C., Olmi, L., Palagi, F., Palla, F., Panella, D., Pareschi, G., Rossi, E., Speroni, N., Tofani, G.: The Arcetri catalogue of H_2_O maser sources update. Astron. Astrophys. Suppl. **103**, 541–572 (1994)
Bronfman, L., Nyman, L.A., May, J.: A CS(2-1) survey of IRAS point sources with color characteristics of ultra-compact HII regions. Astron. Astrophys. Suppl. **115**, 81 (1996)
Caselli, P., Myers, P.C.: The line width-size relation in massive cloud cores. Astrophys. J. **446**, 665 (1995). doi:10.1086/175825
Casoli, F., Combes, F., Dupraz, C., Gerin, M., Boulanger, F.: (C-13)O and (C-12)O observations of cold IRAS unidentified point sources in the galaxy. Astron. Astrophys. **169**, 281–297 (1986)
Cesaroni, R., Galli, D., Lodato, G., Walmsley, C.M., Zhang, Q.: Disks around young O-B (proto)stars: observations and theory. In: Reipurth, B., Jewitt, D., Keil, K. (eds.) Protostars and Planets V, pp. 197–212 (2007)
Churchwell, E.: Ultra-compact HII regions and massive star formation. Ann. Rev. Astron. Astrophys. **40**, 27–62 (2002). doi:10.1146/annurev.astro.40.060401.093845
Churchwell, E., Walmsley, C.M., Cesaroni, R.: A survey of Ammonia and water vapor emission from ultracompact HII regions. Astron. Astrophys., Suppl. **83**, 119–144 (1990)
Dent, W.R.F., Little, L.T., Kaifu, N., Ohishi, M., Suzuki, S.: A plan view of the bipolar molecular outflow source G35.2N. Astron. Astrophys. **146**, 375–380 (1985)
Dobashi, K., Bernard, J.P., Fukui, Y.: Molecular clouds in Cygnus. II. statistical studies of star-forming regions. Astrophys. J. **466**, 282 (1996). doi:10.1086/177509
Fischer, J., Sanders, D.B., Simon, M., Solomon, P.M.: High velocity gas flows associated with h2 emission regions—how are they related and what powers them. Astrophys. J. **293**, 508 (1985). doi:10.1086/163256
Forbrich, J., Menten, K.M., Reid, M.J.: A 1.3 cm wavelength radio flare from a deeply embedded source in the Orion BN/KL region. Astron. Astrophys. **477**, 267–272 (2008). doi:10.1051/0004-6361:20078070,0711.2017
Gao, Y., Solomon, P.M.: The star formation rate and dense molecular gas in galaxies. Astrophys. J. **606**, 271–290 (2004). arXiv:astro-ph/0310339
Garden, R.P., Hayashi, M., Hasegawa, T., Gatley, I., Kaifu, N.: A spectroscopic study of the DR 21 outflow source. III—the CO line emission. Astrophys. J. **374**, 540–554 (1991). doi:10.1086/170143
Gregory, P.C.: The 87GB catalog of radio sources covering delta between O and +75 deg at 4.85 GHz. Astrophys. J. Suppl. **75**, 1011–1291 (1991). doi:10.1086/191559
Griffith, M.R., Wright, A.E., Burke, B.F.: The Parkes-MIT-NRAO (PMN) surveys. 3: source catalog for the tropical survey (−29 deg less than delta less than −9 deg.5). Astrophys. J. Suppl. **90**, 179–295 (1994). doi:10.1086/191863
Griffith, M.R., Wright, A.E., Burke, B.F., Ekers, R.D.: The Parkes-MIT-NRAO (PMN) surveys. 6: source catalog for the equatorial survey (−9.5 deg less than delta less than +10.0 deg). Astrophys. J. Suppl. **97**, 347–453 (1995). doi:10.1086/192146
Guan, X., Ju, B.: A mapping survey of massive CO cores. Mon. Not. RAS **391**, 869–880 (2008). doi:10.1111/j.1365-2966.2008.13937.x

Guilloteau, S., Lucas, R.: Imaging at the IRAM plateau de Bure interferometer. In: Mangum, J.G., Radford, S.J.E. (eds.) Imaging at Radio Through Submillimeter Wavelengths. Astronomical Society of the Pacific Conference Series, vol. **217**, p. 299 (2000)

Harju, J., Walmsley, C.M., Wouterloot, J.G.A.: Ammonia clumps in the Orion and Cepheus clouds. Astron. Astrophys., Suppl. **98**, 51–75 (1993)

Harju, J., Lehtinen, K., Booth, R.S., Zinchenko, I.: A survey of SiO emission towards interstellar masers. I. SiO line characteristics. Astron. Astrophys. Suppl. **132**, 211–231 (1998). doi:10.1051/aas:1998448

Hartquist, T.W., Caselli, P., Rawlings, J.M.C., Ruffle, D.P., Williams, D.A.: The chemistry of star forming regions. In: Hartquist, T.W., Williams, D.A. (eds.) The Molecular Astrophysics of Stars and Galaxies, pp. 101, 101 (1998)

Jijina, J., Myers, P.C.: Dense cores mapped in ammonia: a database. Astrophys. J. Suppl. **125**, 161–236 (1999). doi:10.1086/313268

Kennicutt, R.C. Jr.: The global Schmidt law in star-forming galaxies. Astrophys. J. **498**, 541 (1998). doi:10.1086/305588, arXiv:astro-ph/9712213

Keto, E.: An ionized accretion flow in the ultracompact H II region G10.6-0.4. Astrophys. J. **568**, 754–760 (2002). doi:10.1086/339056

Kim, K.T., Kurtz, S.E.: Occurrence frequency of CO outflows in massive protostellar candidates. Astrophys. J. **643**, 978–984 (2006). doi:10.1086/502961, arXiv:astro-ph/0601532

Knee, L.B.G., Sandell, G.: The molecular outflows in NGC 1333. Astron. Astrophys. **361**, 671–684 (2000)

Ladd, E.F., Myers, P.C., Goodman, A.A.: Dense cores in dark clouds. 10: ammonia emission in the Perseus molecular cloud complex. Astrophys. J. **433**, 117–130 (1994). doi:10.1086/174629

Larson, R.B.: Turbulence and star formation in molecular clouds. Mon. Not. RAS **194**, 809–826 (1981)

Lee, Y., Jung, J.H.: A molecular cloud complex above the galactic plane.: I. extended CO observations of the NGC 281 region. New Astron. **8**, 191–207 (2003). doi:10.1016/S1384-1076(02)00227-0

MacLaren, I., Richardson, K.M., Wolfendale, A.W.: Corrections to virial estimates of molecular cloud masses. Astrophys. J. **333**, 821–825 (1988). doi:10.1086/166791

Matthews, H.I.: High resolution radio observations of bright rims in IC 1396. Astron. Astrophys. **75**, 345–350 (1979)

Molinari, S., Brand, J., Cesaroni, R., Palla, F.: A search for precursors of ultracompact HII regions in a sample of luminous IRAS sources. I. Association with Ammonia cores. Astron. Astrophys. **308**, 573–587 (1996)

Motte, F., Bontemps, S., Schilke, P., Schneider, N., Menten, K.M., Broguière, D.: The earliest phases of high-mass star formation: a 3 square degree millimeter continuum mapping of Cygnus X. Astro. Astrophys. **476**, 1243–1260 (2007). doi:10.1051/0004-6361:20077843,0708.2774

Myers, P.C., Linke, R.A., Benson, P.J.: Dense cores in dark clouds. I—CO observations and column densities of high-extinction regions. Astrophys. J. **264**, 517–537 (1983). doi:10.1086/160619

Myers, P.C., Ladd, E.F., Fuller, G.A.: Thermal and nonthermal motions in dense cores. Astrophys. J. Lett. **372**, L95–L98 (1991). doi:10.1086/186032

Palla, F., Brand, J., Comoretto, G., Felli, M., Cesaroni, R.: Water masers associated with dense molecular clouds and ultracompact H II regions. Astron. Astrophys. **246**, 249–263 (1991)

Plume, R., Jaffe, D.T., Evans, N.J., Martin-Pintado, J., Gomez-Gonzalez, J.: Dense gas and star formation: characteristics of cloud cores associated with water masers. Astrophys. J. **476**, 730 (1997). doi:10.1086/303654, arXiv:astro-ph/9609061

Price, S.D., Egan, M.P., Carey, S.J., Mizuno, D.R.: Midcourse space experiment survey of the galactic plane. Astron. J. **121**, 2819–2842 (2001). doi:10.1086/320404

Richards, P.J., Little, L.T., Heaton, B.D., Toriseva, M.: HCO(+) survey of unassociated compact molecular clouds in the IRAS point source catalog. Mon. Not. RAS **228**, 43–54 (1987)

Ridge, N.A., Wilson, T.L., Megeath, S.T., Allen, L.E., Myers, P.C.: A ^{13}CO and C^{18}O survey of the molecular gas around young stellar clusters within 1 Kiloparsec of the sun. Astron. J. **126**, 286–310 (2003). doi:10.1086/375455, arXiv:astro-ph/0303401

Rodriguez, L.F., Carral, P., Ho, P.T.P., Moran, J.M.: Anisotropic mass outflow in regions of star formation. Astrophys. J. **260**, 635–646 (1982). doi:10.1086/160285

Saito, H., Mizuno, N., Moriguchi, Y., Matsunaga, K., Onishi, T., Mizuno, A., Fukui, Y.: The most massive C^{18}O molecular complex in centaurus and star formation therein. Publ. ASJ **53**, 1037–1051 (2001)

Schmidt, M.: The rate of star formation. Astrophys. J **129**, 243 (1959). doi:10.1086/146614

Sridharan, T.K., Beuther, H., Saito, M., Wyrowski, F., Schilke, P.: High-mass starless cores. Astrophys. J. Lett. **634**, L57–L60 (2005). doi:10.1086/498644, arXiv:astro-ph/0508421

Sun, K., Kramer, C., Ossenkopf, V., Bensch, F., Stutzki, J., Miller, M.: A KOSMA 7 deg^2 ^{13}CO 2-1 and ^{12}CO 3-2 survey of the Perseus cloud. I. structure analysis. Astron. Astrophys. **451**, 539–549 (2006). doi:10.1051/0004-6361:20054256

Szymczak, M., Hrynek, G., Kus, A.J.: A survey of the 6.7 GHz methanol maser emission from IRAS sources. I. Data. Astron. Astrophys. Suppl. **143**, 269–301 (2000)

Wang, K., Wu, Y.F., Ran, L., Yu, W.T., Miller, M.: The relation between ^{13}CO J = 2–1 line width in molecular clouds and bolometric luminosity of associated IRAS sources. Astron. Astrophys. **507**, 369–376 (2009). doi:10.1051/0004-6361/200811104,0909.3312

Wood, D.O.S., Churchwell, E.: Massive stars embedded in molecular clouds—their population and distribution in the galaxy. Astrophys. J. **340**, 265–272 (1989). doi:10.1086/167390

Wouterloot, J.G.A., Walmsley, C.M., Henkel, C.: Ammonia towards IRAS sources in the Orion and Cepheus clouds. Astron. Astrophys. **203**, 367–377 (1988)

Wouterloot, J.G.A., Brand, J., Fiegle, K.: IRAS sources beyond the solar circle. III—observations of H2O, OH, CH3OH and CO. Astron. Astrophys. Suppl. **98**, 589–636 (1993)

Wu, J., Evans, N.J.: Indications of inflow motions in regions forming massive stars. Astrophys. J. Lett. **592**, L79–L82 (2003). doi:10.1086/377679, arXiv:astro-ph/0306543

Wu, Y., Wu, J., Wang, J.: A search for massive dense cores with ^{13}CO J = 1–0 line. Astron. Astrophys. **380**, 665–672 (2001). doi:10.1051/0004-6361:20011498

Wu, Y., Wang, J., Wu, J.: A search for extremely young stellar objects. Chin. Phys. Lett. **20**, 1409–1412 (2003)

Wu, Y., Wei, Y., Zhao, M., Shi, Y., Yu, W., Qin, S., Huang, M.: A study of high velocity molecular outflows with an up-to-date sample. Astron. Astrophys. **426**, 503–515 (2004). doi:10.1051/0004-6361:20035767, arXiv:astro-ph/0410727

Wu, J., Evans, N.J., Gao, Y., Solomon, P.M., Shirley, Y.L.: Connecting dense gas tracers of star formation in our galaxy to high-z star formation. Astrophys. J. Lett. **635**, L173–L176 (2005a). doi:10.1086/499623, arXiv:astro-ph/0511424

Wu, Y., Zhang, Q., Chen, H., Yang, C., Wei, Y., Ho, P.T.P.: CO J = 2–1 maps of bipolar outflows in massive star-forming regions. Astron. J. **129**, 330–347 (2005b). doi:10.1086/426361

Wu, Y., Zhang, Q., Yu, W., Miller, M., Mao, R., Sun, K., Wang, Y.: Ammonia cores in high mass star formation regions. Astron. Astrophys. **450**, 607–616 (2006). doi:10.1051/0004-6361:20053203

Yamashita, T., Suzuki, H., Kaifu, N., Tamura, M., Mountain, C.M., Moore, T.J.T.: A new CO bipolar flow and dense disk system associated with the infrared reflection nebula GGD 27 IRS. Astrophys. J. **347**, 894–900 (1989). doi:10.1086/168180

Zhang, Q.: Massive star disks. In: Cesaroni, R., Felli, M., Churchwell, E., Walmsley, M. (eds.) Massive Star Birth: A Crossroads of Astrophysics, IAU Symposium, vol. 227, pp. 135–144 (2005). doi:10.1017/S174392130500445X

Zhang, Q., Hunter, T.R., Sridharan, T.K.: A rotating disk around a high-mass young star. Astrophys. J. Lett. **505**, L151–L154 (1998). doi:10.1086/311609

Zhang, Q., Hunter, T.R., Brand, J., Sridharan, T.K., Cesaroni, R., Molinari, S., Wang, J., Kramer, M.: Search for CO outflows toward a sample of 69 high-mass protostellar candidates. II. Outflow properties. Astrophys. J. **625**, 864–882 (2005). doi:10.1086/429660

Zhao, M., Wu, Y., Miller, M., Mao, R.: CO studies of IRAS 00117+6412. Acta Astron. Sinica **44**, 103–105 (2003)
Zhu, L., Wu, Y.F.: Molecular cores in different evolutionary stages near luminous IRAS sources and UC HII regions. Chin. J. Astron. Astrophys. **7**, 331–334 (2007). doi:10.1088/1009-9271/7/3/01

Chapter 3
The "Dragon" Nebula G28.34+0.06

Abstract This chapter presents new SMA and JVLA observations of an infrared dark cloud G28.34+0.06. Located in the quiescent southern part of the G28.34 cloud, the region of interest is a massive ($>10^3\,M_\odot$) molecular clump P1 with a luminosity of $\sim 10^3\,L_\odot$, where our previous SMA observations at 1.3 mm have revealed a string of five dust cores of 22–64 $M_\odot$ along the 1 pc IR-dark filament. The cores are well aligned at a position angle of 48° and regularly spaced at an average projected separation of 0.16 pc. The new high-resolution, high-sensitivity 0.88 mm image further resolves the five cores into ten compact condensations of 1.1–17.2 $M_\odot$, with sizes a few thousands AU. The spatial structure at clump ($\sim$1 pc) and core ($\sim$0.1 pc) scales indicates a hierarchical fragmentation. While the clump fragmentation is consistent with a cylindrical collapse, the observed fragment masses are much larger than the expected thermal Jeans masses. All the cores are driving CO (3–2) outflows up to 38 km s^{-1}, majority of which are bipolar, jet-like outflows. Multiple NH_3 transitions reveal the heated gas widely spread in the 1 pc clump. The temperature distribution is highly structured; the heated gas is offset from the protostars, and matches the outflows in morphology. Hot spots of spatially compact, spectrally broad NH_3 (3,3) emission features are also found coincident with the outflows. A weak NH_3 (3,3) maser is discovered at the interface between an outflow jet and the ambient gas. The moderate luminosity of the P1 clump sets a limit on the mass of protostars of 3–7 $M_\odot$. Because of the large reservoir of dense molecular gas in the immediate medium and ongoing accretion as evident by the jet-like outflows, we speculate that P1 will grow and eventually form a massive star cluster. This study provides a first glimpse of massive, clustered star formation that currently undergoes through an intermediate-mass stage. The findings suggest that protostellar heating may not be effective in suppressing fragmentation during the formation of massive cores.

3.1 Introduction

Stars are born in dense molecular clouds through gravitational collapse. A classic picture of low-mass star formation has been described in Shu et al. (1987). During the collapse, a parsec-scale molecular clump fragments into gaseous cores

K. Wang, *The Earliest Stages of Massive Clustered Star Formation: Fragmentation of Infrared Dark Clouds*, Springer Theses,
DOI 10.1007/978-3-662-44969-1_3

that subsequently collapse and fragment to condensations which eventually form individual or a group of stars. After the formation of an accretion disk, a bipolar wind develops to shed angular momentum in the disk so that circumstellar matter can accrete onto the protostar. Interactions between such a wind and the ambient molecular cloud may produce highly collimated molecular outflows (or "molecular jets") at parsec scales (Shang et al. 2006, 2007).

Massive protostars are often found embedded in massive molecular clumps of $10^3\,M_\odot$ (Plume et al. 1997; Molinari et al. 2000; Beuther et al. 2002b; Beltrán et al. 2006). Their presence is marked by high luminosity ($>10^3\,L_\odot$), copious spectra from organic molecules (Blake et al. 1987; Schilke et al. 1997), active accretion (Zhang 2005; Cesaroni et al. 2006), and strong molecular outflows (Zhang et al. 2001, 2005; Beuther et al. 2002c). However, the stage prior to the high mass protostellar phase is not clear. Do massive protostars evolve through a low to intermediate-mass stage? How does accretion proceed? Do cores harboring massive young stellar objects collect all the mass before the formation of a protostar? These questions can potentially be addressed by studying massive infrared dark clouds (IRDCs).

IRDCs are dense ($>10^4\,\mathrm{cm}^{-3}$) and cold ($<25\,\mathrm{K}$) molecular clouds that absorb Galactic background mid-infrared emission while emit at longer wavelengths ($\gtrsim 100\,\mu\mathrm{m}$). Because of their extreme properties, IRDCs are ideal laboratories to study the early stages of star formation, and thus have been subjected to intense studies since their identification in mid-1990s by the *Infrared Space Observatory* (ISO) and the *Midcourse Space Experiment* (*MSX*; Perault et al. 1996; Egan et al. 1998; Hennebelle et al. 2001). Comprehensive catalogs have been established based on Galactic IR surveys from the *MSX* (Simon et al. 2006a, b) and *Spitzer* (Peretto and Fuller 2010), revealing more than 10,000 IRDCs. Among them, the ones with masses of $10^3\,M_\odot$ and luminosities $<10^3\,L_\odot$ are candidates of massive star formation at a stage prior to the high mass protostellar phase.

G28.34+0.06 (hereafter G28.34), one of the first recognized and well studied IRDCs (Carey et al. 1998, 2000), appears to be a candidate to form massive stars (see Fig. 3.1 for an overview). This IR-dark filamentary complex shapes like a Chinese dragon extending $\sim$6 pc at a distance of $\sim$4.8 kpc. The giant cloud contains several $10^3\,M_\odot$ of dense gas traced by 1 mm dust emission (Carey et al. 2000; Simon et al. 2006b; Rathborne et al. 2006; Pillai et al. 2006; Wang et al. 2008; Zhang et al. 2009). Two prominent dust clumps, P1 and P2, are revealed from dust continuum images obtained from single dish telescopes (Carey et al. 2000; Rathborne et al. 2006). Large amount of dense gas ($\sim 10^3\,M_\odot$ within <1 pc) makes P1 and P2 potential sites of protostellar cluster formation. Zhang et al. (2009) observed P1 and P2 with the SMA at 230 GHz band. They found that, despite similar amount of dense gas contained in the two clumps, P1 and P2 show very different stages of evolution. At a $1''.2$ resolution, the northern clump P2 fragments to two compact cores with masses 49 and 97 $M_\odot$, respectively. The cores emit rich organic molecular line emissions analogous to that observed in hot cores. The southern clump P1, on the other hand, fragments

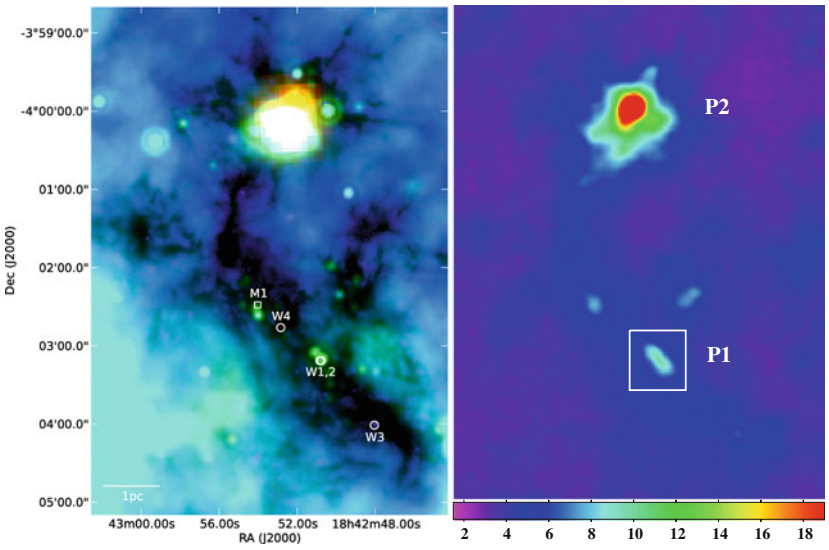

Fig. 3.1 Panoramic view of the Dragon nebula (IRDC G28.34+0.06). *Left Spitzer* composite image (*red/green/blue* = 70/24/8 μm) showing the IRDC complex. Overlaid are the water (W1–4) and methanol (M1) masers detected by our JVLA observations. The positions and spectra of the masers are presented in Fig. 3.8. The *Spitzer* data are taken from the GLIMPSE and MIPSGAL legacy projects (Churchwell et al. 2009; Carey et al. 2009) [*Credit* Wang et al. (2012), reproduced with permission of the AAS] *Right* CSO 350 μm continuum emission image. The *color bar* indicates flux in Jy per 9″.6 beam. The *white box* outlines clump P1 [*Credit* Ke Wang (ESO)]

to a string of five cores regularly spaced along the IR-dark ridge, with masses of 22–64 $M_{\odot}$. In contrast to the cores in P2, the P1 cores show no molecular line emission except faint CO(2–1) across the entire 4 GHz SMA band. This implies a significant CO depletion at a scale over 0.07 pc in the P1 cores. In addition, an enhancement of deuterium fractionation was also found toward P1 (Chen et al. 2010). All these properties point P1 to a quiescent stage much earlier than P2. However, strong H_2O maser (Wang et al. 2006) and enhanced 4.5 μm emission ("green fuzzy"; Chambers et al. 2009), as well as a faint 24 μm source in P1 suggest that star formation may be ongoing.

This chapter presents new SMA and JVLA observations of G28.34-P1. With even higher resolution and better sensitivity, the new observations reveal a great details of the ongoing star formation, including hierarchical structures, multiple jet-like outflows, new masers, an X-shaped filamentary system, and feedback from the star formation activities to the parental clump.

3.2 Observations

3.2.1 Submillimeter Array

We observed the molecular clump P1 in IRDC G28.34+0.06 with the Submillimeter Array[1] (SMA; Ho et al. 2004) at the 345 GHz band from 2009 April 26 through 2009 September 23. During six observing runs, the SMA antennas were in three different array configurations: compact (COM), extended (EXT), and subcompact (SUB), each was used to observe for two nights for this project. Table 3.1 summarizes the observations.

For all the observations, we used a common phase center (R.A., decl.)$_{J2000}$ = ($18^h42^m50.^s74$, $-04°03'15.''3$). Quasars J1751+096 and J1830+063 were observed approximately every 20 min to monitor time dependent antenna gains. The receivers were tuned to a local oscillate frequency of 341.6 GHz, with a uniform spectral resolution of 0.812 MHz (or 0.7 km s^{-1}) across the entire band. The system temperature varies from 120 to 500 K during the six tracks. The full-width-half-maximum (FWHM) primary beam is about $34''$.

For the COM observations, we used quasar 3C273 for frequency dependent bandpass calibration. Absolute flux was obtained by comparing the observed correlator counts with modeled fluxes of dwarf planet Ceres. With an IF of 4–6 GHz, the lower sideband (LSB) covered rest frequencies from 335.7 through 337.7 GHz and the upper sideband (USB) covered 345.6–347.6 GHz.

For the EXT observations, 3C454.3 was used for bandpass calibration, while young star MWC349 or planet Uranus was observed for flux calibration. The observations made use of the newly upgraded capability that doubled the original IF

Table 3.1 SMA observations towards G28.34-P1

Array	UT date (yyyymm)	Number of antenna	Bandwidth (GHz)	Bandpass calibrator	Flux calibrator	T_{sys} (K)	$\tau_{225\,GHz}$[a]
COM	20090426	7	2	3C273	Ceres	200–400	0.09–0.15
COM	20090503	7	2	3C273	Ceres	160–280	0.05
EXT	20090806	8	4	3C454.3	MWC349	260–500	0.09–0.14
EXT	20090826	7	4	3C454.3	Uranus	120–250	0.06–0.07
SUB	20090905	5	4	3C454.3	Ganymede, Callisto	160–300	0.05–0.07
SUB	20090923	7	4	3C454.3	Ganymede, Callisto	150–300	0.07–0.09

[a] Zenith opacity measured from water vapor monitors mounted on CSO or JCMT

[1] The Submillimeter Array is a joint project between the Smithsonian Astrophysical Observatory and the Academia Sinica Institute of Astronomy and Astrophysics and is funded by the Smithsonian Institution and the Academia Sinica.

bandwidth to 4 GHz in each sideband, covering rest frequencies 333.7–337.7 GHz in the LSB and 345.6–349.6 GHz in the USB.

For the SUB observations, bandpass was calibrated by observing 3C454.3 and flux was scaled by observing Jovial satellites Callisto and Ganymede. The frequency coverage was the same as the EXT observations.

The visibility data were calibrated using MIR IDL software package.[2] Calibrated visibility data were then exported to MIRIAD[3] (Sault et al. 1995) for further processing and imaging. CASA[4] (McMullin et al. 2007) was also used for part of the image processing.

Data from different observing runs were calibrated separately, and then combined in the visibility domain for analysis. Continuum emission was generated by averaging line free channels in the visibility domain. In this study, if not otherwise stated, we use the EXT data for continuum analysis and the combined SUB and COM data for spectral analysis. With natural weighting, the synthesized beam is $0''.69 \times 0''.64$, with PA $= -83°.1$ for the continuum image; while for the spectral line, the beam is $3''.23 \times 1''.96$, PA $= -47°.4$. The 1σ rms noise is about 0.8 mJy in the continuum, and about 100 mJy (0.2 K) per 1 km s^{-1} in the spectra. If we use the SUB data only, the beam becomes larger and we obtain a 1σ rms of 0.1 K at the same spectral resolution. Empirically, the absolute flux is accurate to about 15 %. The uncertainty in the absolute position is $\lesssim 0''.1$, obtained by comparing the fitted position of the secondary gain calibrator and its catalog position.

3.2.2 *Very Large Array*

The Karl G. Jansky Very Large Array (JVLA) of NRAO[5] was used to obtain the NH_3 (J,K) = (1,1), (2,2), (3,3), as well as H_2O and CH_3OH maser line emission data in 2010 during the Expanded VLA early science phase. Table 3.2 summarizes the observations. The data were calibrated in CASA and imaged using CASA and Miriad.

The NH_3 (1,1) and (2,2) observed in the C array has a channel width of 0.2 km s^{-1}. Wang et al. (2008) observed NH_3 (1,1) and (2,2) toward the same phase center in the D array with a channel spacing of 0.6 km s^{-1}. We combined the calibrated visibilities of Wang et al. (2008) with the new C array data for imaging. To increase the signal-to-noise ratio in the final images, we averaged the channel width to 0.3 km s^{-1} and tapered the visibilities with a Gaussian function with a FWHM of 180 kλ. We also made images with a 0.6 km s^{-1} channel width to compare with the images at 0.3 km s^{-1} resolution, and found that the latter does not introduce additional features.

[2] http://www.cfa.harvard.edu/~cqi/mircook.html.

[3] http://www.cfa.harvard.edu/sma/miriad, http://www.astro.umd.edu/~teuben/miriad.

[4] http://casa.nrao.edu.

[5] The National Radio Astronomy Observatory is a facility of the National Science Foundation operated under cooperative agreement by Associated Universities, Inc.

Table 3.2 JVLA observations towards G28.34-P1

Parameter/line	NH_3 (1,1)	NH_3 (2,2)	NH_3 (3,3)	H_2O/CH_3OH
Observing date	2010Oct09	2010Oct11	2010May09	2010Nov24
Configuration	C	C	D	C
Rest frequency (GHz)	23.694	23.722	23.870	22.235/24.959
Primary beam ($'$)	2	2	2	2
Gain calibrator	J1851+005	J1851+005	J1851+005	J1851+005
Flux calibrator[a]	3C48	3C48	3C48	3C48
Bandpass calibrator	3C454.3	3C454.3	3C454.3	3C454.3
Phase center[b]	I	I	II	II
Integration time (min)	95	95	21	15/15
Bandwidth (MHz)	4	4	4	4
Polarization	Dual	Dual	Dual	Full
Naive channel width ($km\,s^{-1}$)	0.2	0.2	0.2	0.8
Final channel width ($km\,s^{-1}$)	0.3	0.3	0.3	0.8
Synthesized beam ($''$)[c]	2.7×2.2	2.8×2.0	4.8×2.7	$1.3 \times 1.0/1.5 \times 0.9$
RMS noise (mJy/beam)[d]	1.2–1.5	1.2–1.5	3	1.2–1.5/0.8
Convention factor (K/Jy)	367	388	165	1939/1484
Weighting method	Natural	Natural	Natural	Robust/natural

[a] Absolute flux is accurate to about 5 %
[b] Phase center I at (R.A., decl.)$_{J2000} = 18^h42^m50^s, -04°03'30''$; II at $18^h42^m50^s.82, -04°03'11''.3$
[c] Final NH_3 (1,1) and (2,2) images are made by adding archival D array data (Sect. 3.2)
[d] 1σ rms noise measured in the final images

For the NH_3 (3,3) images we also averaged the channel width to $0.3\,km\,s^{-1}$ to improve the signal-to-noise ratio.

3.3 Results

3.3.1 Hierarchical Fragmentation

There are different definitions of clump, core, and condensation in the literature when describing the spatial structure of dust continuum or molecular line emission. In the following discussion, we refer a clump as a structure with a size of ∼1 pc, a core as a structure with a size of ∼0.1 pc, and a condensation as a substructure of ∼0.01 pc within a core. A clump is capable of forming a cluster of stars, a core may form one or a small group of stars, and a condensation can typically form a single star or a multiple-star system. This nomenclature is consistent with the one adopted by Zhang et al. (2009).

Figure 3.2 presents the 0.88 mm continuum emission. The $0''.69 \times 0''.64$ resolution image resolves the clump into five groups of compact condensations, corresponding

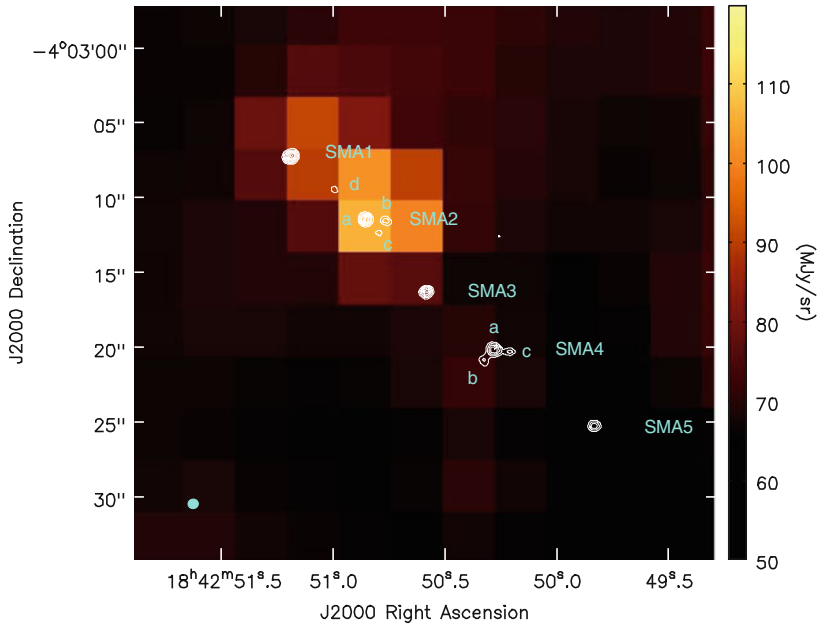

Fig. 3.2 SMA 0.88 mm image of the G28.34-P1 region in contour overlaid on the *Spitzer* 24 μm image in color scale. The SMA image is made from the EXT configuration data only, with synthesized beam $0''.69 \times 0''.64$, PA $= -83°.1$, indicated as an *ellipse* in the *lower left corner* of the panel. The contours start at 4 mJy (5σ) and increase by a step of 1.6 mJy (2σ). Assigned condensation names are also labeled on the image. The SMA image shown here is not corrected for the primary beam attenuation [*Credit* Wang et al. (2011), reproduced with permission of the AAS]

to the five dust cores discovered at 1.3 mm, namely SMA1, SMA2, SMA3, SMA4, and SMA5 (Zhang et al. 2009). Cores SMA1, SMA3, and SMA5 consist of one condensation. Cores SMA2 and SMA4 consist of three condensations, with one dominating over the other two in peak flux. In addition, a faint condensation is also revealed northeast to core SMA2. We tentatively assign this condensation to the SMA2 group. We name all the 10 condensations accordingly and label them on Fig. 3.2. Refining the core positions using the positions of the dominant condensations, the five cores are spaced by an projected distance of 0.16 ± 0.02 pc ($6''.8 \pm 1''.0$), and are well aligned at a position angle (PA, east of north) of 48°. In cores SMA2 and SMA4, the three condensations are spaced by 0.03 ± 0.007 pc ($1''.3 \pm 0''.3$).

We estimate the mass of each condensation. Assuming optically thin dust emission, the dust mass can be estimated following

$$M_{\rm dust} = \frac{F_\nu d^2}{B_\nu(T_{\rm dust})\kappa_\nu},$$

where $M_{\rm dust}$ is the dust mass, F_ν is the continuum flux at frequency ν, d is the source distance, $B_\nu(T_{\rm dust})$ is the Planck function at dust temperature $T_{\rm dust}$, and

$\kappa_\nu = 10(\nu/1.2\,\mathrm{THz})^\beta\ \mathrm{cm^2\,g^{-1}}$ is the dust opacity (Hildebrand 1983). We adopt the dust temperatures from high resolution NH_3 lines (Sect. 3.4.2.1). The dust opacity at millimeter/sub-millimeter wavelengths is uncertain. For dust in the interstellar medium, $\beta = 2$ (Draine and Lee 1984). Rathborne et al. (2010) derived $\beta = 1.5 \pm 0.3$ for the entire P1 clump based on a global spectral energy distribution. We generated a dust opacity map by comparing the continuum image at 345 and 230 GHz, and found β to vary from 1.3 to 2.5 across the map. Given the uncertainties, we adopt $\beta = 1.5$ for all the cores similar to Zhang et al. (2009), and discuss the effect of different β on the mass estimates.

Table 3.3 lists coordinates, size, peak flux, integrated flux, and estimated mass of all the 10 condensations. These parameters are determined by fitting a two dimensional Gaussian function to the observed flux distribution. Fluxes are then corrected for primary beam attenuation. The masses of the condensations range from 1.1 to 17.2 $M_\odot$ with an average of 4.3 $M_\odot$. The mean size is $0''.9 \times 0''.7$, or $0''.6 \times 0''.2$ after deconvolved with the synthesized beam. The deconvolved size corresponds to about 3,000 × 1,000 AU at the source distance. The uncertainty in the mass estimation arises from several factors. First, the flux calibration contributes 15 % in uncertainty. Second, the uncertainty of β contributes in a form of $M_{\mathrm{dust}} \propto 3.5^\beta$. Third, the spatial filtering effect of radio interferometry preferentially picks up the compact structures and filters out the extended emission. Comparing images made from different array configurations, the EXT image recovered 20–30 % fluxes of what covered by COM and SUB images. This filtering effect explains why the masses reported in Table 3.2 are consistently lower than those in Zhang et al. (2009). The EXT image at 345 GHz represents the high contrast structure in these cores—the small, compact condensations tracing the immediate surroundings of the protostars.

Our observations reveal fragmentation at different spatial scales in G28.34-P1 (Fig. 3.3). First, the 1 pc clump fragments into five cores (Zhang et al. 2009);

Table 3.3 Properties of the condensations

Name	RA(J2000)	Dec(J2000)	Size		P.A.	F_{peak}	F_{int}	T^{a}	Mass/$M_\odot$	
	h:m:s	d:m:s	a″ × b″		°	mJy	mJy	K	$\beta = 1.5$	$\beta = 2$
SMA1	18:42:51.19	−04:03:07.2	0.82	0.68	−63.6	25.3	31.6	18	6.2	11.6
SMA2a	18:42:50.85	−04:03:11.4	0.74	0.70	55.2	15.7	18.3	19	3.3	6.2
SMA2b	18:42:50.76	−04:03:11.5	1.18	0.68	56.8	8.5	15.5	18	3.0	5.7
SMA2c	18:42:50.79	−04:03:12.4	0.81	0.62	60.5	5.1	5.8	18	1.1	2.1
SMA2d	18:42:50.99	−04:03:09.5	0.94	0.63	62.2	5.1	6.7	19	1.2	2.3
SMA3	18:42:50.58	−04:03:16.3	0.76	0.63	−82.3	14.4	15.6	18	3.1	5.7
SMA4a	18:42:50.28	−04:03:20.2	0.78	0.75	38.1	12.2	16.0	18	3.2	5.9
SMA4b	18:42:50.32	−04:03:21.0	1.30	0.75	33.2	6.8	15.0	18	3.0	5.5
SMA4c	18:42:50.20	−04:03:20.3	0.93	0.55	−84.7	7.4	8.5	18	1.7	3.1
SMA5	18:42:49.83	−04:03:25.2	0.91	0.74	78.8	16.6	25.1	9	17.2	32.2
Average									4.3	8.0

[a] Measured from JVLA NH_3 transitions, see Fig. 3.9a

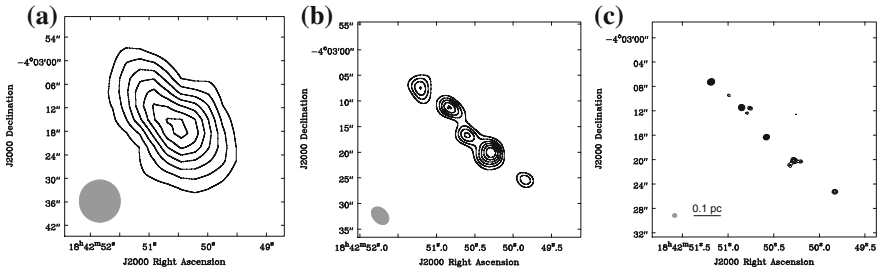

Fig. 3.3 Hierarchical structure of P1 resolved in dust continuum emission images at various resolutions (*gray ellipses*). **a** 1.2 mm emission from IRAM 30 m telescope (Rathborne et al. 2006) contoured at 10 % of the peak flux (260 mJy beam^{-1}) starting at 40 %. **b** SMA 1.3 mm emission (Zhang et al. 2009), contoured in step of 5 mJy beam^{-1} starting at 10 mJy beam^{-1}. **c** SMA 0.88 mm emission (Wang et al. 2011), contoured the same way as in Fig. 3.2 [*Credit* Ke Wang (ESO)]

second, two of the 0.1 pc cores fragment into even smaller condensations of 0.01 pc. The fragmentation at clump and core scales are consistent with a hierarchical fragmentation picture. The clump fragmentation is likely the result of initial physical conditions (density, temperature, turbulence, and magnetic fields), while the core fragmentation results from an increased density after the initial fragmentation. Based on the JVLA NH_3 (1,1) and (2,2) spectra (Wang et al. 2008) and the IRAM 30 m 1.2 mm continuum image (Rathborne et al. 2006), we measure an initial gas temperature of 13 K and density of 3×10^5 cm^{-3}, over a scale of 1 pc toward the P1 clump. These values yield a thermal Jeans mass of 0.8 $M_\odot$. At the core scale, density increases to several 10 times of the initial clump density. For instance, in SMA2 the core density measured from the 230 GHz image is 9.6×10^6 cm^{-3}, 32 times of the initial clump density. This density, together with an increased gas temperature (16 K), leads to a thermal Jeans mass of 0.2 $M_\odot$. These parameters are also listed in Table 3.4.

It is worth stressing that, in both clump and core fragmentation, the observed fragment (core/condensation) masses are significantly (∼10 times or more) larger than the expected thermal Jeans masses (Table 3.4), indicating that thermal pressure is not dominant in the fragmentation processes. Instead, turbulence may play an important role in supporting these large core/condensation masses, as discussed in Zhang et al. (2009) (see further discussion in Sect. 3.3.1.1). The 1σ rms sensitivity in Fig. 3.2 is 0.8 mJy, corresponding to 0.2 $M_\odot$, well below the thermal Jeans mass

Table 3.4 Hierarchical fragmentation in G28.34-P1

Source	T[a] K	$n(H_2)$ cm^{-3}	M_J $M_\odot$	R_J pc	Fragment mass[b] $M_\odot$
P1 to cores	13	3.0×10^5	0.8	0.04	22–64
P1-SMA2 to condensations	16	9.6×10^6	0.2	0.008	>1.1–3.3

[a] Gas temperatures are derived from JVLA NH_3 lines averaged over clump or core scales
[b] Observed core/condensation masses are calculated using a dust opacity index of $\beta = 1.5$

at the clump scale ($0.8\,M_\odot$). However, we did not detect any cores of $0.8\,M_\odot$ in the filament. The non-detection of Jeans mass cores in the clump may suggest that low mass cores are not significantly centrally peaked, thus they cannot be substantiated from the smooth emission in the clump.

3.3.1.1 Cylindrical Collapse

The most intriguing feature in G28.34-P1 is the configuration of well aligned, regularly spaced cores. The alignment and regularity strongly suggest a mechanism that is responsible for shaping the molecular filament into what it is now. Similar features (but at different spatial scales) have been reported in a large number of nearby dark clouds (Schneider and Elmegreen 1979), in a few filamentary IRDCs (e.g., Jackson et al. 2010; Miettinen and Harju 2010), as well as in numerical simulations (Martel et al. 2006). It has been suggested that these fragments are most likely the results of gravitational collapse of a cylinder, as first proposed by Chandrasekhar and Fermi (1953) and followed up by Nagasawa (1987) (also see discussion in Jackson et al. 2010). The theory predicts that, under self gravity, the gas in the cylinder will ultimately beak up into pieces with a certain interval ($\lambda_{\rm max}$) at which the instability grows the fastest and thus dominates the fragmentation process. Such 'sausage' instability produces a chain of equally spaced fragments along the filament, with the spacing roughly the interval $\lambda_{\rm max}$. The mass per unit length along the cylinder (or linear mass density) has a maximum value, $(M/l)_{\rm max} = 2\sigma^2/G = 465\,(\frac{\sigma}{\rm km\,s^{-1}})^2\,M_\odot\,{\rm pc}^{-1}$, where G is the gravitational constant. If the cylinder is supported by thermal pressure, σ is the sound speed c_s; if, on the other hand, it is mainly supported by turbulent pressure, then σ is replaced by the velocity dispersion.

We now compare the observational results with the theoretical predictions. In G28.34-P1, the FWHM line width is $1.7\,{\rm km\,s^{-1}}$, measured form the NH_3 (1,1) spectrum (Wang et al. 2008; Zhang et al. 2009). The line width is equivalent to a velocity dispersion of $\sigma = 0.72\,{\rm km\,s^{-1}}$ if the line profile is Gaussian. This velocity dispersion leads to a maximum mass density of $240\,M_\odot\,{\rm pc}^{-1}$. The total core mass in P1 is $183\,M_\odot$ over 0.8 pc along the filament (Zhang et al. 2009), implying a linear mass density of $230\,M_\odot\,{\rm pc}^{-1}$. Taking into account the missing flux in the interferometer maps, the observations match the theoretical predictions well if G28.34-P1 is mainly supported by turbulence.

The separation between two adjacent fragments, $\lambda_{\rm max}$, depends on the nature of the cylinder. For an incompressible fluid cylinder in absence of magnetic field, $\lambda_{\rm max} = 11R$, where R is the unperturbed cylindrical radius. And the instability manifests at about two free-fall timescales (see Sect. 3.3.2.2). In G28.34-P1, the average separation between cores is $\lambda_{\rm max} = 0.16\,{\rm pc}$, implying an initial radius of $R = 0.014\,{\rm pc}$, several times smaller than the core diameter of 0.1 pc (Zhang et al. 2009). If magnetic field is involved, the strength is of the order of $B = 4\pi\rho R\sqrt{G}$ (see Eq. (93) in Chandrasekhar and Fermi 1953). With $n = 3\times10^5\,{\rm cm^{-3}}$ and $R = 0.014\,{\rm pc}$, we obtain a magnetic field strength of 0.16 mG. This is relatively

small compared to magnetic field strength observed in massive star formation regions (e.g., Girart et al. 2009).

For an isothermal gas cylinder, $\lambda_{\rm max} = 22H$, where $H = v(4\pi G\rho_c)^{-1/2}$ is the scale height, whereas ρ_c is the gas density at the center of the cylinder. The equation can be simplified as

$$\lambda_{\rm max} = \begin{cases} 0.15\,{\rm pc}\left(\frac{c_s}{0.21\,{\rm km\,s^{-1}}}\right)\left(\frac{n}{3\times10^5\,{\rm cm^{-3}}}\right)^{-1/2} & \text{for thermal support,} \\ 0.13\,{\rm pc}\left(\frac{\sigma}{0.72\,{\rm km\,s^{-1}}}\right)\left(\frac{\rm n}{5\times10^6\,{\rm cm^{-3}}}\right)^{-1/2} & \text{for turbulent support.} \end{cases}$$

In the above equations, the sound speed c_s of $0.21\,{\rm km\,s^{-1}}$ is calculated using a gas temperature of 13 K; volume density $3 \times 10^5\,{\rm cm^{-3}}$ is the averaged clump density, while $5 \times 10^6\,{\rm cm^{-3}}$ is the average of clump density ($3 \times 10^5\,{\rm cm^{-3}}$) and core density ($9.6 \times 10^6\,{\rm cm^{-3}}$) given in Table 3.4. We see that both scenarios are in agreement with the observed spacing of $\lambda_{\rm max} = 0.16 \pm 0.02\,{\rm pc}$ if the assumptions are reasonable. However, since the density should be the central density of the cylinder, we suspect that the turbulent support is more likely dominant in G28.34-P1.

Comparison between observational results and theoretical predictions suggests that the fragmentation in the G28.34-P1 filament is well represented by a cylindrical collapse. The filament is likely supported mainly by turbulence rather than thermal pressure.

3.3.1.2 Core Structures

We measure the core density profiles in unresolved cores SMA1, SMA3, and SMA5. The measurements are performed in the visibility domain to avoid defects in image deconvolution. We combine the SUB, COM, and EXT data for analysis for this purpose. The combined visibility data sample the G28.34-P1 region over baseline lengths ranging from about 5 to 200 kλ, offering a fairly well sampled (u, v) measurement.

For a spherical core, the observed flux distribution over radial distance $F(r)$ represents the radial density profile modified with temperature gradient. The dust temperature scales as $T_{\rm dust} \propto r^{-a}$ (Scoville and Kwan 1976) with $a = 0.33$, if the core is internally heated. As long as Rayleigh-Jeans approximation holds, this temperature gradient contributes to the total flux in the form of $\propto r^{-a}$. Assuming a power law density profile, $\rho \propto r^{-b}$, and optically thin dust emission, the observed dust continuum flux integrated along the line of sight, $F \propto \int \rho T_{\rm dust} ds$, or

$$F \propto r^{-(a+b-1)},$$

when $(a + b) > 1$. In the visibility domain, this is Fourier transformed into a form of

$$A_{uv} \propto S_{uv}^{(a+b-3)},$$

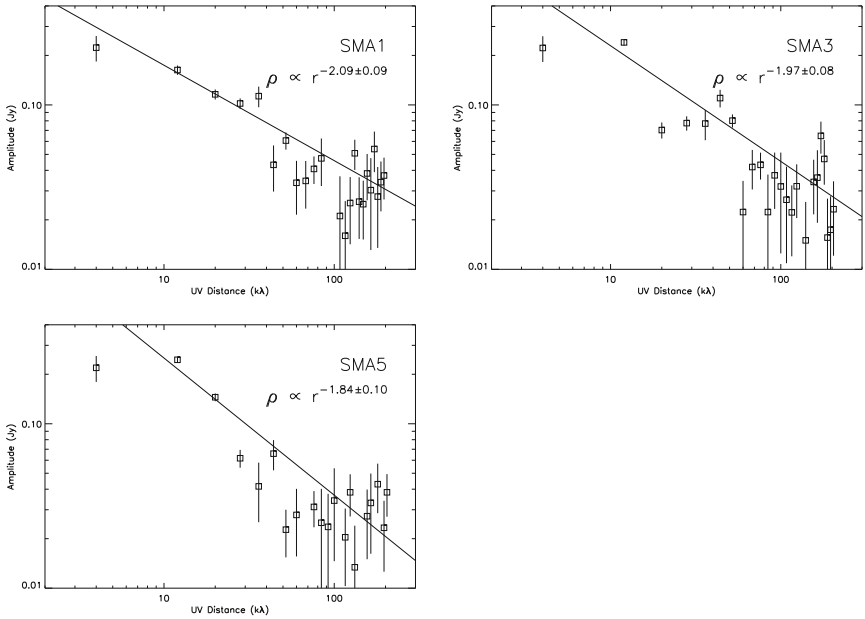

Fig. 3.4 Amplitude distribution against (u, v) distance of cores SMA1, SMA3, and SMA5 [*Credit* Wang et al. (2011), reproduced with permission of the AAS]

where A_{uv} is the visibility amplitude and $S_{uv} = \sqrt{(u^2 + v^2)}$ is the (u, v) distance (Looney et al. 2000; Zhang et al. 2009).

Figure 3.4 plots the amplitude versus (u, v) distance for SMA1, SMA3, and SMA5. The amplitude is a vector average of the visibility data in a concentric annuli defined by a bin of 8 kλ. Least-squares fitting yields $b = 2.09 \pm 0.09$ for SMA1, 1.97 ± 0.08 for SMA3, and 1.84 ± 0.10 for SMA5. The results are consistent with Zhang et al. (2009) measured from the 230 GHz continuum data, where they derived $b = 2.1 \pm 0.2$ for SMA4. The density profiles are similar to that of an isothermal sphere in hydrostatic equilibrium, where the radial density scales as $\propto r^{-2}$. We note that the large error bars and discrepancy at long (u, v) distances reflect sensitivity limits and may be also partly due to unresolved weak sources in the vicinity.

3.3.2 CO Outflows

3.3.2.1 Morphology

Among the entire 8 GHz SMA band, only CO (3–2) is detected above 3σ ($1\sigma \approx 0.1$ K at 1 km s^{-1} resolution). Nevertheless, CO (3–2) reveals high-velocity outflowing gas in P1. Figure 3.5 presents the CO (3–2) channel maps, and Fig. 3.6 plots the integrated

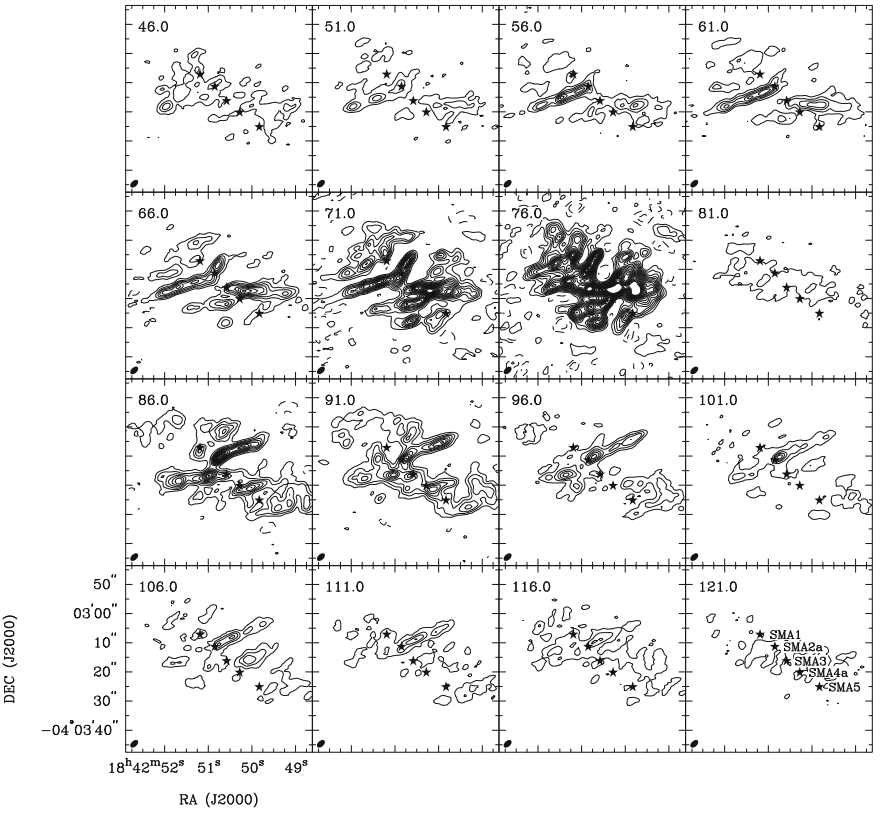

Fig. 3.5 CO (3–2) channel maps towards G28.34-P1. The image is made by averaging the emission over a 5 km s^{-1} velocity interval, with the central velocity labeled on each panel. The contours start at 5σ (240 mJy) and step by $\pm 5\sigma$. The *filled ellipse* on the *bottom left corner* represents the synthesized beam. The stars mark the presumable outflow driving sources as labeled on the last panel (see the text) [*Credit* Wang et al. (2011), reproduced with permission of the AAS]

blueshifted emission in blue contours, and redshifted emission in red contours, superposed on the continuum emission. One can find in Fig. 3.5 that the extended CO emission close to the systemic velocity (78.4 km s^{-1}) is filtered out. This effect actually helped us identify outflows at high velocities. It is intriguing that all the five dust cores are associated with CO outflows, majority of which are bipolar, jet-like outflows.

The outflows are centered on the dust cores and are generally oriented cross the major axis of the filament. The most prominent outflow is centered on core SMA2, with a blue lobe emanating toward southeast (SE; see channels of 51–71 km s^{-1} in Fig. 3.5), and a red lobe toward northwest (NW; 86–116 km s^{-1}). In addition, a minor blue lobe is also seen at NW (66–76 km s^{-1}). The outflow centered on SMA3 is in an east-west orientation, with its blue lobe emanating westbound (51–71 km s^{-1})

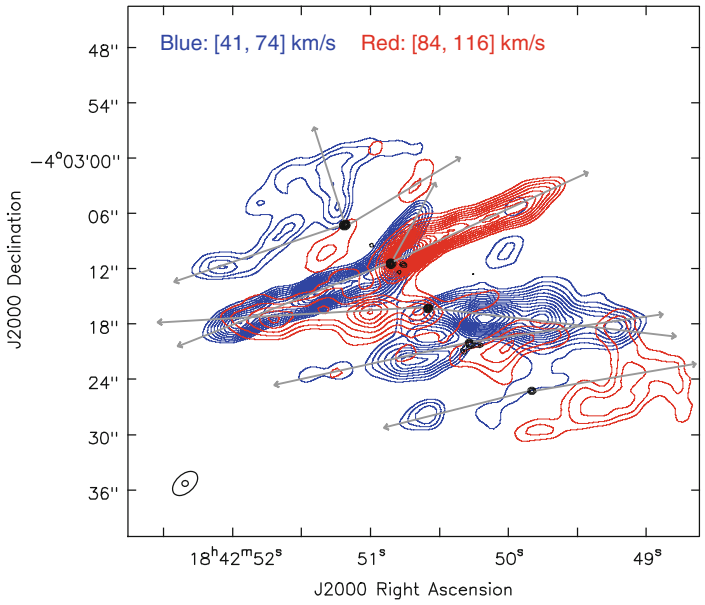

Fig. 3.6 Integrated CO (3–2) emission overlaid on the 0.88 mm continuum emission of the G28.34-P1 region. The velocity ranges used for integration are [41, 74] km s^{-1} for the blueshifted lobe (*blue contours*), and [84, 116] km s^{-1} for the redshifted lobe (*red contours*). The CO contours are $\pm(2, 2.5, 3, \ldots, 9.5) \times 10$ % of the *blue lobe peak*, 39 Jy beam^{-1} km s^{-1}. The continuum contours are the same as in Fig. 3.2. The *arrows* sketch the outflow directions. The synthesized beams indicated in the *lower left corner* are $3''.23 \times 1''.96$, PA $= -47°.4$ for the CO image, while $0''.69 \times 0''.64$, PA $= -83°.1$ for the continuum image [*Credit* Wang et al. (2011), reproduced with permission of the AAS]

and its red lobe eastbound (86–96 km s^{-1}). SMA4 lies in the center of a NW-SE outflow, with a SE blue lobe (66–76 km s^{-1}) and a NW red lobe (86–91 km s^{-1}). SMA1 is associated with a quadrupolar outflow. Its two blue lobes are seen at 66–71 km s^{-1}, emanating toward SE and north, respectively. Its two red lobes are seen from 86 through 91 km s^{-1} toward NW and south, respectively. The outflow centered on SMA5 has an orientation almost parallel to the SMA4 outflow. This outflow is weak compared to others, and its SE blue lobe and NW red lobe can be barely seen at 66–71 km s^{-1} and 86–91 km s^{-1}, respectively. Orientation of all the outflows are sketched as arrows in Fig. 3.6.

The driving sources of these outflows can be identified geometrically. Cores SMA1 to SMA5 are roughly located at the geometric centers of the outflows, respectively. While SMA1, SMA3 and SMA5 are unresolved, SMA2 and SMA4 are resolved into three condensations. In these two cases, we assign the strongest and/or central condensation as the driving source of the relevant outflow. Hence, the outflows are likely driven by condensations SMA1, SMA2a, SMA3, SMA4a, and SMA5.

The CO outflows shown in Figs. 3.5 and 3.6 consist of pairs of knots which are geometrically symmetric with respect to the central protostar. Illustrated in Fig. 3.6, outflows SMA2a and SMA3 have four pairs of knots, and outflow SMA4a has two pairs. The knots are equally spaced by about 0.16 pc. These knots in outflows may represent outbursts due to disk variability arising from episodic, unsteady accretion (e.g., HH 211, Lee et al. 2010; HH 80–81, Qiu and Zhang 2009). With the spacing and maximum outflow velocity $v_{\rm max}$, we estimate the period between two outbursts to be about 4,000 yr. This value lies in the range of roughly 10^3–10^4 yr used in episodic accretion models for low mass stars (Baraffe and Chabrier 2010; Zhu et al. 2010).

The outflows show slight bending (Fig. 3.6). In the outflow SMA3, the red lobe bends 5° toward the south, and the blue lobe bends 6° toward the south, making the outflow C-shaped. In outflows SMA2a and SMA4a, and probably SMA1, the knots seem to trace the propagation of a periodically wiggled, S-shaped molecular jet, most evident at the closest knotty pairs near the protostar. Part of this effect may be contaminated by multiple outflows (e.g., in outflow SMA2a). Nevertheless, the mirror symmetric (C-shaped) wiggles and point symmetric (S-shaped) wiggles may indicate different bending mechanisms like jet precession, orbital motion of the jet source, and Lorentz forces (Fendt and Zinnecker 1998; Masciadri and Raga 2002; Raga et al. 2009). Similar bending effects have been observed in a number of Herbig-Haro jets (e.g., HH 211, Lee et al. 2010) and some of the most collimated high-mass molecular jets (e.g., Su et al. 2007). Because the wiggles are not prominent in CO(3–2), we do not discuss this effect further.

3.3.2.2 Physical Properties

We calculate the physical parameters of each outflow, including mass, momentum, energy, as well as dynamical age and outflow rate. Assuming local thermodynamic equilibrium and optically thin CO emission in the line wings, we first derive the CO column density following Garden et al. (1991),

$$N_{\rm CO}({\rm cm}^{-2}) = 4.81 \times 10^{12}\,(T_{\rm ex} + 0.92)\exp\left(\frac{33.12}{T_{\rm ex}}\right)\int T_{\rm B}\,dv\ ,$$

where dv is the velocity interval in km s^{-1}, and $T_{\rm ex}$ and $T_{\rm B}$ are excitation temperature and brightness temperature in K, respectively. We take the gas temperatures (Table 3.3) to be the excitation temperatures. The outflow mass, momentum, energy, dynamical age, and outflow rate are then given by

$$M = d^2\,[\frac{\rm H_2}{\rm CO}]\,\overline{m}_{\rm H_2}\int_{\Omega} N_{\rm CO}(\Omega')d\Omega'\ ,$$

$$P = Mv\ ,$$

$$E = \frac{1}{2} M v^2 ,$$

$$t_{\rm dyn} = \frac{L_{\rm flow}}{v_{\rm max}},$$

$$\dot{M}_{\rm out} = \frac{M}{t_{\rm dyn}},$$

where d is the source distance, $\overline{m}_{\rm H_2}$ is the mean mass per hydrogen molecule assumed to be 2.33 atomic units, Ω is the total solid angle that the flow subtends, v is the outflow velocity with respect to the systemic velocity of 78.4 km s^{-1}, $v_{\rm max}$ is the maximum outflow velocity, and $L_{\rm flow}$ is the flow length. We adopt an empirical $[\frac{\rm H_2}{\rm CO}]$ abundance ratio of 10^4 (Blake et al. 1987).

Table 3.5 lists derived physical parameters for each outflow. The outflow properties show general symmetry in blue- and redshifted lobes. The energetics are small compared to outflows observed in high mass protostellar objects (Beuther et al. 2002c; Zhang et al. 2005), but are similar to outflows emanating from nearby ($\lesssim$1 kpc) intermediate-mass hot cores (IMHCs: IRAS 22198+6336, Sánchez-Monge et al. 2010; NGC 7129-FIRS 2, Fuente et al. 2005; IC 1396 N, Neri et al. 2007). Particularly, the outflow rate $\dot{M}_{\rm out}$, which amounts to (4–47) $\times 10^{-6}\, M_\odot\, {\rm yr}^{-1}$, and the flow momentum P, which ranges from 1 to 9 $M_\odot$ km s^{-1}, are of the same order to all the three IMHC outflows known to date. The dynamic timescales are (1.5–3.4) $\times 10^4$ yr for all the outflows. These values are comparable to massive outflows but are one order of magnitude higher than the IMHC outflows. Because observations are limited by noise and gas at higher velocities are possible, $t_{\rm dyn}$ is a lower limit of the outflow age and the accretion history of the dominant protostar. Theoretical models suggest that the massive star formation process takes a few times of the free fall timescale ($t_{\rm ff} = \sqrt{\frac{3\pi}{32 G\rho}} = \frac{3.66\times10^7 {\rm yr}}{\sqrt{n({\rm cm}^{-3})}}$) of the core. Beuther et al. (2002c) observed a rough equality between $t_{\rm dyn}$ and $t_{\rm ff}$. For the P1 cores, we obtain $t_{\rm ff}$ of (1.2–6.7) $\times$ 10^4 yr based on the densities given in Table 3.4. We see that $t_{\rm ff}$ approximates $t_{\rm dyn}$ well, and this supports the idea that flow ages are good estimates of protostar lifetimes (Beuther et al. 2002c).

The SMA2a, SMA3, and SMA4a outflows are so well collimated that they resemble "molecular jets" commonly found in low-mass star-forming regions (e.g., L1157, Zhang et al. 2000; OMC-1S, Zapata et al. 2005; HH 211, Lee et al. 2007). Recently, interferometric observations have revealed collimated outflows in high-mass star-forming regions (e.g., AFGL 5142, Hunter et al. 1999; Zhang et al. 2007a; IRAS 20126+4104, Cesaroni et al. 1999; Shepherd et al. 2000; IRAS 05358+3543, 19410+2336, 19217+1651, Beuther et al. 2002a, 2003, 2004; HH80–81, Qiu and Zhang 2009). To measure the collimation, we take the ratio of outflow total length (blue + red lobes) over width measured in Fig. 3.6 as collimation factor. We obtain 14, 10, and 7 for SMA2a, SMA3, and SMA4a outflows, over scales of 0.5–1 pc. These values are comparable to that of the most collimated low-mass outflows and are

Table 3.5 Derived outflow parameters

Parameter[a]	SMA1		SMA2a		SMA3		SMA4a		SMA5	
	Blue	Red	Blue	Red	Blue	Red	Blue	Red	Blue	Red
T_{ex} (K)[b]	18		19		18		18		9	
v ($\mathrm{km\,s^{-1}}$)[c]	[67, 76]	[85, 93]	[41, 76]	[84, 116]	[50, 71]	[85, 99]	[64, 72]	[85, 107]	[66, 73]	[86, 93]
M ($M_\odot$)	0.13	0.05	0.32	0.20	0.15	0.12	0.04	0.08	0.11	0.13
P ($M_\odot\,\mathrm{km\,s^{-1}}$)	0.75	0.48	4.33	3.43	2.12	1.37	0.35	1.01	0.77	1.39
E ($M_\odot\,\mathrm{km^2\ s^{-2}}$)	2.58	2.42	45.44	39.25	18.06	8.75	1.72	7.71	3.10	7.51
L_{flow} (pc)[d]	0.40	0.27	0.51	0.48	0.56	0.51	0.44	0.43	0.34	0.39
t_{dyn} (10^4 yr)	3.43	1.81	1.33	1.25	1.93	2.42	2.99	1.47	2.68	2.61
$\dot{M}_{out}$($10^{-5}\,M_\odot\,\mathrm{yr^{-1}}$)	0.39	0.27	2.43	1.56	0.76	0.50	0.13	0.55	0.42	0.51

[a] Parameters are not corrected for inclination angle
[b] Excitation temperature taken from Table 3.3
[c] Range of velocities used to derive outflow parameters
[d] Projected length of the longer lobe in case of two lobes

higher than that of the high-mass outflows discovered by single dishes and previous interferometers (Wu et al. 2004; Beuther et al. 2002c; Qiu and Zhang 2009). Beuther et al. (2007a) reported one outflow in IRAS 05358+3543 with a collimation factor of ∼10 and claimed that it was the first massive outflow observed with such a high degree of collimation at a scale of 1 pc. In G28.34-P1, the SMA2a and SMA3 outflows are among the best collimated molecular outflows yet discovered in high-mass star-forming regions over parsec scales. We note that these collimation factors should be considered as lower limits because the outflow lengths and widths are not corrected for inclination angle, and are not deconvolved with synthesized beam.

3.3.3 Ammonia Emission

Figure 3.7 presents moment 0, 1 and 2 maps of the NH_3 (1,1), (2,2) and (3,3) main hyperfine emission. The NE-SW orientated filament is traced by the NH_3 (1,1) and (2,2) emission extremely well. Ammonia cores coincide with all the SMA dust cores, indicating that NH_3 traces the dense envelopes of the protostellar cores. As illustrated in the moment 1 images of NH_3 (1,1) and (2,2), there is a velocity gradient of $1.5\,\mathrm{km\,s^{-1}}$ over 1 pc along the filament. This gradient is, however, not uniform; it is enhanced toward southwest starting at SMA5. On the other hand, the velocity field from SMA1 through SMA4 is quite uniform, at about $79\,\mathrm{km\,s^{-1}}$. The moment 2 images show similar velocity dispersion[6] of 0.4–0.8 $\mathrm{km\,s^{-1}}$ along the filament as traced by NH_3 (1,1) and (2,2). The velocity dispersion is enhanced to several local maxima of 0.6–0.8 $\mathrm{km\,s^{-1}}$ which coincide with all the SMA dust cores except SMA3. The enhancements may originate from a combination of spatially unresolved motions such as rotation, infall, and outflow.

In addition to the main filament, the NH_3 (1,1) emission also reveals a fainter northwest-southeast (NW-SE) orientated filament, crossing the main filament at SMA5, making an X shape. This minor filament is located at a slightly different velocity, around $82\,\mathrm{km\,s^{-1}}$. Compared to the main filament, the minor filament shows weaker emission in NH_3 (1,1) and little emission in NH_3 (2,2), indicative of even colder gas. The minor filament is evident in the previous NH_3 (1,1) image at lower resolution (Wang et al. 2006; Zhang et al. 2009), however, it does not correspond to any dust emission feature at 350–1300 μm (Rathborne et al. 2006, 2010; Zhang et al. 2009; Chen et al. 2010; Wang et al. 2011). Therefore, the minor filament is remarkably less dense than the main filament. Like the main filament, the minor filament consists of a velocity gradient of $2\,\mathrm{km\,s^{-1}}$ over 1 pc; it also hosts several NH_3 cores with sizes similar to the NH_3 cores on the main filament. It has a velocity dispersion of $\leq 0.4\,\mathrm{km\,s^{-1}}$ in general, but local enhancements of up to $0.5\,\mathrm{km\,s^{-1}}$ are also presented. We will discuss the nature of the minor filament in Sect. 3.4.3.

[6] For a Gaussian line profile, velocity dispersion σ is related to FWHM line width ΔV as $\sigma = \Delta V/2\sqrt{2\ln 2}$.

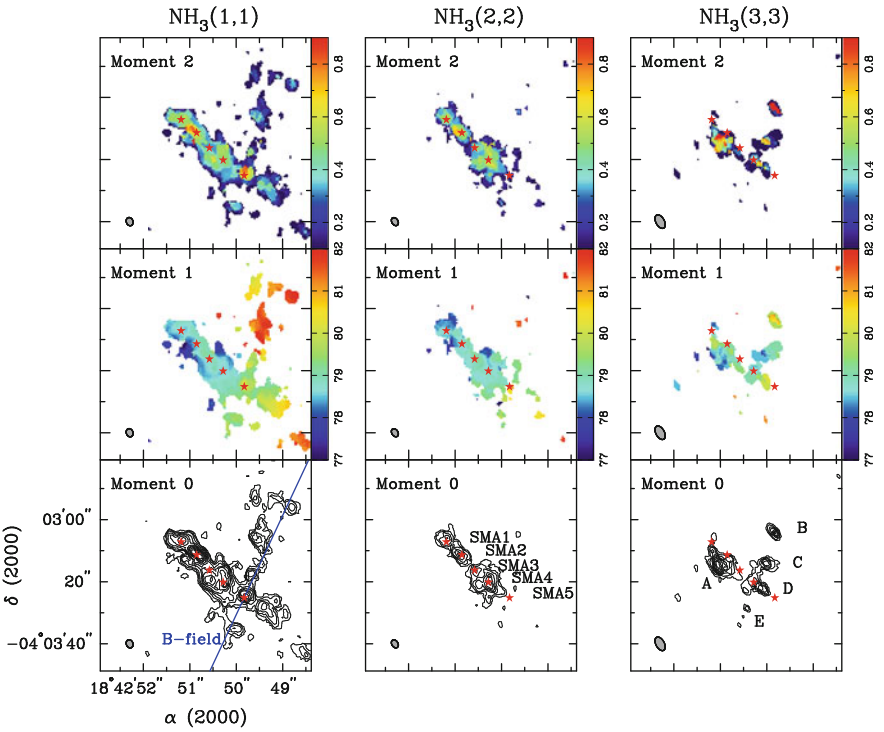

Fig. 3.7 Moment maps of the main hyperfine emission of NH_3 (1,1), (2,2) and (3,3), shown on the *left*, *middle* and *right* columns, respectively. The contours are plotted in steps of 6σ, which is 0.5 mJy beam^{-1} km s^{-1} for (1,1) and (2,2), while 1 mJy beam^{-1} km s^{-1} for (3,3). Units of the color bars are km s^{-1}. The *stars* mark the five dust cores (SMA1-5) which are further resolved into smaller condensations (the *black contours* in Fig. 3.9). The *blue line* on the *bottom-left* panel indicates the direction of the mean magnetic field (Sect. 3.4.3). The *filled ellipses* on the *bottom-left corners* represent synthesized beams [*Credit* Wang et al. (2012), reproduced with permission of the AAS]

In the following text, unless otherwise stated, we refer the main NE-SW filament as "the filament".

It is interesting to note that the clumpy NH_3 (3,3) emission does not follow the dust filament at all. We visually identified five representative peaks from the (3,3) moment 0 map, labeled as A–E in Fig. 3.7. None of these peaks coincide with any dust cores. In fact, the only one that lies on the filament is peak D which is between SMA4 and SMA5; other peaks are offset from the filament. Because NH_3 (3,3) is excited at an energy level of 125 K, these ammonia peaks trace local temperature enhancements relative to the generally cold molecular clump. Another important feature is the large velocity dispersion: all the peaks show centrally condensed distribution of $\sigma > 0.8\,\mathrm{km\,s^{-1}}$, and up to $2.2\,\mathrm{km\,s^{-1}}$ in peak B. Peak B is located down stream of the red lobe of outflow SMA2a, the most energetic outflow in P1 (Wang et al. 2011).

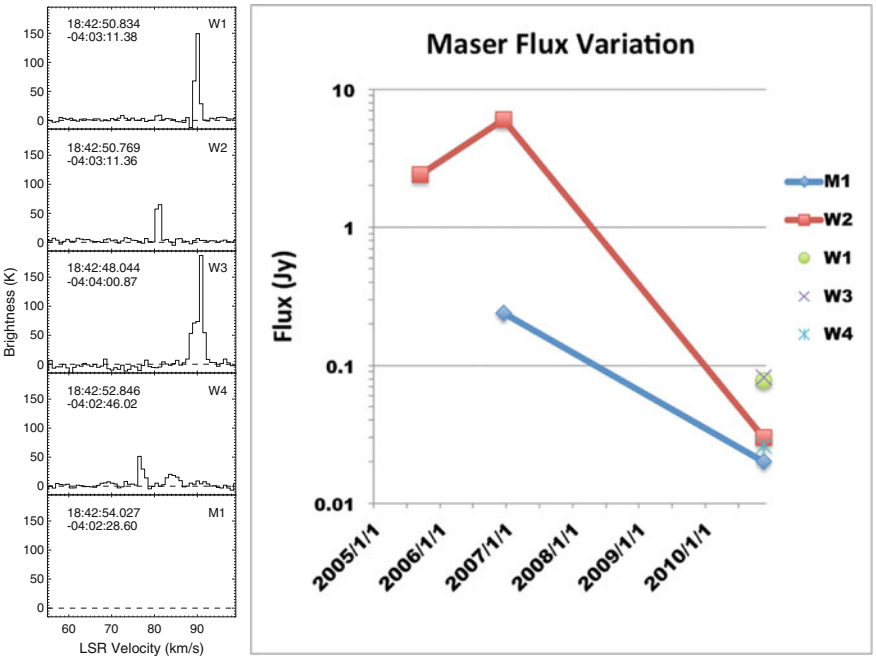

Fig. 3.8 *Left* Spectra and coordinates of the water (W1–4) and methanol (M1) masers detected with JVLA on 2010 November 24. Brightness temperatures have been corrected for primary beam response. See Fig. 3.1 for the location of the masers in the IRDC complex [*Credit* Wang et al. (2012), reproduced with permission of the AAS] *Right* Variation of masers M1 and W2 from 2005 to 2010. W1,3,4 are new detections (see text). [*Credit* Ke Wang (ESO)]

The centroid velocity on peak B is redshifted relative to the filament, consistent with the redshifted CO emission. Indeed, all these NH_3 (3,3) peaks seem to trace the footprint of the jet-like CO (3–2) outflows revealed by the SMA (Wang et al. 2011). We will discuss this further in Sect. 3.4.2.1.

3.3.4 Maser Emission

We report maser detections based on the following criteria: (a) Peak flux $\geq 6\sigma$; (b) Emission continues at least two channels with flux $\geq 4\sigma$; and (c) Within the primary beam response of ≥ 0.3. We adopt these criteria because at some channels the images are contaminated by the side lobes of a strong maser located at P2 (Wang et al. 2006), well outside of the primary beam. Using the criteria, we identify 4 water masers (W1–4) and 1 methanol maser (M1), as presented in Figs. 3.1 and 3.8. Positions of the masers are obtained by fitting a two dimensional Gaussian to the brightness distribution of the maser emission. The positional uncertainty is $\leq 0''.02$.

All masers are either coincident with or close to infrared point sources at 8–24 μm. Their FWHM line widths are less than 1 km s^{-1} with only one exception, the H_2O maser W3 which has a line width of about 2 km s^{-1}. Because maser emission has a narrow line width in nature, this indicates that our observation has spatially resolved the maser knots in most cases.

Comparing the maser positions and velocities with previous observations made with JVLA (Wang et al. 2006, resolution ∼2″) and GBT (Chambers et al. 2009, resolution ∼30″), we find that W1, W3, and W4 are new features, while W2 and M1 are spatially and spectrally coincident with two masers reported previously. Both W2 and M1 have been varying in peak flux during the last several years: W2 was 2.4 Jy on 2005 September 23/24, then brightened to 6 Jy on 2006 December 5, and dimmed dramatically to 0.03 Jy on 2010 November 24; M1 dimmed from 0.24 Jy on 2006 December 5 to 0.02 Jy on 2010 November 24. On the other hand, W1 and W3 were either newly emerged or experienced brightening between 2006 and 2010, otherwise they should have been detected by Chambers et al. (2009). W4 is below the detection limit of Chambers et al. (2009).

Among all the five detected masers, only two (W1, W2) are associated with NH_3 emission above 6σ significance. W1 and W2 locate right on top of the dust condensations SMA2a and SMA2b, respectively, and have distinct velocities (90 and 81 km s^{-1}), thus they are presumably excited by the protostars embedded in their own dust condensations. The position discrepancy between the H_2O maser with its exciting protostar is within a fraction of 1,000 AU. Based on the CO outflow driven by SMA2 we can only identify SMA2a as a protostar. However, the maser emission suggests that SMA2b is also a protostar. It is interesting to note that the water maser reported by Wang et al. (2008) is located between SMA2a and SMA2b (see Fig. 3.4 of Wang et al. (2011) for illustration), but has a velocity of 80 km s^{-1}. Therefore, we suspect that the previous maser detection corresponds to W2.

3.4 Discussion

3.4.1 Massive Star Formation Through an Intermediate-Mass Stage

The presence of highly collimated outflows demonstrates a protostellar nature of the condensations in G28.34-P1. Wang et al. (2008) reported a luminosity of $10^2\,L_\odot$ for the 24 μm source associated with SMA2. Rathborne et al. (2010) obtained a luminosity of $2.1 \times 10^3\,L_\odot$ for the entire P1 clump. These luminosities set a limit on the mass of the embedded stars of 3–7 $M_\odot$, if they are at the zero-age main sequence. The stellar masses put these objects at an intermediate-mass stage. The presence of highly collimated outflows also favors a disk-mediated accretion scenario of massive mass star formation (Zhang et al. 2005; Cesaroni et al. 2007) in a manner similar to low-mass star formation. In addition, the high collimation also indicates that these

outflows are at very early stages since the opening angle of outflows widens as they evolve.

The G28.34-P1 condensations are comparable in mass to the nearby intermediate-mass "cores" (2–5 $M_\odot$) at a similar spatial extent (2,300 × 1,600 AU; Sánchez-Monge et al. 2010). The non-detection of organic molecules (CH_3OH, CH_3CN, etc.) in P1 is likely due to the sensitivity limit of our observations. Sánchez-Monge et al. (2010) observed copious hot core molecular line emissions toward I22198, an intermediate-mass star with a luminosity of 370 $L_\odot$ at a distance of 0.76 kpc. The typical brightness temperature of the lines is 0.8 K. If we scale I22198 to the distance of G28.34, the emission would become 40 times fainter, well below our detection limit of 0.1 K per 1 km s^{-1} resolution (also true for Zhang et al. 2009). Therefore, it is possible that G28.34-P1 may have already experienced an increase in abundance of organic molecules as expected from protostellar heating, similar to I22198. Deep spectroscopy with ALMA will be able to verify the presence of hot core type molecules in G28.34-P1.

Despite the similarities between the G28.34-P1 condensations and the intermediate-mass star forming "cores", there is an important distinction between the two: The G28.34-P1 condensations are embedded in compact (∼0.1 pc), dense cores (∼10^7 cm^{-3}, see Table 3.4) with several tens of solar masses, which are hierarchically embedded in a massive, dense (3×10^5 cm^{-3}, Table 3.4) molecular clump of over 10^3 $M_\odot$, an order of magnitude larger than the mass in a typical intermediate-mass star-forming region. With a typical star formation efficiency of 30 % in dense gas and a standard stellar initial mass function, it is natural to expected that massive stars will eventually emerge in some of the condensations (if not all), at the end of protostellar accretion. At that time, P1 would become a massive star cluster. In the context of evolution, an immediate comparison to G28.34-P1 is the northern clump G28.34-P2 in the same cloud complex, which may represent the future of P1. With a similar clump mass, P2 has a higher gas temperature of 30 K, and a higher luminosity of 2.6×10^4 $L_\odot$ (Rathborne et al. 2010), equivalent to a zero-age main-sequence mass of 14 $M_\odot$. The SMA observations detected molecular lines from CH_3OH and CH_3CN in the P2 cores, while none in the P1 cores (Zhang et al. 2009). Likewise, other massive molecular clumps (e.g., W33A, Galván-Madrid et al. 2010; G31.41, Girart et al. 2009; NGC 6334, Hunter et al. 2006; G10.6, Liu et al. 2010) that have luminosities of 10^4–10^5 $L_\odot$, and are associated with radio continuum emission, may represent an even more evolved phase of massive star formation at which high mass protostellar objects have already emerged.

The large mass reservoir (22–64 $M_\odot$ at ∼0.1 pc; 1,000 $M_\odot$ at <1 pc) in G28.34-P1 and the outflows suggest that the condensations are, and will remain, actively accreting materials through the ambient medium. Materials in the cores fall onto the embedded protostars through disks and at the same time materials in the clump fall onto the cores. Observations of G28.34-P1 seem to indicate a continuous accretion over a spatial scale that spreads two orders of magnitude, from 1 to 0.01 pc, and finally reaches onto the protostars. This is a relatively new picture, but has also been reported in another IRDC, G30.88+0.13 (Zhang and Wang 2011). A comparison with massive and more luminous molecular clumps indicates that the

condensations will grow in mass, and likely emerge as massive stars eventually. The embedded protostars appear to be still intermediate-mass objects and are on their way to eventual massive stars. Our observations of the G28.34-P1 clump provide perhaps the first glimpse of an intermediate-mass stage of massive, clustered star formation.

3.4.2 Feedbacks from Star Formation: Outflow and Radiation

3.4.2.1 Outflow Heating

Intensity ratios of the main and hyperfine components from multiple NH_3 (J,K) transitions constrain rotational temperature which well approximates kinetic temperature in the regime of <20 K (Ho and Townes 1983; Walmsley and Ungerechts 1983). In the following analysis, we assume that the rotational temperature is the same as the kinetic temperature when the former is <20 K. Following the procedure of Ho and Townes (1983), we compute a rotational temperature (T_{21}) map based on the NH_3 (1,1) and (2,2) images. The NH_3 images were first smoothed to a common beam of $2''.8$ before computing the T_{21} map. The uncertainty of T_{21} is estimated to be 3 K. Figure 3.9a shows T_{21} with the dust condensations and the CO (3–2) outflows superposed. The T_{21} map reveals a highly structured temperature profile ranging from 8 to 30 K, opposite to the smooth temperature profiles observed in other IRDCs (Ragan et al. 2011). This may be due to beam dilution since the data in Ragan et al. (2011) have a larger beam. A number of remarkable enhancements ($T_{21} > 26$ K) are present among the entire map, but surprisingly none of the temperature enhancements coincide with any dust condensations. Instead, all the T_{21} enhancements spatially match the footprint of the outflows.

Since the NH_3 (3,3) is more widely spread than the (1,1) toward the northwest where the signal-to-noise ratio of (1,1) prohibits us from computing opacity, it is difficult to derive a reliable rotational temperature map from the NH_3 (1,1) and (3,3) lines. Instead, we compute the intensity ratio of the main hyperfine of (3,3)/(1,1), R_{31}, as plotted in Fig. 3.9b. To compute the intensity ratio, the NH_3 (1,1) image was first smoothed to the beam of the (3,3) image. The intensity ratio is positively correlated with the rotational temperature (Ho and Townes 1983; Zhang et al. 2002). For reference, assuming optically thin emission and the same abundance for the ortho and para NH_3 (Zhang et al. 2007b), $R_{31} = 0.5$, 2, and 5 correspond to rotational temperatures of $T_{31} = 31$, 55, and 109 K, respectively. Like the T_{21} map, the R_{31} map is also highly structured. R_{31} varies continuously from 0.3 to 12.5 over the map. Again several hot spots represented by R_{31} peaks (corresponding to NH_3 (3,3) emission peaks A–E) match the outflow footprint and are offset from the dust condensations. In addition to the peaks, there is a low R_{31} valley along SMA2 to SMA3. Optically thin thermal NH_3 (3,3) emission should have $R_{31} \leqslant 6.4$ (Ho and Townes 1983). Higher R_{31} values are seen toward peaks A–C, indicative of non-thermal emission. Toward peak B, the (3,3) emission is weakly amplified (Fig. 3.10), resembling an NH_3 (3,3)

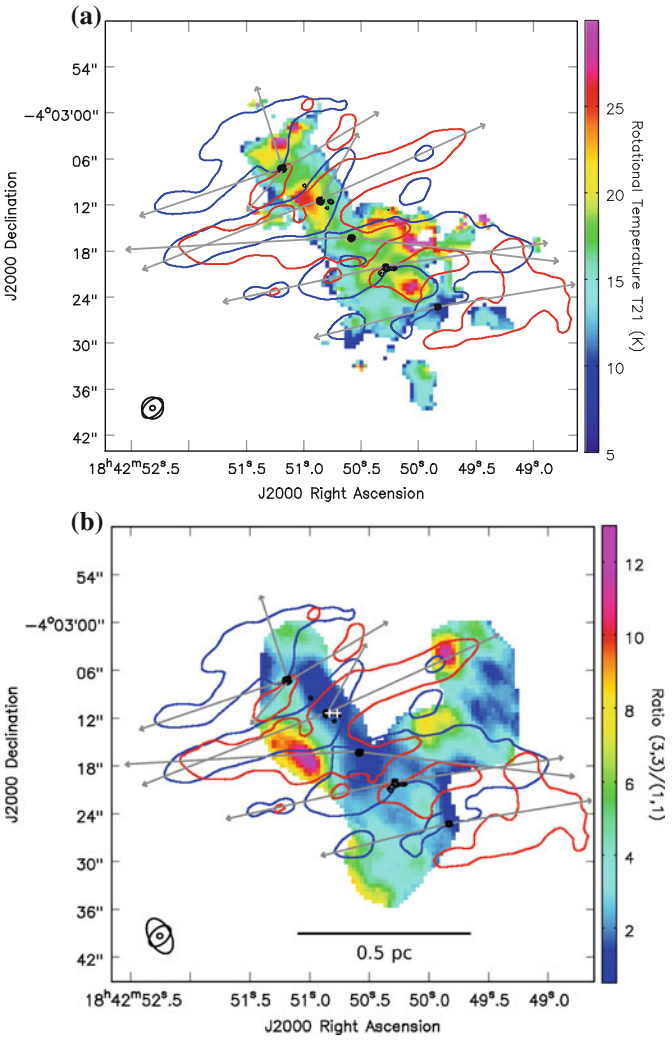

Fig. 3.9 Morphological match between heated gas and protostellar outflows. Plotted in color scales are **a** T_{21}, the rotational temperature derived from NH_3 (1,1) and (2,2), and **b** R_{31}, the integrated intensity ratio of NH_3 (3,3)/(1,1). The *arrows* and *blue/red* contours outline the blue-/redshifted CO (3–2) outflows, and the compact *black* contours represent the five groups of dust condensations, SMA1-5, from *upper-left* to *bottom-right* (contoured the same way as in Fig. 3.2). The two *white crosses* on top of SMA2a and SMA2b represent water masers W1 and W2, respectively. On the *bottom-left* corners are the beams for dust continuum, CO (3–2), and T_{21} (R_{31}), from the smallest to the largest respectively. Note that masks of 5σ were applied to both maps, and additional manual clipping was also performed to R_{31} in order to avoid noisy edge pixels [*Credit* Wang et al. (2012), reproduced with permission of the AAS]

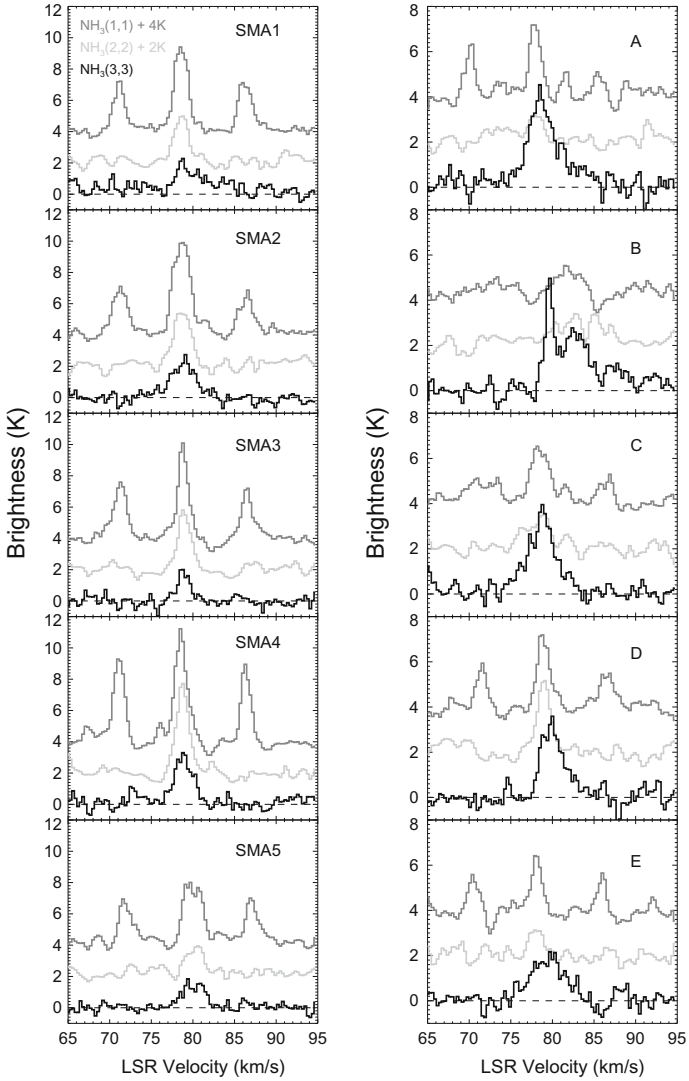

Fig. 3.10 JVLA NH_3 spectra extracted from SMA dust peaks (SMA1–5) and NH_3 (3,3) peaks (A–E). Note at peak B a spectroscopically unresolved NH_3 (3,3) maser at about 84 km s^{-1} [*Credit* Wang et al. (2011), reproduced with permission of the AAS]

maser similar to those found in other massive star formation regions where outflows are present (e.g., Mangum and Wootten 1994; Zhang and Ho 1995; Beuther et al. 2007b; Brogan et al. 2011). However the spatial resolution is insufficient to constrain the brightness of this emission feature.

The morphological match between the heated gas and the outflow footprint suggests that the heating in the P1 region is due to protostellar outflows. Indeed,

all the hot spots exclusively coincide with large NH_3 (3,3) line widths compared to relatively small line width toward the dust condensations (Fig. 3.10), likely indicative of gas motion and extra turbulence injected by the outflow shocks. Collimated outflows also pave an optically thin way through which the protostellar radiation heats up preexisting dense cores without been absorbed significantly, making the heating much more efficient (Hartquist and Dyson 1993; Wiseman and Ho 1996; Cunningham et al. 2011). This may be the case for the hot spot seen at the tip of the red lobe of the SMA2a outflow. The protostellar radiation travels through the outflow cavity and heats up the exposed gas out to 0.5 pc away from the protostar. The outflow heating has two important features. First, the heating alters thermal property of the gas throughout the clump, from a distance 0.1–0.5 pc away from the driving protostars. Second, the heating is localized and far from well mixed. The temperature at the low R_{31} valley is not high enough to suppress further fragmentation into Jeans mass of 1 $M_\odot$ (Wang et al. 2011). We probably have witnessed through JVLA and SMA the very beginning of an outflow induced gas heating.

3.4.2.2 Radiative Heating

It is apparent that protostellar outflows can introduce significant heating to the ambient gas. What is the effect of protostellar radiation? Is radiative heating from low mass protostars sufficient to suppress fragmentation and aid the formation of massive cores? The fact that all dense cores correspond with low R_{31} is intriguing. In addition, the temperature map in Fig. 3.9a indicates that dense cores have typical temperatures of 18 K, and are offset from the high temperature peaks. The temperature distributions suggest that the heating of low mass protostars may not play a significant role in the formation of dense cores detected with the SMA. Otherwise, massive cores should be found at the peaks of the temperature distribution. Longmore et al. (2011) made a similar statement for a hot molecular core G8.68–0.37.

It is also interesting to note that the protostars embedded in the SMA cores have not produced significant heating. SMA1 to SMA4 have a rather uniform T_{21} of 18 K, while SMA5 has a lower T_{21} of 9 K. We caution that the T_{21} map has a $2''.8$ beam, so any temperature structure has been smoothed to a spatial scale of 0.065 pc. How much luminosity is required to heat the gas to 18 or 9 K at a radius of 0.065 pc from the central source? Assuming thermal equilibrium between gas and dust, the luminosity can be estimated following the equation (Scoville and Kwan 1976; Garay and Lizano 1999):

$$T_{\rm dust} = 65 \left(\frac{0.1\,{\rm pc}}{r}\right)^{2/(4+\beta)} \left(\frac{L_{\rm star}}{10^5 L_\odot}\right)^{1/(4+\beta)} \left(\frac{0.1}{f}\right)^{1/(4+\beta)},$$

where $\beta = 1.5$ is the dust emissivity at far infrared wavelengths (Rathborne et al. 2010), $f = 0.08\,{\rm cm^2\,g^{-1}}$ is the dust emissivity at 50 μm (Scoville and Kwan 1976), and $r = 0.065$ pc is the radius from the central protostar. We estimate a luminosity

of 30 $L_\odot$ for each protostar embedded in SMA1, SMA2a, SMA3, and SMA4a, and 1 $L_\odot$ for the protostar SMA5. These values should be taken with caution because the beam dilution may introduce large uncertainty in both temperature and radius. Nevertheless, we note that the luminosity of SMA2a is in rough agreement with the luminosity inferred from SED for the 24 μm source in the SMA2 vicinity ($\sim 10^2\ L_\odot$, Wang et al. 2008). A lack of significant heating from the growing protostars is consistent with non detection of line emission from organic molecules (Zhang et al. 2009; Wang et al. 2011).

3.4.3 Magnetic Fields and the Origin of the X-shaped Filamentary System

The origin of the low-density minor filament is rather interesting. A low-density streak perpendicular to a high-density oblate region is expected if magnetic field is dynamically important compared to self-gravity and turbulence during the formation of the system (Li et al. 2011). In this case, gravitational contraction along the field lines is more efficient, resulting in a high-density region perpendicular to the magnetic field, while on the other hand turbulence is also channeled by the field and gives rise to streaks aligned with the magnetic field in the lower-density region. This phenomenon has been seen in simulations (Price and Bate 2008; Nakamura and Li 2008) and in observations of NGC 2024 in Orion (Li et al. 2011). In G28.34-P1, the X-shaped filamentary system projected on the sky is almost perpendicular. If the system were formed from the same mechanism, one should expect a mean magnetic field along the minor filament and perpendicular to the main filament. Based on the JCMT dust polarization data cataloged by Matthews et al. (2009), we derived a mean B-field direction of P.A. $= -25°.6 \pm 45°$ as labeled on Fig. 3.7. Because the main filament has a P.A. of 48° (Wang et al. 2011), the separation angle between the mean B-field and the main filament is 73°.6. The mean magnetic field at the clump scale is indeed along with the minor filament and roughly perpendicular to the main filament. The large deviation in the B-field direction may indicate that the strong outflows have started to disturb the initially ordered field lines in the inner part of P1 (Li et al. 2009). Therefore we speculate that the minor filament originates from turbulence anisotropy during the formation of the X-shaped filamentary system, and that the formation process has been governed by the interplay between strong magnetic field, self-gravity, and turbulence.

3.5 Conclusions

This chapter presents an observational study of the P1 clump in IRDC G28.34+0.06 using the SMA and JVLA. Our main findings are summarized as follows.

(1) High resolution and high sensitivity image at 0.88 mm reveals hierarchical fragmentation at 1 and 0.1 pc scales. The mass of the dust cores and condensations are much larger than the relevant thermal Jean masses. The clump fragmentation is consistent with a cylindrical collapse.
(2) All five dust cores are driving highly collimated CO (3–2) outflows, indicating a protostellar nature of the condensations embedded in the cores. Bipolar, jet-like outflows suggest a disk-mediated accretion of high-mass star formation.
(3) The outflows inject feedback to the clump scale in the form of heating, turbulence, and excitation of a possible NH_3 maser. At this stage of evolution, heating from outflows is much more significant than radiative heating from protostars. Protostellar heating may not be effective in suppressing fragmentation during the formation of massive cores, unlike suggested in some numerical simulations.
(4) We discovered an X-shaped filamentary system of G28.34-P1 which indicates magnetic fields have been dynamically important compared to self-gravity and turbulence during the formation of the X-shape system. This is the first observation of such a system at a typical distance of massive star formation regions. Our observations can be routinely applied to other similar regions to exam the importance of magnetic fields in the star formation process.
(5) The relatively low luminosity and a lack of detection of organic molecules indicate that the condensations in P1 underline an intermediate-mass stage of massive star formation and will likely form massive stars eventually.

References

Baraffe, I., Chabrier, G.: Effect of episodic accretion on the structure and the lithium depletion of low-mass stars and planet-hosting stars. Astron. Astrophys. **521**, A44 (2010). doi:10.1051/0004-6361/201014979, 1008.4288

Beltrán, M.T., Brand, J., Cesaroni, R., Fontani, F., Pezzuto, S., Testi, L., Molinari, S.: Search for massive protostar candidates in the southern hemisphere. II. Dust continuum emission. Astron. Astrophys. **447**, 221–233 (2006). doi:10.1051/0004-6361:20053999, arXiv:astro-ph/0510422

Beuther, H., Schilke, P., Gueth, F., McCaughrean, M., Andersen, M., Sridharan, T.K., Menten, K.M.: IRAS 05358+3543: Multiple outflows at the earliest stages of massive star formation. Astron. Astrophys. **387**, 931–943 (2002a). doi:10.1051/0004-6361:20020319, arXiv:astro-ph/0203010

Beuther, H., Schilke, P., Menten, K.M., Motte, F., Sridharan, T.K., Wyrowski, F.: High-mass protostellar candidates. II. Density structure from dust continuum and CS emission. Astrophys. J. **566**, 945–965 (2002b). doi:10.1086/338334, arXiv:astro-ph/0110370

Beuther, H., Schilke, P., Sridharan, T.K., Menten, K.M., Walmsley, C.M., Wyrowski, F.: Massive molecular outflows. Astron. Astrophys. **383**, 892–904 (2002c). doi:10.1051/0004-6361:20011808, arXiv:astro-ph/0110372

Beuther, H., Schilke, P., Stanke, T.: Multiple outflows in IRAS 19410+2336. Astron. Astrophys. **408**, 601–610 (2003). doi:10.1051/0004-6361:20030795. arXiv:astro-ph/0306101

Beuther, H., Schilke, P., Gueth, F.: Massive molecular outflows at high spatial resolution. Astrophys. J. **608**, 330–340 (2004). doi:10.1086/386543. arXiv:astro-ph/0402563

Beuther, H., Leurini, S., Schilke, P., Wyrowski, F., Menten, K.M., Zhang, Q.: Interferometric multi-wavelength (sub)millimeter continuum study of the young high-mass protocluster IRAS

05358+3543. Astron. Astrophys. **466**, 1065–1076 (2007a). doi:10.1051/0004-6361:20066742. arXiv:astro-ph/0702560

Beuther, H., Walsh, A.J., Thorwirth, S., Zhang, Q., Hunter, T.R., Megeath, S.T., Menten, K.M.: Hot ammonia in NGC 6334I and I(N). Astron. Astrophys. **466**, 989–998 (2007b). doi:10.1051/0004-6361:20066799, arXiv:astro-ph/0702190

Blake, G.A., Sutton, E.C., Masson, C.R., Phillips, T.G.: Molecular abundances in OMC-1—The chemical composition of interstellar molecular clouds and the influence of massive star formation. Astrophys. J. **315**, 621–645 (1987). doi:10.1086/165165

Brogan, C.L., Hunter, T.R., Cyganowski, C.J., Friesen, R.K., Chandler, C.J., Indebetouw, R.: First results from a 1.3 cm expanded very large array survey of massive protostellar objects: G35.03+0.35. Astrophys. J. Lett. **739**, L16+ (2011). doi:10.1088/2041-8205/739/1/L16, 1106.0942

Carey, S.J., Clark, F.O., Egan, M.P., Price, S.D., Shipman, R.F., Kuchar, T.A.: The physical properties of the midcourse space experiment galactic infrared-dark clouds. Astrophys. J. **508**, 721–728 (1998). doi:10.1086/306438

Carey, S.J., Feldman, P.A., Redman, R.O., Egan, M.P., MacLeod, J.M., Price, S.D.: Submillimeter observations of midcourse space experiment galactic infrared-dark clouds. Astrophys. J. Lett. **543**, L157–L161 (2000). doi:10.1086/317270

Carey, S.J., Noriega-Crespo, A., Mizuno, D.R., Shenoy, S., Paladini, R., Kraemer, K.E., Price, S.D., Flagey, N., Ryan, E., Ingalls, J.G., Kuchar, T.A., Pinheiro Gonçalves, D., Indebetouw, R., Billot, N., Marleau, F.R., Padgett, D.L., Rebull, L.M., Bressert, E., Ali, B., Molinari, S., Martin, P.G., Berriman, G.B., Boulanger, F., Latter, W.B., Miville-Deschenes, M.A., Shipman, R., Testi, L.: MIPSGAL: a survey of the inner galactic plane at 24 and 70 μm. Publ. ASP **121**, 76–97 (2009). doi:10.1086/596581

Cesaroni, R., Felli, M., Jenness, T., Neri, R., Olmi, L., Robberto, M., Testi, L., Walmsley, C.M.: Unveiling the disk-jet system in the massive (proto)star IRAS 20126+4104. Astron. Astrophys. **345**, 949–964 (1999)

Cesaroni, R., Galli, D., Lodato, G., Walmsley, M., Zhang, Q.: The critical role of disks in the formation of high-mass stars. Nature **444**, 703–706 (2006). doi:10.1038/nature05344

Cesaroni, R., Galli, D., Lodato, G., Walmsley, C.M., Zhang, Q.: Disks around young O-B (proto) stars: observations and theory. Protostars and Planets V, pp. 197–212 (2007). arXiv:astro-ph/0603093

Chambers, E.T., Jackson, J.M., Rathborne, J.M., Simon, R.: Star formation activity of cores within infrared dark clouds. Astrophys. J. Suppl. **181**, 360–390 (2009). doi:10.1088/0067-0049/181/2/360

Chandrasekhar, S., Fermi, E.: Problems of gravitational stability in the presence of a magnetic field. Astrophys. J. **118**, 116−+ (1953). doi:10.1086/145732

Chen, H., Liu, S., Su, Y., Zhang, Q.: Deuterium fractionation as an evolutionary probe in the infrared dark cloud G28.34+0.06. Astrophys. J. Lett. **713**, L50–L54 (2010). doi:10.1088/2041-8205/713/1/L50, 1003.1365

Churchwell, E., Babler, B.L., Meade, M.R., Whitney, B.A., Benjamin, R., Indebetouw, R., Cyganowski, C., Robitaille, T.P., Povich, M., Watson, C., Bracker, S.: The Spitzer/GLIMPSE surveys: a new view of the milky way. Publ. ASP **121**, 213–230 (2009). doi:10.1086/597811

Cunningham, A.J., Klein, R.I., Krumholz, M.R., McKee, C.F.: Radiation-hydrodynamic simulations of massive star formation with protostellar outflows. (2011) ArXiv e-prints 1104.1218

Draine, B.T., Lee, H.M.: Optical properties of interstellar graphite and silicate grains. Astrophys. J. **285**, 89–108 (1984). doi:10.1086/162480

Egan, M.P., Shipman, R.F., Price, S.D., Carey, S.J., Clark, F.O., Cohen, M.: A population of cold cores in the galactic plane. Astrophys. J. Lett. **494**, L199+ (1998). doi:10.1086/311198

Fendt, C., Zinnecker, H.: Possible bending mechanisms of protostellar jets. Astron. Astrophys. **334**, 750–755 (1998)

Fuente, A., Neri, R., Caselli, P.: Detection of a hot core in the intermediate-mass class 0 protostar NGC 7129-FIRS 2. Astron. Astrophys. **444**, 481–493 (2005). doi:10.1051/0004-6361:20053301, arXiv:astro-ph/0506649

Galván-Madrid, R., Zhang, Q., Keto, E., Ho, P.T.P., Zapata, L.A., Rodríguez, L.F., Pineda, J.E., Vázquez-Semadeni, E.: From the convergence of filaments to disk-outflow accretion: massive star formation in W33A. Astrophys. J. **725**, 17–28 (2010). doi:10.1088/0004-637X/725/1/17, 1004.2466

Garay, G., Lizano, S.: Massive stars: their environment and formation. Publ. ASP **111**, 1049–1087 (1999). doi:10.1086/316416, arXiv:astro-ph/9907293

Garden, R.P., Hayashi, M., Hasegawa, T., Gatley, I., Kaifu, N.: A spectroscopic study of the DR 21 outflow source. III—the CO line emission. Astrophys. J. **374**, 540–554 (1991). doi:10.1086/170143

Girart, J.M., Beltrán, M.T., Zhang, Q., Rao, R., Estalella, R.: Magnetic fields in the formation of massive stars. Science **324**, 1408 (2009). doi:10.1126/science.1171807

Hartquist, T.W., Dyson, J.E.: Clumps their tails and the global sources they wag. Q. J. RAS **34**, 57−+ (1993)

Hennebelle, P., Pérault, M., Teyssier, D., Ganesh, S.: Infrared dark clouds from the ISOGAL survey. Constraints on the interstellar extinction curve. Astron. Astrophys. **365**, 598–611 (2001). doi:10.1051/0004-6361:20000052

Hildebrand, R.H.: The determination of cloud masses and dust characteristics from submillimetre thermal emission. Q. J. RAS **24**, 267−+ (1983)

Ho, P.T.P., Townes, C.H.: Interstellar ammonia. Ann. Rev. Astron. Astrophys. **21**, 239–270 (1983). doi:10.1146/annurev.aa.21.090183.001323

Ho, P.T.P., Moran, J.M., Lo, K.Y.: The submillimeter array. Astrophys. J. Lett. **616**, L1–L6 (2004). doi:10.1086/423245, arXiv:astro-ph/0406352

Hunter, T.R., Testi, L., Zhang, Q., Sridharan, T.K.: Molecular jets and H_2O masers in the AFGL 5142 hot core. Astron. J. **118**, 477–487 (1999). doi:10.1086/300936

Hunter, T.R., Brogan, C.L., Megeath, S.T., Menten, K.M., Beuther, H., Thorwirth, S.: Millimeter multiplicity in NGC 6334 I and I(N). Astrophys. J. **649**, 888–893 (2006), doi:10.1086/505965, arXiv:astro-ph/0605468

Jackson, J.M., Finn, S.C., Chambers, E.T., Rathborne, J.M., Simon, R.: The "Nessie" nebula: cluster formation in a filamentary infrared dark cloud. Astrophys. J. Lett. **719**, L185–L189 (2010). doi:10.1088/2041-8205/719/2/L185, 1007.5492

Lee, C., Ho, P.T.P., Palau, A., Hirano, N., Bourke, T.L., Shang, H., Zhang, Q.: Submillimeter arcsecond-resolution mapping of the highly collimated protostellar jet HH 211. Astrophys. J. **670**, 1188–1197 (2007). doi:10.1086/522333, 0708.1365

Lee, C., Hasegawa, T.I., Hirano, N., Palau, A., Shang, H., Ho, P.T.P., Zhang, Q.: The reflection-symmetric wiggle of the young protostellar jet HH 211. Astrophys. J. **713**, 731–737 (2010). doi:10.1088/0004-637X/713/2/731, 1003.1355

Li, Hb, Dowell, C.D., Goodman, A., Hildebrand, R., Novak, G.: Anchoring magnetic field in turbulent molecular clouds. Astrophys. J. **704**, 891–897 (2009). doi:10.1088/0004-637X/704/2/891, 0908.1549

Li, H.B., Blundell, R., Hedden, A., Kawamura, J., Paine, S., Tong, E.: Evidence for dynamically important magnetic fields in molecular clouds. Mon. Not. RAS **411**, 2067–2075 (2011). doi:10.1111/j.1365-2966.2010.17839.x, 1007.3312

Liu, H.B., Ho, P.T.P., Zhang, Q.: The high-velocity molecular outflows in massive cluster-forming region G10.6-0.4. Astrophys. J. **725**, 2190–2208 (2010). doi:10.1088/0004-637X/725/2/2190, 1010.2785

Longmore, S.N., Pillai, T., Keto, E., Zhang, Q., Qiu, K.: Is protostellar heating sufficient to halt fragmentation? A case study of the massive protocluster G8.68-0.37. Astrophys. J. **726**, 97−+ (2011). doi:10.1088/0004-637X/726/2/97, 1011.1442

Looney, L.W., Mundy, L.G., Welch, W.J.: Unveiling the circumstellar envelope and disk: a subarcsecond survey of circumstellar structures. Astrophys. J. **529**, 477–498 (2000). doi:10.1086/308239, arXiv:astro-ph/9908301

Mangum, J.G., Wootten, A.: Discovery of (N-14)H3(3, 3) maser emission in the interstellar medium. Astrophys. J. Lett. **428**, L33–L36 (1994). doi:10.1086/187386

Martel, H., Evans II, N.J., Shapiro, P.R.: Fragmentation and evolution of molecular clouds. I. Algorithm and first results. Astrophys. J. Suppl. **163**, 122–144 (2006). doi:10.1086/500090, arXiv:astro-ph/0505008

Masciadri, E., Raga, A.C.: Herbig-haro jets from orbiting sources. Astrophys. J. **568**, 733–742 (2002). doi:10.1086/338767

Matthews, B.C., McPhee, C.A., Fissel, L.M., Curran, R.L.: The legacy of SCUPOL: 850 μm imaging polarimetry from 1997 to 2005. Astrophys. J. Suppl. **182**, 143–204 (2009). doi:10.1088/0067-0049/182/1/143

McMullin, J.P., Waters, B., Schiebel, D., Young, W., Golap, K.: CASA architecture and applications. In: Shaw, R.A., Hill, F., Bell, D.J. (eds.) Astronomical Data Analysis Software and Systems XVI, Astronomical Society of the Pacific Conference Series, vol. 376, p. 127 (2007)

Miettinen, O., Harju, J.: LABOCA mapping of the infrared dark cloud MSXDC G304.74+01.32. Astron. Astrophys. **520**, A102+ (2010). doi:10.1051/0004-6361/200913662, 1003.3732

Molinari, S., Brand, J., Cesaroni, R., Palla, F.: A search for precursors of ultracompact Hii regions in a sample of luminous IRAS sources. III. Circumstellar dust properties. Astron. Astrophys. **355**, 617–628 (2000). arXiv:astro-ph/0001231

Nagasawa, M.: Gravitational instability of the isothermal gas cylinder with an axial magnetic field. Progress Theor. Phys. **77**, 635–652 (1987). doi:10.1143/PTP.77.635

Nakamura, F., Li, Z.Y.: Magnetically regulated star formation in three dimensions: the case of the taurus molecular cloud complex. Astrophys. J. **687**, 354–375 (2008). doi:10.1086/591641, 0804.4201

Neri, R., Fuente, A., Ceccarelli, C., Caselli, P., Johnstone, D., van Dishoeck, E.F., Wyrowski, F., Tafalla, M., Lefloch, B., Plume, R.: The IC1396N proto-cluster at a scale of $\tilde{2}50$ AU. Astron. Astrophys. **468**, L33–L36 (2007). doi:10.1051/0004-6361:20077320, 0705.2663

Perault, M., Omont, A., Simon, G., Seguin, P., Ojha, D., Blommaert, J., Felli, M., Gilmore, G., Guglielmo, F., Habing, H., Price, S., Robin, A., de Batz, B., Cesarsky, C., Elbaz, D., Epchtein, N., Fouque, P., Guest, S., Levine, D., Pollock, A., Prusti, T., Siebenmorgen, R., Testi, L., Tiphene, D.: First ISOCAM images of the Milky Way. Astron. Astrophys. **315**, L165–L168 (1996)

Peretto, N., Fuller, G.A.: A statistical study of the mass and density structure of infrared dark clouds. Astrophys. J. **723**, 555–562 (2010). doi:10.1088/0004-637X/723/1/555, 1009.0716

Pillai, T., Wyrowski, F., Carey, S.J., Menten, K.M.: Ammonia in infrared dark clouds. Astron. Astrophys. **450**, 569–583 (2006). doi:10.1051/0004-6361:20054128, arXiv:astro-ph/0601078

Plume, R., Jaffe, D.T., Evans II, N.J., Martin-Pintado, J., Gomez-Gonzalez, J.: Dense gas and star formation: characteristics of cloud cores associated with water masers. Astrophys. J. **476**, 730−+ (1997). doi:10.1086/303654, arXiv:astro-ph/9609061

Price, D.J., Bate, M.R.: The effect of magnetic fields on star cluster formation. Mon. Not. RAS **385**, 1820–1834 (2008). doi:10.1111/j.1365-2966.2008.12976.x, 0801.3293

Qiu, K., Zhang, Q.: Discovery of extremely high velocity "molecular bullets" in the HH 80-81 high-mass star-forming region. Astrophys. J. Lett. **702**, L66–L71 (2009). doi:10.1088/0004-637X/702/1/L66, 0907.5040

Raga, A.C., Esquivel, A., Velázquez, P.F., Cantó, J., Haro-Corzo, S., Riera, A., Rodríguez-González, A.: Mirror and point symmetries in a ballistic jet from a binary system. Astrophys. J. Lett. **707**, L6–L11 (2009). doi:10.1088/0004-637X/707/1/L6

Ragan, S.E., Bergin, E.A., Wilner, D.: Very large array observations of ammonia in infrared-dark clouds. I. Column density and temperature structure. Astrophys. J. **736**, 163−+ (2011). doi:10.1088/0004-637X/736/2/163, 1105.4182

Rathborne, J.M., Jackson, J.M., Simon, R.: Infrared dark clouds: precursors to star clusters. Astrophys. J. **641**, 389–405 (2006). doi:10.1086/500423, arXiv:astro-ph/0602246

Rathborne, J.M., Jackson, J.M., Chambers, E.T., Stojimirovic, I., Simon, R., Shipman, R., Frieswijk, W.: The early stages of star formation in infrared dark clouds: characterizing the core dust properties. Astrophys. J. **715**, 310–322 (2010). doi:10.1088/0004-637X/715/1/310, 1003.3193

Sánchez-Monge, Á., Palau, A., Estalella, R., Kurtz, S., Zhang, Q., Di Francesco, J., Shepherd, D.: IRAS 22198+6336: discovery of an intermediate-mass hot core. Astrophys. J. Lett. **721**, L107–L111 (2010). doi:10.1088/2041-8205/721/2/L107, 1007.5258

Sault, R.J., Teuben, P.J., Wright, M.C.H.: A Retrospective view of MIRIAD. In: Shaw, R.A., Payne, H.E., Hayes, J.J.E. (eds.) Astronomical Data Analysis Software and Systems IV, Astronomical Society of the Pacific Conference Series, vol. 77, p. 433 (1995). arXiv:astro-ph/0612759

Schilke, P., Groesbeck, T.D., Blake, G.A., Phillips, T.G.: A line survey of orion KL from 325 to 360 GHz. Astrophys. J. Suppl. **108**, 301 (1997). doi:10.1086/312948

Schneider, S., Elmegreen, B.G.: A catalog of dark globular filaments. Astrophys. J. Suppl. **41**, 87–95 (1979). doi:10.1086/190609

Scoville, N.Z., Kwan, J.: Infrared sources in molecular clouds. Astrophys. J. **206**, 718–727 (1976). doi:10.1086/154432

Shang, H., Allen, A., Li, Z., Liu, C., Chou, M., Anderson, J.: A unified model for bipolar outflows from young stars. Astrophys. J. **649**, 845–855 (2006). doi:10.1086/506513

Shang, H., Li, Z., Hirano, N.: Jets and bipolar outflows from young stars: theory and observational tests. Protostars and Planets V, pp. 261–276 (2007)

Shepherd, D.S., Yu, K.C., Bally, J., Testi, L.: The molecular outflow and possible precessing jet from the massive young stellar object IRAS 20126+4104. Astrophys. J. **535**, 833–846 (2000). doi:10.1086/308873

Shu, F.H., Adams, F.C., Lizano, S.: Star formation in molecular clouds—observation and theory. Annu. Rev. Astron. Astrophys. **25**, 23–81 (1987). doi:10.1146/annurev.aa.25.090187.000323

Simon, R., Jackson, J.M., Rathborne, J.M., Chambers, E.T.: A catalog of midcourse space experiment infrared dark cloud candidates. Astrophys. J. **639**, 227–236 (2006a). doi:10.1086/499342, arXiv:astro-ph/0511079

Simon, R., Rathborne, J.M., Shah, R.Y., Jackson, J.M., Chambers, E.T.: The characterization and galactic distribution of infrared dark clouds. Astrophys. J. **653**, 1325–1335 (2006b). doi:10.1086/508915

Su, Y., Liu, S., Chen, H., Zhang, Q., Cesaroni, R.: The outflow from the luminous young stellar object IRAS 20126+4104: From 4000 AU to 0.4 pc. Astrophys. J. **671**, 571–580 (2007). doi:10.1086/522919

Walmsley, C.M., Ungerechts, H.: Ammonia as a molecular cloud thermometer. Astron. Astrophys. **122**, 164–170 (1983)

Wang, K., Zhang, Q., Wu, Y., Zhang, H.: Hierarchical fragmentation and jet-like outflows in IRDC G28.34+0.06: a growing massive protostar cluster. Astron. Astrophys. **735**, 64−+ (2011). doi:10.1088/0004-637X/735/1/64, 1105.4559

Wang, K., Zhang, Q., Wu, Y., Li, Hb, Zhang, H.: Protostellar outflow heating in a growing massive protocluster. Astrophys. J. Lett. **745**, L30 (2012). doi:10.1088/2041-8205/745/2/L30, 1112.1885

Wang, Y., Zhang, Q., Rathborne, J.M., Jackson, J., Wu, Y.: Water masers associated with infrared dark cloud cores. Astrophys. J. Lett. **651**, L125–L128 (2006). doi:10.1086/508939

Wang, Y., Zhang, Q., Pillai, T., Wyrowski, F., Wu, Y.: NH_3 observations of the infrared dark cloud G28.34+0.06. Astrophys. J. Lett. **672**, L33–L36 (2008). doi:10.1086/524949, 0711.1999

Wiseman, J.J., Ho, P.T.P.: Heated gaseous streamers and star formation in the Orion molecular cloud. Nature **382**, 139–141 (1996). doi:10.1038/382139a0

Wu, Y., Wei, Y., Zhao, M., Shi, Y., Yu, W., Qin, S., Huang, M.: A study of high velocity molecular outflows with an up-to-date sample. Astron. Astrophys. **426**, 503–515 (2004). doi:10.1051/0004-6361:20035767, arXiv:astro-ph/0410727

Zapata, L.A., Rodríguez, L.F., Ho, P.T.P., Zhang, Q., Qi, C., Kurtz, S.E.: A highly collimated, young, and fast CO outflow in OMC-1 south. Astrophys. J. Lett. **630**, L85–L88 (2005). doi:10.1086/491470, arXiv:astro-ph/0505045

Zhang, Q.: Massive star disks. In: Cesaroni, R., Felli, M., Churchwell, E., Walmsley, M. (eds.) Massive Star Birth: A Crossroads of Astrophysics, IAU Symposium, vol. 227, pp. 135–144 (2005). doi:10.1017/S174392130500445X

Zhang, Q., Ho, P.T.P.: Ammonia maser in a molecular outflow toward W51. Astrophys. J. Lett. **450**, L63 (1995). doi:10.1086/316772

Zhang, Q., Wang, K.: IRDC G030.88+00.13: a tale of two massive clumps. Astrophys. J. **733**, 26−+ (2011). doi:10.1088/0004-637X/733/1/26, 1103.5092

Zhang, Q., Ho, P.T.P., Wright, M.C.H.: The SIO and CS emission in the molecular outflow toward L1157. Astron. J. **119**, 1345–1351 (2000). doi:10.1086/301274

Zhang, Q., Hunter, T.R., Brand, J., Sridharan, T.K., Molinari, S., Kramer, M.A., Cesaroni, R.: Search for CO outflows toward a sample of 69 high-mass protostellar candidates: frequency of occurrence. Astrophys. J. Lett. **552**, L167–L170 (2001). doi:10.1086/320345

Zhang, Q., Hunter, T.R., Sridharan, T.K., Ho, P.T.P.: A disk/jet system toward the high-mass young star in AFGL 5142. Astrophys. J. **566**, 982–992 (2002). doi:10.1086/338278

Zhang, Q., Hunter, T.R., Brand, J., Sridharan, T.K., Cesaroni, R., Molinari, S., Wang, J., Kramer, M.: Search for CO outflows toward a sample of 69 high-mass protostellar candidates. II. Outflow properties. Astrophys. J. **625**, 864–882 (2005). doi:10.1086/429660

Zhang, Q., Hunter, T.R., Beuther, H., Sridharan, T.K., Liu, S., Su, Y., Chen, H., Chen, Y.: Multiple jets from the high-mass (proto)stellar cluster AFGL 5142. Astrophys. J. **658**, 1152–1163 (2007a). doi:10.1086/511381, arXiv:astro-ph/0612027

Zhang, Q., Sridharan, T.K., Hunter, T.R., Chen, Y., Beuther, H., Wyrowski, F.: A jet-like outflow toward the high-mass (proto) stellar object IRAS 18566+0408. Astron. Astrophys. **470**, 269–279 (2007b). doi:10.1051/0004-6361:20077094, 0704.2767

Zhang, Q., Wang, Y., Pillai, T., Rathborne, J.: Fragmentation at the earliest phase of massive star formation. Astrophys. J. **696**, 268–273 (2009). doi:10.1088/0004-637X/696/1/268, 0902.0647

Zhu, Z., Hartmann, L., Gammie, C.: Long-term evolution of protostellar and protoplanetary disks. II. Layered accretion with infall. Astrophys. J. **713**, 1143–1158 (2010). doi:10.1088/0004-637X/713/2/1143, 1003.1756

Chapter 4
The "Snake" Nebula G11.11–0.12

Abstract This chapter presents SMA $\lambda = 0.88$ and 1.3 mm broad-band observations, and JVLA observations in NH_3 $(J, K) = (1,1)$ up to (5,5), H_2O and CH_3OH maser lines toward the two most massive molecular clumps in IRDC G11.11–0.12, also known as the "Snake" nebula. Sensitive high-resolution images reveal hierarchical fragmentation in dense molecular gas from the ~1 pc clump scale down to ~0.01 pc condensation scale. At each scale, the mass of the fragments is orders of magnitude larger than the Jeans mass. This is common to all four IRDC clumps we studied, suggesting that turbulence plays an important role in the early stages of clustered star formation. Masers, shock heated NH_3 gas, and outflows indicate intense ongoing star formation in some cores while no such signatures are found in others. Furthermore, chemical differentiation may reflect the difference in evolutionary stages among these star formation seeds. A similar chemical differentiation is also found in clumps and condensations. We find NH_3 ortho/para ratios of 1.1 ± 0.4, 2.0 ± 0.4, and 3.0 ± 0.7 associated with three outflows, and the ratio tends to increase along the outflows downstream. Our combined SMA and JVLA observations of several IRDC clumps present the most in depth view so far of the early stages prior to the hot core phase, revealing snapshots of physical and chemical properties at various stages along an apparent evolutionary sequence, subject to further tests by detailed modelling.

4.1 Introduction

4.1.1 Initial Fragmentation and Star Formation

Because high-mass stars form deeply embedded in dense gas and in distant clustered environments, observational studies face severe limitations of optical depth and spatial resolution. Heavy dust extinction ($N_{H_2} \sim 10^{23}\mathrm{cm}^{-2}$, $A_v > 100$ mag) obscures the forming young protostars and also the Galactic background radiation even at mid-infrared wavelengths (Churchwell et al. 2009; Carey et al. 2009), when viewed against the Galactic plane. This is what led to the cloud complexes containing such regions to be coined "infrared-dark clouds" (IRDCs; Perault et al. 1996; Egan et al. 1998; Hennebelle et al. 2001; Simon et al. 2006a, b; Peretto and Fuller 2009). The cold

K. Wang, *The Earliest Stages of Massive Clustered Star Formation: Fragmentation of Infrared Dark Clouds*, Springer Theses,
DOI 10.1007/978-3-662-44969-1_4

dust in IRDCs transitions to emission at longer wavelengths, from far-infrared to sub-millimeter and millimeter wavelengths (Molinari et al. 2010; Schuller et al. 2009; Rosolowsky et al. 2010; Aguirre et al. 2011). One key outcome of the recent *Herschel* surveys has been the identification of a population of deeply embedded protostellar cores, which appear as point sources (∼0.1 pc at typical 3 kpc distance to IRDCs) in the *Herschel* PACS bands (Henning et al. 2010; Ragan et al. 2012a). However, detailed case studies beyond the core scale, the key to understand the early fragmentation that directly initiates subsequent clustered star formation, are only possible by deep interferometric imaging. To maximize the mass sensitivity, the preferred wavelength of observations is in the sub-millimeter regime, accessible by the Submillimeter Array (SMA) and by the recently inaugurated Atacama Large Millimeter/submillimeter Array (ALMA).

Compared to the numerous interferometric studies on massive proto-clusters (e.g., Rathborne et al. 2008; Hennemann et al. 2009; Beuther and Henning 2009; Longmore et al. 2011; Palau et al. 2013) and NH_3 observations of IRDCs (Wang et al. 2008; Devine et al. 2011; Ragan et al. 2011, 2012b; Wang et al. 2012), there have been few high angular resolution studies dedicated to pre-cluster clumps in the literature (Rathborne et al. 2007; Swift 2009; Zhang et al. 2009; Busquet et al. 2010; Zhang and Wang 2011; Wang et al. 2011; Pillai et al. 2011; Beuther et al. 2013; Lee et al. 2013). Among these, only a small portion reached a resolution better than the 0.1 pc core scale. Therefore, in the past years we have used SMA and JVLA to peer into several IRDC clumps to study their fragmentation (Zhang et al. 2009; Zhang and Wang 2011; Wang et al. 2011, 2012, 2013; Wang and Zhang 2014). We use SMA dust continuum emission to resolve hierarchical structures, and JVLA NH_3 inversion transitions to precisely measure the gas temperature. We strictly limit our sample to dense molecular clumps that represent the extreme early phases (prior to the appearance of hot molecular cores). This makes our programme unique in probing the early fragmentation.

In G28.34-P1, we found hierarchical fragmentation where turbulent pressure dominates over thermal pressure (Chap. 3; Wang et al. 2011, 2012). This is in contrast with low-mass star formation regions where thermal Jeans fragmentation matches well with observations (e.g., Lada et al. 2008), and is consistent with studies that turbulence becomes more important in high-mass star formation regions (Wang et al. 2008, 2009, and references therein). Whether this kind of fragmentation is a common mode of the initial fragmentation, and how the fragments grow physically and chemically, are of great importance, yet remain unexplored. In this chapter, we address these questions by extending our study to two early clumps.

4.1.2 Targets: Dense Clumps in IRDC G11.11–0.12

G11.11–0.12, also known as the "Snake" nebula, is one of the first IRDCs identified by Egan et al. (1998) from the *Midcourse Space Experiment* images owing to its remarkable sinuous dark features in the mid-IR (see Fig. 4.1 for an overview). Shortly

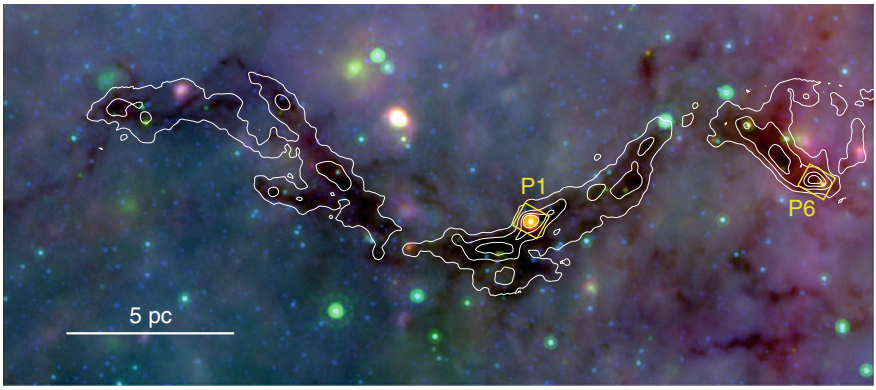

Fig. 4.1 Multi-wavelength composite image of the 'Snake' nebula, IRDC G11.11–0.12. Continuum emission at 70 μm (Molinari et al. 2010), 24 μm (Carey et al. 2009), and 8 μm (Churchwell et al. 2009) are color coded in *red*, *green*, and *blue*, respectively. The contours show 850 μm emission (Carey et al. 2000) from JCMT at 0.05, 0.3, 0.6, and 0.9 Jy per 14″.5 beam. Note this figure is plotted in the Galactic coordinate system. The *two yellow boxes* outline the approximate spatial extend of clumps P1 and P6 as plotted in Fig. 4.2 [*Credit* Ke Wang (ESO)]

after the discovery of Egan et al. (1998), Carey et al. (1998) observed H_2CO line emission, a tracer of dense gas, in the central part of the Snake, and thus directly confirmed (in addition to the infrared extinction) the existence of dense gas in the IRDC. A kinematic distance of 3.6 kpc was then inferred based on the radial velocity of the H_2CO line, putting the Snake on the near side of the Scutum-Centaurus arm [see Tackenberg et al. (2012) and Goodman et al. (2014) for a Galactic illustration]. Later, Carey et al. (2000) and Johnstone et al. (2003) obtained JCMT 450 and 850 μm continuum images for the entire Snake, and identified seven major emission clumps P1 through P7. Pillai et al. (2006a) mapped the entire cloud in NH_3 using the Effelsberg 100-m Radio Telescope and found a consistent $V_{\rm LSR}$ around 29.8 km s^{-1} along the Snake, thus the elongated (aspect ratio 28 pc/0.77 pc = 36:1) cloud is indeed a physically coherent entity, not a chance alignment.

As a demonstration case for the *Herschel* key project "Earliest Phases of Star Formation" (EPoS), Henning et al. (2010) studied G11.11–0.12 with deep *Herschel* images in multiple wavelengths and identified 18 protostellar "cores" along the Snake filament, which they call "seeds of star formation". By fitting the spectral energy distributions (SEDs) of individual cores, Henning et al. (2010) obtained physical parameters including dust temperature, mass, and luminosity. Among all these cores, two massive and luminous cores stand out. With masses of 240 and 82 $M_\odot$ and luminosities of 1.3×10^3 and 1.4×10^2 $L_\odot$ respectively, the two cores distinguish from other cores of much lower mass and luminosity, and therefore are the most likely sites to form massive stars in the entire cloud. The two cores reside in clumps P1 and P6 respectively, coincident with two mid-IR point sources which dominate the luminosities of the clumps (Fig. 4.1). P1 and P6 lie in the centre and the head of the Snake respectively. These clumps, with sizes less than 1 pc, are likely results of global

fragmentation (see Sect. 4.4.1.2), while further fragmentation towards smaller scales are less affected by the global environment but rather depend on local properties of the clumps themselves (Kainulainen et al. 2013). Both clumps have a mass reservoir of $\sim 10^3 M_\odot$ within 1 pc (Sect. 4.4.1). Therefore, P1 and P6 are two massive, relatively low-luminosity molecular clumps that are the most likely sites of high-mass star formation in the "Snake" IRDC. Hence, resolving the initial star formation processes in P1 and P6 is of great interest.

Although G11.11–0.12 is one of the most well studied IRDCs, previous studies are mostly limited to angular resolution achieved with single dish telescopes (Carey et al. 1998, 2000; Johnstone et al. 2003; Pillai et al. 2006a; Tackenberg et al. 2012). The only interferometric studies are still yet to resolve underlying fine structures (Pillai et al. 2006b; Gómez et al. 2011). Here, we present new SMA and JVLA observations of P1 and P6 which resolve great details of the star formation activities that capture the growth of these star formation seeds in action.

4.2 Observations

4.2.1 Submillimeter Array

4.2.1.1 230 GHz Band

The Submillimeter Array[1] (SMA; Ho et al. 2004) was pointed towards G11.11–0.12 P1 and P6 to obtain continuum and spectral line emission in the 230 GHz band during four tracks in 2010, when SMA was in its subcompact, compact, and extended configurations. Time-dependent antenna gains were monitored by periodic observations of quasars NRAO530 and J1911-201; frequency-dependent bandpass responses were calibrated by quasars 3C273, 3C279 and 3C454.3; and absolute flux was scaled by observed correlator counts with modelled fluxes of Solar system moons Titan, Callisto, and Ganymede. The empirical flux uncertainty is about 15 %. For the four tracks, we used the same correlator setup which covers 4 GHz in each of the lower and upper sidebands (LSB, USB), with a uniform channel width of 0.812 MHz (equivalent velocity 1.1 km s^{-1} at 230 GHz) across the entire band. System temperatures varied from 80 to 150 K, and the zenith opacity at 225 GHz ranges from 0.05 to 0.12 during the four tracks. The full width at half-maximum (FWHM) primary beam is about 52″ at the observed frequencies. Table 4.1 summarizes the observations.

The visibility data were calibrated using the IDL superset MIR.[2] Calibrated visibility data were then exported out for imaging and analysis in MIRIAD[3]

[1] The Submillimeter Array is a joint project between the Smithsonian Astrophysical Observatory and the Academia Sinica Institute of Astronomy and Astrophysics and is funded by the Smithsonian Institution and the Academia Sinica.

[2] http://www.cfa.harvard.edu/~cqi/mircook.html.

[3] http://www.cfa.harvard.edu/sma/miriad, http://www.astro.umd.edu/~teuben/miriad.

Table 4.1 SMA and JVLA Observations of P1 and P6

Telescope Config.	Date (UT)	Pointing[a]	Lines	Calibrator[b]			Bandwidth (MHz)	Chan. width[c] ($km s^{-1}$)	Pol.	Int. Time (min)
				Gain	Flux	Bandpass				
JVLA K band (primary beam 2′)										
JVLA-D	2001-Oct-27	P1.I	NH_3 (1,1)	Q1	Q6	Q5	3.125	0.3	1	10
JVLA-D	2001-Nov-11	P1.I	NH_3 (1,1)	Q3	Q6	Q5	3.125	0.3	1	22
JVLA-D	2004-Aug-24	P1.II	H_2O	Q1	Q6	Q1, Q6	3.125	0.3	2	20
JVLA-D	2004-Aug-24	P1.II	NH_3 (2,2), (3,3)	Q1	Q6	Q1, Q6	3.125	0.6	2	50
JVLA-D	2004-Aug-29	P1.II	NH_3 (2,2), (3,3)	Q1	Q6	Q1, Q6	3.125	0.6	2	50
JVLA-C	2010-Dec-24	P6.I	H_2O, CH_3OH	Q1	Q6	Q4	4	0.8	4	10, 6
JVLA-C	2010-Dec-28	P6.I	NH_3 (1,1), (2,2)	Q1	Q6	Q4	4	0.2	2	7, 8
JVLA-C	2011-Jan-18	P6.I	NH_3 (2,2), (3,3)	Q1	Q6	Q4	4	0.4	2	20
JVLA-D	2013-Mar-17	P6.I	NH_3 (1,1) to (5,5), H_2O	Q1	Q8	Q7	4/8	0.1/0.2	2	45
JVLA-D	2013-Apr-18	P6.I	NH_3 (1,1) to (5,5), H_2O	Q1	Q8	Q7	4/8	0.1/0.2	2	45
SMA 230 GHz (1.3 mm) band (primary beam 52″)										
SMA-Sub	2010-Mar-19	P1.III, P6.II	Many, see Table 4.5	Q1, Q2	M1	Q4	2 × 4000	1.1	1	5.8/6.2 h[d]
SMA-Com	2010-Jun-15	P1.III, P6.II	Many, see Table 4.5	Q1, Q2	M1	Q5, Q7	2 × 4000	1.1	1	
SMA-Ext	2010-Aug-27	P1.III, P6.II	Many, see Table 4.5	Q1, Q2	M2, M3	Q7	2 × 4000	1.1	1	
SMA-Ext	2010-Sep-20	P1.III, P6.II	Many, see Table 4.5	Q1, Q2	M2, M3	Q7	2 × 4000	1.1	1	
SMA 345 GHz (880 μm) band (primary beam 34″)										
SMA-Sub	2011-Mar-15	P1.IV, P6.III	Many, see Table 4.5	Q1, Q2	M1	Q5	2 × 4000	0.7	1	2.2/3.5 h[d]
SMA-Ext	2011-Jul-22	P1.IV, P6.III	Many, see Table 4.5	Q1, Q2	M3	Q5	2 × 4000	0.7	1	

[a] Phase centres in J2000 Equatorial coordinates: P1.I = 18:10:28.3, −19:22:29; P1.II = 18:10:30.475, −9:22:29.39; P1.III = 18:10:28.4, −19:22:38; P1.IV = 18:10:28.21, −19:22:33.34; P6.I = 18:10:07.42, −19:29:07.7, P6.II = 18:10:07.2, −19:28:59; P6.III = 18:10:07.38, −19:29:08.00

[b] vCalibrators are Quasars and Moons: Q1 = NRAO530 (J1733-130), Q2 = J1911-201, Q3 = J1743-038, Q4 = 3C273, Q5 = 3C279, Q6 = 3C286, Q7 = 3C454.3, Q8 = 3C48; M1 = Titan, M2 = Callisto, M3 = Ganymede

[c] Native channel width, subject to smoothing for some lines (Sect. 4.2.2)

[d] Total on-source integration time combining data from all SMA array configurations for P1 and P6, respectively

Table 4.2 Image properties

Image[a]	P1		P6	
	Beam	RMS[b]	Beam	RMS[b]
1.3 mm continuum	$2''.2 \times 1''.6$	0.9	$2''.1 \times 1''.5$	0.9
1.3 mm spec. lines[c]	$2''.7 \times 1''.7$	25–30	$2''.7 \times 1''.7$	25–30
880 μm continuum	$1''.6 \times 1''.2$	3.3	$1''.2 \times 1''.0$	2.3
			$0''.8 \times 0''.6$	1.7
880 μm spec. lines[a]	$2''.1 \times 1''.3$	110	$2''.1 \times 1''.3$	110
NH_3 (1,1)	$5'' \times 3''$	14	$7''.1 \times 2''.8$	4
NH_3 (2,2)	$5'' \times 3''$	3.5	$6''.1 \times 2''.7$	2.5
NH_3 (3,3)	$5'' \times 3''$	6.5	$6''.9 \times 2''.9$	2.8
NH_3 (4,4)	No data	No data	$7''.7 \times 3''.0$	2.3
NH_3 (5,5)	No data	No data	$6''.7 \times 3''.0$	2.5
H_2O maser	$5'' \times 3''$	13	$2''.4 \times 1''.0$	2.7
			$7''.0 \times 3''.2$	4
			$7''.2 \times 3''.2$	2
CH_3OH maser class I	No data	No data	$2''.0 \times 0''.9$	2.2

[a] All images are made with natural weighting to achieve the highest sensitivity
[b] 1σ RMS noise in mJy beam^{-1}
[c] For spectral line images, beam varies slightly from line to line, hence a typical beam is listed

(Sault et al. 1995) and CASA[4] (Petry and CASA Development Team 2012). Data from different tracks were calibrated separately, and then combined in the visibility domain for imaging. Continuum emission was generated by averaging line free channels in the visibility domain. Table 4.2 lists the synthesized beam and 1σ RMS noise of the images.

4.2.1.2 345 GHz Band

In 2011, we revisited P1 and P6 with SMA at the 345 GHz band in two tracks, one in subcompact and another in extended array configuration. The two tracks used the same correlator setup which covers rest frequencies 333.7–337.7 GHz in the LSB, and 345.6–349.6 GHz in the USB, with a uniform spectral resolution of 0.812 MHz (or 0.7 km s^{-1}) across the entire band. System temperatures were in the range of 200–300 K, and the zenith opacity $\tau_{225\,\mathrm{GHz}}$ was stable at 0.06 during the observations. Other parameters are listed in Table 4.1. The data were reduced and imaged in the same way as the 230 GHz data. Additionally for P1, we made an image using data from the extended configuration only and achieved a higher resolution (see Sect. 4.3.3.1). Image properties are tabulated in Table 4.2.

[4] http://casa.nrao.edu.

4.2.2 Very Large Array

The Karl G. Jansky Very Large Array (JVLA) of NRAO[5] was pointed towards P1 in its D configuration in two observation runs in 2001 to observe the NH_3 (J,K) = (1,1) transition. The 3.125 MHz band was split into 128 channels with a channel spacing of 24.4 kHz (or 0.3 km s^{-1}). In 2004, P1 was revisited with another phase centre to obtain 22 GHz H_2O maser and NH_3 (2,2) and (3,3) transitions. The H_2O maser was observed in a single IF, dual polarization mode, with the same bandwidth and channel spacing as the 2001 observations. The NH_3 (2,2) and (3,3) were observed in a 2IF, dual polarization mode, splitting the 3.125 MHz band into 64 channels, each with a 0.6 km s^{-1} channel width.

Observations of P6 were carried out in C configuration in three observation runs during the expanded JVLA early science phase in 2010–2011, and two runs in the 2013 D configuration. Thanks to the flexibility of the new correlator, we observed the NH_3 (1,1), (2,2), (3,3), (4,4), and (5,5) transitions as well as 22 GHz H_2O maser and 25 GHz class I CH_3OH maser lines, with various bandwidth and spectral resolutions (see Table 4.1).

For all the experiments, gain, bandpass, and flux variations were calibrated by strong, point-like quasars. See Table 4.1 for details. The visibility data were calibrated using CASA, and then imaged and analyzed in MIRIAD and CASA. Data from different observation runs were calibrated separately, and then combined in the visibility domain for imaging with the exception for maser for which we make individual images from different observing runs, to investigate potential time variations. The final image cubes keep the native channel width listed in Table 4.1, except for the NH_3 (1,1), (2,2), and (3,3) images of P6 where the final channel width is 0.4 km s^{-1} in order to include both the C and D configuration data. Observational parameters are summarized in Table 4.1 and image properties are listed in Table 4.2.

4.3 Results

4.3.1 Hierarchical Structure

In the literature, there have been different definitions for a clump, core, and condensation when describing the spatial structure of molecular clouds. For consistency, we adopt the terminology of *clump*, *core*, and *condensation* suggested by Zhang et al. (2009) and Wang et al. (2011). We refer a clump as a structure with a size of ∼1 pc, a core as a structure with a size of ∼0.1 pc, and a condensation as a substructure of ∼0.01 pc within a core. A clump is capable of forming a cluster of stars, a core may form one or a small group of stars, and a condensation can typically form

[5] The National Radio Astronomy Observatory is a facility of the National Science Foundation operated under cooperative agreement by Associated Universities, Inc.

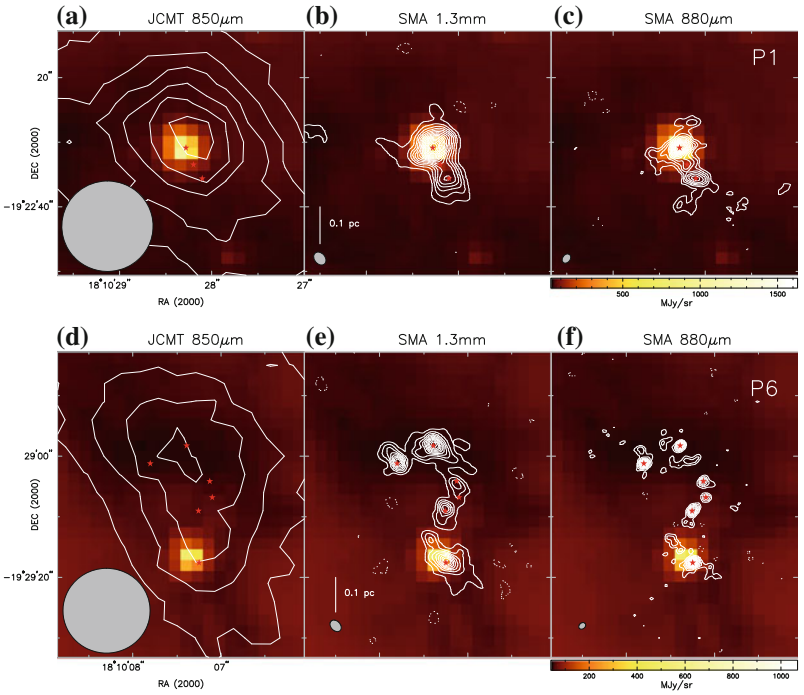

Fig. 4.2 Hierarchical structures in G11.11-P1 (**a–c**) and G11.11-P6 (**d–f**), as seen by JCMT at 850 μm, SMA at 1.3 mm, and SMA at 880 μm (contours), superposed on *Spitzer* 8 μm image (color scale). The JCMT continuum emission is contoured at 0.3 Jy beam^{-1}. The SMA 1.3 mm emission is contoured at $\pm(3, 6, 9, \ldots)\,\sigma$, where $\sigma = 0.9$ mJy beam^{-1} for both P1 and P6. The SMA 880 μm emission is contoured at $\pm(3, 5, 7, \ldots)\,\sigma$, where $\sigma = 3.3$ mJy beam^{-1} for P1 and $\sigma = 2.3$ mJy beam^{-1} for P6. The *shaded ellipse* in the *bottom left corner* of each panel represents the beam size of the contoured image. The *red stars* mark dominant condensations identified from the SMA 880 μm images. The *scale bars* represent a spatial scale of 0.1 pc at the source distance of 3.6 kpc. Negative contours are *dashed* throughout this chapter. **a** JCMT 850 μm **b** SMA 1.3 mm **c** SMA 880 μm **d** JCMT 850 μm **e** SMA 1.3 mm **f** SMA 880 μm [*Credit* Wang et al. (2014), reproduced with permission © the authors]

a single star or a multiple-star system. These structures are dense enough that gas and dust are well coupled (Goldsmith 2001), thus we use the NH_3 gas temperature as a direct measure of the dust temperature throughout this chapter.

Dust continuum images at various resolutions reveal hierarchical structures in P1 and P6. Figure 4.2 plots JCMT 850 μm, SMA 1.3 mm, and SMA 880 μm images superposed on *Spitzer* 8 μm images. The JCMT images outline IRDC clumps P1 and P6, where P1 exhibits a bright MIR source in its centre, while P6 shows a less bright MIR source in its southern part. As the resolution increases, structures at different scales are highlighted: from ∼1 pc scale clumps seen in JCMT 850 μm images, to the ∼0.1 pc scale cores resolved by the SMA 1.3 mm images, and to the ∼0.01 pc scale condensations resolved by the SMA 880 μm images. These structures show in

general a good spatial correlation with the *Herschel* 70 μm emission and the *Spitzer* 8/24 μm extinction, where two IR-bright protostars have already developed (Fig. 4.2; Henning et al. 2010; Ragan et al. 2012a).

We identify the smallest structure, condensations, based on the highest resolution SMA 880 μm images as shown in Fig. 4.2c, f. All features above 5σ rms are identified as in Wang et al. (2011) and Zhang et al. (2009). We first identify "major" emission peaks with fluxes >9σ (the 4th contour) and assign them as SMA1, SMA2, SMA3,…, in order from east to west and from north to south. Three major peaks are identified in P1 and six identified in P6, denoted by red stars in Fig. 4.2. Then we identify "minor" emission peaks with fluxes >5σ (the 2nd contour). Three minor peaks are identified in P1, and we assign them as SMA4, SMA5, SMA6, from north to south. In P6, 11 minor peaks are identified. These emission peaks are relatively weak and are associated in position with the 6 major peaks. We thus assign these minor peaks to the associated major peaks. For instance, the two minor peaks associated with P6-SMA5 are assigned as P6-SMA5b and P6-SMA5c. All the identified major and minor peaks are of the size of condensations. Associated condensations may have been fragmented from a common parent core. In summary, we identify 6 condensations in P1 which may belong to 6 cores (P1-SMA1,2,3,4,5,6), respectively, and 17 condensations in P6 which may belong to 6 cores (P6-SMA1,2,3,4,5,6), respectively. For each condensation, we fit a 2D Gaussian function to the observed SMA 880 μm image and list the results in Table 4.3. All except one (P6-SMA4) "major" condensations (red stars in Fig. 4.2) coincide with the cores resolved in the SMA 1.3 mm images. Condensation P1-SMA1 is coincident with protostar #9 identified by Henning et al. (2010) from multi-band *Herschel* images, and condensation P6-SMA6 is coincident with the protostar #18.

Dust mass is estimated with the assumption that dust emission is optically thin (which is valid at 0.88 and 1.3 mm), following

$$M_{\rm dust} = \frac{S_\nu d^2}{B_\nu(T_{\rm dust})\kappa_\nu}\,, \tag{4.1}$$

where $M_{\rm dust}$ is the dust mass, S_ν is the continuum flux at frequency ν, d is the source distance, $B_\nu(T_{\rm dust})$ is the Planck function at dust temperature $T_{\rm dust}$, and $\kappa_\nu = 10(\nu/1.2\,{\rm THz})^\beta\,{\rm cm^2\,g^{-1}}$ is the dust opacity (Hildebrand 1983). In the calculation we adopt the temperature measured from NH_3 (Sect. 4.3.5.2) and the dust opacity index $\beta = 1.5$. If $\beta = 2$ the mass would be a factor of 2 larger. Dust mass is then translated to gas mass accounting for a gas:dust ratio of 100. The computed total mass for each condensation is reported in Table 4.3. Note that interferometric images filter out relatively smooth emission due to imperfect (u, v) sampling, leading to "missing flux". Thus the total mass of the dense cores or condensations revealed by SMA (Fig. 4.2) is less than the clump mass determined from single dish JCMT observations. Our analysis (Sect. 4.4.1) does not rely on the smooth emission but on clumpy structures, therefore is not affected by the missing flux. For reference, the SMA 880 μm images recover 7 and 14 % of the total JCMT 850 μm flux in P1

Table 4.3 Physical parameters of the condensations

Source ID	RA (J2000)	Dec (J2000)	Flux[a] (mJy)	T (K)	Mass[b] ($M_\odot$)	Size[c]		
						Maj. (″)	Min. (″)	PA (°)
P1-SMA								
1	18:10:28.27	−19:22:30.9	205.0	25	14.1	2.1	1.3	114
2	18:10:28.19	−19:22:33.2	46.7	19	4.7	1.9	0.4	86
3	18:10:28.09	−19:22:35.7	197.0	17	23.7	3.4	1.7	69
4	18:10:28.15	−19:22:27.0	57.6	18	6.3	2.5	1.2	99
5	18:10:28.56	−19:22:31.9	53.5	18	5.9	2.1	1.1	60
6	18:10:28.27	−19:22:39.7	54.5	15	8.0	2.3	1.6	156
P6-SMA								
1	18:10:07.80	−19:29:01.2	109.7	11	27.9	1.1	0.9	147
1b	18:10:07.83	−19:28:59.3	83.8	11	21.3	3.4	1.3	48
2	18:10:07.39	−19:28:58.3	78.8	10	24.2	1.5	1.1	135
2b	18:10:07.58	−19:28:57.9	33.0	10	10.1	1.5	0.7	167
2c	18:10:07.22	−19:29:00.6	38.2	10	11.7	2.1	0.6	131
2d	18:10:07.30	−19:29:00.8	54.9	10	16.9	2.5	1.0	91
2e	18:10:07.39	−19:29:01.3	35.2	10	10.8	2.5	0.7	109
3	18:10:07.12	−19:29:04.3	66.4	14	10.9	1.7	1.2	55
4	18:10:07.10	−19:29:06.8	35.3	15	5.2	1.0	1.0	83
5	18:10:07.25	−19:29:09.0	82.1	21	7.2	1.6	0.8	143
5b	18:10:07.32	−19:29:10.8	30.9	21	2.7	1.4	1.2	16
5c	18:10:07.27	−19:29:11.0	21.5	21	1.9	1.7	1.1	23
6	18:10:07.25	−19:29:17.6	157.0	19	15.9	1.4	1.0	105
6b	18:10:07.51	−19:29:13.5	29.0	19	2.9	1.3	0.7	50
6c	18:10:07.46	−19:29:14.3	44.5	19	4.5	2.0	0.9	41
6d	18:10:07.39	−19:29:15.4	28.7	19	2.9	1.3	1.0	35
6e	18:10:07.06	−19:29:18.4	32.7	19	3.3	1.5	0.6	36

[a] Integrated flux obtained from 2D Gaussian fitting and corrected for primary beam attenuation
[b] Mass computed assuming dust opacity index $\beta = 1.5$. The mass scales with β in a form of $M \propto 3.5^{\beta}$. For reference, if $\beta = 2$, the mass will be 1.87 times larger
[c] Deconvolved source size

and P6, respectively. This is consistent with the fact that P6 contains more compact structures than P1 (Fig. 4.2).

The sensitivity in the 880 μm images (Fig. 4.2 and Table 4.2) corresponds to 0.2–0.5 $M_\odot$ for the 15–25 K gas temperature in the P1 clump (Sect. 4.3.5.2), and 0.2–0.7 $M_\odot$ in P6 for a 10–21 K temperature range (Sect. 4.3.5.2). Therefore, the identified condensation is complete to a 5σ mass limit of 1–3.5 $M_\odot$, depending on the temperature.

4.3.2 H_2O *and* CH_3OH *Masers*

No H_2O or CH_3OH maser line emission was detected above 3σ in P6. In P1, we detect two 22 GHz H_2O masers which we name as W1 and W2, in decreasing order of brightness (white and black crosses in Fig. 4.6). W1 is located at (RA, Dec)$_{J2000}$ = (18:10:32.902, −19:22:23.339), close to the eastern border of the dark filament. It has a flux of 3 Jy at $V_{LSR} = 30.5\,km\,s^{-1}$. W2 is located at (RA, Dec)$_{J2000}$ = (18:10:28.298, −19:22:30.759), coincident with P1-SMA1. It has a flux of 0.25 Jy and is seen at $V_{LSR} = 37.5\,km\,s^{-1}$. Both W1 and W2 show a typical maser spectrum with a single velocity component and has a narrow linewidth (FWHM $< 1\,km\,s^{-1}$). The spectral profile is not resolved at the $0.3\,km\,s^{-1}$ channel width.

In addition to the two water masers, Pillai et al. (2006b) reported a 6.7 GHz class II CH_3OH maser using the Australia Telescope Compact Array (ATCA), which we assign as M1. Located at (RA, Dec)$_{J2000}$ = (18:10:28.248, −19:22:30.45), M1 is 0″.7 (2500 AU) west of W2 (Figs. 4.3, 4.10 and 4.11). Unlike a single velocity component seen in the water masers, M1 has multiple velocity components ranging from 22 to $34\,km\,s^{-1}$. Pillai et al. (2006b) noted that M1 consists of six maser spots which are spatially distributed along a 0″.3 north-south arc, and exhibits an ordered velocity field red-shifting from north to south. Based on the position and velocity distribution, Pillai et al. (2006b) suggested that the CH_3OH maser spots trace a rotating Keplerian disc seen edge-on. Our detection of an East-West molecular outflow centred on W2 strongly supports this speculation (see Sect. 4.3.3.1).

4.3.3 *Protostellar Outflows*

4.3.3.1 Outflow Driven by P1-SMA1

Our SMA observations clearly reveal a bipolar outflow oriented east-west in P1. The outflow is seen in many molecular tracers including CO, SO, SiO, H_2CO, and CH_3OH, but only in SiO do both the blue and red lobes appear; other tracers only reveal the blue (eastern) lobe. Figure 4.3 plots the blue shifted SiO emission (18–$28\,km\,s^{-1}$, blue contours) to the east, the SiO emission close to the systemic velocity (29–$31\,km\,s^{-1}$, gray background), and red shifted SiO emission (32–$39\,km\,s^{-1}$, red contours) to the west, in comparison with the SMA 880 μm continuum (black contours). A bipolar SiO outflow is clearly defined by the blue/red lobes with respect to the dust continuum, which is probably produced in shocks by an underlying jet. We schematically draw the axis of the outflow on the plot, and measure a position angle of 94 ± 12°. The geometric centre of the outflow is close to P1-SMA1, and we speculate that the outflow driving source is a protostar embedded in the dust condensation P1-SMA1, likely the #9 protostar identified by Henning et al. (2010). (See more discussion on the driving source later in Sect. 4.4.3). Previous studies have shown indirect evidence of an outflow associated with P1, for example broadening

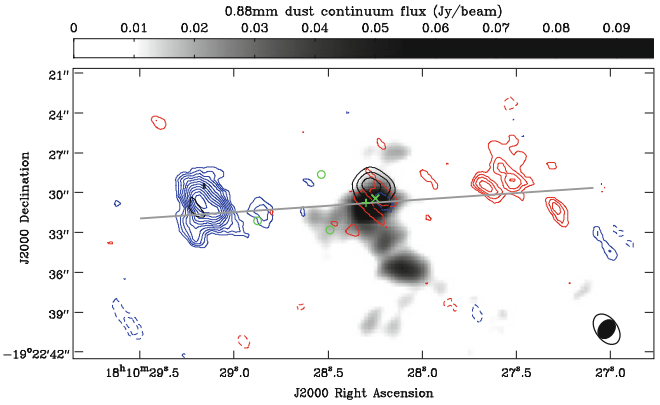

Fig. 4.3 The SiO(5–4) outflow in G11.11-P1. *Blue/red* contours show the *blue-/red*-shifted SiO emission integrated over [18, 28] $\mathrm{km\,s^{-1}}$ and [32, 39] $\mathrm{km\,s^{-1}}$, respectively, whereas the *black* contours represent SiO emission near the systemic velocity integrated over [29, 31] $\mathrm{km\,s^{-1}}$. The SiO contours are $\pm\,(3, 4, 5, \ldots)\,\sigma$, where $\sigma = 85\,\mathrm{mJy\,km\,s^{-1}}$. For comparison, the SMA 880 μm continuum image is shown as *grey* scale in the background. *Labelled symbols* denote H_2O maser W2 (+), class II CH_3OH maser M1 (×), and the three 2MASS point sources (○). In the *bottom right corner* the *open/filled ellipses* represent synthesized beams of the SiO/880 μm images. The *thick grey line* marks schematically the underlying bipolar jet that propels the observed molecular outflow. The *grey line* centres on W2 and extends 0.3 pc eastbound and westbound, respectively [*Credit* Wang et al. (2014), reproduced with permission © the authors]

of line wings, possible extended 4.5 μm emission, and enrichment of outflow tracers (Carey et al. 2000; Pillai et al. 2006b; Leurini et al. 2007; Cyganowski et al. 2008; Gómez et al. 2011). Our high-sensitivity, high-resolution, broad-band SMA observations directly reveal this outflow in multiple tracers for the first time, providing critical support for a previously speculated outflow-disc system in P1 (Sect. 4.4.3).

The SiO outflow extends 0.3 pc away from the protostar in the east-west direction (Fig. 4.3). While the blue lobe further propagates towards the eastern edge of the main filament, it induced the NH_3 emission peaks A, B and D, and probably excited the water maser W1 (see first paragraph in Sect. 4.3.5.1). The projected separation of the NH_3 peaks are $l_{AB} = 0.3$ pc, and $l_{AD} = 1$ pc (Fig. 4.6), i.e., the molecular outflow extends at least 1 pc away from the driving source in the eastern lobe. Further to the east from D, there is no dense gas to be heated and shocked. In the western lobe, however, there is no dense gas beyond the red shifted SiO lobe which is 0.3 pc from the protostar. Because the powering source is located near the edge of the dense filament, there is more dense gas in the eastern lobe to be heated (and therefore being detected) than in the western lobe. The special location and orientation of this outflow provides a unique case to study environment dependence of outflow chemistry, which deserves further study.

We compute outflow parameters assuming LTE and optically thin SiO emission in the line wings, following the formulas given in Sect. 3.3.2.2 Wang et al. (2011). We adopt an abundance of $[\mathrm{SiO/H_2}] = 5 \times 10^{-10}$ based on recent chemistry surveys

Table 4.4 Outflow parameters

Parameter[a]	P1-SMA1		P6-SMA2		P6-SMA5	P6-SMA6	
	Blue	Red	Blue	Red	Blue	Blue	Red
Tracer	SiO	SiO	CH_3OH	CH_3OH	CH_3OH	CH_3OH	CH_3OH
Fractional abundance $[X/H_2]$[b]	5×10^{-10}	5×10^{-10}	5×10^{-8}	5×10^{-8}	5×10^{-8}	5×10^{-8}	5×10^{-8}
Excitation temperature T_{ex} (K)	25	25	21	21	21	21	21
Inclination angle θ (degree)[c]	77	77	57.3	57.3	57.3	57.3	57.3
Velocity range ($km\,s^{-1}$)	[18,28]	[32,39]	[22,29]	[31,35]	[22,29]	[22,29]	[31,35]
Total mass M ($M_\odot$)	2.0	1.1	1.1	0.4	2.1	1.2	0.1
Momentum P ($M_\odot\,km\,s^{-1}$)	10.8/48.2	4.6/20.7	1.8/3.3	0.8/1.5	6.1/11.3	4.1/7.5	0.3/0.5
Energy E ($M_\odot\,km^2\,s^{-2}$)	40.0/791.0	12.4/245.6	1.8/6.2	1.0/3.4	12.3/42.3	8.8/30.3	0.4/1.4
Lobe length L_{flow} (pc)	0.30/0.31	0.30/0.31	0.17/0.20	0.07/0.08	0.24/0.29	0.28/0.34	0.08/0.10
Dynamical age t_{dyn} (10^3 yr)	24.9/5.7	31.9/7.4	20.8/13.3	12.5/8.0	30.2/19.4	35.7/22.9	15.8/10.1
Outflow rate $\dot{M}_{out}$ ($10^{-5}\,M_\odot\,yr^{-1}$)	8.0/34.8	3.3/14.3	5.4/8.4	3.2/5.1	6.9/10.8	3.5/5.4	0.7/1.1

[a] Parameters corrected for inclination follow after the "/"
[b] Adopted abundances are based on (Sanhueza et al. 2012) and (Leurini et al. 2007) for SiO and CH_3OH, respectively
[c] Angle between outflow axis and the line of sight, see Sects. 4.3.3.1 and 4.3.3.2

towards IRDCs by Sanhueza et al. (2012). The inclination angle of this outflow can be inferred based on the CH_3OH masers discovered by Pillai et al. (2006b). The masers outline (part of) an ellipse with an eccentricity of ~0.2. Suppose the masers trace a circular disc, we infer an inclination angle of ~77° between the axis of the disc (also the outflow jet) and the line of sight. Therefore, the disc is almost edge-on to us and the outflow jet is almost parallel to the plane of sky. Table 4.4 shows the derived outflow parameters with and without correction for inclination. The P1-SMA1 outflow is a massive outflow judging from its energetics, in comparison with other outflows emanating from high mass protostellar objects (Beuther et al. 2002; Zhang et al. 2005).

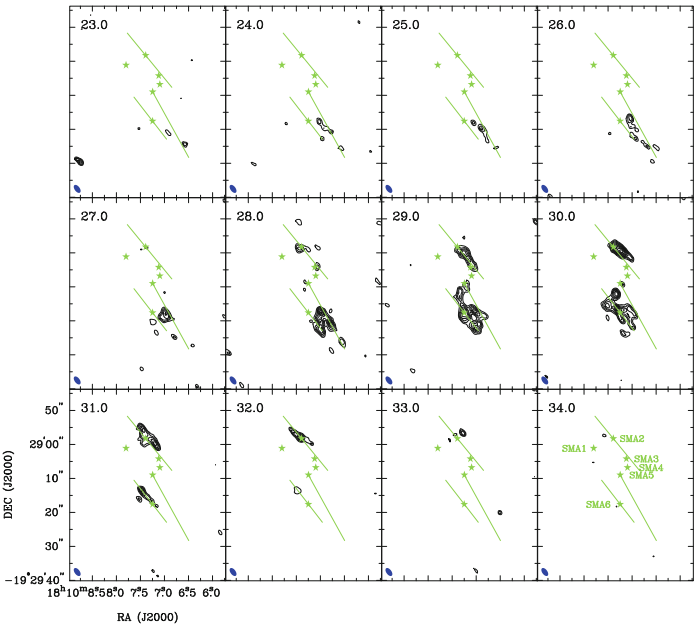

Fig. 4.4 Channel maps of CH_3OH $(4-3)$ in G11.11-P6. All panels share the same coordinates as labelled on the *lower-left panel*. Central velocity ($km\,s^{-1}$) of each channel is labelled on the *upper left corner*. The contours are $\pm(3, 4, 5, 6, \ldots)\sigma$, where $\sigma = 25\,mJy\,km\,s^{-1}$. The *stars* denote six cores identified in G11.11-P6 (SMA1–6, labelled in the last panel). SMA2, SMA5, and SMA6 drive either bipolar or uni-polar outflows, as outlined by *schematic lines*. The *filled ellipse* represents synthesized beam [*Credit* Wang et al. (2014), reproduced with permission © the authors]

4.3.3.2 Outflows Driven by P6-SMA2,5,6

We also detect molecular outflows in P6. These outflows are seen in many molecular tracers including CO, SO, SiO, H_2CO, but are best seen in CH_3OH. Figure 4.4 shows channel maps of CH_3OH (4–3), where one can see that SMA2,5,6 drive relatively collimated outflows. Outflows associated with SMA2 and SMA6 show both blue and red shifted lobes extending about 0.1–0.3 pc, whereas the SMA5 outflow only shows a blue lobe approximately 0.3 pc long. All these outflows are oriented in a NE-SW direction, coincident with emission from the NH_3 (3,3) and higher transitions (Fig. 4.7). The outflow parameters (Table 4.4) are also calculated in a similar way as for P1. The inclination angles for the P6 outflows are unknown. We list outflow parameters without correction and with correction for an inclination of 57.3°, the most probable value for a random distribution of outflow orientations (Bontemps et al. 1996; Semel et al. 2009). Compared with outflow P1-SMA1, the P6 outflows are slightly less energetic but are still comparable with other high-mass outflows (Beuther et al. 2002; Zhang et al. 2005).

The cores in G11.11-P1 and G11.11-P6 exhibit similar characteristics (mass, size, and global mass reservoir) to those in G28.34-P1. The cores driving powerful outflows are undergoing accretion to build up stellar mass. With a typical star formation efficiency of 30 % in dense gas and a standard stellar initial mass function, the $\sim 10^3$ $M_\odot$ clumps will eventually form massive stars in some of the cores once the protostellar accretion is completed. At that time, these clumps will become massive star clusters. One key difference is that we detect copious molecular emission in the cores in G11.11-P1 and G11.11-P6, which we can use to assess their evolutionary state (Sect. 4.3.4).

4.3.4 Chemical Differentiation

Our SMA broad-band observations covered a total of 16 GHz in two observing bands, and detected many molecular lines in P1 and P6. Table 4.5 lists all detected lines and Fig. 4.5 plots spectra of the nine "major" cores. Besides CO isotopologues, P1 and P6 show several complex molecular lines like OCS, HNCO, CH_3CN, and CH_3OH, and molecules enriched by outflow shocks like SO and SiO. The number of detected lines vary from core to core and may reflect chemical evolution, despite that the cores are fragmented from the same parent clumps. Typical hot core lines CH_3CN and/or CH_3OH are seen towards cores P1-SMA1,2, P6-SMA6,2,5, suggesting their protostellar nature. This is consistent with the detection of protostellar outflows emanating from most of these cores. Deep *Herschel* 70 μm image revealed point sources coincident with P1-SMA1 and P6-SMA6 and relatively diffuse 70 μm emission in good agreement with our SMA 1.3 mm images of P1 and P6, suggesting that P1-SMA1 and P6-SMA6 have developed an increased luminosity than their fellow cores (Ragan et al. 2012a).

The diagnosis in outflow, hot core lines, and 70 μm emission show that P1-SMA1,2, P6-SMA6,2,5 are protostellar cores, while the other cores P1-SMA3, P6-SMA1,4,3 are likely of prestellar nature. Moreover, the line richness and strength reveal detailed chemical differentiation, likely reflecting an evolutionary sequence from core to core, as we plot in order in Fig. 4.5. Ideally, one would compare cores with the same/similar mass, as a lower mass core can be more evolved but does not have detectable line emission. However, this does not seem to affect our results, since the most massive core P6-SMA1 is not most evolved, and the most evolved core P1-SMA1 is not most massive. P1-SMA1 is in a "warm core" phase because it has not yet reached the hot core phase defined by Cesaroni (2005): temperature ≥ 100 K, size < 0.1 pc, mass 10–1000 $M_\odot$, and luminosity $> 10^4$ $L_\odot$. The prestellar cores all show H_2CO, a mid-product along the sequential hydrogenation from CO to CH_3OH (Zernickel et al. 2012), thus they are slightly more evolved than the cores in IRDC clumps G28.34-P1 and G30.88-C1 where only ^{12}CO is detected (Zhang et al. 2009; Zhang and Wang 2011; Wang et al. 2011). Distance effect cannot explain the difference, see discussion in Sect. 4.4.4. Within each core, the grouped condensations show similar chemical difference.

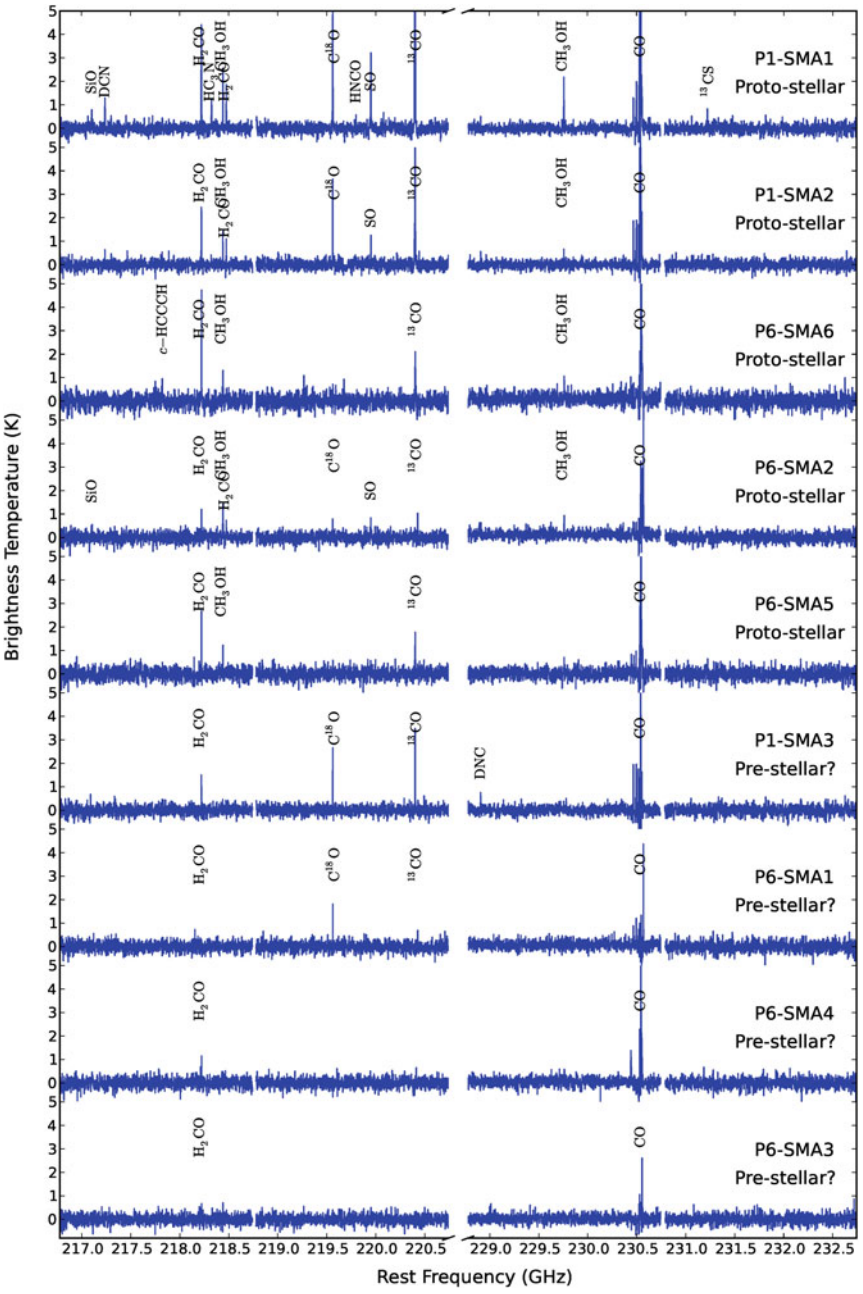

Fig. 4.5 SMA 230 GHz spectra extracted from the "major" cores, plotted in inverse order of evolution. The brightness temperature has been corrected for the primary beam attenuation. The small gaps around 218.75 and 230.75 GHz are due to our correlator setup, while the larger gap separates LSB and USB. Detected molecules are labelled [*Credit* Wang et al. (2014), reproduced with permission © the authors]

Table 4.5 Observed molecular lines

Rest freq.[b] (GHz)	Molecule[a]	Transition	Clump[c]	Remark
217.10498	SiO	$5-4$	P1, P6	Outflow, Fig. 4.3
217.23853	DCN	$3-2$	P1	
217.82215	*c*-HCCCH	$6_{1,6}-5_{0,5}$	P1	
218.22219	H_2CO	$3_{0,3}-2_{0,2}$	P1, P6	Outflow
218.32472	HC_3N	$24-23$	P1	
218.44005	CH_3OH	$4_{2,2}-3_{1,2}$	P1, P6	Outflow, Fig. 4.4
218.47563	H_2CO	$3_{2,2}-2_{2,1}$	P1, P6	Outflow
218.90336	OCS	$18-17$	P1	
219.56037	$C^{18}O$	$2-1$	P1, P6	Outflow
219.79828	HNCO	$10_{0,10}-9_{0,9}$	P1	
219.94943	SO	6_5-5_4	P1, P6	Outflow
220.39868	^{13}CO	$2-1$	P1, P6	Outflow
228.91047	DNC	$3-2$	P1	
229.75881	CH_3OH	$8_{-1,8}-7_{0,7}$	P1, P6	
230.53797	CO	$2-1$	P1, P6	Outflow
231.22100	^{13}CS	$5-4$	P1	
337.06110	$C^{17}O$	$3-2$	P1, P6	
335.56021	$^{13}CH_3OH$	$12_{1,11}-12_{0,12}$	P1	
345.79599	CO	$3-2$	P1, P6	
346.52940	CH_3CHO	$18_{17,1}-17_{17,0}$	P1	
346.97089	CH_3CH_2CN	$17_{8,9}-17_{7,10}$	P1, P6	
346.99834	HCO^+	$4-3$	P1, P6	
346.99991	CH_3CHO	$18_{7,11}-17_{7,10}$	P1, P6	

[a] Lines observed above 3σ at bands 230 and 345 GHz
[b] Rest frequency obtained from Splatalogue (http://splatalogue.net)
[c] Clump in which the line is observed

4.3.5 NH_3 *Emission and Temperature*

4.3.5.1 Shock Heated NH_3

We detect ammonia emission in all the observed transitions both in P1 and P6. Figure 4.6 (left panel) shows the NH_3 integrated images of P1 superposed on *Spitzer* 24 μm and JCMT 850 μm images. The sensitive *Spitzer* 24 μm image reveals details in the central part of the Snake Nebula: a filamentary system that consists of a main NE-SW oriented dark filament and two minor filaments joining from the South. This configuration resembles the filamentary system discussed by Myers (2009) and may arise from compression of an elongated clump embedded in a thin cloud sheet, as seen in IRDC G14.225–0.506 (Busquet et al. 2013). Dense gas traced by the JCMT dust image is mostly concentrated on the main filament, and NH_3 appears only on the

main filament. The NH_3 (1,1) emission is relatively continuous, whereas NH_3 (2,2) and (3,3) emission are highly clumpy. We identify four representative NH_3 emission peaks A, B, C, and D, and plot the corresponding spectra in Fig. 4.6 (right panel). Peak A shows the strongest NH_3 emission, and is associated with the IR point source, dust core P1-SMA1, and masers W2 and M1. Following A, peaks B, C, and D are roughly aligned on a line eastward inside the main filament, with D located near the eastern edge of the dense filament close to the water maser W1. All peaks except C show broad line wings in all three transitions. Peak A shows nearly symmetric blue and red line wings, whereas peaks B and D show only the blue wings extending greater than $15\,\mathrm{km\,s^{-1}}$ from the systematic velocity. Broad line wings, geometric alignment, and association with masers strongly suggest that peaks A, B, and D are associated with outflow activities. Indeed, these peaks are located on the extension of the blue lobe of the SiO outflow driven by P1-SMA1. The line broadening increases with higher

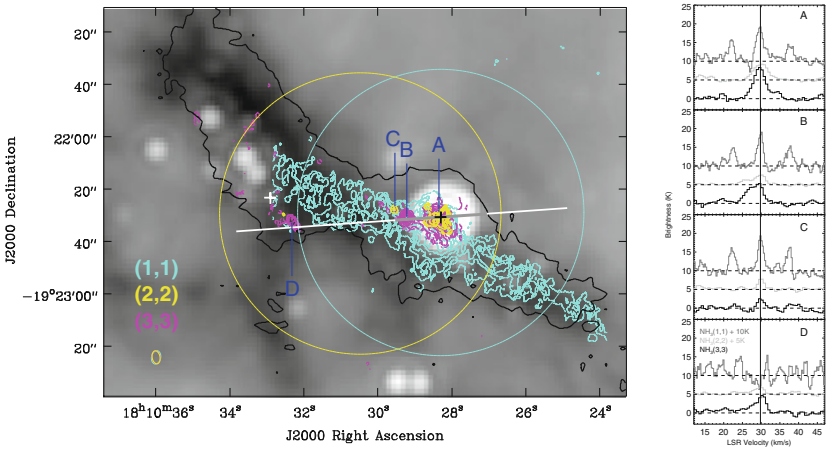

Fig. 4.6 *Left* JVLA observations of G11.11-P1: NH_3 (1,1), (2,2), (3,3) line emission integrated over the main hyperfine shown in *cyan*, *yellow*, and *pink* contours, respectively. The background is *Spitzer* 24 μm image stretched from 22 (*black*) to 100 (*white*) MJy sr^{-1}, and the *black thick* contour outlines JCMT 850 μm continuum emission at 0.31 Jy per 14″.5 beam. The contours for the NH_3 (1,1) emission are (4, 7, 10, . . . , 25) σ, where $\sigma = 7.4\,\mathrm{mJy\,km\,s^{-1}}$; the contours for the NH_3 (2,2) emission are (4, 6, 8, . . . , 24) σ, where $\sigma = 2.8\,\mathrm{mJy\,km\,s^{-1}}$; the contours for the NH_3 (3,3) emission are (4, 7, 10, . . . , 28) σ, where $\sigma = 5\,\mathrm{mJy\,km\,s^{-1}}$. The two (*black and white*) crosses denote the two water masers detected by JVLA. *Dashed cyan/yellow circles* represent two phase centres P1.I/P1.II (Table. 4.1) and their relative FWHM primary beams. Synthesis beams of the NH_3 images are shown as *ellipses* in the *bottom left corner* with the same color as the contours. Four representative NH_3 emission peaks are labelled as *A*, *B*, *C*, and *D*. The *grey line* is the same as in Fig. 4.3 and represents the SiO (5–4) outflow driven by P1-SMA1. The *white line* is the extension of the *grey line*. For scale, $l_{AB} = 0.3$ pc, and $l_{AD} = 1$ pc. *Right* NH_3 spectra extracted from emission peaks *A*–*D* as shown in the left panel. The spectra are smoothed by a 2-point boxcar function to enhance features. The brightness temperature has been corrected for the primary beam attenuation. The vertical line represents the systematic velocity $V_{LSR} = 29.8\,\mathrm{km\,s^{-1}}$ [*Credit* Wang et al. (2014), reproduced with permission © the authors]

transition, and becomes more prominent in (2,2) and (3,3) than in (1,1). This suggests that a significant fraction of the higher excited (2,2) and (3,3) emission may arise from the passage of outflow shocks which releases the NH_3 molecules from dust mantle into the gas phase (Zhang et al. 1999; Nicholas et al. 2011). The statistical equilibrium value for the fractional abundance ratio of ortho/para NH_3 is 1.0. But ortho-NH_3 ($K = 3n$) is easier to release than para-NH_3 ($K \neq 3n$) because it requires less energy (Umemoto et al. 1999). Therefore, NH_3 (3,3) is expected to be enriched more than (2,2) and (1,1). The relative emission strength $I_{(3,3)} > I_{(2,2)} > I_{(1,1)}$ in D supports this scenario. We will test this quantitatively for P6 for which we have more transitions observed (Sect. 4.4.2).

Shock enhanced NH_3 emission has been observed in a number of sources: a similar IRDC clump G28.34-P1 (Chap. 3; Wang et al. 2012), the high-mass disc/jet system IRAS 20126+4104 (Zhang et al. 1998, 1999), the Orion BN/KL hot core (Goddi et al. 2011), and the low-mass L1157 outflow (Umemoto et al. 1999). We note that in a recent single dish study of a large EGO sample (shocked 4.5 μm emission sources), Cyganowski et al. (2013) fit the NH_3 spectra with a fixed ortho-to-para ratio of unity. The fittings systematically underestimate the strength of NH_3 (3,3) (see Fig. 4.3 in their paper), which is suggestive to either (a) an elevated gas temperature traced by NH_3 (3,3), or (b) an enhanced ortho-NH_3, or a mixture of both. Both factors are the consequences of outflow activities.

Peak C is 3″ offset from the outflow jet defined by A, B, and D. The spectral profiles are narrow and symmetric which indicates that the gas is unaffected by the outflow. This also suggests that the outflow is well collimated.

NH_3 emission also reveals an ordered velocity field towards P1. As an example, Fig. 4.11 plots the moment 1 map of NH_3 (2,2) which clearly shows an NW-SE velocity field, varying more than 2 km s^{-1} over 0.16 pc. We will discuss this velocity field in Sect. 4.4.3. The velocity dispersion of NH_3 centres on P1-SMA1. On the main filament the overall velocity dispersion is about 0.8 km s^{-1}, which increases to 1.1 km s^{-1} towards P1-SMA1.

In P6, the NH_3 (1,1) and (2,2) emission follow the IR-dark dust ridge in general and are concentrated in two clumps: one lying between SMA2 and SMA3 and another southwest of SMA6, offset from the IR source (Fig. 4.7 left panel). The (3,3), (4,4) and (5,5) emission lie on a slightly bent filament connecting the two NH_3 clumps and extending further towards southwest. While the NH_3 (1,1) and (2,2) are less affected by outflows, higher transitions are clearly associated with outflows (Sect. 4.3.5.2). The velocity dispersion peaks on the two NH_3 clumps with values up to 0.9 km s^{-1}. Towards the dust cores, the velocity dispersion varies from 0.4 to 0.7 km s^{-1} with an average of 0.6 km s^{-1}. These numbers are used in the fragmentation analysis (Sect. 4.4.1).

4.3.5.2 NH_3 Temperature

Metastable NH_3 inversion lines provide a robust thermometer for cold and dense gas in star formation regions (Ho and Townes 1983; Walmsley and Ungerechts 1983;

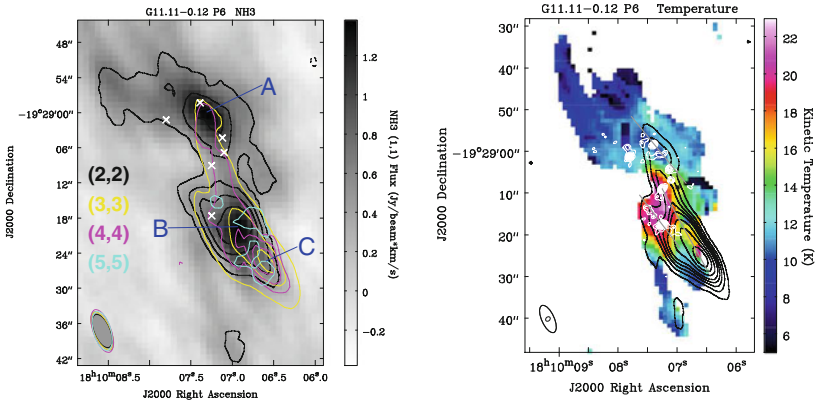

Fig. 4.7 *Left* JVLA observations of G11.11-P6: NH_3 (1,1), (2,2), (3,3), (4,4), and (5,5) integrated line emission plotted in *gray* scale, *black*, *yellow*, *pink* and *cyan* contours, respectively. The (2,2) contours are $\pm(3, 6, 9, 12)\,\sigma$, where $\sigma = 12\,\mathrm{mJy\,km\,s^{-1}}$; the (3,3) contours are $\pm(6, 20, 30)\,\sigma$, where $\sigma = 25\,\mathrm{mJy\,km\,s^{-1}}$; the (4,4) and (5,5) contours are $\pm(4, 6, 8, \ldots)\sigma$, where $\sigma = 6$ and $8\,\mathrm{mJy\,km\,s^{-1}}$, respectively. The beams shown in the *bottom left corner* are color coded in the same way as the contours. The *white crosses mark* the six dust cores SMA1–6. Selected regions (A,B,C) for OPR analysis are labelled. *Right* Kinetic temperature map of G11.11-P6 computed from NH_3 (1,1), (2,2), and (4,4) transitions. Overlaid are the SMA 880 μm contours as in Fig. 4.2 (f), and the integrated NH_3 (3,3) emission with primary beam corrected shown in *black* contours $[\pm(3, 6, 9, 12, 15, 20, 25, 30)\,\sigma$, where $\sigma = 25\,\mathrm{mJy\,km\,s^{-1}}]$. The *small* and *large ellipses* in the *bottom left corner* denote the resolution of the SMA image and the temperature map, respectively. *Grey lines* denote the outflows as in Fig. 4.4. The temperature map has been masked by 0.25 Jy (3σ) integrated NH_3 (1,1) emission [*Credit* Wang et al. (2014), reproduced with permission © the authors]

Juvela and Ysard 2012). To deduce the NH_3 temperature, we model the (1,1), (2,2), and (4,4) cubes simultaneously on a pixel-by-pixel basis, following the method developed by Rosolowsky et al. (2008). The model assumes LTE and Gaussian line profiles, and describes the spectra with five free parameters, including kinetic temperature, excitation temperature, NH_3 column density, velocity dispersion, and line central velocity. The level population is governed by the rotational temperature of the NH_3 system, which is related to kinetic temperature with collision coefficients (Danby et al. 1988). For details of the method see Rosolowsky et al. (2008). Only para species are included in the fitting to avoid any difference in the origin of ortho and para NH_3. The three NH_3 images were restored in a common beam, and then corrected for primary beam attenuation before input for the fitting procedure. Only pixels with $>3\sigma$ (0.25 Jy) in integrated NH_3 (1,1) emission are fitted; other pixels are masked out.

Figure 4.7 (right panel) shows the fitted kinetic temperature map of P6. The temperature distribution shows a single relatively-high-temperature spot of $\gtrsim$20 K located between SMA5 and SMA6, comparing to 10–15 K in other cores. This "hot" spot is also likely related with the outflows originated from SMA5 and SMA6 (Sect. 4.3.3.2). In P1, however, due to the outflow broadening, the fitting

is inappropriate. Instead of fitting, we adopt the method used for G28.34-P1 (Wang et al. 2012). This method estimates the rotational temperature by comparing the NH_3 (1,1) and (2,2) emission integrated over a $1.5\,km\,s^{-1}$ velocity range centred on the systematic velocity. The rotational temperature approximates kinetic temperature very well in the regime of $\lesssim$20 K (Ho and Townes 1983; Walmsley and Ungerechts 1983).

The resolutions of the NH_3 images and therefore the temperature map are high enough to resolve the cores but not the condensations. We assume all condensations in a given core share the same core-averaged temperature. A higher resolution map is needed to resolve the fine temperature structures associated with individual condensations. We list the temperature of each condensation in Table 4.3. Gas and dust are coupled in such a dense environment, so the gas temperature equals to the dust temperature, and is used to calculate the condensation masses. The error in the fitting is about 1 K across P6, while for P1 we estimate a 3 K error bar, similar to Wang et al. (2012). The estimated temperature for the SMA cores and condensations range from 15 to 25 K in P1 and 10 to 21 K in P6. The upper bounds of the temperature range are consistent with the *Herschel* SED estimates (Henning et al. 2010; Ragan et al. 2012a). This means that there is no evidence of significant external heating in this cloud. At the clump scale, we adopt an average temperature 15 K for both P1 and P6 based on previous single dish studies (Pillai et al. 2006b; Leurini et al. 2007).

4.4 Analysis and Discussion

4.4.1 Fragmentation Analysis

The hierarchical structures seen in Fig. 4.2 indicate fragmentation at different spatial scales: a clump with its initial physical conditions (density, temperature, turbulence, and magnetic fields) fragments into cores, and some cores continue to fragment into condensations with increased density and temperature. These structures resemble what we see in IRDC clump G28.34-P1, thus we discuss the fragmentation of P1 and P6 as in Wang et al. (2011). First, we estimate the density and temperature averaged over clump and core scales for fragmentation analysis. On clump scale, Gaussian fitting to the JCMT 850 μm image (Carey et al. 2000; Johnstone et al. 2003) yields an integrated flux of 8.7 Jy in a FWHM size of $40'' \times 25''$ (0.7×0.4 pc) for P1. The average temperature of clump P1 is 15 K (Sect. 4.3.5.2), leading to a clump mass of $1.2 \times 10^3 M_\odot$ and a mean density of $8.6 \times 10^4\,cm^{-3}$ for P1. For P6, the JCMT image is best fitted with a 2D elliptical Gaussian function with 7 Jy integrated flux in FWHM $43'' \times 23''$ (0.75×0.4 pc). Similarly, we obtain a clump mass of $9.3 \times 10^2 M_\odot$ and a mean density of $7.6 \times 10^4\,cm^{-3}$. On core scale, we fit the SMA 1.3 mm image shown in Fig. 4.2b, e and compute core masses 10–$92 M_\odot$ and average core density $7.5 \times 10^6\,cm^{-3}$. Calculated temperature and density on both scales, as well as the corresponding Jeans mass and length, are tabulated in Table 4.6. In this section we

Table 4.6 Hierarchical fragmentation in P1 and P6

Fragmentation level[a]	T[b] (K)	n (cm^{-3})	M_{Jeans} ($M_\odot$)	λ_{Jeans} (10^{-2} pc)	M_{frag}[c] ($M_\odot$)	λ_{frag}[c] (10^{-2} pc)
Clump→cores	15	8.0×10^4	1.8	9.0	10–92	7.5–14
Core→ condensations	10–25	7.5×10^6	0.1–0.4	0.8–1.2	1.9–27.9	1.6–8.3

[a] Listed are average or range of properties measured in all the clumps, cores, or condensations. The clump properties are measured from JCMT data, and others from SMA data
[b] Coupled dust and gas temperature estimated from multiple NH_3 lines, see Sect. 4.3.5.2
[c] Observed mass/separation of/between "fragments" (core or condensation)

compare the observational results with theoretical predictions of Jeans fragmentation and cylindrical fragmentation, which are summarized in Fig. 4.8.

4.4.1.1 Jeans Fragmentation

If the fragmentation is governed by Jeans instability, the initially homogeneous gas characterized by particle density n (or equivalently, mass density ρ)[6] and temperature T has a Jeans length of

$$\lambda_J = c_s \left(\frac{\pi}{G\rho}\right)^{1/2} = 0.066\,\mathrm{pc} \left(\frac{T}{10\,\mathrm{K}}\right)^{1/2} \left(\frac{n}{10^5\,\mathrm{cm}^{-3}}\right)^{-1/2}, \tag{4.2}$$

where G is the gravitational constant, and $c_s = \sqrt{\frac{kT}{\mu m_H}}$ is the speed of sound at temperature T. The Jeans mass is the gas mass contained in a sphere with an radius of $\lambda_J/2$:

$$M_J = \frac{\pi^{5/2} c_s^3}{6\sqrt{G^3\rho}} = 0.877\,M_\odot \left(\frac{T}{10\,\mathrm{K}}\right)^{3/2} \left(\frac{n}{10^5\,\mathrm{cm}^{-3}}\right)^{-1/2}, \tag{4.3}$$

In the above two equations, the sound speed c_s represents pressure from thermal motions. Massive clumps often contain non-thermal motions likely dominated by micro turbulence. If the internal pressure of the gas is dominated by turbulence, then c_s is replaced by the turbulent linewidth which is well approximated by the velocity dispersion measured from dense gas tracers like NH_3. As Table 4.6 shows, at both fragmentation levels (clump or core), the masses of the observed "fragments" (core or condensation, respectively) are consistent with the prediction of Jeans fragmentation

[6] Particle number density n and mass density ρ are related as $\rho = \mu m_H n$, where $\mu = 2.37$ is the mean molecular weight per "free particle" (H_2 and He, the number of metal particles is negligible). We use particle number density throughout this chapter. Note this is different to the H_2 number density which counts hydrogen molecules only and thus a higher molecular weight of 2.8 should be applied. See discussion in Kauffmann et al. (2008). For a molecular cloud made with $N(H)/N(He) = 10$ and negligible metals, $n_{particle} : n_{H_2} = 1.2$.

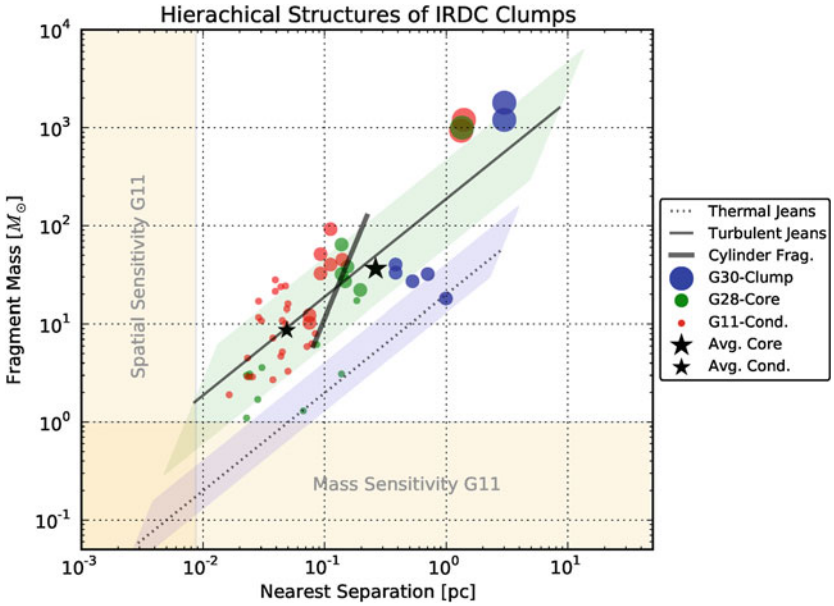

Fig. 4.8 Fragment mass versus projected separation to the nearest fellow fragment. *Circles* filled with various sizes denote clump, core, and condensation. Sources are color coded as G11.11-P1 and G11.11-P6 (G11, *red*; this chapter; Wang et al. 2014; Wang and Zhang 2014), G28.34-P1 (G28, *green*; Chap. 3; Wang et al. 2011, 2012), G30.88-C1 and G30.88-C2 (G30, *blue*; Chap. 5; Zhang and Wang 2011). The *orange shaded regions* show the sensitivity and resolution limit of the G11 observations. The *stars* denote average observed properties of all the cores or condensations. The *dotted line* shows thermal Jeans fragmentation with $T = 15\,\mathrm{K}$ and $n = [10^2, 10^8]\,\mathrm{cm}^{-3}$, and the *blue shaded region* corresponds to the same density range but with $T = [10, 30]\,\mathrm{K}$. The *thin solid line* shows turbulent Jeans fragmentation with $\sigma = 0.7\,\mathrm{km\,s}^{-1}$ and the same density range, and the *green shaded region* corresponds to the same density range but with $\sigma = [0.4, 1.1]\ \mathrm{km\,s}^{-1}$. The *thick solid line* shows cylinder fragmentation with central density $n_c = 3.75 \times 10^6\,\mathrm{cm}^{-3}$ and $\sigma = [0.4, 1.1]\ \mathrm{km\,s}^{-1}$. This figure shows clearly that the fragmentation from clump to cores and from core to condensations are dominated by turbulence over thermal pressure. See text in Sect. 4.4.1 for discussion [*Credit* Wang et al. (2014), reproduced with permission © the authors]

only if we account for the turbulent pressure; otherwise, thermal pressure alone predicts much smaller fragment mass. This suggests that turbulence dominates over thermal pressure in the hierarchical fragmentation, the same as we found in IRDC clump G28.34-P1 (Wang et al. 2011), and in contrast to low-mass star formation regions (Lada et al. 2008).

4.4.1.2 Cylindrical Fragmentation

Similar to the case of G28.34-P1, the cores in G11.11-P6 and perhaps also in G11.11-P1 appear to be regularly spaced along a "cylinder", although these "cylinders" are

not straight. The so-called "sausage instability" of a gas cylinder has been suggested to explain such fragmentation, as first proposed by Chandrasekhar and Fermi (1953) and followed up by many others (e.g., Ostriker 1964; Nagasawa 1987; Bastien et al. 1991; Inutsuka and Miyama 1992; Fischera and Martin 2012; see also discussion in Jackson et al. 2010 and Wang et al. 2011). In an isothermal gas cylinder, self gravity overcomes internal pressure (represented by σ) once the mass per unit length along the cylinder (or linear mass density) exceeds a critical value of

$$(M/l)_{\rm crit} = 2\sigma^2/G = 465 \left(\frac{\sigma}{1\,{\rm km\,s^{-1}}}\right)^2 M_\odot\,{\rm pc^{-1}}. \tag{4.4}$$

Under this condition, the cylinder becomes gravitationally unstable and fragments into a chain of equally spaced fragments with a typical spacing of

$$\lambda_{\rm cl} = 22v(4\pi G\rho_c)^{-1/2} = 1.24\,{\rm pc}\left(\frac{\sigma}{1\,{\rm km\,s^{-1}}}\right)\left(\frac{n_c}{10^5\,{\rm cm^{-3}}}\right)^{-1/2}. \tag{4.5}$$

In the above two equations, ρ_c or n_c is the gas density at the centre of the cylinder. The fragment mass is therefore

$$M_{\rm cl} = (M/l)_{\rm crit} \times \lambda = 575.3 M_\odot \left(\frac{\sigma}{1\,{\rm km\,s^{-1}}}\right)^3 \left(\frac{n_c}{10^5\,{\rm cm^{-3}}}\right)^{-1/2}. \tag{4.6}$$

Similarly, if the cylinder is supported by thermal pressure, σ is the sound speed $c_{\rm s}$; if, on the other hand, it is mainly supported by turbulent pressure, then σ is replaced by the velocity dispersion.

Assuming the initial temperature of the cylinder that represents clumps P1 and P6 is the average clump temperature (15 K), then the corresponding sound speed is $c_s = 0.23\,{\rm km\,s^{-1}}$, while the average velocity dispersion is $\sigma \sim 0.7\,{\rm km\,s^{-1}}$. According to Eq. 4.4 these lead to a linear mass density of $298\,M_\odot\,{\rm pc^{-1}}$ for turbulence support which is in agreement with the observed core masses in P1 and P6, while for thermal support this value becomes $25\,M_\odot\,{\rm pc^{-1}}$, inconsistent with the observations. On the other hand, the projected separations of the cores are 0.08–0.14 pc (Table 4.6). We estimate the central density of the cylinder on the verge of collapse to be the average of the clump density and core density, which amounts to $n = 3.75 \times 10^6 {\rm cm^{-3}}$. We calculate a separation of 0.1 pc for turbulent support and 2 pc for thermal support. Clearly the observations favor the former against the latter scenario. On larger scales, taking the entire Snake filament as a cylinder, the mass/separation between the clumps is also consistent with a cylindrical fragmentation. Adopting an average velocity dispersion of $0.7\,{\rm km\,s^{-1}}$ and an initial central density of $1 \times 10^4\,{\rm cm^{-3}}$ (Kainulainen et al. 2013), the predicted clump mass and separation are $624 M_\odot$ and 2.7 pc, in agreement with the measured average values of $1100 M_\odot$ and 3 pc.

Similar turbulence dominated fragmentation and cylindrical collapse have been observed by SMA and JVLA in another IRDC G30.88+0.13 (Fig. 5.1). There, in the

clump G30.88-C2, dust cores SMM2,3,4 lie aligned in a north-south filament also seen in NH_3. The filament may extend further north where an H_2O maser and an NH_3 core coincide with each other (unfortunately this is far beyond the coverage of the SMA observations), and further south to a 24 μm point source. All these features together form a north-south, 1.5 pc filamentary structure. The core mass and separation support a fragmentation and cylindrical collapse similar to G11.11-P1, G11.11-P6, and G28.34-P1.

The fragmentation analysis is summarized in Fig. 4.8. For a given core, we plot its mass against the separation to the nearest core. Similarly, clumps and condensations are also plotted. Fragments in different IRDCs are plotted with different colors: G11.11–0.12 in red, G28.34+0.06 in green, and G30.88+0.13 in blue. The two clumps in G30.88+0.13 overlap completely along the line of sight, and are apparently isolated. We assign a nominal separation of 3 pc (the approximate long axis of the G30.88-C1 filament) for illustration only. The shaded regions represent Jeans mass and length (Eqs. 4.2, 4.3) for a range of physical properties. For thermal Jeans fragmentation (shaded blue), the mass and separation are determined by temperature and density. The adopted temperature range $T = [10, 30]$ K is observed in these IRDCs, and the density $n = [10^2, 10^8]\,\mathrm{cm}^{-3}$ is a wide range representative for molecular clouds to dense condensations. For turbulent Jeans fragmentation (shaded green), the temperature is replaced by the observed velocity dispersion range $\sigma = [0.4, 1.1]\,\mathrm{km\,s}^{-1}$. Overlapped on the shaded regions are lines for a representative temperature (15 K) or an average velocity dispersion ($0.7\,\mathrm{km\,s}^{-1}$). In addition, cylindrical fragmentation (Eqs. 4.5, 4.6) for central density $n_c = 3.75 \times 10^6\,\mathrm{cm}^{-3}$ and $\sigma = [0.4, 1.1]\,\mathrm{km\,s}^{-1}$ is plotted as a thick solid line. We find that most cores and condensations are located within the shaded green region corresponding to the turbulent fragmentation, and the average properties of cores and condensations (denoted by black filled stars) lie almost along the thin solid line. The cores are also well represented by the thick solid line corresponding to cylindrical fragmentation. On the other hand, thermal Jeans fragmentation (shaded blue) predicts much smaller fragment masses than observed. This figure shows that the hierarchical fragmentation observed in these IRDC clumps are the same in nature, i.e., turbulence dominated fragmentation, and furthermore, the fragmentation from the clump to the core scale can be well explained by turbulence supported gravitational collapse of an isothermal cylinder. Our combined SMA and JVLA observations have resolved similar fragmentation and cylindrical collapse in four IRDC clumps that are in different evolutionary stages (Sect. 4.4.4), suggesting that turbulence supported fragmentation is common in the early stages of massive star formation. There is a lack of direct measurements of magnetic fields in IRDC clumps. However, magnetic fields at a few mG levels are reported in protocluster regions such as G31.41 (Girart et al. 2009), indicating the importance of the B field relative to turbulence.

4.4.2 NH_3 *Ortho/Para Ratio*

Following Sect. 4.3.5.1, the enrichment of ortho- over para-NH_3 can be quantitatively quested by comparing the fractional abundance ratio, [ortho/para], or OPR. We estimate the OPR by means of rotational diagram (Turner 1991; Goldsmith and Langer 1999). This technique requires measurement of many transitions so we only apply to P6. Assuming that the NH_3 gas is in local thermaldynamic equilibrium (LTE), all transitions are characterized by a single excitation temperature $T_{\rm rot}$, and the level population follows a Boltzmann distribution,

$$\frac{N_{\rm u}}{g_{\rm u}} = \frac{N_{\rm tot}}{Q_{\rm rot}} \exp\left(\frac{-E_{\rm u}}{kT_{\rm ex}}\right) , \tag{4.7}$$

where $N_{\rm u}$, $E_{\rm u}$, $g_{\rm u}$ are the column density, energy, and total degeneracy, of the upper state respectively, $N_{\rm tot}$ is the total column density summing up all transitions, $Q_{\rm rot}$ is the rotational partition function at $T_{\rm rot}$, and k is the Boltzmann constant. For a given NH_3 (J, K) transition, the total degeneracy $g_{\rm u}$ is a product of rotational and spin degeneracies, $g_{\rm u} \equiv g_{\rm J}\, g_{\rm K}\, g_{\rm I}$, where $g_{\rm J} = 2J + 1$, $g_{\rm K} = 2$ for $K \neq 0$, and $g_{\rm I} = \frac{4}{8}$ for ortho-NH_3 ($K = 3n$), or $g_{\rm I} = \frac{2}{8}$ for para-NH_3 ($K \neq 3n$). Taking the natural logarithm of the above equation leads to

$$\ln\left(\frac{N_{\rm u}}{g_{\rm u}}\right) = \ln\left(\frac{N_{\rm tot}}{Q_{\rm rot}}\right) - \frac{E_{\rm u}}{kT_{\rm ex}} . \tag{4.8}$$

This linear equation is used to construct rotational diagram. Let $\ln\left(\frac{N_{\rm u}}{g_{\rm u}}\right) = a + bE_{\rm u}$, then the slope b is related to the rotational excitation temperature as $T_{\rm rot} = -1/b$, and the intercept a is related to the total column density as $N_{\rm tot} = Q_{\rm rot} e^a$. The OPR is inferred by comparing the observed NH_3 (3,3) intensity to the fitted intensity should OPR equals unity: OPR $= N_{\rm tot}^{\rm obs}/N_{\rm tot}^{\rm fit} = \exp(a^{\rm obs} - a^{\rm fit})$.

As long as the Rayleigh-Jeans approximation ($h\nu \ll kT_{\rm rot}$) holds, and $T_{\rm rot} \gg T_{\rm bg}$, the column density can be computed from the observed intensity:

$$\begin{aligned} N_{\rm u} &= \frac{3k}{8\pi^3 \nu S \mu^2} C_\tau \int T_{\rm B}\, dv \\ &= \frac{7.75 \times 10^{13} {\rm cm}^{-2}}{\nu\,({\rm GHz})} \frac{J(J+1)}{K^2} C_\tau \int T_{\rm B}\, dv\,({\rm K\,km\,s^{-1}}) \end{aligned} \tag{4.9}$$

where ν is the rest frequency of the transition, $\mu = 1.468$ Debye (1 Debye $= 10^{-18}$ esu cm in cgs units) is the dipole moment for NH_3, $S = \frac{K^2}{J(J+1)}$ is the line strength for $(J, K) \rightarrow (J, K)$ transitions, and $C_\tau = \tau/(1 - e^{-\tau})$ is a correction factor for optical depth (Goldsmith and Langer 1999). The optical depth τ is determined by comparing hyperfine line ratios (Ho and Townes 1983; Li et al. 2003). We find transitions (2,2) and higher are optically thin.

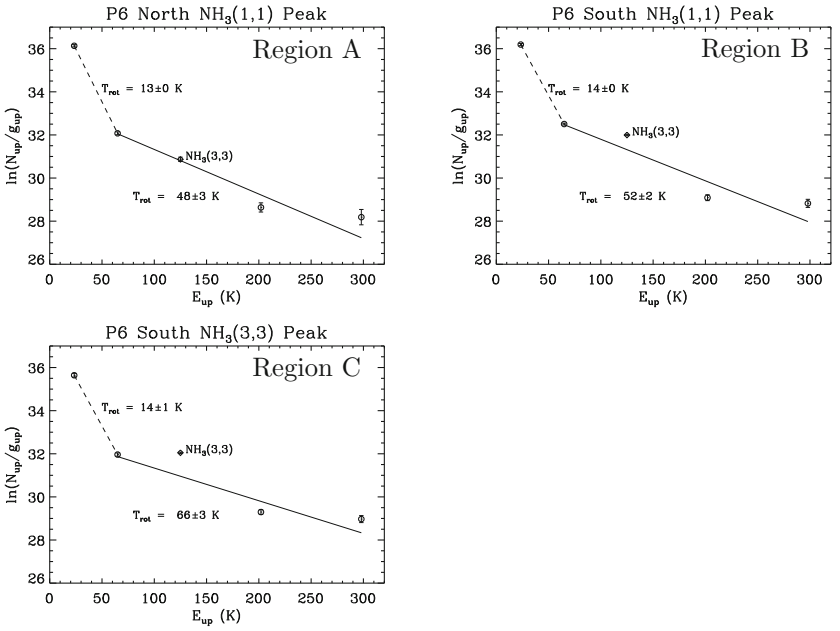

Fig. 4.9 NH_3 rotational diagrams of selected regions in P6 (see locations in Fig. 4.7). The error bars correspond to 1σ in the data points. The data are fitted with two temperature components, one fits (2,2), (4,4), and (5,5) (*solid lines*) and another fits the residual of (1,1) and (2,2) after subtraction from the first fit. The *dashed lines* connect (1,1) and (2,2) emission summed from the two fits. The corresponding rotational temperatures are labelled for each fit. Other fitting results including the column density and OPR are reported in Table 4.7 [*Credit* Wang et al. (2014), reproduced with permission © the authors]

Table 4.7 NH_3 Ortho/Para Ratio (OPR) associated with outflows in P6

Region[a]	OPR	$N_{\rm ortho}$ (10^{16} cm^{-2})	$N_{\rm para}$ (10^{16} cm^{-2})
A	1.1 ± 0.4	1.3 ± 0.6	1.2 ± 0.1
B	2.0 ± 0.4	3.6 ± 0.9	1.8 ± 0.1
C	3.0 ± 0.7	3.3 ± 1.1	1.1 ± 0.1

[a] See locations in Fig. 4.7 and parameter fitting in Fig. 4.9

We make rotational diagrams (Fig. 4.9, Table 4.7) with the outflows in P6 (Sect. 4.3.3.2): the northern NH_3 (1,1) peak (A), the southern NH_3 (1,1) peak (B), and the southern tip of the NH_3 (3,3) emission (C). These regions (labelled in Fig. 4.7) are chosen to (a) have a high signal-to-noise ratio and (b) represent different locations along outflows: region A overlays with the driving source of outflow SMA2, region B is close to SMA6, and region C is farther away but along the direction of outflows SMA5 and SMA6. Integrated NH_3 emission is extracted from a circular region with a diameter of $\sim 7''$, corresponding to the major axis of the largest beam of the NH_3 images. Obviously, the diagrams (Fig. 4.9) cannot

be fitted well with a single temperature because (1,1) traces a lower temperature than other transitions. We fit the diagrams with two temperature components in the following approach: (i) fit one temperature to (2,2), (4,4), (5,5); (ii) subtract the fit from (2,2) and (1,1); and then (iii) fit another temperature to the residual of (1,1) and (2,2). This approach is chosen keeping in mind that emissions from (2,2) and higher transitions are dominated by outflow heating, judging from the broad ling wings. Indeed, the fit to (1,1) and (2,2) results 13–14 K which likely traces the dense envelope, and a fit to (2,2), (4,4), (5,5) results a much higher temperature of 48–66 K due to outflow heating. We assume that NH_3 (3,3) has the same temperature as the second fit, and find OPRs of 1.1 ± 0.4 (A), 2.0 ± 0.4 (B), and 3.0 ± 0.7 (C). The results indicate that (i) ortho-NH_3 is enhanced in all these regions, and (ii) the enhancement increases along the outflow downstream. This is consistent with the idea that NH_3 molecules have been released to gas phase from dust grains by outflow shocks, and that ortho-NH_3 is preferentially desorbed than para-NH_3. The NH_3 (3,3) spectra in P6 and P1 are free of maser lines, so the high OPRs are not due to masing emission. Ammonia OPRs greater than 1.0 (up to 1.6) have been reported in the Galactic centre (Nagayama et al. 2009) and Galactic star formation regions (L1157 and Orion Umemoto et al. 1999; Goddi et al. 2011). Even higher OPRs (>6) have been reported in starburst galaxies (Takano et al. 2002). OPR has also been found to be <1.0 (Faure et al 2013).

It is noteworthy that our analysis has adopted a standard technique used in many similar studies (e.g., Umemoto et al. 1999; Henkel et al. 2000; Mauersberger et al. 2003; Ao et al. 2011), and presents comparable results. Ideally, a more sophisticated approach would require data from transitions up to (6,6) (i.e., including at least two data points from ortho-NH_3) and radiative transfer modelling incorporated with a temperature distribution.

4.4.3 P1-SMA1: An Outflow/Disc System in a Proto-Binary?

The east-west outflow corresponds surprisingly well with the north-south edge-on disc suggested by Pillai et al. (2006b) based on CH_3OH masers. Without direct evidence of outflow, Pillai et al. hypothesized an outflow perpendicular to the disc which is responsible for illuminating the small dust knots seen as three point sources in 2MASS images (Fig. 4.10). Pillai et al. further speculated a geometric orientation of this hypothesized outflow-disc system, see Fig. 4.6 in their paper. Our discovery of the east-west outflow strongly support their suggestion. Moreover, class II CH_3OH masers are exclusively associated with massive young stars (Hill et al. 2005), therefore, M1 provides additional evidence that P1-SMA1 is forming massive star(s).

From the morphology of high velocity SiO emission we locate the outflow driving source to be within the dust condensation P1-SMA1. However, the large scale SiO emission cannot pinpoint the driving source, because P1-SMA1 is closely associated with multiple sources: the CH_3OH maser M1, the H_2O maser W2, the *Herschel* point source, and the SMA dust condensation. The *Herschel* and *Spitzer* images however

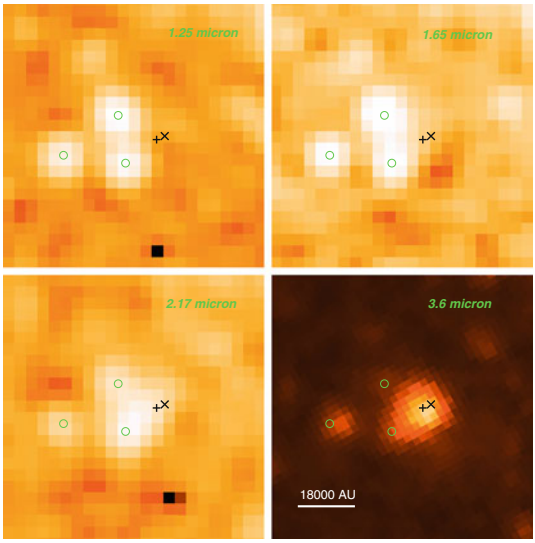

Fig. 4.10 Infrared images of G11.11-P1: 2MASS J, H, K_s bands and *Spitzer* 3.6 μm. Labelled symbols denote H_2O maser W2 (+), class II CH_3OH maser M1 (×), and the three 2MASS point sources (○) [*Credit* Wang et al. (2014), reproduced with permission © the authors]

do not have sufficient resolution to distinguish dust structures associated with M1 and W2. To reach the highest possible resolution with SMA, we make an 880 μm image using only the data from the extended configuration, and obtain a $0''.8 \times 0''.6$ (3,000 × 2,000 AU) synthesis beam. The image is plotted with white contours in Fig. 4.11, in comparison to the masers, the outflow axis, and large scale velocity field from NH_3 (2,2). Surprisingly, P1-SMA1 contains an elongated dust structure, and the major axis of the structure matches the axis of the outflow. The elongated structure has an integrated flux of 76 mJy ($5 M_\odot$ assuming 25 K dust temperature), and is composed of at least two substructures. The eastern feature ($3\,M_\odot$) coincides with W2, and the western feature ($2\,M_\odot$) near M1. Plausibly, these two dust features indicate a proto-binary system with a separation of 2,500 AU. High-mass stars are known to be born mostly as twins (Chini et al. 2011, 2013), and a recent ALMA discovery also suggests a disc associated with a proto-binary system in G35.20-0.74N (Sánchez-Monge et al. 2013), suggesting the multiplicity can be traced back to the embedded phase. It is also possible that one of the dust features is heated by the outflow driven by a protostar embedded in another dust feature.

We discuss two possibilities on the location of the outflow driving source. Possibility I: the driving source is located within the disc traced by the CH_3OH maser spots, therefore coincides with M1. This supports that CH_3OH masers trace disc other than outflow (Pestalozzi et al. 2004). W2 would locate in the blue lobe of the outflow, but its velocity is red-shifted ($37.5\,km\,s^{-1}$; Sect. 4.3.2). Possibility II: the driving source coincides with W2 and the more massive eastern dust feature. The NH_3 velocity field seems to support this scenario since W2 resides closer than M1 to the transition from blue- to red-shifted velocity (Fig. 4.11). In this scenario, M1 traces the red lobe of the outflow (De Buizer 2003; Kurtz et al. 2004), but its velocity range

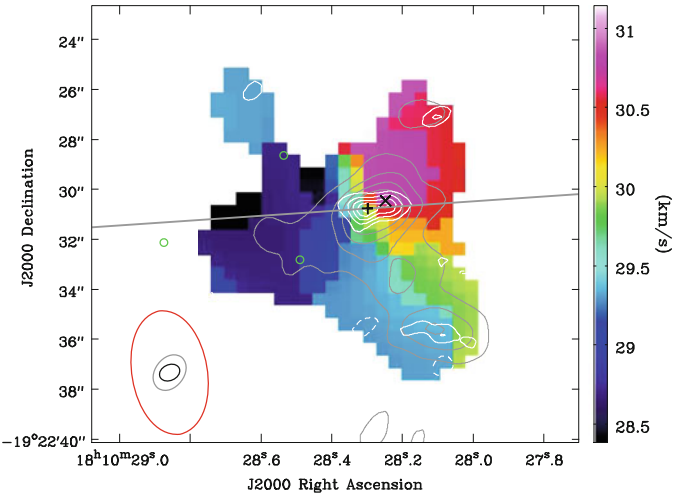

Fig. 4.11 Flux weighted velocity field of NH_3 (2,2). The *grey* contours show the SMA 880 μm continuum image as in Fig. 4.2(c), but contoured by 20 % of the peak (76 mJy) for clarity. The *white* contours show the highest resolution SMA 880 μm image made from the Extended configuration only; the contours are $\pm$ (3, 6, 9, ...) σ, where $\sigma = 1.7$ mJybeam^{-1}. Labelled symbols denote H_2O maser W2 (+), class II CH_3OH maser M1 (×), and the three 2MASS point sources (○). The *ellipses* in the *bottom left corner* represent synthesized beams for the NH_3 image and the two SMA 880 μm images, from the largest to the smallest respectively. The *thick grey line* denotes the SiO outflow as in Fig. 4.3 [*Credit* Wang et al. (2014), reproduced with permission © the authors]

spans blue to red (22–34 km s^{-1}; Sect. 4.3.2), and it becomes difficult to explain the ordered velocity field of M1 that could otherwise perfectly trace a disc (Pillai et al. 2006b). Among all the pieces of evidence, the strongest evidence seems to be the maser spots associated with M1. We therefore regard the possibility I is more likely compared to possibility II. Deep near to far-infrared imaging with higher resolution is needed to pinpoint the driving source, and thereby help further disentangle the controversy about class II methanol masers tracing disc (Pestalozzi et al. 2004) or shocked gas (De Buizer 2003; Kurtz et al. 2004). As far as we see with current data, our results combined with Pillai et al. (2006b) supports the disc scenario.

4.4.4 Evolutionary Sequence

In Sect. 4.3.4 we have seen that the chemical differentiation in cores suggests an evolutionary sequence of the cores. On larger scales, the 1 pc clumps in the Snake appear to be at different evolutionary stages as well. P1 and P6 are the most evolved clumps, where P1 is slightly more advanced than P6. Other clumps appear to be younger. For example, Tackenberg et al. (2012) identified five starless clumps within the Snake nebula. The brightness temperature of the detected lines in P1 and P6

are typically 1–5 K (Fig. 4.5). If G11.11–0.12 were located at the distances of G28.34-P1 or G30.88-C1, the brightness would be 2 or 3 times lower even if the structures are unresolved, whereas in reality the structures within clumps are well resolved by SMA. The sensitivities of the SMA observations (Zhang et al. 2009; Wang et al. 2011; Zhang and Wang 2011) were enough to detect such lines. The fact that previous SMA observations did not detect lines except CO in G28.34-P1 and G30.88-C1 suggest that those clumps are chemically younger than G11.11-P1 and G11.11-P6. In Chap. 6 we infer an evolutionary sequence for all the IRDC clumps based on their observed properties.

4.4.5 Condensation Mass Function

The 23 condensations identified in P1 and P6 are of the size of ∼0.01 pc and mass 2–28 $M_\odot$, subject to form individual stars or a small stellar system. These condensations are equivalent to the structures often used to study "Core Mass Function" (CMF), or the probability density as a function of mass. CMF is converted to the well observed stellar initial mass function (IMF) through star formation process, hence the detailed functional form of CMF is of fundamental importance to discriminate various star formation scenarios. Robust studies of CMF in low-mass case have been carried out based on samples containing hundreds of dense cores (e.g., Alves et al. 2007; André et al. 2010), while in high-mass case the sample is still largely limited by resolving power (see, for example, the study of Beuther and Schilke 2004 based on 24 sources identified in IRAS 19410+2336). In addition, it has been shown that improper binning of the data points (which is often the case in the study of CMF) can introduce significant biases in results (Apellániz and Úbeda 2005).

We use the maximum-likelihood method (Clauset et al. 2007; Swift and Beaumont 2010; Klaus et al. 2011; Alstott et al. 2014) to directly fit the mass spectrum to a given distribution without binning the data. The sample contains 33 condensations in total, including 23 condensations in P1 and P6 and 10 condensations in G28.34-P1 (Wang et al. 2011) with updated masses according to the new temperature (Wang et al. 2012, Chap. 3). We find that the mass spectrum can be fitted with a power law with a slope (in log-log space of dN/dM vs. dM) $\alpha = 2.0 \pm 0.2$ and a turnover at 2.7 $M_\odot$ condensation mass. Fitting only the 23 condensations in G11.11-P1 and G11.11-P6 yields $\alpha = 1.9 \pm 0.2$ if assuming the same turn over. The slope is consistent with Beuther and Schilke (2004) who obtained $\alpha = 2.5 \pm 0.3$. We caution, however, the mass function cannot be distinguished from a power law with a turnover, or a lognormal distribution. As discussed by Swift and Beaumont (2010), a large sample of hundreds of sources is required for a sophisticated study.

Our result is encouraging yet largely limited to the sample size and the still insufficient resolving power including dynamic range, angular resolution, and sensitivity needed to routinely resolve the smallest structures (e.g., the P1-SMA1 binary system, Sect. 4.4.3). Moreover, P1 and P6 are the most evolved clumps in the Snake. A deep view of the entire Snake will enable a complete census of individual

condensations to thoroughly study the form of CMF. The newly inaugurated ALMA is now capable of resolving a large number of similar condensations with a high dynamic range, therefore will enable us to study CMF in high-mass star formation regions with statistical significance. G11.11–0.12 is obviously a well suited region thanks to its youth and complexity.

4.5 Conclusions

We study fragmentation of two massive ($\gtrsim 10^3 M_\odot$), low-luminosity ($\lesssim 10^3 L_\odot$), and dense ($\sim 8\times 10^4\,\mathrm{cm}^{-3}$) molecular clumps P1 and P6, the most likely sites of high-mass star formation in IRDC G11.11–0.12, using high resolution SMA and JVLA observations. The achieved mass sensitivity is better than the Jeans mass at the clump scale, and our main findings are as follows.

(1) High-resolution, high-sensitivity SMA continuum images at 1.3 and 0.88 mm resolve two levels of fragmentation in both P1 and P6: the clump fragments into 6 dense cores, some of which further fragment into even smaller condensations. While the clump fragmentation is consistent with a cylindrical collapse, the masses of the dust cores and condensations are much larger than the respective thermal Jeans masses. This is similar to what was found in IRDC clumps G28.34-P1 and G30.88-C2, suggesting that turbulence supported fragmentation is common in the initial stages of massive star formation.
(2) Molecular outflows, masers, shocked NH_3 emission, as well as hot core lines and mid-IR point sources all indicate active ongoing star formation in cores P1-SMA1,2 and P6-SMA6,2,5. The discovery of an east-west outflow associated with P1-SMA1, together with previous studies, points to an outflow-disc system. A close-up view of the system further suggests a possible proto-binary system, which deserves further study with better resolution.
(3) Enrichment of ortho-NH_3 is found associated with all the three identified outflows in clump P6, and the enrichment tends to increases along the outflow downstream. The derived ortho/para abundance ratios are 1.1 ± 0.4, 2.0 ± 0.4, and 3.0 ± 0.7, among the largest OPRs ever observed in Galactic star formation regions while less than that in starburst galaxies, although observations of even higher transitions are needed to confirm the high ratios.
(4) Chemical differentiation between cores suggests variations in evolutionary stages among the cores. This effect is also seen at smaller scales down to condensations, and to larger scales up to clumps. Accordingly, an evolutionary sequence is inferred for cores and clumps, respectively.
(5) With a detection limit of 1–3.5 $M_\odot$, we identify 23 condensations that are subject to form individual stars or a small stellar system. The mass spectrum of these condensations is consistent with a powerlaw with a slope of $\alpha = 2.0 \pm 0.2$ and a turnover at $2.7 M_\odot$ condensation mass. Deeper images with improved resolving

power toward all the six clumps in the Snake will reveal a complete census of individual condensations for a robust study of the CMF.

References

Aguirre, J.E., Ginsburg, A.G., Dunham, M.K., Drosback, M.M., Bally, J., Battersby, C., Bradley, E.T., Cyganowski, C., Dowell, D., Evans NJ II, Glenn, J., Harvey, P., Rosolowsky, E., Stringfellow, G.S., Walawender, J., Williams, J.P.: The bolocam galactic plane survey: survey description and data reduction. Astrophys. J. Suppl. **192**(4), (2011). doi:10.1088/0067-0049/192/1/4, arXiv:1011.0691

Alstott, J., Bullmore, E., Plenz, D.: Powerlaw: a Python package for analysis of heavy-tailed distributions. PLoS ONE **9**, 85777 (2014) ArXiv e-prints 1305.0215. doi:10.1371/journal.pone.0085777

Alves J, Lombardi M, Lada CJ (2007) The mass function of dense molecular cores and the origin of the IMF. Astron. Astrophys. **462**, L17–L21, doi:DOIurl10.1051/0004-6361:20066389, arXiv:astro-ph/0612126

André, P., Men'shchikov, A., Bontemps, S., Könyves, V., Motte, F., Schneider, N., Didelon, P., Minier, V., Saraceno, P., Ward-Thompson, D., di Francesco, J., White, G., Molinari, S., Testi, L., Abergel, A., Griffin, M., Henning, T., Royer, P., Merín, B., Vavrek, R., Attard, M., Arzoumanian, D., Wilson, CD., Ade, P., Aussel, H., Baluteau, J., Benedettini, M., Bernard, J., Blommaert, J.A.D.L., Cambrésy, L., Cox, P., di Giorgio, A., Hargrave, P., Hennemann, M., Huang, M., Kirk, J., Krause, O., Launhardt, R., Leeks, S., Le Pennec, J., Li, J.Z., Martin, P.G., Maury, A., Olofsson, G., Omont, A., Peretto, N., Pezzuto, S., Prusti, T., Roussel, H., Russeil, D., Sauvage, M., Sibthorpe, B., Sicilia-Aguilar, A., Spinoglio, L., Waelkens, C., Woodcraft, A., Zavagno, A.: From filamentary clouds to prestellar cores to the stellar IMF: initial highlights from the Herschel Gould belt survey. Astron. Astrophys. **518**, L102+ (2010). doi:10.1051/0004-6361/201014666, 1005.2618

Ao, Y., Henkel, C., Braatz, J.A., Weiß, A., Menten, K.M., Mühle, S.: Ammonia (J, K) = (1,1) to (4,4) and (6,6) inversion lines detected in the Seyfert 2 galaxy NGC 1068. Astron. Astrophys. **529**, A154 (2011). doi:10.1051/0004-6361/201116595, 1104.1124

Bastien, P., Arcoragi, J.P., Benz, W., Bonnell, I., Martel, H.: Fragmentation of elongated cylindrical clouds. I—Isothermal clouds. Astrophys. J. **378**, 255–265 (1991). doi:10.1086/170424

Beuther, H., Henning, T.: Multiple low-turbulence starless cores associated with intermediate- to high-mass star formation. Astron. Astrophys. **503**, 859–867 (2009). doi:10.1051/0004-6361/200912036, 0907.4565

Beuther, H., Linz, H., Tackenberg, J., Henning, T., Krause, O., Ragan, S., Nielbock, M., Launhardt, R., Bihr, S., Schmiedeke, A., Smith, R., Sakai, T.: Fragmentation and dynamical collapse of the starless high-mass star-forming region IRDC 18310-4. Astron. Astrophys. **553**, A115 (2013). doi:10.1051/0004-6361/201220475, 1304.6820

Beuther, H., Schilke, P., Sridharan, T.K., Menten, K.M., Walmsley, C.M., Wyrowski, F.: Massive molecular outflows. Astron. Astrophys. **383**, 892–904 (2002). doi:10.1051/0004-6361:20011808, arXiv:astro-ph/0110372

Beuther, H., Schilke, P.: Fragmentation in massivestar formation. Science. **303** 1167–1169 (2004). doi:10.1126/science.1094014, arXiv:astro-ph/0402501

Bontemps, S., Andre, P., Terebey, S., Cabrit, S.: Evolution of outflow activity around low-mass embedded young stellar objects. Astron. Astrophys. **311**, 858–872 (1996)

Busquet, G., Zhang, Q., Palau, A., Liu, H.B., Sánchez-Monge, Á., Estalella, R., Ho, PTP., de Gregorio-Monsalvo, I., Pillai, T., Wyrowski, F., Girart, J.M., Santos, F.P., Franco, G.A.P.: Unveiling a network of parallel filaments in the infrared dark cloud G14.225-0.506. Astrophys. J. Lett. **764**, L26 (2013). doi:10.1088/2041-8205/764/2/L26, 1212.5917

Busquet. G., Palau, A., Estalella, R., Girart, J.M., Sánchez-Monge, Á., Viti, S., Ho, P.T.P., Zhang, Q.: The NH_2D/NH_3 ratio toward pre-protostellar cores around the UC H II region in IRAS 20293+3952. Astron. Astrophys. **517**, L6 (2010). doi:10.1051/0004-6361/201014866, 1006.4280

Carey, S.J., Clark, F.O., Egan, M.P., Price, S.D., Shipman, R.F., Kuchar, T.A.: The physical properties of the midcourse space experiment galactic infrared-dark clouds. Astrophys. J. **508**, 721–728 (1998). doi:10.1086/306438

Carey, S.J., Feldman, P.A., Redman, R.O., Egan, M.P., MacLeod, J.M., Price, S.D.: Submillimeter observations of midcourse space experiment galactic infrared-dark clouds. Astrophys. J. Lett. **543**, L157–L161 (2000). doi:10.1086/317270

Carey, S.J., Noriega-Crespo, A., Mizuno, D.R., Shenoy, S., Paladini, R., Kraemer, K.E., Price, S.D., Flagey, N., Ryan, E., Ingalls, J.G., Kuchar, T.A., Pinheiro Gonçalves, D., Indebetouw, R., Billot, N., Marleau, F.R., Padgett, D.L., Rebull, L.M., Bressert, E., Ali, B., Molinari, S., Martin, P.G., Berriman, G.B., Boulanger, F., Latter, W.B., Miville-Deschenes, M.A., Shipman, R., Testi, L.: MIPSGAL: A survey of the inner galactic plane at 24 and 70 μm. Publ. ASP **121**, 76–97 (2009). doi:10.1086/596581

Cesaroni, R.: Hot molecular cores. In: Cesaroni, R., Felli, M., Churchwell, E., Walmsley, M. (eds.) Massive Star Birth: A Crossroads of Astrophysics, IAU Symposium, vol. 227, pp. 59–69 (2005). doi:10.1017/S1743921305004369

Chandrasekhar, S., Fermi, E.: Problems of gravitational stability in the presence of a magnetic field. Astrophys. J. **118**, 116 (1953). doi:10.1086/145732

Chini, R., Barr, A., Buda, L.S., Dembsky, T., Drass, H., Nasseri, A., Hoffmeister, V.H., Fuhrmann, K.: The Multiplicity of high-mass stars. Cent. Eur. Astrophys. Bull. **37**, 295–310. (2013). 1306.1811

Chini, R., Nasseri, A., Hoffmeister, V.H., Buda, L.S., Barr, A.: Most high-mass stars are born as twins. In: Schmidtobreick, L., Schreiber, M.R., Tappert, C. (eds.) Evolution of Compact Binaries, Astronomical Society of the Pacific Conference Series, vol. 447, p. 67 (2011)

Churchwell, E., Babler, B.L., Meade, M.R., Whitney, B.A., Benjamin, R., Indebetouw, R., Cyganowski, C., Robitaille, T.P., Povich, M., Watson, C., Bracker, S.: The Spitzer/GLIMPSE surveys: a new view of the milky way. Publ. ASP **121**, 213–230 (2009). doi:10.1086/597811

Clauset, A., Rohilla Shalizi, C., Newman, M.E.J.: Power-law distributions in empirical data (2007) ArXiv e-prints 0706.1062

Cyganowski, C.J., Koda, J., Rosolowsky, E., Towers, S., Donovan Meyer, J., Egusa, F., Momose, R., Robitaille, T.P.: A water maser and NH_3 survey of GLIMPSE extended green objects. Astrophys. J. **764**, 61 (2013). doi:10.1088/0004-637X/764/1/61, 1210.5528

Cyganowski, C.J., Whitney, B.A., Holden, E., Braden, E., Brogan, C.L., Churchwell, E., Indebetouw, R., Watson, D.F., Babler, B.L., Benjamin, R., Gomez, M., Meade, M.R., Povich, M.S., Robitaille, T.P., Watson, C.: A catalog of extended green objects in the GLIMPSE survey: a new sample of massive young stellar object outflow candidates. Astron. J. **136**, 2391–2412 (2008). doi:10.1088/0004-6256/136/6/2391, 0810.0530

Danby, G., Flower, D.R., Valiron, P., Schilke, P., Walmsley, C.M.: A recalibration of the interstellar ammonia thermometer. Mon. Not. Roy. Astron. Soc. **235**, 229–238 (1988)

De Buizer, J.M.: Testing the circumstellar disc hypothesis: a search for H_2 outflow signatures from massive young stellar objects with linearly distributed methanol masers. Mon. Not. R. Astron.Soc. **341**, 277–298 (2003). doi:10.1046/j.1365-8711.2003.06419.x, arXiv:astro-ph/0301445

Devine, K.E., Chandler, C.J., Brogan, C., Churchwell, E., Indebetouw, R., Shirley, Y., Borg, K.J.: Very large array observations of the infrared dark cloud G19.30+0.07. Astrophys. J. **733**, 44 (2011). doi:10.1088/0004-637X/733/1/44, 1103.0328

Egan, M.P., Shipman, R.F., Price, S.D., Carey, S.J., Clark, F.O., Cohen, M.: A population of cold cores in the galactic plane. Astrophys. J. Lett. **494**, L199 (1998). doi:10.1086/311198

Faure, A., Hily-Blant, P., Le Gal, R., Rist, C., Pineau des Forêts, G.: Ortho-para selection rules in the gas-phase chemistry of interstellar ammonia. Astrophys. J. Lett. **770**, L2 (2013). doi:10.1088/2041-8205/770/1/L2

Fischera, J., Martin, P.G.: Physical properties of interstellar filaments. Astron. Astrophys. **542**, A77 (2012). doi:10.1051/0004-6361/201218961, 1204.3608

Girart, J.M., Beltrán, M.T., Zhang, Q., Rao, R., Estalella, R.: Magnetic fields in the formation of massive stars. Science **324**, 1408 (2009). doi:10.1126/science.1171807

Goddi, C., Greenhill, L.J., Humphreys, E.M.L., Chandler, C.J., Matthews, L.D.: Unveiling sources of heating in the vicinity of the orion BN/KL hot core as traced by highly excited inversion transitions of ammonia. Astrophys. J. Lett. **739**, L13 (2011). doi:10.1088/2041-8205/739/1/L13, 1106.4202

Goldsmith, P.F., Langer, W.D.: Population diagram analysis of molecular line emission. Astrophys. J. **225**, 517 (1999). doi:10.1086/307195

Goldsmith, P.F.: Molecular depletion and thermal balance in dark cloud cores. Astrophys. J. **557**, 736–746 (2001). doi:10.1086/322255

Gómez, L., Wyrowski, F., Pillai, T., Leurini, S., Menten, K.M.: High-angular resolution observations of methanol in the infrared dark cloud core G11.11-0.12P1. Astron. Astrophys. **529**, A161 (2011). doi:10.1051/0004-6361/201016315, 1103.1320

Goodman, A.A., Alves, J., Beaumont, C.N., Benjamin, R.A., Borkin, M.A., Burkert, A., Dame, T.M., Jackson, J., Kauffmann, J., Robitaille, T., Smith, R.J.: The Bones of the Milky Way (2014). ArXiv e-prints 1408.0001

Henkel, C., Mauersberger, R., Peck, A.B., Falcke, H., Hagiwara, Y.: Dense gas in nearby galaxies. XIV. Detection of hot ammonia in Maffei 2. Astron. Astrophys. **361**, L45–L48 (2000). arXiv:astro-ph/0010519

Hennebelle, P., Pérault, M., Teyssier, D., Ganesh, S.: Infrared dark clouds from the ISOGAL survey. Constraints on the interstellar extinction curve. Astron. Astrophys. **365**, 598–611 (2001). doi:10.1051/0004-6361:20000052

Hennemann, M., Birkmann, S.M., Krause, O., Lemke, D., Pavlyuchenkov, Y., More, S., Henning, T.: Star-forming cores embedded in a massive cold clump: fragmentation, collapse, and energetic outflows. Astrophys. J. **693**, 1379–1391 (2009). doi:10.1088/0004-637X/693/2/1379, 0812.2187

Henning, T., Linz, H., Krause, O., Ragan, S., Beuther, H., Launhardt, R., Nielbock, M., Vasyunina, T.: The seeds of star formation in the filamentary infrared-dark cloud G011.11-0.12. Astron. Astrophys. **518**, L95+ (2010). doi:10.1051/0004-6361/201014635, 1005.1939

Hildebrand, R.H.: The determination of cloud masses and dust characteristics from submillimetre thermal emission. Q. J. Roy. Astron. Soc. **24**, 267 (1983)

Hill, T., Burton, M.G., Minier, V., Thompson, M.A., Walsh, A.J., Hunt-Cunningham, M., Garay, G.: Millimetre continuum observations of southern massive star formation regions - I. SIMBA observations of cold cores. Mon. Not. Roy. Astron. Soc. **363** 405–451 (2005). doi:10.1111/j.1365-2966.2005.09347.x, arXiv:astro-ph/0506402

Ho, P.T.P., Moran, J.M., Lo, K.Y.: The submillimeter array. Astrophys. J. Lett. **616**, L1–L6 (2004). doi:10.1086/423245, arXiv:astro-ph/0406352

Ho, P.T.P., Townes, C.H.: Interstellar ammonia. Ann. Rev. Astron. Astrophys. **21**, 239–270 (1983). doi:10.1146/annurev.aa.21.090183.001323

Inutsuka, S.I., Miyama, S.M.: Self-similar solutions and the stability of collapsing isothermal filaments. Astrophys. J. **388**, 392–399 (1992). doi:10.1086/171162

Jackson, J.M., Finn, S.C., Chambers, E.T., Rathborne, J.M., Simon, R.: The "Nessie" Nebula: cluster formation in a filamentary infrared dark cloud. Astrophys. J. Lett. **719**, L185–L189 (2010). doi:10.1088/2041-8205/719/2/L185, 1007.5492

Johnstone, D., Fiege, J.D., Redman, R.O., Feldman, P.A., Carey, S.J.: The G11.11-0.12 infrared-dark cloud: anomalous dust and a nonmagnetic isothermal model. Astrophys J. Lett. **588**, L37–L40 (2003). doi:10.1086/375524, arXiv:astro-ph/0303651

Juvela, M., Ysard, N.: The effect of temperature mixing on the observable (T, β)-relation of interstellar dust clouds. Astron. Astrophys. **539**, A71 (2012). doi:10.1051/0004-6361/201118258, 1201.4356

Kainulainen, J., Ragan, S.E., Henning, T., Stutz, A.: High-fidelity view of the structure and fragmentation of the high-mass, filamentary IRDC G11.11-0.12. Astron. Astrophys. **557**, A120 (2013). doi:10.1051/0004-6361/201321760, 1305.6383

Kauffmann, J., Bertoldi, F., Bourke, T.L., Evans N.J II, Lee, C.W.: MAMBO mapping of spitzer c2d small clouds and cores. Astron. Astrophys. **487**, 993–1017 (2008). doi:10.1051/0004-6361:200809481, 0805.4205

Klaus, A., Yu, S., Plenz, D.: Statistical analyses support power law distributions found in neuronal avalanches. PLoS ONE **6**(19), 779 (2011)

Kurtz, S., Hofner, P., Álvarez, C.V.: A catalog of CH_3OH 7_0-6_1 A^+ maser sources in massive star-forming regions. Astrophys. J. Suppl. **155**, 149–165 (2004). doi:10.1086/423956

Lada, C,J., Muench, A.A., Rathborne, J., Alves, J.F., Lombardi, M.: The nature of the dense core population in the pipe nebula: thermal cores under pressure. Astrophys. J. **672**, 410–422 (2008). doi:10.1086/523837, 0709.1164

Lee, K., Looney, L.W., Schnee, S., Li, Z.Y.: Earliest stages of protocluster formation: substructure and kinematics of starless cores in orion. Astrophys. J. **772**, 100 (2013). doi:10.1088/0004-637X/772/2/100, 1306.6716

Leurini, S., Schilke, P., Wyrowski, F., Menten, K.M.: Methanol as a diagnostic tool of interstellar clouds. II. Modelling high-mass protostellar objects. Astron. Astrophys. **466**, 215–228 (2007). doi:10.1051/0004-6361:20054245

Li, D., Goldsmith, P.F., Menten, K.: Massive quiescent cores in orion. I. Temperature structure. Astrophys. J. **587**, 262–277 (2003). doi:10.1086/368078, arXiv:astro-ph/0301060

Longmore, S.N., Pillai, T., Keto, E., Zhang, Q., Qiu, K.: Is protostellar heating sufficient to halt fragmentation? A case study of the massive protocluster G8.68-0.37. Astrophys. J. **726**, 97, (2011). doi:10.1088/0004-637X/726/2/97, 1011.1442

Apellániz, J.M., Úbeda, L.: Numerical biases on initial mass function determinations created by binning. Astrophys. J. **629**, 873–880 (2005). doi:10.1086/431458, 0505012

Mauersberger, R., Henkel, C., Weiß, A., Peck, A.B., Hagiwara, Y.: Dense gas in nearby galaxies. XV. Hot ammonia in NGC 253, Maffei 2 and IC 342. Astron. Astrophys. **403**, 561–571 (2003). doi:10.1051/0004-6361:20030386, arXiv:astro-ph/0303247

Molinari, S., Swinyard, B., Bally, J., Barlow, M., Bernard, J.P., Martin, P., Moore, T., Noriega-Crespo, A., Plume, R., Testi, L., Zavagno, A., Abergel, A., Ali, B., André, P., Baluteau, J.P., Benedettini, M., Berné, O., Billot, N.P., Blommaert, J., Bontemps, S., Boulanger, F., Brand, J., Brunt, C., Burton, M., Campeggio, L., Carey, S., Caselli, P., Cesaroni, R., Cernicharo, J., Chakrabarti, S., Chrysostomou, A., Codella, C., Cohen, M., Compiegne, M., Davis, C.J., de Bernardis, P., de Gasperis, G., Di Francesco. J., di Giorgio, A.M., Elia, D., Faustini, F., Fischera, J.F., Fukui, Y., Fuller, G.A., Ganga, K., Garcia-Lario, P., Giard, M., Giardino, G., Glenn, J., Goldsmith, P., Griffin, M., Hoare, M., Huang, M., Jiang, B., Joblin, C., Joncas, G., Juvela, M., Kirk, J., Lagache, G., Li, J.Z., Lim. T.L., Lord, S.D., Lucas, P.W., Maiolo, B., Marengo, M., Marshall, D., Masi, S., Massi, F., Matsuura. M., Meny, C., Minier, V., Miville-Deschênes, M.A,, Montier, L., Motte, F., Müller, T.G., Natoli, P., Neves, J., Olmi, L., Paladini, R., Paradis, D., Pestalozzi, M., Pezzuto, S., Piacentini, F., Pomarès, M., Popescu, C.C., Reach, W.T., Richer, J., Ristorcelli, I., Roy, A., Royer, P., Russeil, D., Saraceno, P., Sauvage, M., Schilke, P., Schneider-Bontemps, N., Schuller, F., Schultz, B., Shepherd, D.S., Sibthorpe, B., Smith, H.A., Smith, M.D., Spinoglio, L., Stamatellos, D., Strafella, F., Stringfellow, G., Sturm, E., Taylor, R., Thompson, M.A., Tuffs, R.J., Umana, G., Valenziano, L., Vavrek, R., Viti, S., Waelkens, C., Ward-Thompson, D., White, G., Wyrowski. F., Yorke. H.W, Zhang, Q.: Hi-GAL: the herschel infrared galactic plane survey. Publ. ASP **122**, 314–325 (2010). doi:10.1086/651314, 1001.2106

Myers, P.C.: Filamentary structure of star-forming complexes. Astrophys. J. **700**, 1609–1625 (2009). doi:10.1088/0004-637X/700/2/1609, 0906.2005

Nagasawa, M.: Gravitational instability of the isothermal gas cylinder with an axial magnetic field. Prog. Theoret. Phys. **77**, 635–652 (1987). doi:10.1143/PTP.77.635

Nagayama, T., Omodaka, T., Handa, T., Toujima, H., Sofue, Y., Sawada, T., Kobayashi, H., Koyama, Y.: NH_3 in the galactic center is formed under cool conditio. Publ. ASJ **61**, 1023- (2009). 0906.0227

Nicholas, B., Rowell, G., Burton, M.G., Walsh, A., Fukui, Y., Kawamura, A., Longmore, S., Keto, E.: 12 mm line survey of the dense molecular gas towards the W28 field TeV gamma-ray sources. Mon. Not. Roy. Astron. Soc. **411**, 1367–1385, (2011). doi:10.1111/j.1365-2966.2010.17778.x, 1009.4745

Ostriker, J.: The equilibrium of polytropic and isothermal cylinders. Astrophys. J. **140**, 1056 (1964). doi:10.1086/148005

Palau, A., Fuente, A., Girart, J.M., Estalella, R., Ho, PTP., Sánchez-Monge , Á., Fontani, F., Busquet, G., Commerçon, B., Hennebelle, P., Boissier, J., Zhang, Q., Cesaroni, R., Zapata, L.A.: Early stages of cluster formation: fragmentation of massive dense cores down to $\lesssim$1000 AU. Astrophys. J. **762**, 120 (2013). doi:10.1088/0004-637X/762/2/120, 1211.2666

Perault, M., Omont, A., Simon, G., Seguin, P., Ojha, D., Blommaert, J., Felli, M., Gilmore, G., Guglielmo, F., Habing, H., Price, S., Robin, A., de Batz, B., Cesarsky, C., Elbaz, D., Epchtein, N., Fouque, P., Guest, S., Levine, D., Pollock, A., Prusti, T., Siebenmorgen, R., Testi, L., Tiphene, D.: First ISOCAM images of the milky way. Astron. Astrophys. **315**, L165–L168 (1996)

Peretto, N., Fuller, G.A.: The initial conditions of stellar protocluster formation. I. A catalogue of spitzer dark clouds. Astron. Astrophys. **505**, 405–415, (2009). doi:10.1051/0004-6361/200912127, 0906.3493

Pestalozzi, M.R., Elitzur, M., Conway, J.E., Booth, R.S.: A circumstellar disk in a high-mass star-forming region. Astrophys. J. Lett. **603**, L113–L116 (2004)

Petry, D., CASA Development Team.: Analysing ALMA data with CASA. In: Ballester, P., Egret, D., Lorente, N.P.F. (eds.) Astronomical Data Analysis Software and Systems XXI, Astronomical Society of the Pacific Conference Series, vol. 461, p. 849 (2012). 1201.3454

Pillai, T., Kauffmann, J., Wyrowski, F., Hatchell, J., Gibb, A.G., Thompson, M.A.: Probing the initial conditions of high-mass star formation. II. Fragmentation, stability, and chemistry towards high-mass star-forming regions G29.96-0.02 and G35.20-1.74. Astron. Astrophys. **530**, A118 (2011). doi:10.1051/0004-6361/201015899, 1105.0004

Pillai, T., Wyrowski, F., Carey, S.J., Menten, K.M.: Ammonia in infrared dark clouds. Astron. Astrophys. **450**, 569–583 (2006a). doi:10.1051/0004-6361:20054128, arXiv:astro-ph/0601078

Pillai, T., Wyrowski, F., Menten, K.M., Krügel, E.: High mass star formation in the infrared dark cloud G11.11-0.12. Astron. Astrophys. 447:929–936 (2006b). doi:10.1051/0004-6361:20042145, arXiv:astro-ph/0510622

Ragan, S.E., Bergin, E.A., Wilner, D.: Very large array observations of ammonia in infrared-dark clouds. I. Column density and temperature structure. Astrophys. J. **736**, 163 (2011). doi:10.1088/0004-637X/736/2/163, 1105.4182

Ragan, S.E., Heitsch, F., Bergin, E.A., Wilner, D.: Very large array observations of ammonia in infrared-dark clouds. II. Internal kinematics. Astrophys. J. **746**, 174 (2012b). doi:10.1088/0004-637X/746/2/174, 1201.1402

Ragan, S., Henning, T., Krause, O., Pitann, J., Beuther, H., Linz, H., Tackenberg, J., Balog, Z., Hennemann, M., Launhardt, R., Lippok, N., Nielbock, M., Schmiedeke, A., Schuller, F., Steinacker, J., Stutz, A., Vasyunina, T.: The earliest phases of star formation (EPoS): a Herschel key program. The precursors to high-mass stars and clusters. Astron. Astrophys. **547**, A49 (2012a). doi:10.1051/0004-6361/201219232, 1207.6518

Rathborne, J.M., Jackson, J.M., Zhang, Q., Simon, R.: Submillimeter array observations of infrared dark clouds: A tale of two cores. Astrophys. J. **689**, 1141–1149 (2008). doi:10.1086/592733, 0808.2973

Rathborne, J.M., Simon, R., Jackson, J.M.: The detection of protostellar condensations in infrared dark cloud cores. Astrophys. J. **662**, 1082–1092 (2007). doi:10.1086/513178

Rosolowsky, E., Dunham, M.K., Ginsburg, A., Bradley, E.T., Aguirre. J., Bally, J., Battersby, C., Cyganowski, C., Dowell, D., Drosback, M., Evans, N.J. II, Glenn, J., Harvey, P., Stringfellow,

G.S., Walawender, J., Williams, J.P.: The bolocam galactic plane survey. II. Catalog of the image data. Astrophys. J. Suppl. **188**, 123 (2010). doi:10.1088/0067-0049/188/1/123, 0909.2871

Rosolowsky, E.W, Pineda, J.E, Foster, J.B, Borkin, M.A, Kauffmann, J., Caselli, P., Myers, P.C., Goodman, A.A.: An ammonia spectral atlas of dense cores in perseus. Astrophys. J. Suppl. **175**, 509–521 (2008). doi:10.1086/524299, 0711.0231

Sánchez-Monge, Á., Cesaroni, R., Beltrán, M.T., Kumar, M.S.N., Stanke, T., Zinnecker, H., Etoka, S., Galli, D., Hummel, C.A., Moscadelli, L., Preibisch, T., Ratzka, T., van der Tak, F.F.S., Vig, S., Walmsley, C,M., Wang, K.S.: A candidate circumbinary keplerian disk in G35.20-0.74 N: a study with ALMA. Astron. Astrophys. **552**, L10 (2013). doi:10.1051/0004-6361/201321134, 1303.4242

Sanhueza, P., Jackson, J.M., Foster, J.B., Garay, G., Silva, A., Finn, S.C.: Chemistry in infrared dark cloud clumps: a molecular line survey at 3 mm. Astrophys. J. **756**, 60 (2012). doi:10.1088/0004-637X/756/1/60, 1206.6500

Sault, R.J., Teuben, P.J., Wright, M.C.H.: A retrospective view of MIRIAD. In: Shaw, RA., Payne, H.E., Hayes, J.J.E. (eds.) Astronomical Data Analysis Software and Systems IV, Astronomical Society of the Pacific Conference Series, vol. 77, p. 433 (1995). arXiv:astro-ph/0612759

Schuller, F., Menten, K.M., Contreras, Y., Wyrowski, F., Schilke, P., Bronfman, L., Henning, T., Walmsley., C.M., Beuther, H., Bontemps, S., Cesaroni, R., Deharveng, L., Garay, G., Herpin, F., Lefloch, B., Linz, H., Mardones, D., Minier, V., Molinari, S., Motte, F., Nyman, L.A., Reveret, V., Risacher, C., Russeil, D., Schneider, N., Testi, L., Troost, T., Vasyunina, T., Wienen, M., Zavagno, A., Kovacs, A., Kreysa, E., Siringo, G., Weiß, A.: ATLASGAL—The APEX telescope large area survey of the galaxy at 870 μm. Astron. Astrophys. **504**, 415–427 (2009). doi:10.1051/0004-6361/200811568, 0903.1369

Semel, M., Ramírez Vélez, J.C., Martínez González, M.J., Asensio Ramos, A., Stift, M.J., López Ariste, A., Leone, F.: Multiline zeeman signatures through line addition. Astron. Astrophys. **504**, 1003–1009 (2009). doi:10.1051/0004-6361/200810428, 0906.4226

Simon, R., Jackson, J.M., Rathborne, J.M., Chambers, E.T.: A catalog of midcourse space experiment infrared dark cloud candidates. Astrophys. J. **639**, 227–236 (2006a). doi:10.1086/499342, arXiv:astro-ph/0511079

Simon, R., Rathborne, J.M., Shah, R.Y., Jackson, J.M., Chambers, E.T.: The characterization and galactic distribution of infrared dark clouds. Astrophys. J. **653**, 1325–1335 (2006b). doi:10.1086/508915

Swift, J.J., Beaumont, C.N.: Discerning the form of the dense core mass function. Publ. ASP. **122**, 224–230 (2010). doi:10.1086/650398, 0912.0933

Swift, J.J.: Two massive, low-luminosity cores toward infrared dark clouds. Astrophys. J. **705**, 1456–1461 (2009). doi:10.1088/0004-637X/705/2/1456, 0909.4910

Tackenberg, J., Beuther, H., Henning, T., Schuller, F., Wienen, M., Motte, F., Wyrowski, F., Bontemps, S., Bronfman, L., Menten, K., Testi, L., Lefloch, B.: Search for starless clumps in the ATLASGAL survey. Astron. Astrophys. **540**, A113 (2012). doi:10.1051/0004-6361/201117412, 1201.4732

Takano, S., Nakai, N., Kawaguchi, K.: Observations of ammonia in external galaxies I. NGC 253 and M 82. Pub. Astron. Soc. Jpn. **54**, 195–207 (2002)

Turner, B.E.: A molecular line survey of sagittarius B2 and orion-KL from 70 to 115 GHz. II - analysis of the data. Astrophys. J. Suppl. **76**, 617–686 (1991). doi:10.1086/191577

Umemoto, T., Mikami, H., Yamamoto, S., Hirano, N.: The ortho-to-para ratio of ammonia in the L1157 outflow. Astrophys. J. Lett. **525**, L105–L108, (1999). doi:10.1086/312337, arXiv:astro-ph/9909328

Walmsley, C.M., Ungerechts, H.: Ammonia as a molecular cloud thermometer. Astron. Astrophys. **122**, 164–170 (1983)

Wang, K., Wu, Y.F., Ran, L., Yu, W.T., Miller, M.: The relation between ^{13}CO J = 2–1 line width in molecular clouds and bolometric luminosity of associated IRAS sources. Astron. Astrophys. **507**, 369–376 (2009). doi:10.1051/0004-6361/200811104, 0909.3312

Wang, K., Zhang ,Q., Wu, Y., Li, H.b., Zhang, H.: Protostellar outflow heating in a growing massive protocluster. Astrophys. J. Lett. **745**, L30 (2012). doi:10.1088/2041-8205/745/2/L30, 1112.1885

Wang, Y., Zhang, Q., Pillai, T., Wyrowski, F., Wu, Y.: NH_3 observations of the infrared dark cloud G28.34+0.06. Astrophys. J. Lett. **672**, L33–L36 (2008). doi:10.1086/524949, 0711.1999

Wang, K., Zhang, Q., Testi, L., Tak, Fvd., Wu, Y., Zhang, H., Pillai, T., Wyrowski, F., Carey, S., Ragan, S.E., Henning, T.: Hierarchical fragmentation and differential star formation in the Galactic 'Snake': infrared dark cloud G11.11-0.12. Mon. Not. Roy. Astron. Soc. **439**, 3275–3293 (2014). doi:10.1093/mnras/stu127, 1401.4157

Wang, K., Zhang, Q., Testi, L., Wu, Y., Zhang, H., van der Tak F, Pillai, T., Wyrowski, F., Carey. S., Ragan, S., Henning, T.: The sequential growth of star formation seeds in the galactic snake: infrared dark cloud G11.11-0.12. In: Protostars and Planets VI, Heidelberg, 15–20 July 2013. Poster #1S025, p. 25

Wang, K., Zhang, Q., Wu, Y., Zhang, H.: Hierarchical fragmentation and jet-like outflows in IRDC G28.34+0.06: a growing massive protostar cluster. Astrophys. J. **735**, 64 (2011). doi:10.1088/0004-637X/735/1/64, 1105.4559

Wang, K., Zhang, Q.: Most in-depth view of the initial stages of massive clustered star formation. SMA Newsl. **18**, 9 (2014). http://www.cfa.harvard.edu/sma/newsletter

Zernickel, A., Schilke, P., Schmiedeke, A., Lis, D.C., Brogan, C.L., Ceccarelli, C., Comito, C., Emprechtinger, M., Hunter, T.R., Möller, T.: Molecular line survey of the high-mass star-forming region NGC 6334I with herschel/HIFI and the submillimeter array. Astron. Astrophys. **546** A87 (2012). doi:10.1051/0004-6361/201219803, 1208.5516

Zhang, Q., Wang, Y., Pillai, T., Rathborne, J.: Fragmentation at the earliest phase of massive star formation. Astrophys. J. **696**, 268–273 (2009). doi:10.1088/0004-637X/696/1/268, 0902.0647

Zhang, Q., Wang, K.: IRDC G030.88+00.13: a tale of two massive clumps. Astrophys. J. **733**, 26 (2011). doi:10.1088/0004-637X/733/1/26, 1103.5092

Zhang, Q., Hunter, T.R., Sridharan, T.K.: A rotating disk around a high-mass young star. Astrophys. J. Lett. **505**, L151–L154 (1998). doi:10.1086/311609

Zhang, Q., Hunter, T.R., Sridharan, T.K., Cesaroni, R.: Shock-heated NH_3 in a molecular jet associated with a high-mass young star. Astrophys J. Lett. **527**, L117–L120 (1999). doi:10.1086/312411

Zhang, Q., Hunter, T.R., Brand, J., Sridharan, T.K., Cesaroni, R., Molinari, S., Wang, J., Kramer, M.: Search for CO outflows toward a sample of 69 high-mass protostellar candidates. II. Outflow properties. Astrophys. J. **625**, 864–882 (2005). doi:10.1086/429660

Chapter 5
The Infrared Dark Cloud G30.88+0.13

Abstract Massive stars form from collapse of parsec-scale molecular clumps. How molecular clumps fragment to give rise to massive stars in a cluster with a distribution of masses is unclear. In this chapter, we search for cold cores that may lead to future formation of massive stars in a massive ($>10^3\,M_\odot$), low luminosity ($4.6\times10^2\,L_\odot$) infrared dark cloud (IRDC) G030.88+00.13. The NH_3 data from JVLA and GBT reveal that the extinction feature seen in the infrared consists of two distinctive clumps along the same line of sight. The C1 clump at $97\,\mathrm{km\,s^{-1}}$ coincides with the extinction in the *Spitzer* 8 and 24 μm. Therefore, it is responsible for the majority of the IRDC. The C2 clump at $107\,\mathrm{km\,s^{-1}}$ is more compact and has a peak temperature of 45 K. Compact dust cores and H_2O masers revealed in the SMA and JVLA observations are mostly associated with C2, and none is within the IRDC in C1. The luminosity indicates that neither the C1 nor C2 clump has yet to form massive protostars. But C1 might be at a precluster forming stage. The simulated observations rule out 0.1 pc cold cores with masses above $8\,M_\odot$ within the IRDC. The core masses in C1 and C2, and those in high-mass protostellar objects suggest an evolutionary trend that the mass of cold cores increases over time. Based on our findings, we propose an empirical picture of massive star formation that protostellar cores and the embedded protostars undergo simultaneous mass growth during the protostellar evolution.

5.1 Introduction

Formation of OB clusters has been a subject of intense studies for several decades. It is well known that massive stars form in clusters that contain a distribution of stellar masses (Lada and Lada 2003). How dense molecular clouds contract and fragment to give rise to a cluster of stars has been a subject of intense studies for decades. It is often suggested that the stellar mass at the peak of the Initial Stellar Function (IMF) is related to and perhaps is determined by the characteristic mass in molecular clouds. The value of such mass is dictated by the interplay of gravity, internal pressure due to thermal and turbulent motions, and/or magnetic fields (Larson 2005). A typical

K. Wang, *The Earliest Stages of Massive Clustered Star Formation: Fragmentation of Infrared Dark Clouds*, Springer Theses,
DOI 10.1007/978-3-662-44969-1_5

proto cluster forming clump[1] with massive young stellar objects contains $10^3\,M_\odot$ of dense molecular gas (Molinari et al. 2000; Beuther et al. 2002; Beltrán et al. 2006) within a size scale of about 1 pc. The average density ($10^5\,\mathrm{cm}^{-3}$) and temperature (15 K, Rathborne et al. 2007; Pillai et al. 2006) in these clumps yield a Jeans mass of approximately $1\,M_\odot$. This characteristic mass explains naturally the peak of the IMF in a cluster (Larson 2005).

Massive stars, on the other hand, contain masses at least an order of magnitude larger than the global thermal Jean mass in a molecular clump. This presents a theoretical puzzle, since cores and stars significantly larger than the global Jeans mass are unstable against fragmentation to less massive objects. While the origin of low mass stars could be linked to the Jeans mass, how massive stars form in a cluster has been a matter of debate. Do massive stars form in cores of Jeans mass similar to their low mass counterpart, or form in cores far more massive than the thermal Jeans mass? Observations of high-mass protostellar objects often find hot molecular cores with masses of 10–$10^2\,M_\odot$ (Garay and Lizano 1999), consistent with Jeans mass at elevated gas temperatures of over 100 K. However, the typical Jeans mass in a molecular clump prior to massive star formation is much smaller because of a lower temperature (<20 K) in these regions (Pillai et al. 2006). In a sequence of evolution, cores that give rise to massive stars must be relatively cold in the early stage due to a lack of strong stellar heating, and later enter the hot core phase characterized by strong emission from organic molecules as a result of evaporation of grain mantles and subsequent high temperature gas phase chemistry. In contrast to hot molecular cores with embedded high-mass protostars, we refer entities that ultimately form massive stars, i.e., precursors of hot molecular cores, as *cold cores*. What is typical mass of these cold cores? Do they contain $10^2\,M_\odot$ as postulated in some theoretical models (McKee and Tan 2002)? Studies of infrared dark clouds (IRDCs), massive clouds at low temperatures and high densities (Egan et al. 1998; Carey et al. 1998, 2000; Hennebelle et al. 2001; Simon et al. 2006a, b; Rathborne et al. 2006), can provide clues to these questions, and shed light on the process of massive star formation.

The studies of G28.34+0.06 and G11.11–0.12 (Chaps. 3 and 4) are insightful in revealing the properties of cold cores. Here, as part of our high resolution mini survey of IRDCs, we present results from SMA, JVLA and GBT of a massive IRDC clump G30.88+0.13 (hereafter G30.88) with a mass and luminosity similar to G28.34 and G11.11. The object, which is dark from 8 to 24 μm in the *Spitzer* images, contains a mass of $>10^3\,M_\odot$ estimated from 850 μm continuum emission, embedded in a $2\times10^4\,M_\odot$ cloud seen in CO (Swift 2009). The region, at a reported kinematic distance of 6.7–7.2 kpc, has a luminosity of only $460\,L_\odot$ (Swift 2009). Swift (2009) presented arcsecond resolution image at 870 μm with the SMA, which identified a massive core of $110\,M_\odot$. The NH_3 data from the new JVLA and GBT observations

[1] As in Chaps. 3 and 4, we refer a molecular clump as an entity with a size scale of 1 pc, which is capable of forming a cluster of stars, while a molecular core as an entity with a size scale of 0.1 pc, which forms one or a small group of stars.

reveal two velocity components along the line of sight: one component coincides with the IRDC G30.88; the other component, likely at a different distance, is associated with the massive core detected with the SMA and an H_2O maser emission. No compact cores more massive than $8\,M_\odot$ (4σ) are found to be associated with the IRDC clump. Thus, this IRDC component may represent a precluster clump.

5.2 Observations

5.2.1 Very Large Array

We observed IRDC G30.88 in the NH_3 (J, K) = (1,1) and the (2,2) lines with the Karl G. Jansky Very Large Array (JVLA) of NRAO[2] on 2010 January 8 in its D configuration. The phase center of the observations was RA(J2000) = 18:47:13.70, Dec (J2000) = −01:45:03.70. The 25 m-dish of the JVLA antennas yields a FWHM primary beam of approximately $2'$ at the observing frequencies. We employed the 2IF mode that splits the 256-channel correlator into two sections to observe the NH_3 (1,1) and (2,2) lines simultaneously in one polarization for each line. The channel separation was 24.4 KHz (∼0.3 km s^{-1} at the line frequencies). The time variation of antenna gains was calibrated using quasar J1851+005, observed at a cycle of about 20 min. The absolute flux density is established by bootstrapping to 3C286. The bandpass is calibrated via observations of 3C454.3.

Subsequently, we observed the NH_3 (J, K) = (3,3) line with the JVLA on 2010 May 09 in its D configuration. We observed two polarizations using a bandwidth of 4 MHz that splits into 256 channels. The time variation of antenna gains was calibrated using quasar J1851+005, observed at a cycle of about 6 min. The absolute flux density is established by bootstrapping to 3C48. The bandpass is calibrated via observations of 3C454.3.

Data on the 22 GHz H_2O maser transition were obtained with the JVLA on 2010 December 16 in its C configuration. We observed two polarizations using a bandwidth of 4 MHz that splits into 64 channels. The time variation of antenna gains was calibrated using quasar J1851+005, observed at a cycle of about 7 min. The absolute flux density is established by bootstrapping to 3C48. The bandpass is calibrated via observations of 3C454.3.

The visibilities were calibrated and imaged using the AIPS (Associated Universities 1999) and CASA (McMullin et al. 2007) software packages of the NRAO. The synthesis beam is about $4'' \times 3''$ for the D array data, and $2'' \times 1''$ for the C array data. The detailed observational parameters are summarized in Table 5.1.

[2] The National Radio Astronomy Observatory is operated by Associated Universities, Inc., under cooperative agreement with the National Science Foundation.

Table 5.1 JVLA, SMA, and GBT observations of G30.88+0.13

Instrument	Date of observations	Line	Bandwidth (MHz)	Spectral res. ($km\,s^{-1}$)	rms (mJy)	Angular res. ($''$)
JVLA-D	2010/01/08	NH_3 (1,1), (2,2)	3.12	0.64	2.5	4×3
	2010/05/09	NH_3 (3,3)	4	0.20	2.5	4×3
JVLA-C	2010/11/24	H_2O	4	0.84	1.5	2×1
GBT	2010/02/27	NH_3 (1,1), (2,2), (3,3), (4,4)	8	0.025	20	30
SMA compact	2007/07/07	–	4,000	–	5.7[a]	1.9×1.8
	2007/10/19	–	4,000	–		
	2008/06/02	–	4,000	–		
	2008/10/15	–	4,000	–		

[a] 1σ rms in the combined SMA image

5.2.2 Green Bank 100 m Telescope

Observations of G30.88 were carried out with the Green Bank Telescope (GBT)[1] in the NH_3 (J, K) = (1,1), (2,2), (3,3), and (4,4) transitions during 2010 February 27 through March 1, and 2010 April 29. We used the K-band receiver and a spectrometer setup in the frequency switching mode that covers four windows, each with 12.5 MHz bandwidth split into 4,096 channels. System temperatures varied from 50 to 100 K during the observations mostly due to changes in elevation. The 100 m aperture of the GBT gives a $30''$ FWHM in the primary beam. Data were processed using GBTIDL. We only present data of the (3,3) line.

5.2.3 Submillimeter Array

Observations with the SMA[3] (Ho et al. 2004) were made with 8 antennas in the compact configuration from 2007 July 7 through 2008 June 15, in a mosaic of 18 pointings by Swift (2009). The zenith opacity at 225 GHz were 0.08–0.15 for the four nights, with double sideband system temperatures of 400 during the transit. The receivers were tuned to an LO frequency of 351 GHz for the 2007 observations, and 340 GHz for the 2008 observations. Table 5.1 summarizes the main observational parameters.

The visibility data were calibrated with the IDL superset MIR package developed for the Owens Valley Interferometer. The absolute flux level is accurate to about 25 %. After calibrations in MIR, the visibility data were exported to the MIRIAD (Sault et al. 1995) format for further processing and imaging. The continuum is

[3] The Submillimeter Array is a joint project between the Smithsonian Astrophysical Observatory and the Academia Sinica Institute of Astronomy and Astrophysics, and is funded by the Smithsonian Institution and the Academia Sinica.

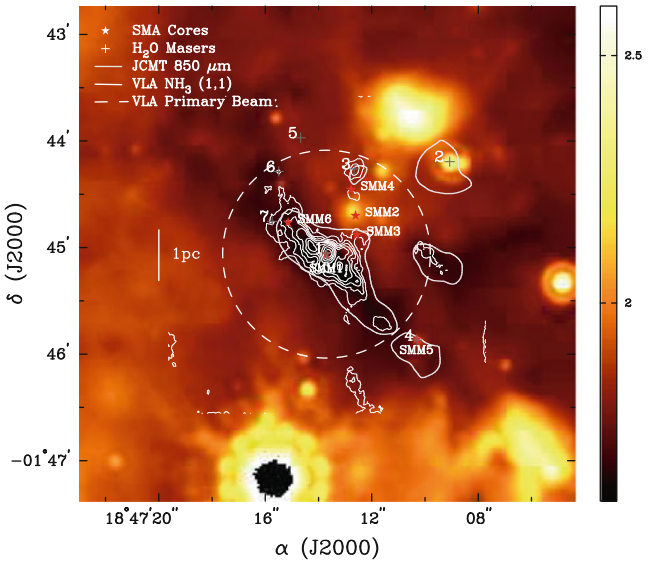

Fig. 5.1 False color 24 μm image from the *Spitzer* MIPS for the IRDC G30.88 region. The color bar indicates the logarithmic flux scale in units of MJy sr^{-1}. The *thin white* contours represent the NH_3 (1,1) emission from the JVLA. The *thick yellow* contour outlines the JCMT 850 μm continuum emission. The *dashed circle* indicates the FWHM primary beam of the NH_3 observations from the JVLA. The *star* symbols mark the dust peaks detected with the SMA. The cross symbols mark the position of the H_2O masers [*Credit* Zhang and Wang (2011), reproduced with permission of the AAS]

constructed from line free channels in the visibility domain. We combined the continuum data from four tracks, which yields a 1σ rms of 5.7 mJy and a synthesized beam of about $1.9''$ with the naturally weighting of the visibilities.

5.3 Results

5.3.1 Dense Molecular Gas and Dust Continuum

Figure 5.1 shows an overview of the G30.88 region in 24 μm obtained from the *Spitzer* MIPSGAL (Carey et al. 2009), overlaid with contours of the NH_3 (1,1) emission from the JVLA. The 850 μm continuum from the JCMT archive (see also Swift 2009) is also outlined in the yellow contour. The H_2O masers detected with the JVLA are marked with the plus sign, and the continuum sources detected with the SMA are marked by the star symbol. At 24 μm, G30.88 is dark against the galactic IR background. The IR extinction matched the NH_3 and the 850 μm continuum emission well.

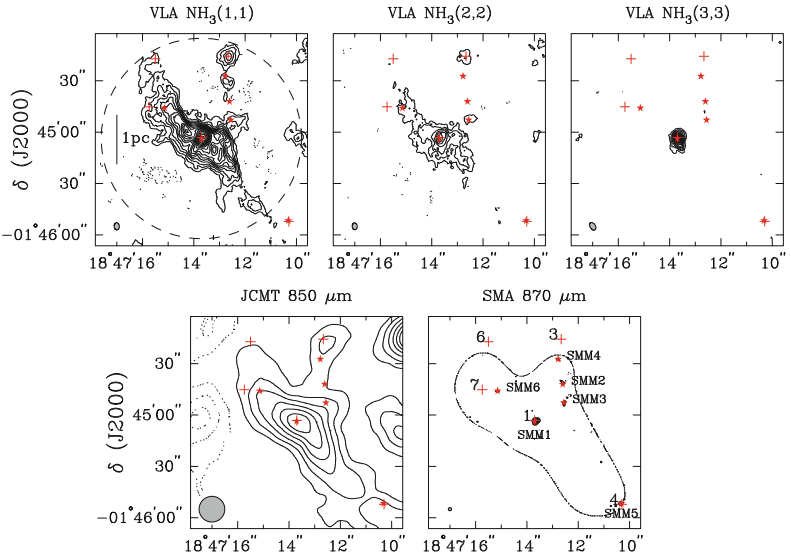

Fig. 5.2 Integrated intensity of the NH_3 (1,1), (2,2) and (3,3) emission from the JVLA, the 850 μm emission from JCMT, and 870 μm emission from the SMA. The NH_3 images are contoured at an interval of 15 mJy beam^{-1} × km s^{-1}. The JCMT data are plotted at every 10 % of the peak (2 Jy beam^{-1}). The SMA data are contoured in steps of 25 mJy beam^{-1}. The *star* symbols mark the dust peaks detected with the SMA. The *cross* symbols mark the position of the H_2O masers. The *dashed circle* indicates the FWHM primary beam of the JVLA NH_3 observations. The *thin dashed line* outlines the 100 % sensitivity of the SMA observations. The spatial resolution of each dataset is marked by the *shaded ellipse* at the *bottom-left corner* of each panel [*Credit* Zhang and Wang (2011), reproduced with permission of the AAS]

Figure 5.2 presents the integrated NH_3 $(J, K) = (1,1)$, (2,2) and (3,3) emission from the JVLA, the 850 μm continuum from JCMT, and 870 μm continuum from the SMA. The range of velocities for the integrated emission is from 95 through 110 km s^{-1}. The NH_3 data reveal a dense gas filament that follows the dust emission from JCMT (approximately 14″ resolution). It appears that the NH_3 emission is spatially extended in the (1,1) transition, and becomes far more compact in the (3,3) line. Since the NH_3 emission of the (1,1), (2,2) and (3,3) arises from energy levels of 23, 65 and 125 K, respectively, a progressively smaller spatial extent in higher excitation lines indicates that the extended NH_3 gas is at relatively lower temperatures.

The SMA observations resolved the dust emission seen at lower resolution into a dominant compact feature as reported in Swift (2009). This source is slightly resolved at a resolution of $1''.9 \times 1''.8$, and consists of two peaks. The maximum and the integrated flux of the source is 119 and 255 mJy, respectively. In addition to the dominant core which we name SMM1, there appear to be emission peaks at a level of 4–8σ rms. We identify all dust peaks above 5σ rms. Following SMM1, we name other five peaks SMM2 through SMM6, ordered in decreasing fluxes. The parameters

Table 5.2 Physical parameters of cores

Name	R.A.(J2000) (^{h} ^{m} ^{s})	Dec.(J2000) ($^{\circ}$ $'$ $''$)	Flux[a] (Jy)	Mass[b] ($M_{\odot}$)	Association[c]
SMM1	18:47:13.68	−01:45:03.6	0.26	32	C2
SMM2	18:47:12.61	−01:44:42.1	0.10	40	C2
SMM3	18:47:12.56	−01:44:52.9	0.082	33	C2
SMM4	18:47:12.78	−01:44.27.4	0.067	27	C2
SMM5	18:47:10.32	−01:45:51.7	0.060	19	C1
SMM6	18:47:15.14	−01:44:46.0	0.044	18	C2

[a] Integrated flux

[b] We adopt dust temperatures of 45 K for SMM1, and 19 K for SMM2 through SMM6. We use a dust emissivity index β of 1.5, and the dust opacity law of Hildebrand (1983). The source distances used are 6.5 kpc for the C1 clump and 7.3 kpc for the C2 clump, respectively

[c] Association of dust continuum sources with the two cloud components

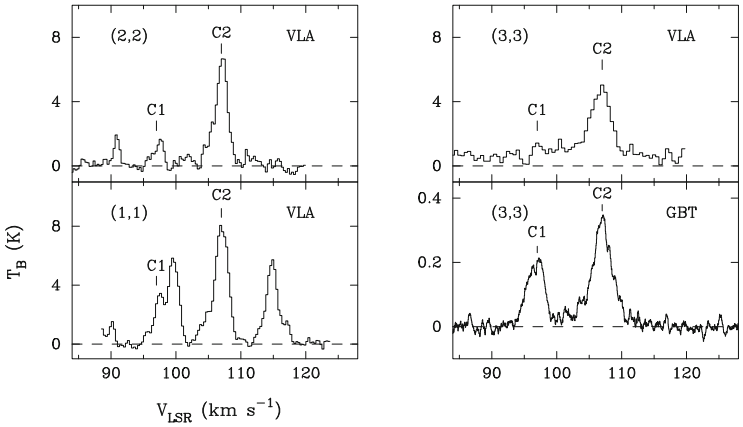

Fig. 5.3 Spectra of the NH_3 (J, K) = (1,1), (2,2) and (3,3) from the JVLA, and the NH_3 (3,3) transition from the GBT toward the position of the SMM1. The two velocity components are marked as "C1" and "C2" [*Credit* Zhang and Wang (2011), reproduced with permission of the AAS]

of the continuum sources are given in Table 5.2. Of the six sources, only SMM1 was reported in Swift (2009). With a more accurate temperature measurement (45 K, see Sect. 5.3.2) for SMM1, we find a gas mass of 32 $M_{\odot}$, about 1/3 of the value in Swift (2009). The difference is mainly due to the temperature values used. By comparing the dust peaks with the NH_3 and H_2O data, we confirm that all the dust peaks are robust detections (Sect. 5.4.1).

Figure 5.3 presents the JVLA spectra of the NH_3 (1,1), (2,2) and (3,3) transitions toward SMM1. For comparison, we also present the NH_3 (3,3) spectrum from the GBT for the same position. The NH_3 metastable lines have 18 distinctive hyperfines that normally appear in 5 separate components due to blending (Ho and Townes 1983). For the (1,1) transition, the inner and outer satellite pairs appear at 7.7 and 19.4 km s^{-1} from the main hyperfine. For the (2,2) transition, the inner

satellite pair is 16.6 km s^{-1} from the main hyperfine. Both the (1,1) and (2,2) spectra show complex features indicative of multiple velocity components. The (3,3) line, for which the inner hyperfines are further out from the main line and are much fainter, clearly reveals two line-of-sight velocity components, C1 at a $V_{\rm LSR}$ velocity of 97 km s^{-1}, and C2 at 107 km s^{-1}. The relative strength in brightness temperatures between the JVLA and GBT spectra indicates that the C2 component is spatially compact, thus is much brighter at a higher angular resolution (0.35 K in GBT versus 5.0 K in the JVLA map). On the other hand, the C1 component is more extended: It is detected by the GBT at a peak temperature of 0.2 K, and is not seen in the JVLA spectrum at a 1σ rms of 0.5 K. This comparison suggests that the faint (3,3) emission seen in C1 is spatially extended and fills the GBT beam.

5.3.2 Two Cloud Components Along Line-of-Sight

Due to the crowded hyperfine structures in the (J, K) = (1,1) line, the main hyperfine of the C1 component is blended with the first satellite hyperfine of the C2 component. Since the hyperfines of the (2,2) line are further separated, we compute its moment 0, 1, and 2 maps for the two velocity components, which are presented in Fig. 5.4. As one can see, the morphology of the C1 component is more extended, and correlates well with the extinction feature in the 24 μm image and sub-millimeter continuum emission from the JCMT. The C2 component is spatially compact and is more centrally peaked than the C1 component. An NH_3 extension to the northeast of SMM1 seen in the C2 component coincides with the IR extinction and probably contributes to the IRDC. However, the integrated flux of the extension amounts only 20 % of the integrated flux over the same area in the C1 component. Therefore, IRDC is predominantly associated with the C1 component. SMM1, on the other hand, coincides with the peak of the NH_3 emission of the C2 component, and falls in the trough in the NH_3 emission of the C1 component. Thus, SMM1 is likely associated with the 107 km s^{-1} C2 component. We will further discuss the association of other continuum sources with the two cloud components in Sect. 5.4.1.

The LSR velocities of the dense NH_3 gas yield a kinematic distance of 6.5 and 7.3 kpc for the two cloud components, respectively. The integrated fluxes of the NH_3 (2,2) emission within the IR extinction are 1.9 and 1.0 Jy km s^{-1} for the 97 and 107 km s^{-1} components, respectively. The JCMT 850 μm flux integrated within the IRDC region amounts to 9 Jy. Assuming that the dust continuum emission from the two components is proportional to the fluxes of the corresponding NH_3 emission, we obtain an 850 μm flux of 5.9 Jy for C1, and 3.1 Jy for C2, respectively. Using an average dust temperature of 19 K (see temperature estimate later in this section), a dust opacity law of Hildebrand (1983) with a spectral index of 1.5, and a dust to gas ratio of 1:100, we obtain a mass of $1.8 \times 10^3\ M_\odot$ for C1, and $1.2 \times 10^3\ M_\odot$ for C2. With a size of $40'' \times 26''$ for C1, the average density amounts to 2.0×10^4 cm^{-3} and 1.0×10^{23} cm^{-2}, respectively. The dust opacity law adopted here gives an opacity value $\kappa(850\,\mu\text{m}) = 0.015\,\text{cm}^{-2}\,\text{g}^{-1}$, consistent with that used in Swift (2009).

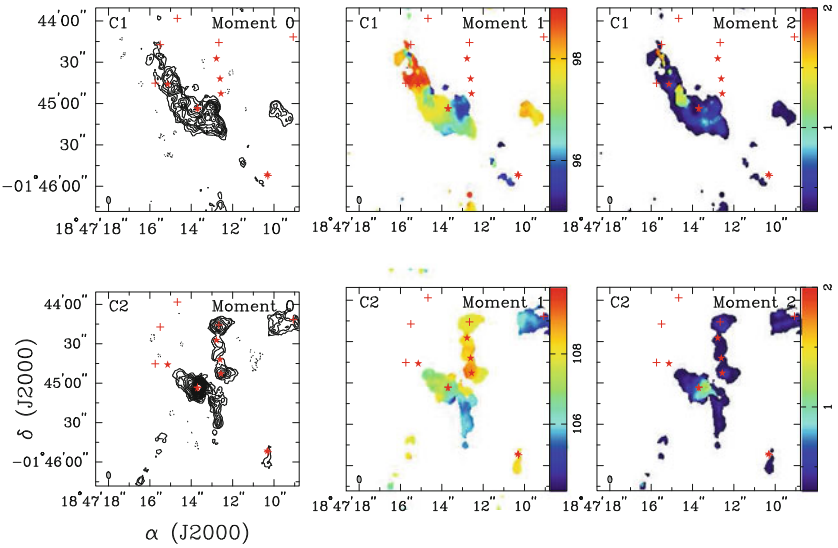

Fig. 5.4 Moment 0, 1 and 2 maps of the NH_3 (2,2) line from the JVLA for the two velocity components at 97 km s^{-1} (C1), and 107 km s^{-1} (C2) respectively. The contours for the moment 0 map starts at 4 mJy beam^{-1} × km s^{-1} and in increments of the same value. The *star* symbols mark the dust peaks detected with the SMA. The *cross* symbols mark the position of the H_2O masers. The synthesized beam is marked at the *lower-left corner* of each panel [*Credit* Zhang and Wang (2011), reproduced with permission of the AAS]

Adopting a spectral index of 2 for the dust opacity law results in a nearly factor of 2 larger in gas mass.

We estimate the NH_3 gas temperature (Ho and Townes 1983) using the JVLA data. Since the hyperfines of the C1 component is blended, we cannot reliably obtain its optical depth. Assuming optically thin emission for the C1 component, we derive a rotational temperature of 20 K. The rotational temperature $T_R(2, 2 : 1, 1)$ is related to the flux ratio of the main hyperfine component $F(1,1)$ and $F(2,2)$ (see Eq. 4 in Ho and Townes 1983) via

$$T_R(2, 2 : 1, 1) = -41.5 \div ln\{\frac{-0.283}{\tau_m(1, 1)} ln[1 - \frac{F(2, 2)}{F(1, 1)} \times (1 - e^{-\tau_m(1,1)})]\}.$$

When $F(2, 2) < F(1, 1)$, which is the case for C1, the optically thin assumption causes the rotation temperature to be over estimated. For $\tau_m(1, 1) = 1$ and 5, the gas temperature of 20 K under the optically thin assumption becomes 19 and 12 K, respectively. The NH_3 (1,1) emission likely has a moderate optical depth, thus the gas temperature of the C1 component should be lower than 20 K. For the C2 component at 107 km s^{-1}, the NH_3 emission is detected in the (3,3) line toward SMM1. We find a rotation temperature of 45 K toward SMM1, and 19 K outside of SMM1.

As shown in Fig. 5.4, the line width of the C1 component revealed by the moment two map is rather uniform, with an average line width of 0.55 km s^{-1} (or a FWHM of 1.4 km s^{-1} [4]). There appears to be two areas with slightly larger line widths of >1 km s^{-1}. The one northeast of SMM1 is due to broadening by a feature at a slightly different velocity as shown in the moment 1 image. The other one 11″ south of SMM1 has a line width of 2 km s^{-1}. This region coincides with a tentative detection of an SMA peak at RA(J2000) = 18:47:13.46, Dec(J2000) = −01:45:13.0 and with a peak flux of 27 mJy. Since the flux is lower than the 5σ cutoff limit, we do not report the source in Table 5.2. Future deeper observations will help confirming this dust peak.

The Doppler line width of the C2 component varies from 0.34 (or FWHM of 0.8 km s^{-1}) to 1.3 km s^{-1} (or FWHM of 2.5 km s^{-1}) toward the SMM1 dust peak. Both C1 and C2 components show a velocity gradient. There is a velocity shift of approximately 3 km s^{-1} over a projected length of 40″ (or 1.7 pc) along the filament in the northeast-southwest direction in C1. For C2, there appears to be a shift of 1 km s^{-1} across SMM1 at a position angle of 60°. This motion is likely due to rotation in the core similar to that found in high-mass protostellar objects (e.g. IRAS 20126+4104 Zhang et al. 1998; Keto and Zhang 2010; G10.6–0.4 Keto et al. 1987).

The NH_3 (3,3) emission is clearly detected with the GBT toward the position of SMM1. As shown in Fig. 5.3, the brightness temperatures of the (3,3) line are 0.19 K and 0.33 K for C1 and C2, respectively (using a beam efficient of 67 % for this frequency band). The (4,4) line is marginally detected only for the 107 km s^{-1} component at a brightness temperature of 0.04 K. Using these values, and assuming the same filling factor for the two transitions, we derive a gas temperature of 40 K for the C2 component, and an upper limit of 40 K for the C1 component. With a beam of 30″, we cannot constrain the spatial extent of the warm gas. Future high resolution observations with the JVLA will help revealing the spatial distribution of the warm gas.

5.3.3 H_2O *Masers*

As signposts of star formation, H_2O masers trace protostellar activities of a wide range of stellar masses (Wouterloot and Walmsley 1986; Churchwell et al. 1990; Palla and Stahler 1993; Claussen et al. 1996). Since their excitation requires high density and temperature (Elitzur et al. 1989; Felli et al. 1992), H_2O masers normally arise in the close proximity of a protostar, thus mark the position of the protostar that may not be revealed otherwise. A total of seven H_2O masers are detected in the region. Table 5.3 reports the maser positions and the peak brightness temperatures in a descending order. Figure 5.5 presents the maser spectra. The H_2O maser fluxes reported are not corrected for the primary beam of the JVLA. This is because outside the FWHM of the primary beam (∼120″), a symmetric two dimensional Gaussian

[4] If the line profile is Gaussian, the FWHM linewidth is related to the Doppler linewidth by a multiplicative factor of $2\sqrt{2ln2}$.

Table 5.3 Properties of H_2O Masers

Name	R.A.(J2000) (^{h} ^{m} ^{s})	Dec.(J2000) ($^\circ$ $'$ $''$)	Flux[a] (K)	Association[b]
1	18:47:13.70	−01:45:03.2	215.8	C2
2	18:47:09.07	−01:44:11.7	175.4	C2
3	18:47:12.67	−01:44:15.7	128.3	C2
4	18:47:10.30	−01:45:52.2	64.0	C1
5	18:47:14.67	−01:43:58.2	17.4	C1
6	18:47:15.50	−01:44:17.2	16.8	C2
7	18:47:15.74	−01:44:45.2	14.4	C2

[a] To avoid introducing additional error, brightness temperatures reported here are not corrected for the primary beam attenuation. Assuming a Gaussian primary beam with a FWHM of 120″, we find a peak brightness temperature of 808.6 K for maser feature 2, a maser knot outside the FWHM of the primary beam. The Jansky to Kelvin conversion factor is 1.11×10^3 Jy K^{-1}

[b] Association of the H_2O masers with the two cloud components

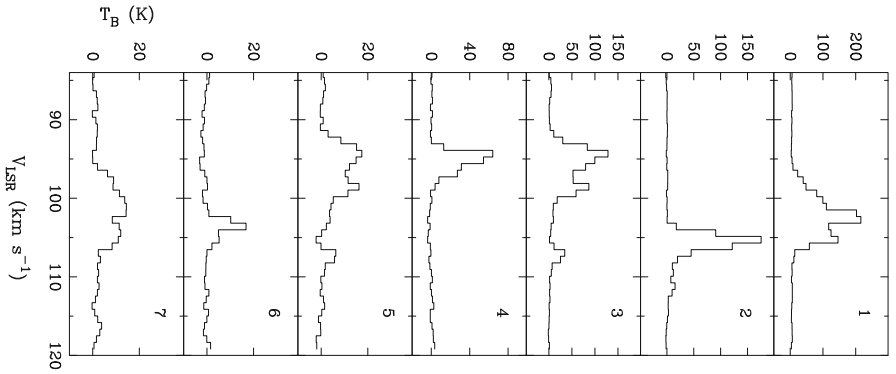

Fig. 5.5 H_2O maser spectra for maser features *1, 2, 3, 4, 5, 6,* and *7* [*Credit* Zhang and Wang (2011), reproduced with permission of the AAS]

profile does not represent the beam accurately. Applying a Gaussian correction to the data may introduce additional error in the maser brightness temperature, especially for masers outside of the FWHM of the primary beam. Should such a correction be applied to the data, the maser feature *2*, the one furthest away from the pointing center, is about a factor of 5 brighter.

As seen in Fig. 5.5, all masers exhibit complex spectra and have a broad linewidth of 3–8 km s^{-1}. Since a typical maser feature has a line width of ∼1 km s^{-1} as required by coherent amplification, the broad linewidths seen here indicate spatially unresolved maser features in the synthesized beam of 2″ × 1″. Masers *1, 2, 6* and *7* have centroid velocities close to 107 km s^{-1}. Therefore, they are likely associated with the C2 cloud component (see more discussions in Sect. 5.4.1). On the other hand, maser *4* has a centroid velocity close to 97 km s^{-1}. Thus, it is likely associated with the 97 km s^{-1} component. We caution that masers are often excited in protostellar outflows, and may have velocities offset from that of the cloud. This is shown in

masers *3,* and *5*, who have features detected close to 97 and 107 km s^{-1}. We will discuss associations of the dust continuum sources and H_2O masers with the thermal NH_3 gas in Sect. 5.4.1.

Other than SMM1 and SMM5, no other SMA dust peaks coincide with H_2O masers. On the other hand, most H_2O masers are associated with either NH_3 peaks, mid-IR sources or with the JCMT 850 μm continuum emission.

5.4 Discussion

5.4.1 *Association of Dust Peaks and* H_2O *Masers with the* NH_3 *Gas*

The continuum image from the SMA reveals at least six dust peaks with masses of 18–40 $M_\odot$. Except spatially extended CO, no other molecular line emissions are detected toward most of the dust peaks despite a total passband of 4 GHz. Thus, we cannot determine the V_{LSR} velocity of these continuum sources based on the SMA data. In this section, we compare the spatial positions of the SMA dust peaks with the NH_3 (1,1) data and the H_2O positions from the JVLA to determine the association of the sources with the two cloud components. Figure 5.6 presents the NH_3 (1,1) channel maps of the two cloud components with dust continuum peaks and H_2O maser positions. It is clear that SMM1, the dominant dust peak, coincides with the peak NH_3 emission (see velocity channels with V_{LSR} of 106.3 through 106.9 km s^{-1} and 109.1 through 109.7 km s^{-1} in Fig. 5.6). In addition, the peak velocity of the maser feature *1* is also close to the cloud velocity of component C2. Therefore, SMM1 and maser *1* are associated with the C2 component. The dust cores SMM2, SMM3, SMM4 and maser *3* are aligned in the north–south direction, and coincide with an NH_3 filament (see channels with V_{LSR} of 106.9 through 109.4 km s^{-1} in Fig. 5.6). Thus, they are likely associated with the C2 cloud component. SMM5 and maser *4* are not close in projection to any NH_3 emission in the C2 component, but is in close proximity of the extended NH_3 emission in the velocity channel of 95.8 km s^{-1}. Since SMM5/maser *4* lie outside of the primary beam of the JVLA, the extended NH_3 emission is attenuated. Given that the maser velocity is close to that of the C1 cloud, we suggest that SMM5/maser *4* are associated with the C1 component. Finally, SMM6 coincides with the NH_3 emission in V_{LSR} of 106.3 through 107.2 km s^{-1} and 97.3 through 98.2 km s^{-1}. It appears that the NH_3 (1,1) emissions in 106.3 through 107.2 km s^{-1} are more centrally peaks. Therefore, we tentatively assign SMM6 to the C2 cloud component. No strong NH_3 emissions are detected toward masers *6* and *7*. The peak velocities of the masers, however, indicate that they are associated with the C2 component. Tables 5.2 and 5.3 summarize the association of the SMA dust peaks and H_2O masers with the two cloud components.

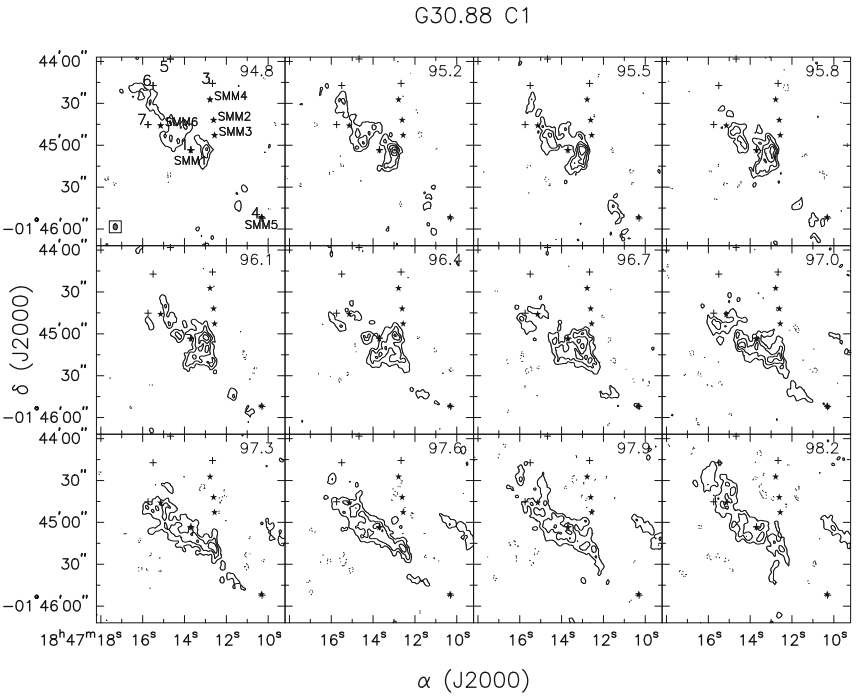

Fig. 5.6 NH_3 (1,1) emission in different velocity channels for the C1 ($97\,km\,s^{-1}$) component (*upper panel*) and C2 ($107\,km\,s^{-1}$) component (*lower panel*). The contour levels are in steps of $8\,mJy\,beam^{-1}$ starting from $8\,mJy\,beam^{-1}$. The *star* symbols mark the dust peaks detected with the SMA. The *cross* symbols mark the position of the H_2O masers. The synthesized beam is marked at the *lower-left corner* of the first panel. The corresponding LSR velocity of the channel is indicated at the *top-right corner* of each panel [*Credit* Zhang and Wang (2011), reproduced with permission of the AAS]

5.4.2 Nature of the C2 Clump: A Massive Protocluster in the Making

It appears that the majority of the SMA dust peaks (SMM1, SMM2, SMM3, SMM4, SMM6), and H_2O masers (*1, 2, 3, 6, 7*) are associated with the C2 cloud component. The presence of H_2O maser emission indicates protostellar activities. The dominant dust continuum source, SMM1, is the only continuum source associated with strong NH_3 (3,3) emission from the warm gas of 45 K. Other continuum sources are not detected in NH_3 (3,3) and are associated with gas of about 19 K.

Assuming that the dust is in a thermodynamic equilibrium with the gas in this high density environment, we approximate the dust temperature by the NH_3 gas temperature. For a dust temperature of 45 K and a source size of 1.1″ for SMM1, we estimate a luminosity of $420\,L_\odot$ for SMM1 following Scoville and Kwan (1976). This value is consistent with the luminosity of $460\,L_\odot$ in Swift (2009), derived from

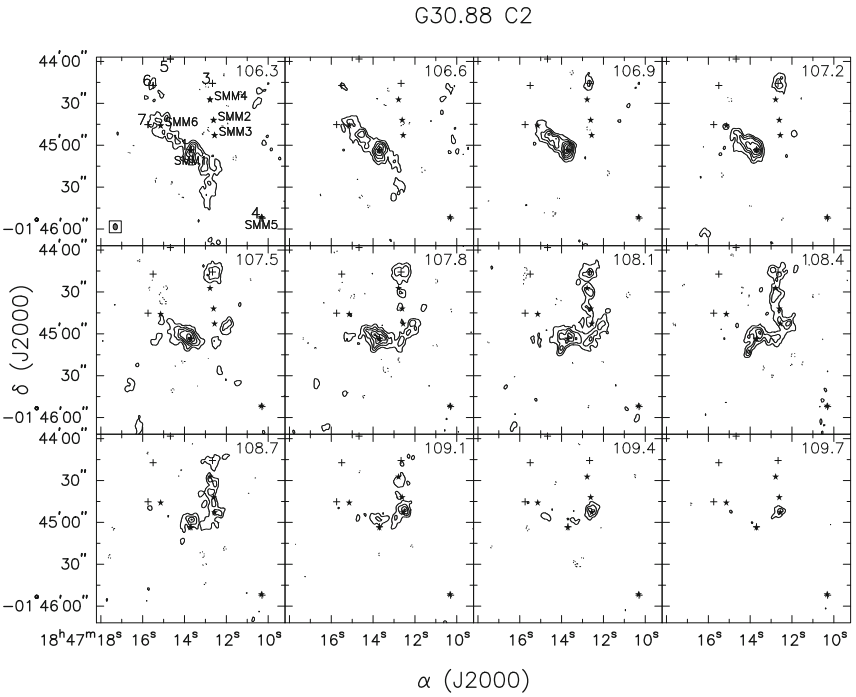

Fig. 5.6 (continued)

the spectral energy distribution. These luminosities correspond to a zero age main sequence star of $5\,M_\odot$. Since the star is under active accretion, which contributes to the total luminosity, the stellar mass is likely smaller. This young protostar is surrounded by $32\,M_\odot$ of dense gas within a scale of 0.04 pc, and several $10^3\,M_\odot$ gas on larger scales. There is a large reservoir of dense gas for the protostar to accrete. The amount of dense gas and the size scale of the molecular clump are similar to those that harbor massive stars with bright hypercompact and ultra compact HII regions. For instance, one of the nearest examples of massive star formation, Orion KL, contains a dense molecular clump of several $10^3\,M_\odot$ within a scale of 1.5 pc (Chini et al. 1997; Lis et al. 1998; Johnstone and Bally 1999). This region, with a luminosity of $10^5\,L_\odot$ is forming a cluster of stars (Beuther et al. 2005; Zapata et al. 2009). As a similar example but at a larger distance of 6 kpc, G10.6–0.4 is a bright hyper compact HII region embedded in a flattened molecular clump of $>10^3\,M_\odot$ in its inner 0.5 pc region (Keto et al. 1987; Sollins et al. 2005; Liu et al. 2010). The region has a luminosity of $9 \times 10^5\,L_\odot$, and contains a cluster of stars of $195\,M_\odot$ (Sollins et al. 2005) based on its ionization flux and total luminosity. The presence of several massive cores and H_2O masers in G30.88 C2 indicates active ongoing star formation. The similar large amount of dense gas and the low luminosity suggest that the G30.88 C2 region is a younger cousin of Orion KL and G10.6–0.4, with

the most massive protostar(s) still at an intermediate mass stage. It is reasonable to expect that it will form a massive cluster when accretion is complete.

5.4.3 Nature of the C1 Clump: A Massive Precluster Clump?

Beside the tentative detection of the dust peak at RA(J2000) = 18:47:13.46, Dec(J2000) = −01:45:13.0, there appear to be no dust continuum sources nor H_2O masers associated with the C1 cloud component within the IR dark region. Since the C1 cloud component contains $1.8 \times 10^3\ M_\odot$ over a scale of 2 pc, similar to that of C2, a lack of compact cores is intriguing. The relatively flat distribution of the NH_3 gas shown in Figs. 5.4 and 5.6 suggests that C1 is likely at an earlier evolutionary stage than C2, which makes it a candidate for probing the onset of massive star formation.

It is often debated whether massive stars form from the monolithic collapse of cold, dense molecular cores of $10^2\ M_\odot$ (e.g. Krumholz et al. 2005), or they form as an integral part of a cluster formation in a $10^3\ M_\odot$ clump (e.g. Bonnell et al. 2004; Li and Nakamura 2004). A key difference between the two pictures is whether cold cores forming massive stars acquire all the mass initially before the birth of a protostar. It appears that the C1 clump bears the closest resemblance in conditions to the onset of a massive star formation. In this clump, we find an upper limit of temperature of 20 K, an average density of $2.0 \times 10^4\ \mathrm{cm}^{-3}$, and a line width of $0.55\ \mathrm{km\,s}^{-1}$ (or FWHM of $1.4\ \mathrm{km\,s}^{-1}$). There appear to be no massive cold cores of $10^2\ M_\odot$ detected in the C1 clump, in contrast to what has be assumed in the monolithic collapse model.

However, interferometers filter out spatially extended emission. To test possible bias in the SMA observations, we examine the filtering effect and the ability in detecting faint cores by simulating observations using the JCMT image presented in Fig. 5.2. We choose a single SMA pointing centered at RA(J2000) = 18:47:12.70, Dec(J2000) = −1:45:22.90 for the simulation. A single pointing is preferred over simulating multi-field mosaic in order to avoid amplifications of noise toward the edge of the primary beam in mosaic. This particular pointing, which lies in between SMM1 and SMM5, is chosen since it is more than one primary beam away from any dust peaks. Thus, the image is less affected by the side lobes from SMM1. Figure 5.7 presents a comparison of the SMA data with simulated images. The dust emission model, shown in Fig. 5.7b, is derived from the JCMT image tapered by the SMA primary beam, approximately 34″ at 345 GHz. The peak flux of the JCMT data is 1.37 Jy at a beam of 14″. Assuming that the emission is smooth within the 14″ beam, we derive a flux of 24 mJy per $1''.9 \times 1''.8$ beam. This is about the 4σ noise level of the SMA observations. Therefore, the continuum emission would have been barely detectable with the SMA, if it is smooth and if there was no spatial filtering effect of the interferometer. A simulated observation using the JCMT data as the source model, and using the (u, v) coverage and noise characteristics of the actual SMA data is shown in Fig. 5.7c. As one can see, nearly no emission is detected due to a missing flux. However, if there were a compact core with a flux of 30 mJy embedded in the extended molecular clump as a result of core formation, SMA observations

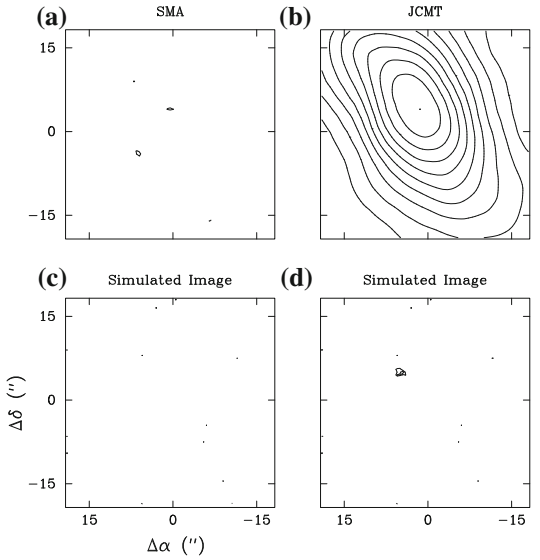

Fig. 5.7 Comparison between the SMA continuum image and simulated observations using the JCMT data as the model. Panel **a** presents the SMA continuum image at 850 μm from a single pointing centered at RA(J2000) = 18:47:12.70, Dec(J2000) = −1:45:22.90. Panel **b** presents the source model based on the JCMT data tapered by the 34″ FWHM primary beam response of the SMA. The contour levels in (**b**) are plotted at every 10 % of the peak flux of 1.37 Jy per 14″ beam. Panel **c** presents the simulated image of the model dust emission in (**b**) using the (u, v) coverage of the SMA observations. Panel **d** presents the simulated image of the model in (**b**) plus a point source of 30 mJy at (5″, 5″) offset from the pointing center. The contour levels in (**a**), (**c**), and (**d**) are plotted ±17 and ±23 mJy beam^{-1}. The synthesized beam in the simulated images is $1''.9 \times 1''.8$, same as the SMA image in Fig. 5.2 [*Credit* Zhang and Wang (2011), reproduced with permission of the AAS]

would have reliably detected such an object, as shown in Fig. 5.7d. The fact that SMA does not detect them limits the presence of compact cores of 8 $M_\odot$ at a 4σ level.

These simulated observations reinforce identification of the dust cores in the SMA image reported in Table 5.2. In addition, the simulation indicates that at very early stages of massive star formation, no massive cold cores are spatially distinct from the molecular clump. Our study of G30.88 rules out the presence of 0.1 pc cores of 8 $M_\odot$ at a 4σ level in the C1 region. This implies that cores giving birth to massive stars may not be initially massive (e.g. 10^2 $M_\odot$).

5.4.4 Fragmentation and Massive Star Formation

The core masses detected in the G30.88 C2 clump range from 18 to 40 $M_\odot$. They are likely the sites to form massive stars. A density of 2.0×10^4 cm^{-3} and a temperature

of 19 K yield a thermal Jeans mass of 5 $M_\odot$, and a Jeans length of 0.2 pc for the region. Although the SMA observations are not deep enough to detect cores of one Jeans mass, the cores revealed here are 4 times or more massive than the Jeans mass, similar to the case seen in IRDCs G28.34 (Chap. 3, Zhang et al. 2009; Wang et al. 2011, 2012) and G11.11 (Chap. 4, Wang et al. 2014; Wang and Zhang 2014), and hot core G8.68 (Longmore et al. 2011). Assuming an isotropic turbulence for which its velocity is characterized by the NH_3 line width of 0.55 km s^{-1}, we find a turbulent Jeans mass of 37 $M_\odot$, a value more compatible with the masses detected in the region. This reinforces the notion that massive cores arise from a turbulent supported fragmentation.

Similar to C2, the C1 region contains a large mass of 1.8×10^3 $M_\odot$. However, in contrast to strong dust cores revealed by the SMA, no apparent compact cores are detected at a 4σ mass of 8 $M_\odot$. Assuming that C1 and C2 represent two stages along a common evolutionary sequence, this implies that cold cores forming massive stars are probably less massive than 8 $M_\odot$ initially. These cores will continue to grow in mass by gathering material from the clump, and become compact cores as seen in C2.

5.5 Conclusions

In conclusion, this chapter presents spectral line and continuum images of a massive IRDC G30.88. The cloud appears to consist of two line-of-sight components C1 and C2 with LSR velocities of 97 and 107 km s^{-1}, respectively. Both molecular clumps are massive enough ($>10^3$ $M_\odot$) to form massive stars, but only C2 exhibits protostellar activities. Among the seven H_2O masers detected with the JVLA, five have velocities or positions associated with C2, and none is within the IRDC in C1. The SMA observations reveal six dust features SMM1 through SMM6 with masses from 18 to 40 $M_\odot$, much more massive than the thermal Jeans mass. Among the six cores, five are associated with the C2 region, and one is associated with the C1 component away from the main extinction region. The H_2O maser emission and dust peaks in the C2 clump indicate active star formation, but the low luminosity constrains the protostar(s) at an intermediate mass stage. A lack of dust peaks and H_2O maser emission in C1 puts the IRDC at an even earlier stage of star formation, and does not support the idea of cold cores of 10^2 $M_\odot$. Observations of G30.88 and other IRDCs such as G28.34 and G11.11 seem to point to the early evolution of massive star formation, in which cores gain mass from the clump while protostars accrete gas from the core.

References

Associated Universities I. AIPS: Astronomical image processing system. Astrophysics Source Code Library (1999). 9911.003

Beltrán, M.T., Brand, J., Cesaroni, R., Fontani, F., Pezzuto, S., Testi, L., Molinari, S.: Search for massive protostar candidates in the southern hemisphere. II. Dust continuum emission. Astron. Astrophys. **447**, 221–233 (2006), doi:10.1051/0004-6361:20053999. arXiv:astro-ph/0510422

Beuther, H., Schilke, P., Menten, K.M., Motte, F., Sridharan, T.K., Wyrowski, F.: High-mass protostellar candidates. II. Density sructure from dust continuum and CS emission. Astrophys. J. **566**, 945–965 (2002). doi:10.1086/338334, arXiv:astro-ph/0110370

Beuther, H., Zhang, Q., Greenhill, L.J., Reid, M.J., Wilner, D., Keto, E., Shinnaga, H., Ho, P.T.P., Moran, J.M., Liu, S.Y., Chang, C.M.: Line imaging of orion KL at 865 μm with the submillimeter array. Astrophys. J. **632**, 355–370 (2005). doi:10.1086/432974, arXiv:astro-ph/0506603

Bonnell, I.A., Vine, S.G., Bate, M.R.: Massive star formation: nurture, not nature. Mon. Not. RAS **349**, 735–741 (2004). doi:10.1111/j.1365-2966.2004.07543.x, arXiv:astro-ph/0401059

Carey, S.J., Clark, F.O., Egan, M.P., Price, S.D., Shipman, R.F., Kuchar, T.A.: The physical properties of the midcourse space experiment galactic infrared-dark clouds. Astrophys. J. **508**, 721–728 (1998). doi:10.1086/306438

Carey, S.J., Feldman, P.A., Redman, R.O., Egan, M.P., MacLeod, J.M., Price, S.D.: Submillimeter observations of midcourse space experiment galactic infrared-dark clouds. Astrophys. J. Lett. **543**, L157–L161 (2000). doi:10.1086/317270

Carey, S.J., Noriega-Crespo, A., Mizuno, D.R., Shenoy, S., Paladini, R., Kraemer, K.E., Price, S.D., Flagey, N., Ryan, E., Ingalls, J.G., Kuchar, T.A., Indebetouw, R., Billot, N., Marleau, F.R., Padgett, D.L., Rebull, L.M., Bressert, E., Ali, B., Molinari, S., Martin, P.G., Berriman, G.B., Boulanger, F., Latter, W.B., Miville-Deschenes, M.A., Shipman, R., Testi, L.: MIPSGAL: a survey of the inner galactic plane at 24 and 70 μm. Publ. ASP **121**, 76–97 (2009). doi:10.1086/596581

Chini, R., Reipurth, B., Ward-Thompson, D., Bally, J., Nyman, L.A., Sievers, A., Billawala, Y.: Dust filaments and star formation in OMC-2 and OMC-3. Astrophys. J. Lett. **474**, L135 (1997). doi:10.1086/310436

Churchwell, E., Walmsley, C.M., Cesaroni, R.: A survey of ammonia and water vapor emission from ultracompact HII regions. Astron. Astrophys. **83**, 119–144 (1990)

Claussen, M.J., Wilking, B.A., Benson, P.J., Wootten, A., Myers, P.C., Terebey, S.: A monthly survey of water masers associated with low-mass stars. Astrophys. J. Suppl. **106**, 111 (1996). doi:10.1086/192330

Egan, M.P., Shipman, R.F., Price, S.D., Carey, S.J., Clark, F.O., Cohen, M.: A population of cold cores in the galactic plane. Astrophys. J. Lett. **494**, L199+ (1998). doi:10.1086/311198

Elitzur, M., Hollenbach, D.J., McKee, C.F.: H2O masers in star-forming regions. Astrophys. J. **346**, 983–990 (1989). doi:10.1086/168080

Felli, M., Palagi, F., Tofani, G.: Molecular outflows and H2O masers—What type of connection? Astron. Astrophys. **255**, 293–322 (1992)

Garay, G., Lizano, S.: Massive stars: their environment and formation. Publ. ASP **111**, 1049–1087 (1999). doi:10.1086/316416, arXiv:astro-ph/9907293

Hennebelle, P., Pérault, M., Teyssier, D., Ganesh, S.: Infrared dark clouds from the ISOGAL survey. Constraints on the interstellar extinction curve. Astron. Astrophys. **365**, 598–611 (2001). doi:10.1051/0004-6361:20000052

Hildebrand, R.H.: The determination of cloud masses and dust characteristics from submillimetre thermal emission. Q. J. RAS **24**, 267-+ (1983)

Ho, P.T.P., Townes, C.H.: Interstellar ammonia. Ann. Rev. Astron. Astrophys. **21**, 239–270 (1983). doi:10.1146/annurev.aa.21.090183.001323

Ho, P.T.P., Moran, J.M., Lo, K.Y.: The submillimeter array. Astrophys. J. Lett. **616**, L1–L6 (2004). doi:10.1086/423245, arXiv:astro-ph/0406352

Johnstone, D., Bally, J.: JCMT/SCUBA submillimeter wavelength imaging of the integral-shaped filament in orion. Astrophys. J. Lett. **510**, L49–L53 (1999). doi:10.1086/311792

Keto, E., Zhang, Q.: The standard model of star formation applied to massive stars: accretion discs and envelopes in molecular lines. Mon. Not. RAS. **406**, 102–111 (2010). doi:10.1111/j.1365-2966.2010.16672.x, 1002.1864

Keto, E.R., Ho, P.T.P., Haschick, A.D.: Temperature and density structure of the collapsing core of G10.6-0.4. Astrophys. J. **318**, 712–728 (1987). doi:10.1086/165405

Krumholz, M.R., McKee, C.F., Klein, R.I.: The formation of stars by gravitational collapse rather than competitive accretion. Nature **438**, 332–334 (2005). doi:10.1038/nature04280

Lada, C.J., Lada, E.A.: Embedded clusters in molecular clouds. Annu. Rev. Astron. Astrophys. **41**, 57–115 (2003). doi:10.1146/annurev.astro.41.011802.094844, arXiv:astro-ph/0301540

Larson, R.B.: Thermal physics, cloud geometry and the stellar initial mass function. Mon. Not. RAS **359**, 211–222 (2005). doi:10.1111/j.1365-2966.2005.08881.x, arXiv:astro-ph/0412357

Li, Z.Y., Nakamura, F.: Magnetically regulated star formation in turbulent clouds. Astrophys. J. Lett. **609**, L83–L86 (2004). doi:10.1086/422839, arXiv:astro-ph/0405615

Lis, D.C., Serabyn, E., Keene, J., Dowell, C.D., Benford, D.J., Phillips, T.G., Hunter, T.R., Wang, N.: 350 Micron continuum imaging of the orion a molecular cloud with the submillimeter high angular resolution camera. Astrophys. J. **509**, 299–308 (1998). doi:10.1086/306500

Liu, H.B., Ho, P.T.P., Zhang, Q.: The high-velocity molecular outflows in massive cluster-forming region G10.60.4. Astrophys. J. **725**, 2190–2208 (2010). doi:10.1088/0004-637X/725/2/2190.2785

Longmore, S.N., Pillain, T., Keto, E., Zhang, Q., Qiu, K.: Is protostellar heating sufficient to halt fragmentation? A case study of the massive protocluster G8.68-0.37. Astrophys. J. **726**, 97 (2011). doi:10.1088/0004-637X/726/2/97.1442

McKee, C.F., Tan, J.C.: Massive star formation in 100,000 years from turbulent and pressurized molecular clouds. Nature **416**, 59–61 (2002). arXiv:astro-ph/0203071

McMullin, JP., Waters, B., Schiebel, D., Young, W., Golap, K.: CASA architecture and applications. In: Shaw, RA., Hill, F., Bell, DJ. (eds.) Astronomical Data Analysis Software and Systems XVI, Astronomical Society of the Pacific Conference Series, vol. 376, p. 127 (2007)

Molinari, S., Brand, J., Cesaroni, R., Palla, F.: A search for precursors of ultracompact Hii regions in a sample of luminous IRAS sources. III. Circumstellar dust properties. Astron. Astrophysics. **355**, 617–628 (2000). arXiv:astro-ph/0001231

Palla, F., Stahler, S.W.: The pre-main-sequence evolution of intermediate-mass stars. Astrophys. J. **418**, 414 (1993). doi:10.1086/173402

Pillai, T., Wyrowski, F., Menten, K.M., Krügel, E.: High mass star formation in the infrared dark cloud G11.11-0.12. Astron. Astrophysics. **447**, 929–936 (2006). doi:10.1051/0004-6361:20042145, arXiv:astro-ph/0510622

Rathborne, J.M., Jackson, J.M., Simon, R.: Infrared dark clouds: precursors to star clusters. Astrophys. J. **641**, 389–405 (2006). doi:10.1086/500423, arXiv:astro-ph/0602246

Rathborne, J.M., Simon, R., Jackson, J.M.: The detection of protostellar condensations in infrared dark cloud cores. Astrophys. J. **662**, 1082–1092 (2007). doi:10.1086/513178

Sault, RJ., Teuben, PJ., Wright, MCH.: A retrospective view of MIRIAD. In: Shaw, RA., Payne, HE., Hayes, JJE. (eds.) Astronomical Data Analysis Software and Systems IV, Astronomical Society of the Pacific Conference Series, vol. 77, p. 433 (1995). arXiv:astro-ph/0612759

Scoville, N.Z., Kwan, J.: Infrared sources in molecular clouds. Astrophys. J. **206**, 718–727 (1976). doi:10.1086/154432

Simon, R., Jackson, J.M., Rathborne, J.M., Chambers, E.T.: A catalog of midcourse space experiment infrared dark cloud candidates. Astrophys. J. **639**, 227–236 (2006a). doi:10.1086/499342, arXiv:astro-ph/0511079

Simon, R., Rathborne, J.M., Shah, R.Y., Jackson, J.M., Chambers, E.T.: The characterization and galactic distribution of infrared dark clouds. Astrophys. J. **653**, 1325–1335 (2006b). doi:10.1086/508915

Sollins, P.K., Zhang, Q., Keto, E., Ho, P.T.P.: Spherical infall in G10.6-0.4: accretion through an ultracompact H II region. Astrophys. J. Lett. **624**, L49–L52 (2005). doi:10.1086/430270, arXiv:astro-ph/0410604

Swift, J.J.: Two massive, low-luminosity cores toward infrared dark clouds. Astrophys. J. **705**, 1456–1461 (2009). doi:10.1088/0004-637X/705/2/1456, 0909.4910

Wang, K., Zhang, Q.: Most in-depth view of the initial stages of massive clustered star formation. SMA Newsl. **18**, 9-+ (2014). http://www.cfa.harvard.edu/sma/newsletter

Wang, K., Zhang, Q., Wu, Y., Zhang, H.: Hierarchical fragmentation and jet-like outflows in IRDC G28.34+0.06: a growing massive protostar cluster. Astrophys. J. **735**, 64-+ (2011). doi:10.1088/0004-637X/735/1/64, 1105.4559

Wang, K., Zhang, Q., Wu, Y., Zhang, H.: Protostellar outflow heating in a growing massive protocluster. Astrophys. J. Lett. **745**, L30 (2012). doi:10.1088/2041-8205/745/2/L30, 1112.1885

Wang, K., Zhang, Q., Testi, L., Zhang, H., Pillai, T., Wyrowski, F., Carey, S., Ragan, S.E., Henning, T.: Hierarchical fragmentation and differential star formation in the Galactic 'Snake': infrared dark cloud G11.11-0.12. Mon. Not. RAS. **439**, 3275–3293 (2014). doi:10.1093/mnras/stu127, 1401.4157

Wouterloot, J.G.A., Walmsley, C.M.: H2O masers associated with IRAS sources in regions of star formation. Astron. Astrophysics. **168**, 237–247 (1986)

Zapata, L.A., Schmid-Burgk, J., Ho, P.T.P., Rodríguez, L.F., Menten, K.M.: Explosive disintegration of a massive young stellar system in orion. Astrophys. J. Lett. **704**, L45–L48 (2009). doi:10.1088/0004-637X/704/1/L45, 0907.3945

Zhang, Q., Wang, K.: IRDC G030.88+00.13: a tale of two massive clumps. Astrophys. J. **733**, 26-+ (2011). doi:10.1088/0004-637X/733/1/26, 1103.5092

Zhang, Q., Hunter, T.R., Sridharan, T.K.: A rotating disk around a high-mass young star. Astrophys. J. Lett. **505**, L151–L154 (1998). doi:10.1086/311609

Zhang, Q., Wang, Y., Pillai, T., Rathborne, J.: Fragmentation at the earliest phase of massive star formation. Astrophys. J. **696**, 268–273 (2009). doi:10.1088/0004-637X/696/1/268, 0902.0647

Chapter 6
A New Evolutionary Picture

6.1 Thesis Summary

This thesis presents two dedicated surveys that we designed to reveal the early phase of massive clustered star formation. Our studies provide the most in-depth view so far for the stages prior to hot core phase, and suggest a new evolutionary picture, which will be tested in the coming years with observations made by major telescopes including ALMA.

The first survey used the KOSMA telescope to obtain ^{13}CO (2–1) emission toward a sample of 135 far-infrared IRAS sources, color-selected to be potential young stellar objects (YSOs). We find that the ^{13}CO line width is correlated with the bolometric luminosity of the associated YSOs, and that massive YSOs tend to form in more turbulent molecular cloud structures (Chap. 2).

The second is a mini survey which employed the SMA and JVLA to image a sample of 5 dense clumps in three well studies IRDCs, the earliest observed stages of massive star forming regions. Thanks to the high resolution images of different tracers, we are able to probe the fragmentation in dense IRDC clumps systematically for the first time. Initial results of the survey have yielded encouraging clues to the formation of massive stars. We find a common picture of hierarchical fragmentation in the different sources (Fig. 6.1): an elongated 1 pc *clump* (or "filament") encompassing $10^3\,M_\odot$ fragments into a string of regularly spaced *cores* with several $\times 10\,M_\odot$ in mass and 0.1 pc in size, and a core may further fragment into a few *condensations* with several $\times 1\ M_\odot$ in mass and 0.01 pc in size. The fragmentation likely halts at condensation scale and launches star formation, evident by outflows and masers. In some cases the clump itself is one of the fragments of a cloud-scale filamentary structure (Chap. 4). The filament fragmentation is consistent with gravitational collapse of a gas cylinder. The fragments at all scales are of super Jeans mass and are offset from heated gas. These findings challenge some of the leading theoretical models and suggest an observational-driven empirical picture of how massive star formation in a clustered environment may begin: it is initiated by hierarchical fragmentation of a

K. Wang, *The Earliest Stages of Massive Clustered Star Formation: Fragmentation of Infrared Dark Clouds*, Springer Theses,
DOI 10.1007/978-3-662-44969-1_6

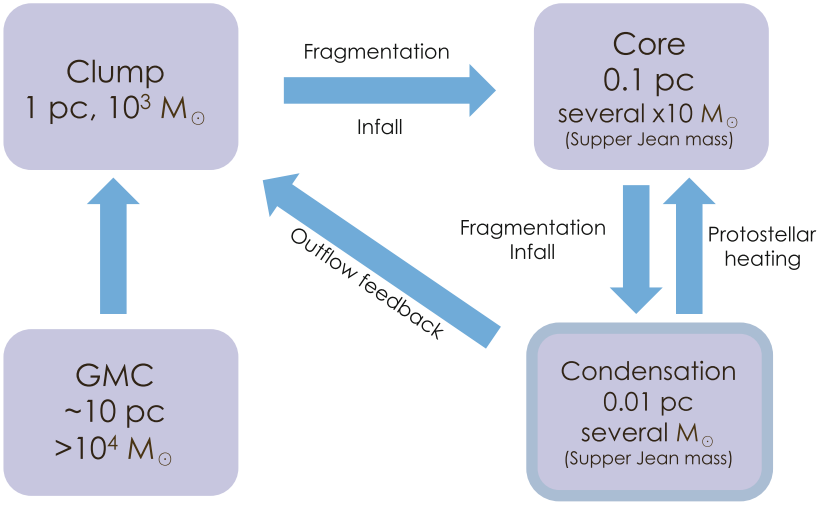

Fig. 6.1 Summary of the observed hierarchical fragmentation and star formation in IRDC clumps. This thesis focuses on detailed structure at scales <1 pc. Larger scales will be the focuses of future studies (Sect. 6.4) [*Credit* Ke Wang (ESO)]

dense filament from ∼1 pc down to 0.01 pc, and the mass build up is simultaneously fed by hierarchical accretion at similar scales (see more in Sect. 6.3).

6.2 Evolutionary Sequence

Thanks to our coordinated SMA and JVLA observations, we are now able to compare the relative evolutionary stages of the five aforementioned IRDC clumps. The basis of this comparison is that the clumps are of similar mass and size ($\sim 10^3\ M_\odot$, ∼1 pc), and that they evolve along the same path. Table 6.1 lists the observed properties of the clumps, including global properties (mass and luminosity), and star formation signatures (dense molecular lines, outflows, dense cores, cylindrical collapse, and maser detection). Among all the clumps, only G11.11-P1 shows all the star formation signatures and only G30.88-C1 shows none of the signatures. Thus, clump G30.88-C1 is the youngest and G11.11-P1 is the most evolved clump, while other clumps are in between. This relative evolution is consistent with the global luminosity-to-mass ratio (Table 6.1). Clumps with a similar mass but at a later evolutionary stage have a higher luminosity due to increased protostellar activity, resulting a higher luminosity-to-mass ratio (Sridharan et al. 2002; Molinari et al. 2008; Rathborne et al. 2010).

Our sensitive high-resolution observations offer a first view of how chemical and physical properties may evolve over time at various spatial scales in relevant to the hierarchical fragmentation. Evolution is found at scales from 1 pc clumps,

Table 6.1 Clump Properties

Clump[a]	d[b] (kpc)	M ($10^3\,M_\odot$)	L ($10^2\,L_\odot$)	Line[c]	Outflow	Dense core	Cylinder collapse	H_2O maser	CH_3OH class I	CH_3OH class II	Ref.[d]
G30.88-C1	6.5	1.8	$\ll$4.6	−	−	−	−	−	−	···	1, 2
G30.88-C2	7.3	1.2	4.6	+	−	+	+	+	−	···	1, 2
G11.11-P6	3.6	0.9	1.5	+	+	+	+	−	−	···	3, 8
G28.34-P1	4.8	1.0	1–21	−	+	+	+	+	−	···	4, 5, 6
G11.11-P1	3.6	1.2	12–14	+	+	+	+	+	+	+	3, 7, 8

[a] + means yes; − means no; . . . means no data
[b] Kinematic distance
[c] Detection of lines other than CO isotopologues
[d] References for mass and luminosity: 1. Swift (2009), 2. Zhang and Wang (2011), 3. Ragan et al. (2012), 4. Zhang et al. (2009), 5. Wang et al. (2008), 6. Rathborne et al. (2010) 7. Pillai et al. (2006), 8. Wang et al. (2014)

to 0.1 pc cores, and down to 0.01 pc condensations. The reason behind this may be due to an inhomogenous initial condition or a somewhat competitive mechanism among these star formation seeds. The spectra of these "star formation seeds", like the ones presented in Fig. 4.5 provides an excellent testbed for chemical models. In particular, comparing spectra from one region avoids systematic and calibration uncertainties, offering a powerful tool for assessing how the seeds grow chemically (e.g. Gerner et al. 2014).

6.3 A New Picture

An empirical picture of massive star formation appears to emerge from observations in the past several years. Surveys of cluster forming clumps reveal blue-red asymmetry in optically thick tracers (e.g. HCN and HCO^+, Wu and Evans 2003; Fuller et al. 2005; Wu et al. 2007), consistent with infall of 1–2 km s^{-1} at the cluster forming scale of approximately 1 pc. These surveys with single dish telescopes at $>10''$ resolution are in agreement with high resolution work in UCHII region G10.6-0.4, in which global infall is observed in both molecular and ionized gas toward a cluster of stars with a total stellar mass of 195 $M_\odot$ (Ho et al. 1986; Keto et al. 1987; Sollins et al. 2005; Liu and Ho 2010). Recently, Galván-Madrid et al. (2009) reported studies of an HII region G20.08-0.14, where inverse P-Cygni profiles are detected toward a cluster of HII regions with a linear size of 0.3 pc. The infall motion appears to continue toward a hot molecular core in which the youngest hyper compact HII region is embedded.

The wide spread infall motion, together with the fragmentation studies in this thesis suggests a picture of massive star formation in a cluster forming environment (Fig. 6.1): Collapse of 10^3 $M_\odot$ molecular clumps as a result of losing internal turbulent support leads to the formation of dense molecular cores. Among the cores, those leading to the birth of massive stars are more massive than the thermal Jeans mass. How these clumps fragment to super Jeans masses is not certain, but turbulence in these cores appears to be sufficient to provide the support. During the early evolution, cores continue to draw material from the molecular clump while the protostar embedded undergoes accretion. This picture is somewhat similar to the competitive accretion by Bonnell et al. (2004). However, it differs in two important aspects: Firstly, dense cores harboring massive stars are more massive than the thermal Jeans mass; and secondly, accretion is likely dominated by gas accretion in response to gravity as suggested in Wang et al. (2010), rather than Bondi-Hoyle accretion. This empirical picture is derived from limited observations. ALMA will deliver orders of magnitude improvement in continuum and spectral line sensitivity as compared to current (sub) mm interferometers. More importantly, large number of antennas will improve the dynamic range, and allow detection of lower mass cores in the vicinity of bright objects. It is hopeful that more sensitive studies of cold and massive molecular clumps in the future will lead to a clearer and more complete picture of cluster formation.

6.4 Future: Importance of Filaments

Elongated clumps, ridges, or filaments, are commonly seen IRDCs. In particular, all clustered star formation sites in the three IRDCs studied in this thesis are resulted from cylindrical collapse and subsequent fragmentation of dense filaments within the clouds. This indicates the importance of filaments in star formation. Since more than three decades ago, filamentary structure has been recognized as the dominant morphology of the ISM (Schneider and Elmegreen 1979). In recent years, sensitive *Spitzer* and *Herschel* surveys revealed tremendous filamentary structures widely distributed throughout the Milky Way (e.g., Devine and GLIMPSE 2004; Molinari et al. 2010). The prevalence of dense molecular filaments in the Galaxy opens a new door to understand how high-mass stars form in the context of filamentary clouds, and have triggered a renewed, increasing interest from the community.

The structure of the interstellar medium (ISM) is highly hierarchical and filamentary at all spatial scales. Its molecular content, although occupying a small volume fraction, determines its "stellar fate", i.e., to form stars. Giant molecular clouds (GMCs) are often organized in complex filamentary networks, and star-forming cores are preferentially found along the filaments due to over-density therein. After core formation, filaments then provide a preferential dimension for mass flows to feed the star forming cores (Liu et al. 2012; Peretto et al. 2014).

Recent *Herschel* observations of the nearest low-mass molecular clouds have revealed a "new paradigm" of star formation, whereby pre-existing filaments collapse due to self-gravity to give rise of star forming cores (André et al. 2013, and references therein). In the upcoming years, this new paradigm has to be tested in

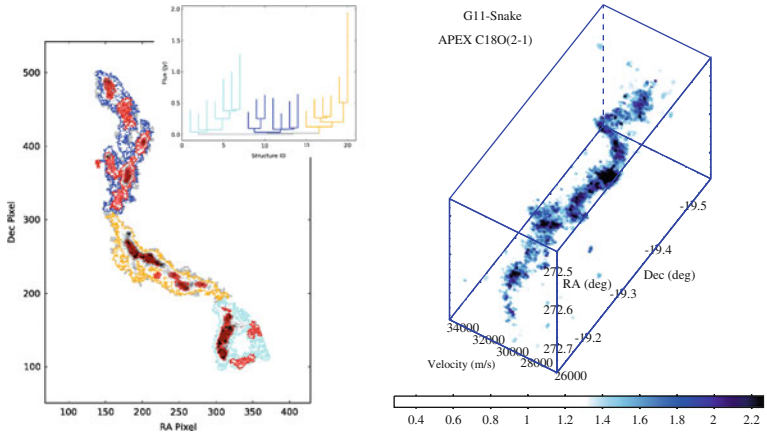

Fig. 6.2 *Left* 2D dendrogram of the Snake filament IRDC G11.11–0.12, performed on JCMT 850 μm image. Three major branches are color coded the same way as in the image and in the tree plot. The smallest identified structures (clumps) are denoted with *red* filled ellipses. *Right* 3D position-position-velocity view of the Snake, revealing a Helix-like structure [*Credit* Ke Wang (ESO)]

distant, high-mass star forming clouds. One example of such distant clouds is the IRDC G11.11–0.12. In this thesis we have resolved the 2D structure from 1 to 0.01 pc, but the entire Snake nebula has a rich structure up to 30 pc both in 2D and 3D (Fig. 6.2). Coherent filamentary structures are found up to Galactic scales on and off spiral arms (Jackson et al. 2010; Beuther et al. 2011; Battersby and Bally 2012; Li et al. 2013; Goodman et al. 2014; Ragan et al. 2014). Characterizing the kinematic connection (e.g., Hacar et al. 2013; Henshaw et al. 2014) of the multi-scale structures, from local star formation sites up to Galactic scales, will be the key to eventually reveal a full picture of Galactic star formation. This will be enabled by the synergy of (a) detailed studies of selected regions (e.g., this thesis), (b) large scale surveys[1] and (c) theoretical works (e.g. Dobbs and Pringle 2013; Smith et al. 2014; Moeckel and Burkert 2014).

References

Aguirre, J.E., Ginsburg, A.G., Dunham, M.K., Drosback, M.M., Bally, J., Battersby, C., Bradley, E.T., Cyganowski, C., Dowell, D., Evans II, N.J., Glenn, J., Harvey, P., Rosolowsky, E., Stringfellow, G.S., Walawender, J., Williams, JP.: The bolocam galactic plane survey: survey description and data reduction. Astrophys. J. Suppl. **192**, 4 (2011). doi:10.1088/0067-0049/192/1/4.0691, arXiv:1011.0691

André, P., Di Francesco, J., Ward-Thompson, D., Si, Inutsuka, Pudritz, R.E., Pineda, J.: From filamentary networks to dense cores in molecular clouds: toward a new paradigm for star formation. PPVI Rev. Chapter (2013). arXiv:1312.6232

Barnes, P.J., Yonekura, Y., Fukui, Y., Miller, A.T., Mühlegger, M., Agars, L.C., Miyamoto, Y., Furukawa, N., Papadopoulos, G., Jones, S.L., Hernandez, A.K., O'Dougherty, S.N., Tan, J.C.: The galactic census of high- and medium-mass protostars. I. Catalogs and first results from mopra HCO^+ maps. Astrophys. J. Suppl. **196**, 12 (2011). doi:10.1088/0067-0049/196/1/12, arXiv:1103.2350

Battersby, C., Bally, J.: An 80 pc long massive molecular filament in the galactic mid-plane (2012). arXiv:1208.4608

Beuther, H., Kainulainen, J., Henning, T., Plume, R., Heitsch, F.: The coalsack near and far. Astron. Astrophys. **533**, A17 (2011). doi:10.1051/0004-6361/201116746, arXiv:1107.2298

Bonnell, I.A., Vine, S.G., Bate, M.R.: Massive star formation: nurture, not nature. Mon. Not. RAS **349**, 735–741 (2004). doi:10.1111/j.1365-2966.2004.07543.x, arXiv:astro-ph/0401059

Dempsey, J.T., Thomas, H.S., Currie, M.J.: CO(3–2) high-resolution survey of the galactic plane: R1. Astrophys. J. Suppl. **209**, 8 (2013). doi:10.1088/0067-0049/209/1/8

Devine, K.E., GLIMPSE.: Dark clouds in the GLIMPSE survey. In: Bulletin of the American Astronomical Society, vol. 36, pp. 1569 (2004)

Dobbs, C.L., Pringle, J.E.: The exciting lives of giant molecular clouds. Mon. Not. RAS **432**, 653–667 (2013). doi:10.1093/mnras/stt508, arXiv:1303.4995

[1] Existing or ongoing surveys include: Hi-GAL, ATLASGAL, BGPS, GRS, SEDIGISM, ThrUMMS, CHaMP, HOPS, MALT90, SuperMALT, COHRS, CORNISH and JCMT Legacy Survey, among many others (Molinari et al. 2010; Schuller et al. 2009; Aguirre et al. 2011; Jackson et al. 2006; Barnes et al. 2011; Walsh et al. 2011; Jackson et al. 2011; Dempsey et al. 2013; Purcell et al. 2008).

Fuller, G.A., Williams, S.J., Sridharan, T.K.: The circumstellar environment of high mass protostellar objects. III. Evidence of infall? Astron. Astrophys. **442**, 949–959 (2005). doi:10.1051/0004-6361:20042110, arXiv:astro-ph/0508098

Galván-Madrid, R., Keto, E., Zhang, Q., Kurtz, S., Rodríguez, L.F., Ho, P.T.P.: Formation of an O-star cluster by hierarchical accretion in G20.08-0.14 N. Astrophys. J. **706**, 1036–1053 (2009). doi:10.1088/0004-637X/706/2/1036, arXiv:0910.2270

Gerner, T., Beuther, H., Semenov, D., Linz, H., Vasyunina, T., Bihr, S., Shirley, Y.L., Henning, T.: Chemical evolution in the early phases of massive star formation. I. Astron. Astrophys. **563**, A97 (2014). doi:10.1051/0004-6361/201322541, arXiv:1401.6382

Goodman, A.A., Alves, J.F., Beaumont, C., Benjamin, R.A., Borkin, M.A., Burkert, A., Dame, T.M., Kauffmann, J., Robitaille, T., Smith, R.J.: The Bones of the Milky Way (2014). ArXiv e-prints 1408.0001

Hacar, A., Tafalla, M., Kauffmann, J., Kovács, A.: Cores, filaments, and bundles: hierarchical core formation in the L1495/B213 Taurus region. Astron. Astrophys. **554**, A55 (2013). doi:10.1051/0004-6361/201220090, arXiv:1303.2118

Henshaw, J.D., Caselli, P., Fontani, F., Jiménez-Serra, I., Tan, J.C.: The dynamical properties of dense filaments in the infrared dark cloud G035.39-00.33. Mon. Not. RAS **440**, 2860–2881 (2014). doi:10.1093/mnras/stu446, arXiv:1403.1444

Ho, P.T.P., Klein, R.I., Haschick, A.D.: Formation of OB clusters—Radiation-driven implosion? Astrophys. J. **305**, 714–720 (1986). doi:10.1086/164285

Jackson, J.M., Finn, S.C., Chambers, E.T., Rathborne, J.M., Simon, R.: The "Nessie" nebula: cluster formation in a filamentary infrared dark cloud. Astrophys. J. Lett. **719**, L185–L189 (2010). doi:10.1088/2041-8205/719/2/L185.5492, arXiv:1007.5492

Jackson, J.M., Foster, J., Brooks, K., Rathborne, J., Longmore, S.: MALT 90: the millimeter astronomy legacy team 90 GHz survey. In: American Astronomical Society Meeting Abstracts, vol. #218, p. #217.02 (2011)

Jackson, J.M., Rathborne, J.M., Shah, R.Y., Simon, R., Bania, T.M., Clemens, D.P., Chambers, E.T., Johnson, A.M., Dormody, M., Lavoie, R., Heyer, M.H.: The boston university-five college radio astronomy observatory galactic ring survey. Astrophys. J. Suppl. **163**, 145–159 (2006). doi:10.1086/500091, arXiv:astro-ph/0602160

Keto, E.R., Ho, P.T.P., Haschick, A.D.: Temperature and density structure of the collapsing core of G10.6-0.4. Astrophys. J. **318**, 712–728 (1987). doi:10.1086/165405

Li, G.X., Wyrowski, F., Menten, K., Belloche, A.: A 500 pc filamentary gas wisp in the disk of the milky way. Astron. Astrophys. **559**, A34 (2013). doi:10.1051/0004-6361/201322411, arXiv:1310.3267

Liu, H.B., Ho, P.T.P., Zhang, Q.: The high-velocity molecular outflows in massive cluster-forming region G10.6-0.4. Astrophys. J. **725**, 2190–2208 (2010). doi:10.1088/0004-637X/725/2/2190, arXiv:1010.2785

Liu, H.B., Quintana-Lacaci, G., Wang, K., Ho, P.T.P., Li, Z.Y., Zhang, Q., Zhang, Z.Y.: The origin of OB clusters: from 10 pc to 0.1 pc. Astrophys. J. **745**, 61 (2012). doi:10.1088/0004-637X/745/1/61, arXiv:1110.1318

Moeckel, N., Burkert, A.: The formation of filamentary bundles in turbulent molecular clouds (2014). arXiv:1402.2614

Molinari, S., Swinyard, B., Bally, J., Barlow, M., Bernard, J.P., Martin, P., Moore, T., Noriega-Crespo, A., Plume, R., Testi, L., Zavagno, A., Abergel, A., Ali, B., André, P., Baluteau, J.P., Benedettini, M., Berné, O., Billot, N.P., Blommaert, J., Bontemps, S., Boulanger, F., Brand, J., Brunt, C., Burton, M., Campeggio, L., Carey, S., Caselli, P., Cesaroni, R., Cernicharo, J., Chakrabarti, S., Chrysostomou, A., Codella, C., Cohen, M., Compiegne, M., Davis, C.J., de Bernardis, P., de Gasperis, G., Di Francesco, J., di Giorgio, A.M., Elia, D., Faustini, F., Fischera, J.F., Fukui, Y., Fuller, G.A., Ganga, K., Garcia-Lario, P., Giard, M., Giardino, G., Glenn, J., Goldsmith, P., Griffin, M., Hoare, M., Huang, M., Jiang, B., Joblin, C., Joncas, G., Juvela, M., Kirk, J., Lagache, G., Li, J.Z., Lim, T.L., Lord, S.D., Lucas, P.W., Maiolo, B., Marengo, M., Marshall, D., Masi, S., Massi, F., Matsuura, M., Meny, C., Minier, V., Miville-Deschênes, M.A.,

Montier, L., Motte, F., Müller, T.G., Natoli, P., Neves, J., Olmi, L., Paladini, R., Paradis, D., Pestalozzi, M., Pezzuto, S., Piacentini, F., Pomarès, M., Popescu, C.C., Reach, W.T., Richer, J., Ristorcelli, I., Roy, A., Royer, P., Russeil, D., Saraceno, P., Sauvage, M., Schilke, P., Schneider-Bontemps, N., Schuller, F., Schultz, B., Shepherd, D.S., Sibthorpe, B., Smith, H.A., Smith, M.D., Spinoglio, L., Stamatellos, D., Strafella, F., Stringfellow, G., Sturm, E., Taylor, R., Thompson, M.A., Tuffs, R.J., Umana, G., Valenziano, L., Vavrek, R., Viti, S., Waelkens, C., Ward-Thompson, D., White, G., Wyrowski, F., Yorke, H.W., Zhang, Q.: Hi-GAL: The herschel infrared galactic plane survey. Publ. ASP. **122**, 314–325 (2010). doi:10.1086/651314, arXiv:1001.2106

Molinari, S., Pezzuto, S., Cesaroni, R., Brand, J., Faustini, F., Testi, L.: The evolution of the spectral energy distribution in massive young stellar objects. Astron. Astrophys. **481**, 345–365 (2008). doi:10.1051/0004-6361:20078661

Peretto, N., Fuller, G.A., André, P., Arzoumanian, D., Rivilla, V.M., Bardeau, S., Duarte Puertas, S., Guzman Fernandez, J.P., Lenfestey, C., Li, G.X., Olguin, F.A., Röck, B.R., de Villiers, H., Williams, J.: SDC13 infrared dark clouds: longitudinally collapsing filaments? Astron. Astrophys. **561**, A83 (2014). doi:10.1051/0004-6361/201322172, arXiv:1311.0203

Pillai, T., Wyrowski, F., Menten, K.M., Krügel, E.: High mass star formation in the infrared dark cloud G11.11-0.12. Astron. Astrophys. **447**, 929–936 (2006). doi:10.1051/0004-6361:20042145, arXiv:astro-ph/0510622

Purcell, C.R., Hoare, M.G., Diamond, P.: The CORNISH survey of the galactic plane. In: Beuther, H., Linz, H., Henning, T. (eds.) Massive Star Formation: Observations Confront Theory, Astronomical Society of the Pacific Conference Series, vol. 387, p. 389 (2008)

Ragan, S., Henning, T., Krause, O., Pitann, J., Beuther, H., Linz, H., Tackenberg, J., Balog, Z., Hennemann, M., Launhardt, R., Lippok, N., Nielbock, M., Schmiedeke, A., Schuller, F., Steinacker, J., Stutz, A., Vasyunina, T.: The earliest phases of star formation (EPoS): a Herschel key program. The precursors to high-mass stars and clusters. Astron. Astrophys. **547**, A49 (2012). doi:10.1051/0004-6361/201219232, arXiv:1207.6518

Ragan, S.E., Henning, T., Tackenberg, J., Beuther, H., Johnston, K.G., Kainulainen, J., Linz, H.: Giant molecular filaments in the milky way. **568**, A73 (2014). doi:10.1051/0004-6361/201423401arXiv:1403.1450.

Rathborne, J.M., Jackson, J.M., Chambers, E.T., Stojimirovic, I., Simon, R., Shipman, R., Frieswijk, W.: The early stages of star formation in infrared dark clouds:characterizing the core dust properties. Astrophys. J. **715**, 310–322 (2010). doi:10.1088/0004-637X/715/1/310, arXiv:1003.3193

Schneider, S., Elmegreen, B.G.: A catalog of dark globular filaments. Astrophys. J. Suppl. **41**, 87–95 (1979). doi:10.1086/190609

Schuller, F., Menten, K.M., Contreras, Y., Wyrowski, F., Schilke, P., Bronfman, L., Henning, T., Walmsley, C.M., Beuther, H., Bontemps, S., Cesaroni, R., Deharveng, L., Garay, G., Herpin, F., Lefloch, B., Linz, H., Mardones, D., Minier, V., Molinari, S., Motte, F., Nyman, L.A., Reveret, V., Risacher, C., Russeil, D., Schneider, N., Testi, L., Troost, T., Vasyunina, T., Wienen, M., Zavagno, A., Kovacs, A., Kreysa, E., Siringo, G., Weiß, A.: ATLASGAL—the APEX telescope large area survey of the galaxy at 870 μm. Astron. Astrophys. **504**, 415–427 (2009). doi:10.1051/0004-6361/200811568, arXiv:0903.1369

Smith, R.J., Glover, S.C.O., Clark, P.C., Klessen, R.S., Springel, V.: CO-dark gas and molecular filaments in Milky Way-type galaxies. Mon. Not. R. Astron. Soc. **441**, 1628–1645 (2014) doi:10.1093/mnras/stu616, arXiv:1403.1589

Sollins, P.K., Zhang, Q., Keto, E., Ho, P.T.P.: Spherical infall in G10.6-0.4: accretion through an ultracompact H II region. Astrophys. J. Lett. 624, L49–L52 (2005). doi:10.1086/430270, arXiv:astro-ph/0410604

Sridharan, T.K., Beuther, H., Schilke, P., Menten, K.M., Wyrowski, F.: High-mass protostellar candidates. I. The sample and initial results. Astrophys. J. **566**, 931–944 (2002). doi:10.1086/338332, arXiv:astro-ph/0110363

Swift, J.J.: Two massive, low-luminosity cores toward infrared dark clouds. Astrophys. J. **705**, 1456–1461 (2009). doi:10.1088/0004-637X/705/2/1456, arXiv:0909.4910

Walsh, A.J., Breen, S.L., Britton, T., Brooks, K.J., Burton, M.G., Cunningham, M.R., Green, J.A., Harvey-Smith, L., Hindson, L., Hoare, M.G., Indermuehle, B., Jones, P.A., Lo, N., Longmore, S.N., Lowe, V., Phillips, C.J., Purcell, C.R., Thompson, M.A., Urquhart, J.S., Voronkov, M.A., White, G.L., Whiting, M.T.: The H_2O Southern galactic plane survey (HOPS)—I. Techniques and H_2O maser data. Mon. Not. RAS **416**, 1764–1821 (2011). doi:10.1111/j.1365-2966.2011.19115.x, arXiv:1105.4663

Wang, P., Li, Z., Abel, T., Nakamura, F.: Outflow feedback regulated massive star formation in parsec-scale cluster-forming clumps. Astrophys. J. **709**, 27–41 (2010). doi:10.1088/0004-637X/709/1/27, arXiv:0908.4129

Wang, Y., Zhang, Q., Pillai, T., Wyrowski, F., Wu, Y.: NH_3 observations of the infrared dark cloud G28.34+0.06. Astrophys. J. Lett. **672**, L33–L36 (2008). doi:10.1086/524949, arXiv:0711.1999

Wang, K., Zhang, Q., Testi, L., Tak Fvd, WuY, Zhang, H., Pillai, T., Wyrowski, F., Carey, S., Ragan, S.E., Henning, T.: Hierarchical fragmentation and differential star formation in the galactic 'Snake': infrared dark cloud G11.11-0.12. Mon. Not. RAS **439**, 3275–3293 (2014). doi:10.1093/mnras/stu127, arXiv:1401.4157

Wu, J., Evans II, N.J.: Indications of inflow motions in regions forming massive stars. Astrophys. J. Lett. **592**, L79–L82 (2003). doi:10.1086/377679, arXiv:astro-ph/0306543

Wu, Y., Henkel, C., Xue, R., Guan, X., Miller, M.: Signatures of inflow motion in cores of massive star formation: potential collapse candidates. Astrophys. J. Lett. **669**, L37–L40 (2007). doi:10.1086/522958, arXiv:0710.2399

Zhang, Q., Wang, Y., Pillai, T., Rathborne, J.: Fragmentation at the earliest phase of massive star formation. Astrophys. J. **696**, 268–273 (2009). doi:10.1088/0004-637X/696/1/268, arXiv:0902.0647

Zhang, Q., Wang, K.: IRDC G030.88+00.13: a tale of two massive clumps. Astrophys. J. **733**, 26 (2011). doi:10.1088/0004-637X/733/1/26, arXiv:1103.5092